

**EFFECT OF GRAIN BOUNDARY &
INTERFACE MODIFICATION ON
THERMOELECTRIC PROPERTIES AT HIGH
TEMPERATURE**

**Pınar KAYA
PhD Thesis**

Eskisehir, 2017

**EFFECT OF GRAIN BOUNDARY & INTERFACE MODIFICATION ON
THERMOELECTRIC PROPERTIES AT HIGH TEMPERATURE**

Pinar KAYA

PhD Dissertation

Department of Materials Science & Engineering

Supervisor: Prof. Dr. Servet TURAN

Co-Supervisor: Prof. Dr. Joachim MAIER

Eskisehir

Anadolu University

Graduate School of Sciences

July, 2017

This thesis study has been financially supported by Anadolu University Scientific Research Projects Commission under the project number of 1307F282, “The Scientific and Technological Research Council of Turkey” for financial support through the award of 2214 International Research Fellowship Programme and “The Max Planck Institute Solid State Research under IMPRS Programme”.

**EFFECT OF GRAIN BOUNDARY & INTERFACE MODIFICATION ON
THERMOELECTRIC PROPERTIES AT HIGH TEMPERATURE**

Pinar KAYA

Doktors der Naturwissenschaft (Dr. rer. nat.)

Physikalische Festkörperchemie

Supervisor: Prof. Dr. Servet TURAN

Co-Supervisor: Prof. Dr. Joachim MAIER

Stuttgart

Max-Planck-Institut

Für Festkörperforschung

Juli, 2017

FINAL APPROVAL FOR THESIS

This thesis titled “**Effect of Grain Boundary & Interface Modification on Thermoelectric Properties at High Temperature**” has been prepared and submitted by **Pınar KAYA** in partial fulfillment of the requirements in “Anadolu University Directive on Graduate Education and Examination” for the Degree Doctor of Philosophy (PhD) Materials Science and Engineering Department has been examined and approved on 14/07/2017.

Committee Members

Signature

Member (Supervisor) : Prof. Dr. Servet TURAN

Member : Prof. Dr. Gürsoy ARSLAN

Member : Dr. Giuliano GREGORI

Member : Dr. Hanns-Ulrich HABERMEIER

Member : Dr. Gennady LOGVENOV

*Prof. Dr. Joachim Maier (Co-supervisor) attended the PhD defense without voting rights.

Director

Graduate School of Science

*To my parents Nurhan & Güven, and
My brother Çağlar Kaya*

ABSTRACT

EFFECT OF GRAIN BOUNDARY & INTERFACE MODIFICATION ON THERMOELECTRIC PROPERTIES AT HIGH TEMPERATURE

Pınar KAYA

Department of Materials Science and Engineering
Anadolu University, Graduate School of Sciences, July, 2017

Physical Chemistry of Solids

Max Planck Institute Solid State Research, July, 2017

Supervisor: Prof. Dr. Servet TURAN

Co-Supervisor: Prof. Dr. Joachim MAIER

Thermoelectric (TE) power generation is considered to be one most promising emerging clean energy technologies for harvesting electricity from heat without producing any direct emission of greenhouse gases. The conversion efficiency of a TE material is quantified by a dimensionless quantity called figure of merit, $ZT = \alpha^2 T \sigma / \kappa$. A large ZT value corresponds to a TE material with high conversion efficiency, meaning that the TE material is characterized by high Seebeck coefficient (α), high electrical conductivity (σ) and low thermal conductivity (κ). Owing to the tight interrelation between these three physical properties only very few materials currently satisfy these conditions.

New approaches suggested for further understanding the role of surfaces and interfaces on transport properties open new ways to design materials with enhanced properties and new functionalities. Additionally, the need for fundamental understanding of material properties is as equally important as the ability to develop scalable and inexpensive manufacturing process.

It is known that the electrical transport and thermoelectric properties along grain boundaries and interfaces can be improved or depressed, even by several orders of magnitudes. Therefore, microstructural design particularly of interfaces can be crucial for improving the thermoelectric functionality. From this point of view, in this thesis electric transport properties, Seebeck coefficient and thermal conductivity of oxynitride (SiAlON), carbide (SiC) and oxide (SrTiO₃, La₂CuO₄, LaNiO₃) based materials have been investigated by modifying interfaces at the micro, nano and atomic scale. It is found that segregated network approach can improve ZT unusually, La decoration tailored the electrical conductivity whilst multilayer approach is useful for tuning transport properties.

Keywords: Thermoelectricity, microstructural design, interfaces, grain boundaries, defect chemistry

ÖZET

EFFECT OF GRAIN BOUNDARY & INTERFACE MODIFICATION ON THERMOELECTRIC PROPERTIES AT HIGH TEMPERATURE

Pınar KAYA

Malzeme Bilimi ve Mühendisliği Anabilim Dalı

Anadolu Üniversitesi, Fen Bilimleri Enstitüsü, Temmuz, 2017

Max Planck Enstitüsü, Physical Chemistry of Solids Bölümü, Temmuz, 2017

Birinci Danışman: Prof. Dr. Servet TURAN

ikinci Danışman: Prof. Dr. Joachim MAIER

Günümüzde, termoelektrik (TE) enerji üretimi teknolojisi, doğal ısı kaynaklarından enerji eldesi için en umut verici yöntemlerden biri olarak kabul edilir. Termoelektrik (TE) olay kısaca, ısı enerjisinin doğrudan elektrik enerjisine dönüşmesi (termoelektrik jeneratör), ya da tersi olarak, elektrik enerjisinin sıcaklık farkına neden olması (termoelektrik soğutucu) olarak ifade edilebilir. Bir TE cihazın verimliliği, "figure of merit" olarak bilinen boyutsuz ZT parametresine bağlıdır.

Yüzeylerin ve arayüzlerin iletim özellikleri üzerindeki rolünü daha iyi anlamak için önerilen yeni yaklaşımlar, yeni ve geliştirilmiş özelliklere sahip malzemeler dizayn etmek için yeni yollar açarlar. Ayrıca, malzemelerin temel özelliklerinin anlaşılması gereksinimi, bu yüksek performanslı malzemelerden ürünler ve cihazlar geliştirmek amacıyla pahalı olmayan üretim yöntemleri geliştirmek kadar önemlidir.

Tane sınırları ve arayüzler boyunca elektriksel iletkenliğin bir kaç kat geliştirilebileceği ve engellenebileceği bilinmektedir. Bu nedenle mikroyapısal dizayn, özellikle tane sınırları ve arayüzlerin dizaynı istenilen özelliklerin iyileştirilmesi için önemli olmaktadır. Bu bakış açısıyla bu tez kapsamında oksinitrür (SiAlON), karbür (SiC) ve oksit esaslı malzemelerin (SrTiO₃, La₂CuO₄, LaNiO₃) mikro, nano ve atomik ölçüde arayüzlerin dizaynının transport özelliklerine etkisi incelenmiştir. Mikro seviyede ZT parametresini arttırmak için alternatif bir yöntem önerilmiş ve klasik kompozit yöntemlerine göre 140 kat daha fazla ZT parametresi elde edilmiştir. Nano seviyede SrTiO₃ malzemesine La dekorasyonu, tane boyutu etkisi ve sinterleme atmosferinin termoelektrik özellikler üzerindeki etkisi incelenmiştir. Atomik seviyede ise tabaka kalınlığı ve oksijen içeriğinin La₂CuO₄-LaNiO₃ çok katmanlı yapıların termoelektrik özelliklerine etkisi araştırılmıştır.

Anahtar Sözcükler: Termoelektrik, mikroyapısal dizayn, arayüzler, tane sınırları, kusur kimyası

ZUSAMMENFASSUNG

EINFLUSS VON KORNGRENZEN & GRENZFLÄCHENEFFEKTEN AUF DIE THERMOELEKTRISCHEN EIGENSCHAFTEN BEI HOHEN TEMPERATUREN

Pinar KAYA

Von der Fakultät Materialwissenschaft und Werkstofftechnik
der Universität Anadolu, Institut für Wissenschaft, Juli, 2017

Physikalische Festkörperchemie

Max-Planck-Institut für Festkörperforschung, Juli, 2017

Supervisor: Prof. Dr. Servet TURAN

Co-Supervisor: Prof. Dr. Joachim MAIER

Thermoelektrische (TE) Energieerzeugung wird als eine der vielversprechendsten sauberen Energietechnologien angesehen um Elektrizität aus Wärme zu gewinnen, ohne jegliche direkte Emission von Treibhausgasen. Der Umwandlungswirkungsgrad eines TE-Materials wird mit der dimensionslosen Größe $ZT = \alpha^2 T \sigma / \kappa$ quantifiziert, die Leistungszahl genannt wird. Ein hoher ZT-Wert entspricht einem TE-Material mit hohem Umwandlungswirkungsgrad, was bedeutet, dass das TE-Material durch einen hohen Seebeck-Koeffizienten (α), eine hohe elektrische Leitfähigkeit (σ) und eine geringe thermische Leitfähigkeit (κ) charakterisiert ist. Aufgrund der wechselseitigen Beziehung zwischen diesen drei physikalischen Größen erfüllen momentan nur sehr wenige Materialien diese Bedingungen gleichzeitig.

Neue Ansätze wurden vorgeschlagen um ein tieferes Verständnis der Rolle von Oberflächen und Grenzflächen hinsichtlich der Transporteigenschaften zu gewinnen und um neue Wege für das Konstruieren von Materialien mit verbesserten Eigenschaften und Funktionalitäten zu eröffnen. Darüber hinaus ist ein fundamentales Verständnis von Materialeigenschaften genauso wichtig wie das Vermögen skalierbare und kostengünstige Herstellungsprozesse zu entwickeln, mit dem Ziel aus diesen Hochleistungsmaterialien Bauelemente und Produkte zu entwickeln.

Es ist bekannt, dass der elektrische Transport und die thermoelektrischen Eigenschaften entlang von Korngrenzen und Grenzflächen um mehrere Größenordnungen verbessert oder abgeschwächt werden kann. Folglich kann insbesondere das mikrostrukturelle Design von Grenzflächen ausschlaggebend sein, um die thermoelektrische Funktionalität zu verbessern. Unter diesem Gesichtspunkt werden in der vorliegenden Doktorarbeit elektrische Transporteigenschaften, der Seebeck-Koeffizient und die thermische Leitfähigkeit von Oxynitrid (SiAlON), Carbid (SiC) und Oxid (SrTiO₃, La₂CuO₄, LaNiO₃) basierten Materialien untersucht, indem Grenzflächen auf der mikro, nano und atomaren Skala modifiziert wurden.

Schlagworte: Thermoelektrizität, mikrostrukturelles Design, Grenzflächen, Korngrenzen, defektchemie

ACKNOWLEDGEMENT

First of all, I would like to express my gratitude to my supervisors Prof. Dr. Servet Turan, who has given me guidance for many years and offered an insight into this field, and Prof. Dr. Joachim Maier for giving me the chance to carry out my PhD thesis in his group at Max Planck Institute Solid State Research in Stuttgart.

Second and foremost, I would like to express my deepest gratitude to my daily supervisor Dr. Giuliano Gregori. Many thanks to you not only for introducing me many different experiences but also for your trust, patience and incredible support anytime in any occasion. With your help and excellent guidance, I was able to work on different materials systems and improve my thinking way in science. I am also thankful to you for believing in me.

I would like to thank Dr. Hans Georg Libuda for inviting me for the interviews of the IMPRS for Condensed Matter Science. I will always be thankful him giving me an opportunity to be a member of this prestigious research school

I am also thankful to my jury members Dr. Hanns-Ulrich Habermeier, Dr. Gennady Logvenov and Prof. Dr. Gürsoy Arslan. I gained a different point of view from Dr. Habermeier in the field of thermoelectricity. I am also very grateful for the careful reading of this thesis and his helpful comments. Dr. Logvenov was always open to answer my questions and always supported me in terms of discussing my results in MBE grown samples. Prof. Dr. Gürsoy Arslan has been supported me in many occasions since the first year of my university education. I learned from him many things related to both my scientific and daily life. He is a person for me more than a professor who I always get his advice before making a decision.

I am indebted to Prof. Dr. Ali Arslan Kaya who has always encouraged me to overcome apparent limitations.

I would like to express my sincere thanks to Prof. Dr. Müfide Banar. Without her support, it was not possible to overcome all the bureaucratic obstacles. I will be grateful to her through all my life.

I am also thankful to Birdal Savran, Fatma Yigit and Esra Erdogan.

I would like to thank Prof. Dr. Anke Weidenkaff, Dr. Wenjie Xie, and Tianhua Zou for giving the opportunity to carry out some of my experiments in their laboratories and also for their helpful suggestions.

I would like to thank Dr. Petar Yordanov for helping me technically and scientifically in terms of transport measurements and Dr. Erhan Ayas in terms of sintering process.

I gratefully thank Dr. Wilfried Sigle, Y. Eren Suyolcu and Dr. Prof. Peter van Aken for the TEM characterization and Ute Salzberger for the TEM sample preparation.

I would like to thank Dr. Rotraut Merkle for the precious advices in various cases and for the discussions on impedance spectrometer.

Dr. Helga Hoier, Georg. Christiani, Peter Specht, Florian Kaiser, Armin Sorg, Annette Fuchs, Uwe Traub, Barbara Baum, Yvonne and Benjamin Stuhlhofer, Mustafa Cobanli are thanked for their technical support. A special thank goes to Sofia Weiglein, Birgit King, Michael Eppard, Frank Gottschalk for their precious help.

I would like to thank Dr. Hans Boschker and Prof. Dr. Jochen Mannhart for their awesome/helpful lectures on “Quantum Heterostructures and Nanoelectronics” providing unique insights into a variety of topics and a different perspective.

I would like to thank also our collaborators Prof. Dr. Bernard Keimer, Dr. Eva Benckiser, Dr. Frederic Wrobel.

I express my gratitude to my colleague Alessandro Senocrate for our fruitful discussions, which helped me to find out and to solve many problems and also for his valuable friendship. I gratefully thank also former colleagues Dr. Federico Baiutti and Dr. Michael Weissmayer who helped me during my PhD.

Y.E.S.! (Y. Eren Suyolcu) No need to write so many words, just thank you for everything since 2010...

Karo & Cido (Keskinbora family)! We have been friend since 2002! 15 years! I was very lucky that you were in Stuttgart. Thank you for making my life easier with your endless help!

Mathiass Hepting! He made my time happy in MPI-Stuttgart! I always felt his support even from far far away. Hope that you will find a way to stay in science Dr. Hepting!

Filipcigim :) (Filip Podjaski) if one would ask me who makes a smile on your face all the time, he is the one in Stuttgart for me :) We will be keep in touch!

Pascal Wittlich! He is the “SucuK” lower :D If you are with him, a fun time is guarantee for you! does not matter what you are doing (cooking, bbq, drinking, eating...). Thanks man!

At MPI Stuttgart I particularly thank Luzia Germann! It has been always fun with you :) Thank you for providing the delicious Swiss chocolates, smoothies and healthy food when I was writing the PhD thesis but even more I appreciate you for being a good friend of mine. Also would like to thank former PhD representatives + ”1”: Anna Roslawska (shopping times :D, she is a great person!, thank you for helping me whenever I need), Werner Dobrautz (He is the one I never get bored with :) and the one really understand my feelings about the life), Jachym Sykora (Where is the cake? when we are baking again? :D never forget the moment that you played my favorite song of Yiruma in Freudenstadt meeting), Rafael Balderas (He is the coolest guy in the

club with his extremely big cell phone :D one day I will visit you in Mexico ;)), Daniel Putzky (He is our "PoT: "pimp of thrust" and he makes your life energetic even in the lab.) and "1": Tomasz Michnowicz (Where is my Anna :D, he is the expert of salmon burgers and Polish vodka :). Thank you all of you guys for the good memories we had great time during our meetings at MPI and also outside of MPI.

Daniil Mantadakis! All the time on the phone on 7th floor :) of course not in the morning :D We should meet in Greece!

Onur Birsöz and my flatmates Moritz, Franzi, and Thea! My life was enjoyable at home with you guys. Our whisky and Raki nights, sucuk barbecues at our small balcony, our long Sunday breakfasts and hangovers and endless discussions to save the world. It is so valuable to have you in my life.

Yigo (Yigit Mahsereci), Find green plum for me! He is one of the unique person that I have ever met. I am happy to come across you man in my life journey!

I would like to thank once more the organization team for the defense celebration Anna, Eren, Birdal, Karo, Ekin, Umut, Luzia and Pascal and the team who prepared the PhD hat and "Nachprüfung". Everything was perfect, never forget that day!

It also was a great pleasure to meet Elisa Gilardi, Marco Arrigoni, Christopher Dietl, Matteo Minola, Maximilian Krautloher, Gideok Kim, Katrin Fuersich, Evangelos Filis-Tsirakis, Robin Wanke, Ali Teker, Wolfgang Voesch, Sibani Bisoyi Eslam Khalaf, Avaise Mohammed, Ulrike Niemann, Johannes Mitscherling, Parmida Shabestari, James Borchert, Barbara Haller, Julia Kroeger, Frederik Haase, Vesna Srot, Nilesh Vats, Robin Lingstaedt, Kristina Vaklinova, Ciro Taranto.

I also wish to thank Dr. Gamzenur Özsin, for giving me support from both Japan and Turkey and Tugce Karakulak from USA, particularly over the last one year.

Finally, I am also eternally grateful to my parents, Nurhan and Güven Kaya, and my brother Caglar Kaya for their endless support, encouragement and help throughout my life.

STATEMENT OF COMPLIANCE WITH ETHICAL PRINCIPLES AND RULES

I hereby truthfully declare that this thesis is an original work prepared by me; that I have behaved in accordance with the scientific ethical principles and rules throughout the stages of preparation, data collection, analysis and presentation of my work; that I have cited the sources of all the data and information that could be obtained within the scope of this study, and included these sources in the references section; and that this study has been scanned for plagiarism with “scientific plagiarism detection program” used by Anadolu University, and that “it does not have any plagiarism” whatsoever. I also declare that, if a case contrary to my declaration is detected in my work at any time, I hereby express my consent to all the ethical and legal consequences that are involved.

Erklärung über die Eigensändigkeit der Dissertation

Ich versichere, dass ich die vorliegende Arbeit mit dem ”*Effect of Grain boundary & Interface Modification on Thermoelectric Properties at High Temperature*” selbständig verfasst und keine andere angegebenen Quellen und Hilfsmittel benutzt habe; aus fremden Quelle entnommene Passagen und Gedanken sind als solche kenntlich gemacht.

Etik İlke Ve Kurallara Uygunluk Beyannamesi

Bu tezin bana ait, özgün bir çalışma olduğunu; çalışmamın hazırlık, veri toplama, analiz ve bilgilerin sunumu olmak üzere tüm aşamalarında bilimsel etik ilke ve kurallara uygun davrandığımı; bu çalışma kapsamında elde edilemeyen tüm veri ve bilgiler için kaynak gösterdiğimi ve bu kaynaklara kaynakçada yer verdiğimi; bu çalışmanın Anadolu Üniversitesi tarafından kullanılan “bilimsel intihal tespit programı”yla tarandığını ve hiçbir şekilde “intihal içermediğini” beyan ederim. Herhangi bir zamanda, çalışmamla ilgili yaptığım bu beyana aykırı bir durumun saptanması durumunda, ortaya çıkacak tüm ahlaki ve hukuki sonuçlara razı olduğumu bildiririm.

Name/Name/İsim: Pinar Kaya

Unterschrift/ Signature /İmza:

Datum/Date/Tarih: 14.07.2017

TABLE OF CONTENTS

	<u>Page</u>
TITLE.....	i
FINAL APPROVAL FOR THESIS.....	iii
ABSTRACT	v
ÖZET	vi
ZUSAMMENFASSUNG	vii
ACKNOWLEDGEMENT	viii
STATEMENT OF COMPLIANCE WITH ETHICAL PRINCIPLES AND RULES.....	xi
TABLE OF CONTENTS.....	xii
LIST OF FIGURES.....	xv
LIST OF TABLES	xxi
LIST OF SYMBOLS.....	xxii
1. INTRODUCTION AND THEORETICAL BACKGROUND	25
1.1. Interfaces and Interface Effects	25
1.2. Thermoelectric Phenomena	26
1.2.1. Theory of thermoelectric effect	29
1.2.2. Optimization of thermoelectric performance	31
1.3. Crystal Structures and Properties of Investigated Materials	33
1.3.1. SiAlON, SiC, TiCN.....	33
1.3.2. SrTiO ₃	36
1.3.3. La ₂ CuO ₄ and LaNiO ₃	36
1.4. Defect Chemistry of Investigated Materials	38
1.4.1. Gouy-Chapmann case	44
1.4.2. Mott-Schottky case.....	45
1.4.3. Brick layer model.....	46
1.5. Motivation	48
2. EXPERIMENTAL METHODS.....	49
2.1. Sample Preparation	49
2.1.1. Gas pressure and spark plasma sintering	49
2.1.2. Oxide molecular beam epitaxy	50
2.2. Structural and Morphological Characterization.....	51
2.2.1. RHEED	51
2.2.2. X-Ray diffraction.....	52

2.2.3. X-Ray reflectivity	54
2.2.4. Atomic force microscopy	54
2.3. Electrical Resistivity and Thermopower Measurements	55
2.3.1. AC electrochemical impedance spectroscopy	55
2.3.2. ZEM 3-M8	57
2.4. Thermal Diffusivity and Specific Heat Measurements	59
2.5. Microstructural Characterization	61
3. AN ALTERNATIVE COMPOSITE APPROACH TO TAILOR THE THERMOELECTRIC PERFORMANCE	62
3.1. Introduction & Motivation	62
3.2. Sample Preparation and Characterization.....	63
3.3. Results and Discussion.....	65
3.3.1. Comparison of 2 composite approach in TiCN- SiAlON composites..	65
3.3.2. Applying SNC method on SiC	72
3.3.3. Effect of different coating materials on thermoelectric properties in SiC composites.....	78
3.3.4. Applying the SNC method to SrTiO ₃	81
3.4. Section Conclusion	84
4. TUNING THE THERMOELECTRIC PROPERTIES BY GRAIN BOUNDARY DECORATION IN SrTiO₃.....	85
4.1. Introduction & Motivation	85
4.2. Sample Preparation and Characterization.....	87
4.3. Results and Discussion.....	89
4.3.1. Effect of La-decoration on the thermoelectric properties of SrTiO ₃	94
4.3.2. Grain size effect on the thermoelectric properties of decorated SrTiO ₃	99
4.3.3. Impedance spectroscopy analyses.....	101
4.4. Electron Microscopy Studies.....	107
4.5. Section Conclusions	113
5. EFFECT OF INTERFACE MODIFICATION ON THERMOELECTRIC PROPERTIES IN NICKELATE-CUPRATE HYBRID STRUCTURES.....	115
5.1. Introduction & Motivation	115

5.2. Growth Process & Characterization	117
5.3. Results and Discussion.....	118
5.3.1. Single phase films	119
5.3.2. Bilayers	130
5.3.3. Multilayers	133
5.4. Summary	142
6. CONCLUSIONS.....	144
7. REFERENCES.....	146
CURRICULUM VITAE	166

LIST OF FIGURES

	<u>Page</u>
Figure 1.1 Seebeck Effect	26
Figure 1.2 Peltier effect.....	27
Figure 1.3 Optimizing ZT through carrier concentration tuning.....	30
Figure 1.4 Different approaches to increase the Figure of Merit ZT of thermoelectric materials taking into account classical physics or quantum physics.....	33
Figure 1.5 Crystal structure of (a) β -SiAlON (b) α -SiAlON (O●: Al/Si, Δ ▲:O/N)....	34
Figure 1.6 Stacking sequences for five different SiC polytype.....	35
Figure 1.7 Structural models of TiCN; (a) Model I, (b) Model II and (c) Model IV	35
Figure 1.8 Structural models of SrTiO ₃	36
Figure 1.9 Structural models of La ₂ CuO ₄	37
Figure 1.10 Structural models of LaNiO ₃	38
Figure 1.11 Defect concentration of an oxide as a function of partial pressure of oxygen (Kroger-Ving diagram)	40
Figure 1.12 Defect concentration in La ₂ CuO ₄ as a function of oxygen partial pressure at given Sr-content and constant temperature.....	42
Figure 1.13 Schematic diagrams of a brick-layer model for a polycrystalline ceramic (a); an equivalent circuit model (b); impedance spectra (Nyquist plots) expected from the current path 1 (c) and 2 (d)	46
Figure 2.1 Sketch of the MBE growth chamber.....	51
Figure 2.2 RHEED image at the end of the growth of 16x(2//1.5) LNO-LCO superlattice	52
Figure 2.3 (a) Schematic overview of ULVAC ZEM-3 M8 (b) Schematic of the measurement setup (c) The ULVAC ZEM-3 M8 apparatus (d) Sample holder.....	58
Figure 2.4 (a) Schematic view of LFA-457 MicroFlash (Netzsch, Germany) (b) Image of a device analogous to the one used in this study.	60
Figure 3.1 (a-b) Schematic microstructural models of the composites investigated in this study. (c-f) SEM-BSE images of polished surface of the composites: (c) SiAlON (d) PRC-SiALON-10: 10 vol.% TiCN particle reinforced composite (e) SNC-SiALON-5: 5 vol.% TiCN segregated 3D composite (f) SNC-SiAlON-10: 10 vol.% TiCN segregated 3D network composite.	66

Figure 3.2	XRD pattern of TiCN, SiAlON and SiC based composites. (PRC:particle reinforced composite, SNC:segregated 3D network composite).	67
Figure 3.3	(a) Electrical conductivity, σ , (b)&(c) Seebeck coefficient, α , (d) Thermal conductivity, κ , (e) power factor ($\sigma \cdot \alpha^2$) and (f) figure of merit (ZT) measurement of SiAlON based composites as a function of T in He atmosphere. (The uncertainty bars are not visible for the quantities that drawn in log scale).....	69
Figure 3.4	Electrical conductivity, σ , of (a) SiAlON (b) TiCN (c) SiC (d) PRC-composite and (e) SNC-composites as a function of T.....	70
Figure 3.5	(a) Thermal diffusivity, (b) Specific heat, (c) Thermal conductivity, (d) XRD pattern and (e) TG curve taken from TiCN.....	71
Figure 3.6	XRD patterns of SiC based composites.	72
Figure 3.7	SEM-BSE image of polished surface of composites (a) SiC (b) SNC-SiC-5 and (c) SNC-SiC-10.	75
Figure 3.8	(a) Electrical conductivity, σ , (b-c) Seebeck coefficient, α , (d) Thermal conductivity, κ , (e) PF ($\sigma \cdot \alpha^2$) (f) ZT measurements of SiC based composites as a function of T. (The uncertainty bars are not visible for the quantities that drawn in log scale)	76
Figure 3.9	Comparison of SiC and SiAlON based composites (a) Electrical conductivity, σ , (b) Seebeck coefficient, α , (c) Thermal conductivity, κ , (d) PF ($\sigma \cdot \alpha^2$) (e-f) ZT measurement as a function of T. (The uncertainty bars are not visible for the quantities that drawn in log scale).....	77
Figure 3.10	SEM-BSE image of polished surface of composites (a) SNC-SiC-10TiCN, (b) PSNC-SiC-10B ₄ C, (c) PSNC-SiC-10ZrO ₂ (d) SiC-10SiC (PSNC: Partially segregated network composite.).....	78
Figure 3.11	(a) Electrical conductivity, σ ; (b-c) Seebeck coefficient, α ; (d) Thermal conductivity, κ ; (e) PF ($\sigma \cdot \alpha^2$); (f) ZT measurement of SiC based composites as a function of T.....	80
Figure 3.12	SEM-BSE images of polished surface of the composites: (a) SrTiO ₃ (b-c) SNC-STO-LSTO_oxidized (d-e-f) SNC-STO-LSTO_reduced composite.	82
Figure 3.13	(a) Electrical conductivity, σ , (b) Seebeck coefficient, α , (c) Thermal conductivity, κ , (d) PF ($\sigma \cdot \alpha^2$) (e) ZT measurement of SrTiO ₃ based	

	composites as a function of T. (The uncertainty bars are not visible for the quantities that drawn in log scale)	83
Figure 4.1	Conductivity versus oxygen partial pressure for SrTiO ₃ (at T = 544 °C).The symbols are assigned as follows: (red open squares) bulk micro-crystalline SrTiO ₃ ; (blue open triangles) grain boundaries of the micro-crystalline SrTiO ₃ ; (grey diamonds) nano-crystalline SrTiO ₃ with the effective grain size of ≈ 30 nm. The continuous green line illustrates the conductivity behavior of the micro-crystalline bulk as expected from the literature.....	87
Figure 4.2	XRD patterns of decorated SrTiO ₃ powders before and after calcination.....	89
Figure 4.3	SEM-SE image of the SrTiO ₃ samples sintered at 1673 K (a-e) Undecorated oxidized (b-f) Undecorated reduced (c-g) Decorated oxidized (d-h) Decorated reduced.	91
Figure 4.4	SEM-SE image of the SrTiO ₃ samples sintered at 1673 K (a) Decorated oxidized (b) Decorated reduced at higher magnification.	92
Figure 4.5	SEM-SE image of the SrTiO ₃ samples sintered at 1173 K (a-e) Undecorated oxidized (b-f) Undecorated reduced (c-g) Decorated oxidized (d-h) Decorated reduced.	93
Figure 4.6	Schema of predicted microstructure model (a) undecorated and (b) decorated SrTiO ₃ samples after sintering and conduction pathways according to the brick layer model (c) Reducing (d) oxidizing conditions.	94
Figure 4.7	(a) Electrical conductivity, σ , (b) Seebeck coefficient, α , (c) PF ($\sigma \cdot \alpha^2$), (d) Thermal conductivity, κ , (e) ZT measurement of undecorated (triangles) and 7.2 at.% La-decorated (squares) SrTiO ₃ sintered at 1673 K (micro-crystalline) (solid symbols) in air (oxidized) (open symbols) and 2% H ₂ -Ar mixture (reduced) as a function of T.	97
Figure 4.8	(a) Electrical conductivity, σ , (b) Seebeck coefficient, α , (c) PF ($\sigma \cdot \alpha^2$) (d) Thermal conductivity, κ , (e) ZT measurement of undecorated (triangles) and 7.2 at.% La-decorated (squares) SrTiO ₃ sintered at 1173 K (nano-crystalline) in air (oxidized) (open symbols) and 2% H ₂ -Ar mixture (reduced) (solid symbols) as a function of T.....	98
Figure 4.9	(a) Electrical conductivity, σ , (b) Seebeck coefficient, α , (c) PF ($\sigma \cdot \alpha^2$) (d) Thermal conductivity, κ , (e) ZT measurement of nano-crystalline	

	(red) and micro-crystalline (blue) decorated SrTiO ₃ sintered under oxidized (open symbols) and reduced (solid symbols) conditions as a function of T.....	100
Figure 4.10	Impedance and modulus spectra collected at 827 K in oxygen (a) and (b) undecorated oxidized nano-crystalline SrTiO ₃ (c) and (d) decorated oxidized nano-crystalline SrTiO ₃	102
Figure 4.11	Impedance and modulus spectra collected at 827 K in argon (a) and (b) undecorated reduced nano-crystalline SrTiO ₃ (c) and (d) decorated reduced nano-crystalline SrTiO ₃	103
Figure 4.12	Impedance and modulus spectra collected at 827 K in oxygen (a) and (b) undecorated oxidized micro-crystalline SrTiO ₃ (c) and (d) decorated oxidized micro-crystalline SrTiO ₃	104
Figure 4.13	Impedance and modulus spectra collected at 827 K in argon (a) and (b) undecorated reduced micro-crystalline SrTiO ₃ (c) and (d) decorated reduced micro-crystalline SrTiO ₃	105
Figure 4.14	Arrhenius plot of conductivities of micro-crystalline samples, undecorated and decorated SrTiO ₃ under oxidized and reduced condition.	106
Figure 4.15	Arrhenius plot of conductivities of nano-crystalline samples, undecorated and decorated SrTiO ₃ under oxidized and reduced condition.	106
Figure 4.16	(a) STEM HAADF (b) TEM BF images showing the porosity (blue arrows) faults (red arrows) in decorated reduced micro-crystalline sample (c) STEM-HAADF image showing the porosity In of SrTiO ₃ powder.....	108
Figure 4.17	(a) & (b) HRTEM images show the porosity (blue arrows) (c) & (d) Atomically resolved STEM HAADF images showing stacking faults (red arrows) in decorated reduced micro-crystalline sample.	109
Figure 4.18	Atomically resolved STEM HAADF images showing the porosity (dark contrasted area) (a) focused (b) 39 nm defocused in decorated reduced micro-crystalline sample.	110
Figure 4.19	Atomically resolved STEM HAADF images showing the La segregation through the grain boundaries (red arrows) in decorated reduced micro-crystalline sample.....	111

Figure 4.20	(a) STEM HAADF images (b) EELS 1D line scan (c) Relative composition in decorated reduced micro-crystalline sample.....	112
Figure 4.21	EELS 2D maps (La = blue, Sr = green) in decorated reduced micro-crystalline sample.	112
Figure 4.22	Schematic representation of the part of the $\text{La}_2\text{O}_3\text{--TiO}_2\text{--BaO--SrO}$ quaternary-phase diagram	113
Figure 5.1	The resultant final film surface morphology of LNO single phase films, as measured by AFM in panels (a), (b), (c), (d). Rms roughness values are 0.228 nm, 0.601 nm, 1.12 nm, 1.01 nm, respectively.....	119
Figure 5.2	XRD fullscan for (a) 32u.c. (b) 16u.c. (c) 8u.c (d) 4u.c. LaNiO_3 on LaSrAlO_4 (001) (S).	120
Figure 5.3	Low-angle XRR scan for (a) 32u.c. (b) 16u.c. (c) 8u.c (d) 4u.c. LaNiO_3 on LaSrAlO_4 (001) (S).....	121
Figure 5.4	(a) Seebeck coefficient (b) Electrical conductivity of LaNiO_3 with different layer thicknesses as a function of temperature.....	122
Figure 5.5	(a)-(c) Seebeck Coefficient, (b)-(d) Electrical conductivity of 32 u.c. LaNiO_3 as a function of temperature during heating cooling cycle.....	123
Figure 5.6	The resultant final film topography of LCO single phase films, as measured by AFM in panels (a), (b), (c), (d). Rms roughness values are 0.683, 0.420, 0.329 for the micrograph shown in (a), (b), (c) and (d), respectively.	124
Figure 5.7	XRD patterns of (a) 18.5u.c. (b) 12u.c. (c) 6u.c (d) 3u.c. La_2CuO_4 on LaSrAlO_4 (001) (S).....	125
Figure 5.8	Low-angle XRR scan for (a) 18.5u.c. (b) 12u.c. (c) 6u.c (d) 3u.c. La_2CuO_4 on LaSrAlO_4 (001) (S).	126
Figure 5.9	(a) Electrical conductivity and (b) Seebeck coefficient values of La_2CuO_4 with different layer thicknesses as a function of temperature.	127
Figure 5.10	(a) and(c) Seebeck coefficient data, (b) and (d) Electrical conductivity data of 18.5u.c. La_2CuO_4 as a function of temperature during heating and cooling cycle	129
Figure 5.11	XRD patterns after the measurement under He.	130

Figure 5.12	AFM micrographs of (a) LNO/LCO and (b) LCO/LNO bilayers. Rms roughness values are 0.572 nm, 0.155 nm, for the micrograph shown in (a) and (b), respectively.	130
Figure 5.13	XRD patterns for (a) LNO/LCO (b) LCO/LNO bilayers on LaSrAlO ₄ (001) (S).	131
Figure 5.14	Low-angle XRR scan for (a) LNO/LCO (b) LCO/LNO bilayers on LaSrAlO ₄ (001) (S).	131
Figure 5.15	(a) Seebeck coefficient (b) & (c) Electrical conductivity of LNO/LCO and LCO/LNO bilayers as a function of temperature.	132
Figure 5.16	AFM micrograph of LNO/LCO multilayers (a) 4x(8//6), (b) 8x(4//3), (c) 11x(3//2), (d) 16x(2//1.5). Rms roughness values are 0.228 nm, 0.601 nm, 1.12 nm, 1.01 nm, respectively.	133
Figure 5.17	XRD patterns acquired from (a) 4x(8//6), (b) 8x(4//3), (c) 11x(3//2), (d) 16x(2//1.5), multilayers grown on LaSrAlO ₄ (001) (S).	135
Figure 5.18	Low-angle XRR scan for (a)4x(8//6), (b)8x(4//3), (c)11x(3//2), (d)16x(2//1.5), multilayers on LaSrAlO ₄ (001) (S).	136
Figure 5.19	Seebeck coefficient of (8//6) bilayer, 4x(8//6) multilayer as a function of temperature obtained experimentally and calculated by applying Kirchoff's Law.	136
Figure 5.20	(a)-(b) Seebeck coefficient & Electrical conductivity during heating and (c)-(d) Seebeck coefficient & Electrical conductivity during cooling of 4x(8//6) multilayer as a function of temperature.	137
Figure 5.21	(a)-(b) Seebeck coefficient and electrical conductivity measured during heating and (c)-(d) Seebeck coefficient and electrical conductivity measured during cooling.	139
Figure 5.22	STEM images of 4x(8//6)-LCO//LNO sample which were grown on LSAO.	140
Figure 5.23	(a) Seebeck coefficient (b) Electrical conductivity during heating as a function of temperature.	141
Figure 6.1	Schematic of the summary of the findings in the thesis.	145

LIST OF TABLES

	<u>Page</u>
Table 4.1 Geometrical and absolute densities of undecorated and decorated (7.2 at% La) SrTiO ₃ samples prepared under different sintering atmospheres.	90
Table 5.1 Information of MBE-grown samples. For the Sr- δ -doped sample, 1 ml Sr indicates the presence of one monolayer of Sr-O atoms (i.e. a Sr-O plane).	118

LIST OF SYMBOLS

a	: Lattice constant
A	: Cross section area
a_{film}	: Film lattice constant
a_h	: Holes activity
$a_{substrate}$: Substrate lattice constant
$a_{V_o^{\bullet}}$: Oxygen vacancies activity
b	: Burger vector
C	: Capacitance
C_{bulk}	: Bulk capacity
C_{el}	: Capacitance of the electrodes
C_{stray}	: Stray capacitance of a measurement cell
$C_{substrate}$: Capacitance of the substrate
C_{wiring}	: Capacitance of the wires and measurement cell
C_{GB}	: Grain boundaries capacity
$c_{dop,\infty}$: Dopant bulk concentration
c_j	: Concentration of an arbitrary charge carrier j
$c_{j,\infty}$: Bulk concentration of an arbitrary charge carrier j
$c_{maj,\infty}$: Bulk concentration of the enriched charge carrier j in the Gouy – Chapmann case
d_g	: Grain size
$\Delta\phi$: Space charge potential
Δy	: Distance between electrodes
Δz	: Length of the electrode
e^j	: Electrons according to Kroeger Vink notation
e	: Electron charge, $1.602 \cdot 10^{-19}$ C
$E_{a,0}$: Activation energy
$f_{V_o^{\bullet}}$: Oxygen vacancies fugacity
F	: Faraday constant 96485 C mol ⁻¹

f	: Lattice mismatch
G^{\parallel}	: Conductance parallel to the interface
h^{\bullet}	: Holes according to Kroeger Vink notation
H_m	: Migration enthalpy
$I(t)$: Alternate current
i	: Imaginary number ($\sqrt{-1}$)
I_0	: Alternate current at time $t=0$
k	: Boltzmann constant, $1.381 \cdot 10^{-23} \text{ J K}^{-1}$
\bar{K}	: Equilibrium constant at high defects concentration
K^0	: Pre exponential factor
K_B	: Equilibrium constant of the band-band transfer reaction
K_F	: Equilibrium constant of the Frenkel reaction
K_{ox}	: Equilibrium constant of the oxidation reaction
K_{red}	: Equilibrium constant of the reduction reaction
K_S	: Equilibrium constant of the Schottky reaction
L	: Thickness of the film
$u_{V_O^{\bullet}}$: Oxygen vacancies mobility
n	: Electron concentration
p	: Hole concentration
Q	: Constant phase element
R	: Resistance
R_{bulk}	: Bulk resistance
R_{el}	: Electrodes resistance
R_{GB}	: Grain boundaries resistance
$R_{multilayer}$: Total resistance of a multilayer
R_q	: Root Mean Square
$R_{substrate}$: Substrate resistance
R_{wiring}	: Resistance of the wires and measurement cell
t	: Time

T	: Absolute temperature
$V_O^{\bullet\bullet}$: Oxygen vacancies according to Kroeger Vink notation
$V_{Ti}^{\bullet\bullet}$: Titanium vacancies according to Kroeger Vink notation
$V_{Sr}^{\bullet\bullet}$: Strontium vacancies according to Kroeger Vink notation
Y^{\parallel}	: Sheet conductance
Y^{\parallel}_{∞}	: Bulk sheet conductance
Z^*	: Impedance
Z'	: Real part of the Impedance
Z''	: Imaginary part of the Impedance
ϵ_{bulk}	: Bulk relative permittivity
ϵ_{GB}	: Grain boundaries relative permittivity
λ^*	: Space charge width in the Mott – Schottky case,
λ	: Debye length
μ_j^0	: Standard chemical potential of an arbitrary mobile defect j
μ'_j	: Chemical potential of an arbitrary mobile defect j
μ_j	: Electrochemical potential of an arbitrary mobile defect j
ϕ	: Electrostatic potential
ρ	: Local charge density
σ^{\parallel}	: Conductivity parallel to the interface
σ_{bulk}	: Bulk electrical conductivity
σ	: Total electrical conductivity
κ	: Total thermal conductivity
α	: Seebeck coefficient
τ	: Relaxation time constant
θ	: Bragg angle
Θ	: Degree of influence in a symmetrical Gouy Chapmann case

1. INTRODUCTION AND THEORETICAL BACKGROUND

1.1. Interfaces and Interface Effects

The structure and properties of interfaces influence almost all properties of materials. An interface is the cutting plane between two dissimilarly oriented perfect crystals and/or between two chemically different crystals. In other words, an interface is a crystallographic or chemical discontinuity. In terms of crystal structure and chemistry of adjacent crystals, interfaces can be classified into homophase and heterophase boundaries [1]. Homophase boundaries form between grains of identical crystal structure and composition but different orientation, e.g., grain boundaries. On the other hand heterophase boundaries form between regions of different crystal structure and/or chemical composition, e.g., interphase boundaries [2–5].

A grain boundary in a solid crystalline material is a region separating two parts (grains) of the same phase. These two grains differ in mutual orientations and the grain boundary thus represents a transition region, where the atoms are shifted from their regular positions as compared to the crystal interior [6–8]. Thus grain boundaries represent the decisive 2-dimensional defects in polycrystalline materials and can act as sources and sinks for vacancies at high temperatures. Due to the broken lattice symmetry, grain interior and grain boundaries are charged differently to ensure electroneutrality. As electrical conductivity depends on both the density and the mobility of the charge carriers in a material the local charge changes cause rearrangements of the mobile defects and form space charge layers. Whether such core effects or space-charge effects are important for the transport depends on the parameters of the materials and the current direction. In nanosized electrical conduction properties may drastically change due to the fact that boundary properties surpass the bulk and interfaces are so closely spaced that their influence on the overall properties of the material can be significant, if not predominant.

Defect chemistry is the key to the understanding of the ionic and electronic transport properties of solids. Understanding the effect of reduction in grain size on electrical conductivity and effect of redistribution of interfaces not only grain boundaries but also interphase boundaries allow the elucidation of defect chemistry on boundary layers [9–14]. *Tschöpe et. al.* reported that the grain size of nano-crystalline CeO₂ has a significant impact on the magnitude and activation energy of electrical conductivity and described the effects by a model, which takes into account space charge layers along grain boundaries [15]. *Kim et. al.* showed that undoped CeO₂ changes its

conduction mechanism from ionic to electronic when the grain size is reduced [16]. The striking result on the transition from macroscopic to mesoscopic nano-crystalline SrTiO₃ has been reported by *Lupetin et. al* [17].

An impressive example of true size effect on an interface boundary is epitaxially grown ionic heterolayers of CaF₂/BaF₂ which show increased ionic conductivity with decreasing layer thickness [18]. Another example is represented by *Gilardi* [19], in Y₂Zr₂O₇ based heterostructures, enhanced interfacial conductance between film and substrate occurs due to the increase of the mobile charge carrier concentration (owing to space charge effects) and their improved mobility.

1.2. Thermoelectric Phenomena

Thermoelectric (TE) power generation is based on the Seebeck effect, the phenomenon that an electromotive force (voltage) develops when a material is exposed to a temperature gradient. The thermoelectric effect was discovered by Thomas Seebeck in 1821 by noticing a potential difference between two ends of a metal bar when the metal bar is placed in the temperature gradient along its length. The same phenomenon was discovered later for a closed loop of two dissimilar metals in the presence of a temperature difference between the junctions as shown in Figure 1.1.

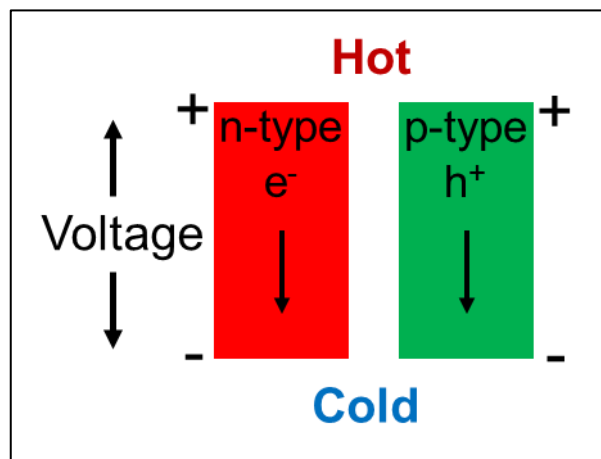


Figure 1.1 Seebeck Effect

The Seebeck-coefficient describes the relation between an electrical current voltage generated by a temperature gradient. In the presence of temperature difference, charge carriers (electrons or holes) tend to diffuse from the hot side to the cold side, hence, creating an internal electric field and building up a thermoelectric

voltage. The internal electric field thus developed opposes the further movement of charge carriers to the cold side when there is an equal amount of charge carriers diffusing back to the hot side. At the equilibrium stage, an increase in the temperature difference is needed to resume the transfer of charge carriers to the cold end to further increase the thermoelectric voltage. The potential difference $V = (\Delta\varphi)$, across the sample caused by the temperature difference ΔT is directly proportional to ΔT and connected via the Seebeck-coefficient α (Equation 1.1).

$$V = (\Delta\varphi) = -\alpha \Delta T \quad (1.1.)$$

The inversion of the Seebeck-effect is the Peltier effect named after Jean Peltier who first observed this phenomenon in 1834. When an electric current pass through junctions of two dissimilar materials such as metals or semiconductors, heat will be absorbed at one junction and cooling will be developed at the other junction as shown in Figure 1.2.

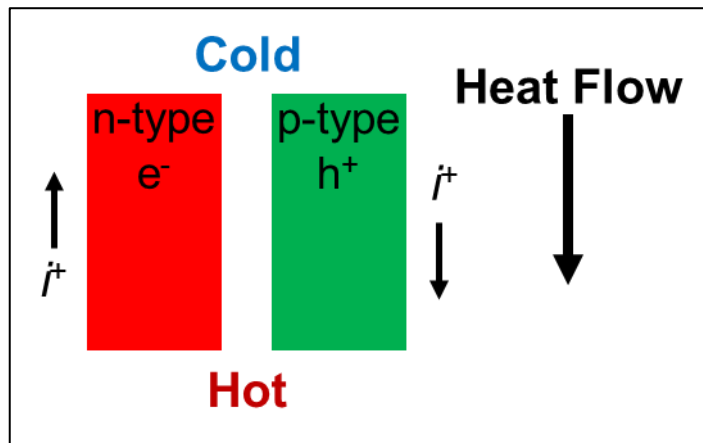


Figure 1.2 Peltier effect

In contrast to the Seebeck-effect, which also emerges in an open circuit, the Peltier-effect is only present in a closed conductor ring. The ratio between the induced current I and the transported heat Q is expressed by the Peltier-coefficient Π and the following expression

$$Q = \Pi \cdot I \quad (1.2.)$$

The third thermoelectric effect is called Thomson effect, named after William Thomson in 1851. Every current carrying conductor when subjected to a temperature

gradient absorbs or emits heat depending on the material. The Thomson coefficient, τ for a conductor carrying current I , can be defined as,

$$dQ = \tau \cdot I \cdot dT \quad (1.3.)$$

The absolute thermoelectric coefficients also obey the Kelvin relationships;

$$\tau = T \frac{\Delta\alpha}{\Delta T} \quad (1.4.)$$

$$\Pi = \alpha T \quad (1.5.)$$

Edmund Altenkirch was the first to use the constant property model to derive the maximum efficiency of a thermoelectric generator (1909) as well as the performance of a cooler (1911) when the design and operating conditions are fully optimized [20,21]. The relation between the material properties and performance later developed into modern theory of thermoelectricity using the concept of the 'figure of merit' ZT, was introduced by Abram Fedorovich Ioffe in 1949. Ioffe was one of the first to promote the use of alloying to reduce lattice thermal conductivity by point defects. In the 1930s, Maria Telkes made a thorough study on the PbS and Zn Sb materials, which had already been observed by Seebeck more than a century ago, and in her report these materials "were stated to produce the best couple for thermoelectric energy conversion" Telkes is known for creating the first (solar) TE power generator in 1947 and the first TE refrigerator in 1953 using the principles of semiconductor thermoelectricity.

One of the first demonstrations of 0 °C cooling was by H. Julian Goldsmid in 1954 using thermoelements based on Bi₂Te₃. Goldsmid was one of the first to utilize the thermoelectric quality factor, identifying the importance of high mobility and effective mass combination and low lattice thermal conductivity in semiconductors that when properly doped would make good thermoelectric materials [22].

In 1995, Glen Slack summarized the material requirements succinctly in the "phonon-glass electron-crystal" concept that the phonons should be disrupted like in a glass but the electrons should have high mobility like in crystalline semiconductors [23]. In 2007, *Dresselhaus et al.* [24] summarized the recent advances up to date in the field of low-dimensional thermoelectrics and showed that nanoparticles also perform an energy-filtering effect that preferentially scatters those phonons that contribute strongly to the thermal conductivity. In 2008, *Snyder and Toberer* [25] mentioned that even though a high-ZT device based on these principles has yet to be demonstrated,

predictions have stimulated a new wave of interest in complex thermoelectric materials. Current concepts based on nanostructuring that affects the design strategies up to date is presented by *Kanatzidis* [26].

1.2.1. Theory of thermoelectric effect

The potential of a material for thermoelectric (TE) applications, both power generation and refrigeration, is determined in general by a measure of material's dimensionless figure of merit, ZT, defined as

$$ZT = \frac{\alpha^2 \sigma}{\kappa_L + \kappa_e} T \quad (1.6.)$$

To maximize the thermoelectric figure of merit (ZT) of a material, a large thermopower (absolute value of the Seebeck coefficient), high electrical conductivity, and low thermal conductivity are required. As these transport characteristics depend on interrelated material properties, a number of parameters need to be optimized to maximize ZT.

The Seebeck effect of a material is caused by two factors: charge carrier diffusion and phonon drag [27]. Hot carriers diffuse from the hot end to the cold end, because there is a lower density of hot carriers at the cold end of the materials, and vice versa. The movement of heat, in the form of hot charge carriers, from one end to the other is a heat current and an electric current as charge carriers are moving. To ensure that the Seebeck coefficient is large, there should only be a single type of carrier [25]. Mixed n-type and p-type conduction will lead to both charge carriers moving to the cold end, cancelling out the induced Seebeck voltages. Low carrier concentration insulators and even semiconductors have large Seebeck coefficients; (see Eq. (1.7)) (Mott formula) where n is the carrier concentration and m^* is the effective mass of the carrier. However, low carrier concentration also results in low electrical conductivity; (see Eq. (1.8)) where the electrical conductivity (σ) is related to n through the carrier mobility μ :

$$\alpha = \frac{8 \pi^2 k_B^2}{3 e h^2} m^* T \left(\frac{\pi}{3 n} \right)^{2/3} \quad (1.7.)$$

$$\sigma = n e \mu \quad (1.8.)$$

Figure 1.3 shows the tradeoffs between Seebeck coefficient and electrical conductivity in thermoelectric materials that must be met to maximize the figure of

merit. This peak typically occurs at carrier concentrations between 10^{19} and 10^{21} carriers per cm^3 (depending on the material system).

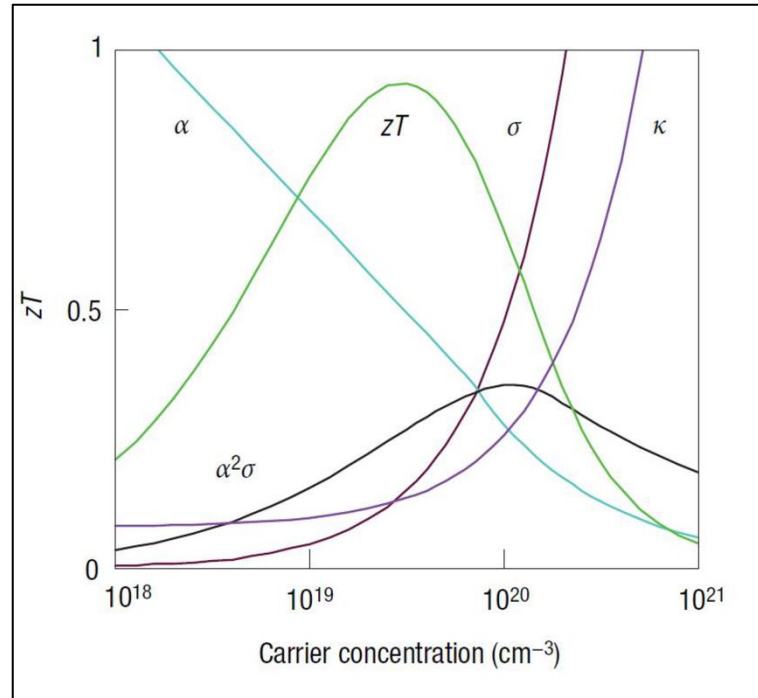


Figure 1.3 Optimizing ZT through carrier concentration tuning [25]

The effective mass of the charge carrier provides another conflict as large effective masses produce high thermopower but low electrical conductivity. The m^* in Equation (1.7) refers to the density-of-states effective mass, which increases with flat, narrow bands with high density of states at the Fermi surface. However, as the inertial effective mass is also related to m^* , heavy carriers will move with slower velocities, and therefore small mobilities, which in turn leads to low electrical conductivity (Equation (1.8)). The exact relationship between effective mass and mobility is complex, and depends on electronic structure, scattering mechanisms and anisotropy.

Phonons are not always in local thermal equilibrium and they move against the thermal gradient. They lose momentum by interacting with electrons, or other carriers, as well as imperfections in the crystal. If the phonon–electron interaction is predominant, the phonons will tend to push the electrons to one end of the material, thus losing momentum and leading to the thermoelectric field. This contribution is most important in the temperature region where phonon–electron scattering is predominant, which is described as:

$$T \approx \frac{1}{5} \theta_D \quad (1.9.)$$

where θ_D is the Debye temperature. At lower temperatures, there are fewer phonons available for drag, whereas they tend to lose momentum in phonon–phonon scattering instead of phonon–electron scattering at higher temperatures [27].

Additional materials design conflicts arise from the necessity for low thermal conductivity. Thermal conductivity in thermoelectrics comes from two sources: (1) electrons and holes transporting heat (κ_e) and (2) phonons travelling through the lattice (κ_L).

$$\kappa = \kappa_L + \kappa_e \quad (1.10.)$$

$$\kappa_e = L \sigma T \quad (1.11.)$$

Most of the electronic term (κ_e) of thermal conductivity is directly related to the electrical conductivity through the Wiedemann–Franz law, where L is the Lorenz factor, $2.4 \times 10^{-8} \text{ J}^2\text{K}^{-2}\text{C}^{-2}$ for free electrons [25].

As is widely known, the temperature-independent thermopower has been analyzed using the Heikes formula [28]. In this formula, entropy per site is associated with the thermopower. The simplest case, the thermopower of the Heikes formula (Equation 1.12.) α_H can be given by where x is the carrier concentration per unit cell [29].

$$\alpha = \frac{k_B}{e} \ln\left(\frac{2x}{1-x}\right) \quad (1.12.)$$

This formula is valid, when the thermal energy $k_B T$ is much larger than the transfer energy t but much smaller than the on-site Coulomb repulsion U ($t \ll k_B T \ll U$).

Additionally, Anderson transition and loeffe-level limit are the two extreme cases that should considered when the Heike's formula is applied to power factor [29].

1.2.2. Optimization of thermoelectric performance

Thermoelectric devices contain many thermoelectric couples consisting of n-type (containing free electrons) and p-type (containing free holes) thermoelectric elements (Figure 1.4).

As explained earlier, charge carriers (electron for n-type and holes for p-type thermoelements) tend to diffuse from the hot side to the cold side in case of power generation and diffuse along with the direction of the applied voltage in the case of cooling.

The efficiency of a thermoelectric power generator is defined as the ratio of electric power delivered to the load W to the total power drawn from heat source Q and can be expressed as equation 1.13.

$$\eta = \frac{W}{Q} = \frac{T_H - T_C}{T_H} \left[\frac{(1 + ZT)^{1/2}}{(1 + ZT)^{1/2} + \frac{T_C}{T_H}} \right] \quad (1.13.)$$

where T_H and T_C are temperatures at hot and cold junctions respectively, ZT is the aforementioned dimensionless figure-of-merit and the term $(T_H - T_C / T_H)$ is known as the Carnot's efficiency. To increase efficiency, ZT should be increased and as mentioned earlier to maximize ZT a large thermopower (absolute value of the Seebeck coefficient), high electrical conductivity, and low thermal conductivity are required.

Many ideas and strategies have been proposed and developed in order to improve ZT , some of them summarized in figure 1.4 [30]. Other than these strategies there are ways to enhance the electrical conductivity and Seebeck coefficient simultaneously such as carrier pocket engineering, invisible doping and interfacial effects [27,31,32]. Detailed information could be found related references given in this section.

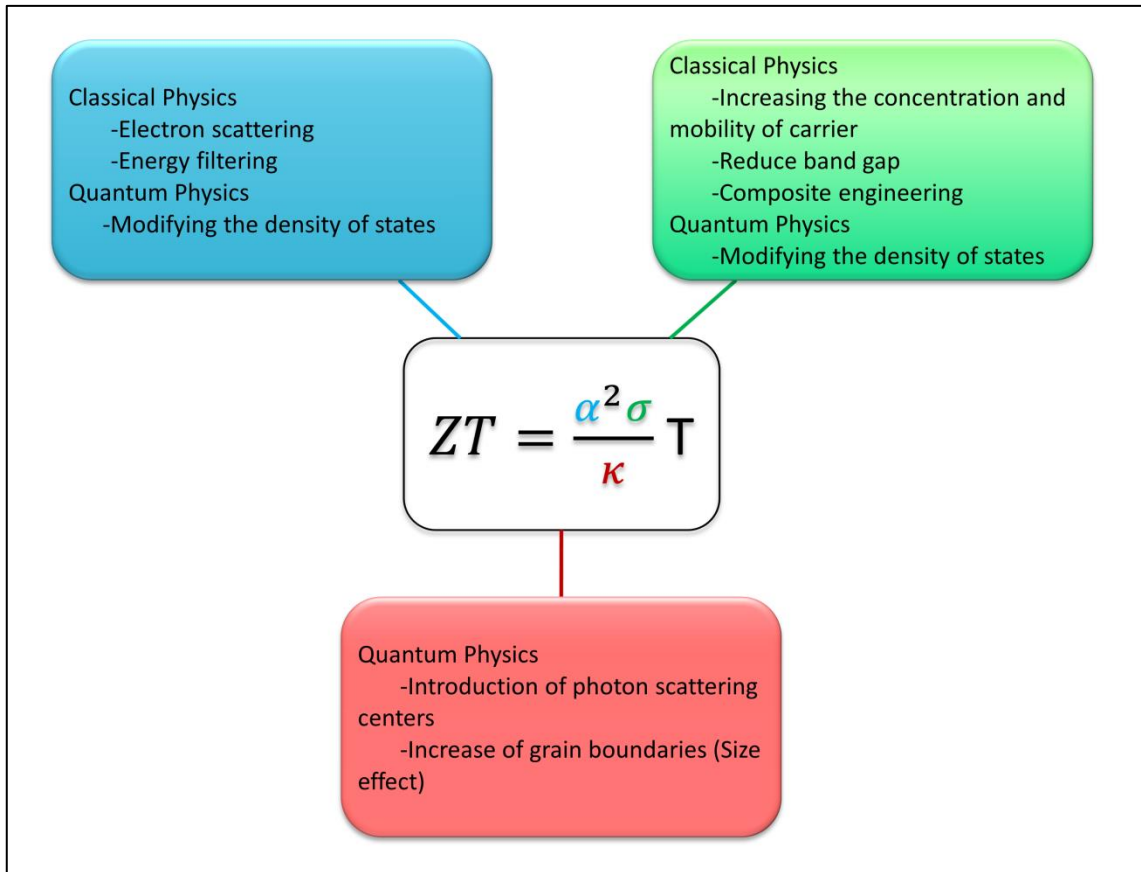


Figure 1.4 Different approaches to increase the Figure of Merit ZT of thermoelectric materials taking into account classical physics or quantum physics [30]

1.3. Crystal Structures and Properties of Investigated Materials

1.3.1. SiAlON, SiC, TiCN

SiAlONs is a general name for a large family of the so-called ceramic alloys based on silicon nitride. There are two SiAlON phases that are of interest as engineering ceramics, α -SiAlON and β -SiAlON, which are solid solutions based on α and β -Si₃N₄ structural modifications, respectively, and designated respectively as α' and β' . β -SiAlON is formed by simultaneous equivalent substitution of Al–O for Si–N and has most commonly been described by the formula Si_{6-z}Al_zO_zN_{8-z} [33]. The crystal structure of SiAlON is similar to Si₃N₄ (Figure 1.5). The lattice parameter of α -SiAlON is changing between 0.562 nm-0.566 nm in c-axis according to the composition and it is 0.291 nm in c-axis for β -SiAlON [34]. The theoretical density of SiAlON is 3.24 g/cm³. The electrical conductivity of β -SiAlON is very low and the application of β -

SiAlON in electric materials restricted to insulating uses. The structure and chemistry of α -SiAlON suggests that sialon ceramics with high electrical conductivity could be prepared [35].

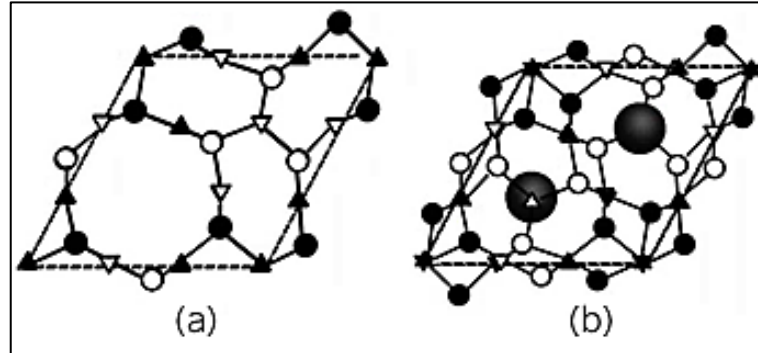


Figure 1.5 Crystal structure of (a) β -SiAlON (b) α -SiAlON (\circ ●: Al/Si, \triangle ▲: O/N) [34]

SiC is a very promising wide band gap material. The theoretical density of SiC is 3.21 g/cm^3 . There is one cubic polytype which crystallizes in the zinc-blende structure and is denoted as β -SiC or 3C-polytype. Large slices of 3C-SiC are grown as epitaxial films on Si (100) substrates with a CVD method; the Si substrate may then be removed. The other hexagonal and rhombohedral polytypes (about 170 are known) are collectively named as α -SiC. The most important polytype is 6H-SiC. All SiC polytypes are indirect semiconductors. The materials properties however depend on polytypes [36–38]. Figure 1.6 shows some possible stacking sequences for SiC. 2H has the most hexagonal structure (Wurtzite) with stacking sequence AB. The technologically important intermediate structures and their stacking sequences are 4H with ABCB and 6H with ABCACB. The stacking ABC of atoms in the 3C polytype leads to the cubic zinc-blend structure. Changing of the stacking sequence has a profound effect on the electrical properties, for example the bandgap changes from 3.2 eV for 2H to 2.4 eV for 3C [38]. Thermoelectric properties of SiC have been investigated since 1988 [39] and the studies showed that it has a high Seebeck coefficient (500-600 $\mu\text{V/K}$), however the thermal conductivity values are too high for the material to reach high ZT values.

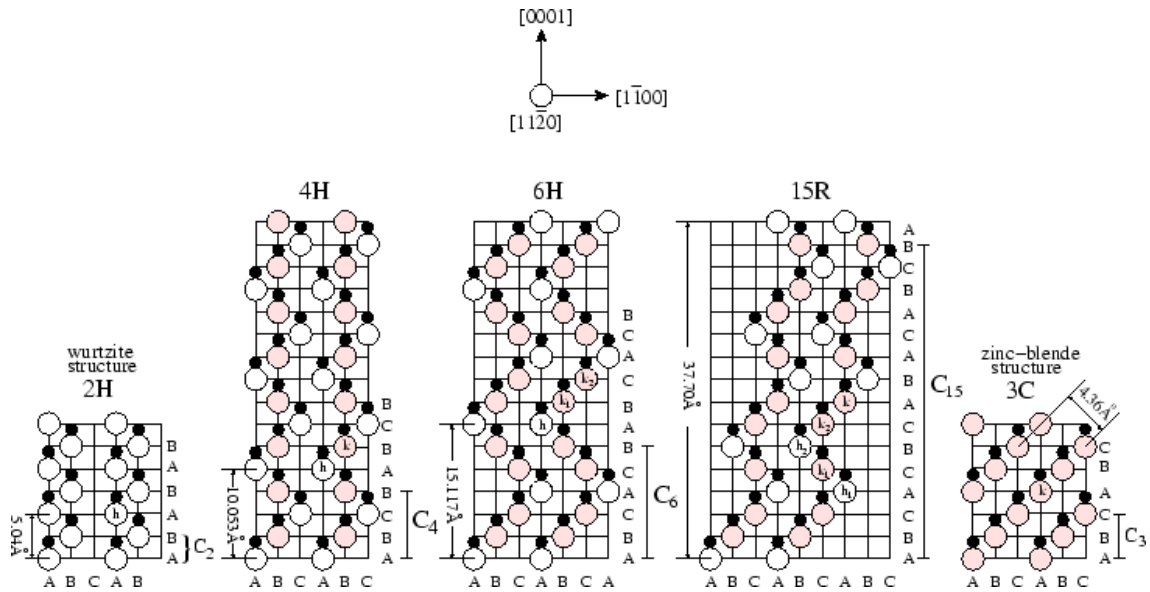


Figure 1.6 Stacking sequences for five different SiC polytypes [38]

$\text{TiC}_x\text{N}_{1-x}$ is a continuous solution of TiC and TiN. Based on phase diagrams of the TiC–TiN system, full solubility of TiC in TiN is expected [40]. TiCN is described as having a completely disordered structure (Figure 1.7). In this model the different atoms (Ti, C, and N) randomly occupy the two Wyckoff generating sites: 4a (0 0 0) and 4b (1/2 1/2 1/2). This structure model contradicts those for pure TiC and TiN, where Ti atoms occupy the 4a (0 0 0) sites and C or N occupy the 4b (1/2 1/2 1/2) Wyckoff sites [41]. TiCN has been used as an additive or coating material to improve the mechanical properties of ceramic materials [42–45]. In addition to its high hardness and toughness it has a high electrical conductivity ($\approx 10^6$ S/m). There are a few studies carried out that TiCN was used as an additive to increase the electrical conductivity [46–49].

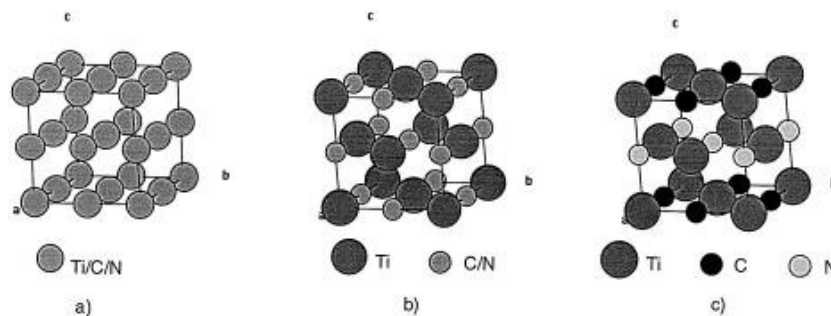


Figure 1.7 Structural models of TiCN; (a) Model I, (b) Model II and (c) Model IV [41]

1.3.2. SrTiO₃

Strontium titanate (SrTiO₃) is an excellent model material for electroceramic applications. At room temperature, SrTiO₃ crystallizes in the ABO₃ cubic perovskite structure (space group Pm3m) with a lattice parameter of 0.3905 nm and a density of 5.12 g / cm. The crystal structure depicted in figure 1.8. The Ti⁴⁺ ions are six fold coordinated by O²⁻ ions, whereas each of the Sr²⁺ ions is surrounded by four TiO₆ octahedra. Therefore, each Sr²⁺ ion is coordinated by 12 O²⁻ ions. Within the TiO₆ octahedra, a hybridization of the O²⁻ p states with the Ti³⁻ d states leads to a pronounced covalent bonding. Sr²⁺ and O²⁻ ions exhibit ionic bonding character. Hence, SrTiO₃ has mixed ionic-covalent bonding properties. This nature of chemical bonding leads to a unique structure, which make it a model electronic material.

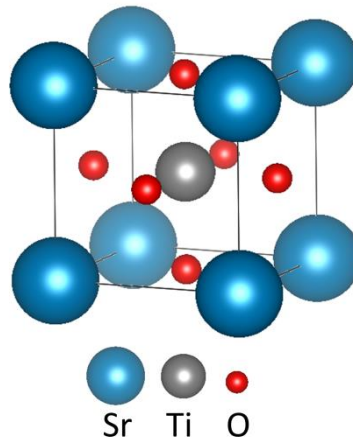


Figure 1.8 Structural models of SrTiO₃

1.3.3. La₂CuO₄ and LaNiO₃

Lanthanum cuprate (La₂CuO₄) is a model material for studying superconductivity phenomena, especially high temperature superconductivity. It has A₂BO₄-type structure with a density 6.93 g/cm³, which is represented in Figure 1.9, a Ruddlesden- Popper (R-P) phases have the general formula A_x(ABX₃)_n; La₂CuO₄ with n=1. The A cation site is, occupied by nine-fold coordinated La⁺³, whereas the B cation Cu⁺² is placed in the center of a BO₆ oxygen octahedra and is six-fold coordinated. The BO₆ structure is highly distorted, with the B-O_{plane} bond length being remarkably shorter (≈ 1.9 Å) than the out-of-plane B-O apical distance (≈ 2.5 Å). A large amount of oxygen

can be easily intercalated in the crystal (in the form of negatively charged interstitial defects between two LaO layers) forming hyperstoichiometric $\text{La}_2\text{CuO}_{4.5}$.

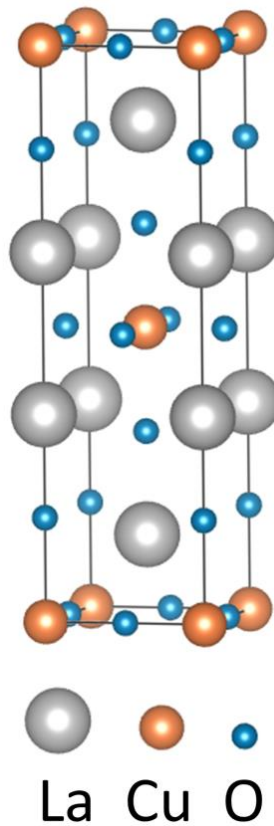


Figure 1.9 *Structural models of La_2CuO_4*

Among the remarkable family of perovskite oxides, lanthanum nickelate LaNiO_3 is a rare example characterized by paramagnetic metallic behavior down to the lowest temperatures and being structurally compatible with many active perovskite functional layers [50,51]. Depending on the oxygen stoichiometry, LaNiO_{3-x} ($x \geq 0$) can show either the metallic, semiconducting ($x > 0.25$) or insulating ($x > 0.5$) behaviors with the carrier concentration varying by a few orders of magnitude [52,53]. Usually, LNO is rhombohedral at room temperature but undergoes a rhombohedral to cubic phase transition at higher temperature [54].

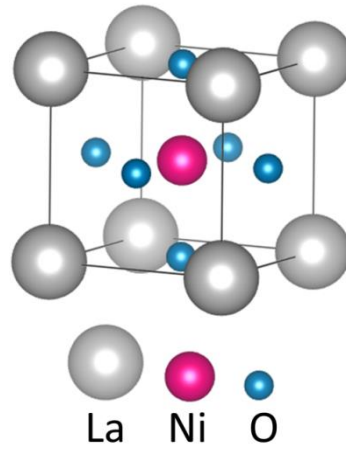


Figure 1.10 Structural models of $LaNiO_3$

1.4. Defect Chemistry of Investigated Materials

Defect chemistry is the key to the understanding of the ionic and electronic transport properties of solids. The defect reactions which dominate the electrical conduction properties of undoped, acceptor and donor doped $SrTiO_3$ will be elucidated using the Kröger-Vink notation [55]. Perovskite structure suggests that the dominant ionic point defects in the bulk are vacancies rather than interstitials, where by Sr vacancies (V_{Sr}'') Sr are compensated by oxygen vacancies $V_O^{\bullet\bullet}$.

In $SrTiO_3$ the dominant point defects in the bulk are vacancies rather than interstitials due to the close packed structure leading to Schottky disorder;



By assuming the activity of SrO is constant, Equation 1.14 results in a simplified mass action law in;

$$K_S = [V_{Sr}''] [V_O^{\bullet\bullet}] = K_S^0 \exp\left(-\frac{\Delta H_S}{kT}\right) \quad (1.15)$$

Another important intrinsic defect reaction is the generation of electrons and holes by thermal excitation in;

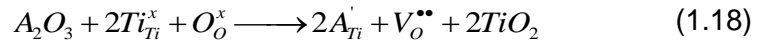


And the corresponding mass action law is given by in;

$$K_B = p \cdot n = K_S^0 \exp\left(-\frac{\Delta H_B}{kT}\right) \quad (1.17)$$

n and p respectively are the electron and hole concentration.

The incorporation of a trivalent acceptor A' in the Ti site and the subsequent formation of oxygen vacancies in SrTiO_3 can be described by the following reaction

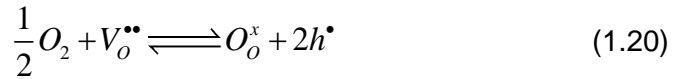


For the temperatures below 1000°C the general expression for electroneutrality is

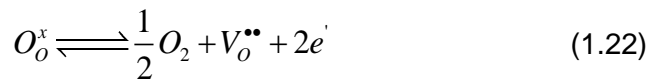
$$2v + p = m + n \quad (1.19)$$

$m = [A'_{Ti}]$ and $v = [V_o^{\bullet\bullet}]$ the oxygen vacancy concentration.

Also the oxygen incorporation (excorporation) equilibrium in oxidizing (reducing) atmosphere are relevant for the formation of defects;



$$K_{ox} = \frac{p^2}{[V_o^{\bullet\bullet}] \cdot pO_2^{1/2}} = \exp\left(-\frac{\Delta G_{ox}^0}{kT}\right) \quad (1.21)$$

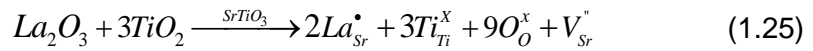
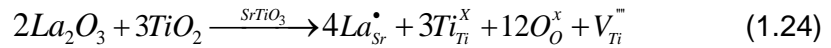


$$K_{red} = [V_o^{\bullet\bullet}] \cdot n^2 \cdot pO_2^{1/2} = K_{red}^0 \left(-\frac{\Delta G_{red}^0}{kT}\right) \quad (1.23)$$

K_{red} and K_{ox} are the mass action equilibrium constant for the oxidation and reduction reaction.

In the reducing regime, the condition of electroneutrality can be simplified as $n \approx 2v$ and for oxidizing regime $2v \approx m$.

In addition, when La^{3+} replaces Sr^{2+} charge imbalance can be compensated by cation vacancies on the A-or B-site (ionic compensation) instead of electrons. In this case the possible mechanism can be identified with the Eq.(1.24) and Eq.(1.25);



A detailed chemical model for La_2CuO_4 has been given by refs. [5,56,57]. A large amount of oxygen can be easily intercalated in the crystal (in the form of negatively charged interstitial defects between two LaO layers) forming hyperstoichiometric $A_2BO_{4+\delta}$ [58–60]. A second way for varying the charge carriers concentration in this compounds is by substituting La^{+3} with an aliovalent cation.

Hole doping h^{\bullet} and also superconductivity can be achieved via incorporation of oxygen and has been obtained using different methods such as high pressure oxygen annealing, ozone annealing or by chemical and electrochemical methods. Oxygen doping occurs according to the equation 1.20 which expresses the external defect equilibrium reaction between La_2CuO_4 and the gas phase (Fig.1.11).

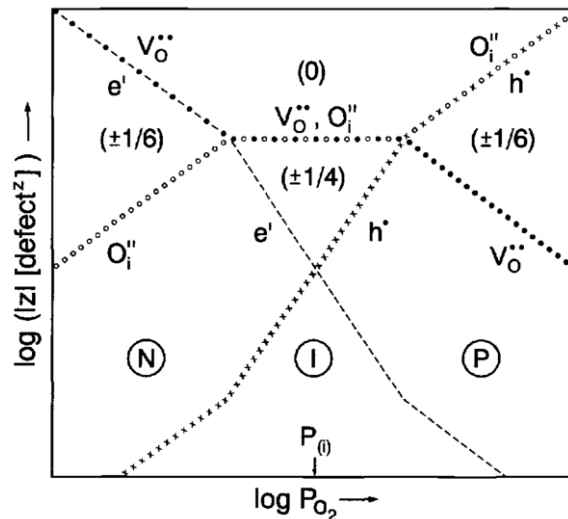
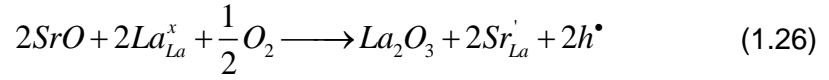


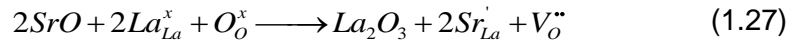
Figure 1.11 Defect concentration of an oxide as a function of partial pressure of oxygen (Kroger-Ving diagram) [5]

As described above, another possibility to increase the hole concentration in La_2CuO_4 is based on acceptor doping, substituting La^{+3} with a divalent cation (general formula $La_{2-x}M_xCuO_4$, $M=Sr, Ca, Ba$). In this dissertation Sr is used as a dopant. Sr incorporation reaction (which is considered as irreversible therefore mass-action law is

not applicable to it leads to an increase of the hole concentration according to the equation 1.20.



One should notice here that an equivalent possibility of formulating the dopant incorporation reaction predicts the formation of oxygen vacancies.



For the defect chemistry of La_2CuO_4 one should also take into account the following equilibria reactions, namely the anti-Frenkel reaction involving an oxygen site;



The relevant mass-action laws read;

$$K_F = [O_i^{\bullet\bullet}][V_i^{\bullet\bullet}] = K_F^0 \exp\left(-\frac{\Delta H_F}{kT}\right) \quad (1.29)$$

$$K_B = p \cdot n = K_B^0 \exp\left(-\frac{\Delta H_B}{kT}\right) \quad (1.30)$$

Where by the electroneutrality condition can be written as

$$2[O_i^{\bullet\bullet}] + [Sr'_{La}] + n = p + 2[V^{\bullet\bullet}] \quad (1.31)$$

In the particular case of the pure material, Equation (1.31) can be simplified as:

$$2[O_i^{\bullet\bullet}] = p \quad (1.32)$$

which, combined with Equation (1.21), results in:

$$p \propto P_{O_2}^{1/6} \quad (1.33)$$

as experimentally verified by conductivity experiments [59,61,62].

In the case of Sr-doped material, the solution can be simplified for different regimes (see Figure 1.12):

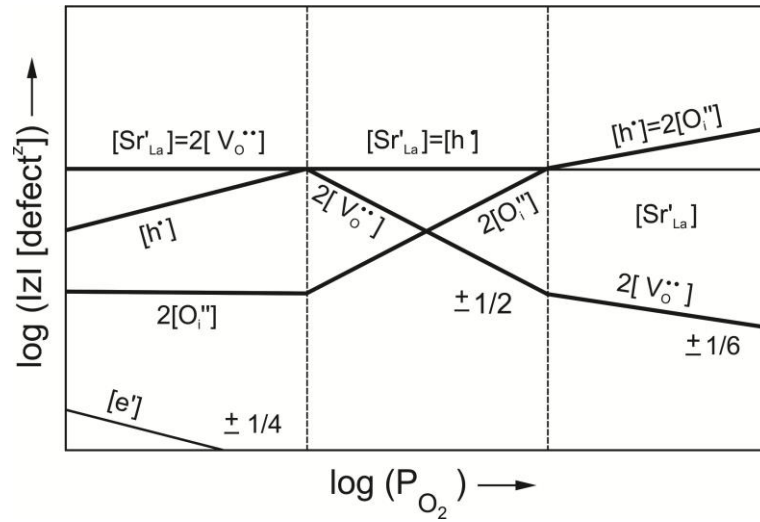


Figure 1.12 Defect concentration in La_2CuO_4 as a function of oxygen partial pressure at given Sr-content and constant temperature [56].

Local excess charge at the grain boundaries and interfaces in thin films lead to defect concentration distributions, which are very different from the bulk [9].

In such situations, the concentration of the different chemical species can be determined starting from considering the equilibrium condition, at which the electrochemical potential of each mobile defect j must be constant in space (here the one-dimensional case is considered):

$$\mu_j(x_1) = \mu_j(x_2) \quad (1.34)$$

where x_1 and x_2 represent two different locations in the sample. Eq. (1.34) can be written in terms of chemical potential μ and electrostatic potential ϕ :

$$\mu_j(x) = \mu_j(x) + z_j e \phi(x) \quad (1.35)$$

Where z_j is the charge number of the charge carrier j and e is the electron charge.

For dilute concentrations of the species j , the chemical potential can be expressed as

$$\mu_j = \mu_j^0 + kT \ln(c_j) \quad (1.36)$$

where μ_j^0 is the standard chemical potential. According to (1.34)

$$\mu_j^0 + kT \ln(c_j(x_1)) + z_j e \phi(x_1) = \mu_j^0 + kT \ln(c_j(x_2)) + z_j e \phi(x_2) \quad (1.37)$$

Results, by referring to the position and from this

$$\left(\frac{c_j(x)}{c_{j\infty}} \right)^{1/z_j} = \exp\left(-\frac{e}{kT} \Delta\phi(x) \right) \quad (1.38)$$

One can recognize that the concentration profiles of the mobile charged defects are determined by the space charge potential $\Delta\phi(x)$, defined as the difference between the space charge potential $\phi(x)$ at the position x and in the bulk $\phi(\infty)$. For $x=0$, $\phi(0) - \phi(\infty) = \Delta\phi_0$ and Eq.(1.38) becomes:

$$\left(\frac{c_j(0)}{c_{j\infty}} \right)^{1/z_j} = \exp\left(-\frac{e}{kT} \Delta\phi_0 \right) \quad (1.39)$$

The determination of the charge carriers' concentration profiles requires the knowledge of the relationship between concentration and electrical potential, which is described by the Poisson equation

$$\frac{\partial^2 \phi(x)}{\partial x^2} = -\frac{\rho(x)}{\epsilon_0 \epsilon_r} \quad (1.40)$$

where $\rho(x)$ is the charge density.

The combination of Eq. (1.38) and Eq. (1.39) results in the Poisson-Boltzmann differential equation [3]:

$$\frac{\partial^2 \phi(x)}{\partial x^2} = -\frac{\sum_j z_j e c_{j\infty}}{\epsilon_0 \epsilon_r} \exp\left(-\frac{z_j e}{kT} \Delta\phi(x) \right) \quad (1.41)$$

For the integration, it is helpful to distinguish two specific cases, the Gouy-Chapmann and the Mott-Schottky case, which are described in the following section.

1.4.1. Gouy-Chapmann case

In this situation, all the charged defects are mobile (note that this holds for example in solids exposed at very high temperatures) and follow the space charge potential. Here, Eq (1.41) can be analytically solved only in the case of two charge carriers with opposite charge ($z_1 = -z_2 \equiv z$) and ($c_{1,\infty} = -c_{2,\infty}$). From this:

$$\phi(x) = \frac{2kT}{ze} \ln \left(\frac{1 + \Theta \exp(-x/\lambda)}{1 - \Theta \exp(-x/\lambda)} \right) \quad (1.42)$$

results, where

$$\Theta = \tanh \left(\frac{ze\Delta\phi}{4kT} \right) \quad (1.43)$$

and

$$\lambda = \sqrt{\frac{\epsilon_r \epsilon_0 kT}{2z^2 e^2 c_{j,\infty}}} \quad (1.44)$$

the Debye length.

The spatial variation of the potential defined in Eq. (1.42) is given by:

$$\frac{d^2\phi}{dx^2} = -\frac{zec_{j,\infty}}{\epsilon_r \epsilon_0} \exp \left(-\frac{ze}{kT} \phi \right) \quad (1.45)$$

The concentration profile is given by

$$\frac{c_j(x)}{c_{j,\infty}} = \left(\frac{1 + \Theta \exp(-x/\lambda)}{1 - \Theta \exp(-x/\lambda)} \right)^{2z} \quad (1.46)$$

The charge density Σ can be calculated as:

$$\Sigma = \sqrt{8kT \epsilon_0 \epsilon_r c_{maj,\infty}} \sinh \left(\frac{z_{maj} e \phi(0)}{2kT} \right) \quad (1.47)$$

where the subscript *maj* indicate the majority defect. In this case, the extent of the space charge layer is approximately equal to 2λ .

1.4.2. Mott-Schottky case

At lower temperatures the Gouy Chapmann case is no longer valid, since not all the charge carriers are mobile enough to redistribute within the SCL. This is also the situation of an oxide doped with an immobile aliovalent cation. In this case, the Mott-Schottky approximation describes the system better. If the depleted charge carriers can be neglected and the charge density is hence fully defined by the dopant concentration (as long as dopant concentration exceeds the concentration of intrinsic defects). The Poisson-equation becomes:

$$\frac{\partial^2 \phi}{\partial x^2} = -\frac{z_{dop} e c_{dop,\infty}}{\epsilon_0 \epsilon_r} \quad (1.48)$$

For a horizontal doping profile integrating Eq. (1.48) with the appropriate boundary conditions:

$$\begin{aligned} \phi'(\lambda^*) &= 0 \\ \phi(\lambda^*) &= \phi_\infty = 0 \end{aligned} \quad (1.49)$$

one obtains:

$$\Delta\phi(x) = -\frac{z_{dop} e c_{dop,\infty}}{\epsilon_0 \epsilon_r} (x - \lambda^*)^2 \quad (1.50)$$

Where

$$\lambda^* = \sqrt{\frac{2\epsilon_0 \epsilon_r \Delta\phi(0)}{z_{dop} e c_{dop,\infty}}} = \lambda \sqrt{\frac{4z_{dop} e}{kT} \Delta\phi(0)} \quad (1.51)$$

Since in a Mott-Schottky situation the majority of the defects cannot redistribute, the space charge width is dependent on the space charge potential and the charge screening ability is reduced. As a consequence λ^* is usually more extended than λ .

The concentration profiles in this case are given by

$$\frac{c_j(x)}{c_{j\infty}} = \exp\left(-z_j \left(\frac{x - \lambda^*}{2\lambda}\right)^2\right) \quad (1.52)$$

And the charge density given by

$$\Sigma = \sqrt{8\epsilon_0\epsilon_r z_{dop} c_{dop,\infty} e\Delta\phi(0)} = 2\lambda^* e z_{dop} c_{dop,\infty} \quad (1.53)$$

1.4.3. Brick layer model

The total conductivity of a polycrystalline material consists of the grain and the grain boundary contributions. These two contributions can be quantified by a.c. impedance spectroscopy, which allows for the determination of corresponding resistance values and capacitances. In order to extract from the experimental data the conductivity and dielectric constant values, one needs to take into consideration the geometry of the grains and the grain boundaries. Employing the brick layer model makes this obviously challenging task easier [63–66]. In the brick layer model, the grains are assumed to be cube-shaped and homogeneous in size, with continuous connection of grain boundaries. This simplified description allows for the determination of the grain and grain boundaries conductivity of polycrystalline materials [67] and of the pathways followed by the mobile charge carriers [16].

As shown in Figure 1.13, in the case of highly conductive grain boundaries, the electrical transport occurs along the grain boundaries, which are parallel to the direction of the current, while in the case of blocking grain boundaries the mobile charge carriers migrate in the grain and across the grain boundaries perpendicular to the direction of the current. When the electrical transport occurs along the grain boundary the system can be described with one RC circuit and when the transport occurs across the grain boundary the system can be described by two RC circuits in series, representing bulk and perpendicular grain boundaries, which in principle correspond in the impedance spectra to two distinct semicircles.

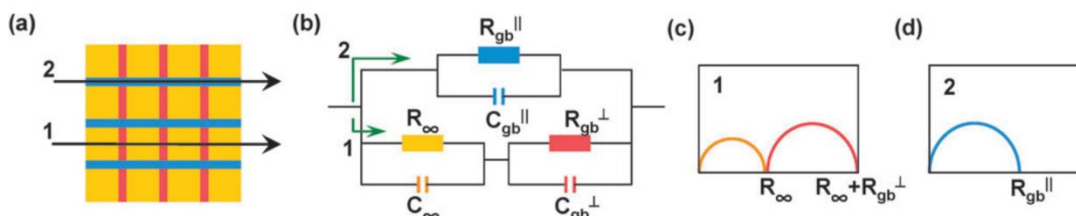


Figure 1.13 Schematic diagrams of a brick-layer model for a polycrystalline ceramic (a); an equivalent circuit model (b); impedance spectra (Nyquist plots) expected from the current path 1 (c) and 2 (d) [68]

Resistance and capacitance obtained from the fit of the data allow for the calculation of bulk and grain boundaries conductivities (σ_{bulk} , σ_{gb}) and dielectric constant (ε_{bulk}) by considering the sample's geometry as:

$$\sigma_{bulk} = \left(\frac{1}{R_{bulk}} \right) \left(\frac{L}{A} \right) \quad (1.54)$$

and

$$\sigma_{gb} = \left(\frac{1}{R_{gb}} \right) \left(\frac{L}{A} \right) \quad (1.55)$$

$$\varepsilon_{bulk} = \frac{C_{bulk}}{\varepsilon_0} \frac{L}{A} \quad (1.56)$$

Where A is the cross section area of the sample, L the distance between the electrodes, R_{bulk} , R_{gb} , C_{bulk} and C_{gb} the bulk and grain boundaries resistance and capacitance respectively.

It is important to note that σ_{gb} as it is defined in Eq. 1.58 represents a measured conductivity that does not refer to the local grain boundary. For this reason, it is more appropriate to consider the local specific grain boundary conductivity $\sigma_{gb,spec}$, which under the assumption that $\varepsilon_{bulk} \approx \varepsilon_{GB}$, can be written as [69]:

$$\sigma_{gb,spec} = \sigma_{bulk} \frac{C_{bulk} R_{bulk}}{C_{gb} R_{gb}} \quad (1.57)$$

From the dependence of the conductivity on the temperature, it is possible to determine its activation energy (E_a): since often the conductivity can be written as

$$\sigma = \frac{A}{T} \exp\left(-\frac{E_a}{kT}\right) \quad (1.58)$$

where A is a temperature independent factor, writing the equation as

$$\ln(\sigma T) = \ln(A) - \frac{E_a}{kT} \quad (1.59)$$

it is clear that if $\ln(\sigma T)$ is plotted as a function of $1/T$ (Arrhenius plot), the resulting slope corresponds to $-\frac{E_a}{k}$.

1.5. Motivation

The investigations in this dissertation work are based on the following strategies to tailor the thermoelectric properties: composite approach, grain boundary engineering, nanostructuring and tuning the interfacial effects.

2. EXPERIMENTAL METHODS

2.1. Sample Preparation

2.1.1. Gas pressure and spark plasma sintering

The gas pressure sintering (GPS) relies on applying a certain gas pressure during high temperature sintering. Such a method is one of the most important sintering techniques, particularly for Si_3N_4 because it prevents its decomposition and allows long sintering times at high temperatures enabling diffusion processes during sintering [70]. Many products which can be shaped by different techniques such as pressing, injection molding, and casting can be easily sintered by this method which has no limitation in terms of shape and quantity. Preformed products are placed in graphite, SiC or BN moulds. BN spray is applied to the product surfaces to prevent reactions with the crucible. Two-step sintering is usually applied during GPS sintering. During the first step, a small amount of gas pressure (0-5 bar) is applied up to a temperature above the liquid phase formation to allow for pore closure and microstructure formation. Then the temperature and pressure are increased at the same time to ensure complete closure of the remaining closed pores in order to achieve full densification [71].

In this work, the SiAlON based samples sintered in a h-BN crucible using a GPS furnace (FCT Systeme GmbH, Germany), capable of operating at temperatures of up to 2000 °C in an inert atmosphere of up to 10MPa pressure. A two-stage sintering process was employed. The first stage of sintering was achieved at 1940 °C for 60 min under a nitrogen gas pressure of 0.2-0.5MPa. In the second stage, both the peak temperature and gas pressure were raised to 1990 °C and 10MPa, respectively, for the same soaking time. The heating and cooling rates were kept at 10 °C/min. Powders were dry pressed with a computer controlled automatic uniaxial press (Dorst, Germany) under 50 kN load.

Spark plasma sintering (SPS) is one favorable compaction method, which has emerged in the last years as a powerful and fast technique for sintering highly covalently bonded materials [72]. It contributes to full densification, reduces the sintering temperature, shortens the sintering time prevents excessive grain growth and improves the mechanical and thermal properties as a result of Joule and direct heating generated by high pulsed electric current [73].

In this study, the SPS system (HPD-50, FCT GmbH, Germany) was used. For the SiC based composites, a single step densification schedule at 2050 °C with a 20 min hold time under 50 MPa uniaxial pressures were carried by using spark plasma

method. The holding time of 15 minutes and heating rate of 200K/min were used. Apart from SiAlON and SiC based composites, the SrTiO₃ based samples sintered by using conventional method. The preparation of the samples is explained more in detail in Chapter 4.

2.1.2. Oxide molecular beam epitaxy

Oxide molecular beam epitaxy is one of the techniques, which allows atomic-scale synthesis of oxide films and heterostructures. Observations of unexpected phenomena [74] and new functionalities of materials, such as enhancement of high T_c in La_{1.55}Sr_{0.45}CuO₄/La₂CuO₄ interface [75] were made on samples prepared according to this technique.

Molecular beam epitaxy is based on the evaporation of metallic elements from resistive thermal sources (Knudsen cells) or from electron-beam sources. Under ultra high vacuum, the atomic flux is conveyed, by using appropriate geometry, onto a substrate, where the cationic species combine in order to form the desired phase. Mechanical shutters, placed in front of each effusion cell, are operated in order to provide each depositing species in the correct order and amount. While keeping ultra high vacuum, a highly reactive oxidizing gas 3x10⁻⁵ Torr (mixed ozone, radical oxygen and molecular oxygen atmosphere), such as oxygen plasma or ozone, is employed for the growth of oxides. The use of molecular oxygen is normally prevented by the need to minimize scattering of the evaporated atoms in the background gas [76–78].

A particular growth technique has been developed [79] which is called atomic-layer-by-layer MBE (ALL-MBE) and provides simultaneous deposition of all the different species constituting the growing phase.

The MBE (and especially the ALL-MBE) technique is particularly suited for the realization of multilayered systems, in which different phases are stacked on top of each other, and of superlattices, in which a fixed structure (superlattice unit, having typical thickness of a few nanometers), is repeated for a predefined number of times [78].

In this study, multilayers of (see Chapter 5) were grown using the oxide MBE system (DCA Instruments). A simplified sketch of the system is shown in Figure 2.1. A detailed description of the oxide MBE setup which has been used to synthesize the samples and for more details please refer to Ref. [80] and [78].

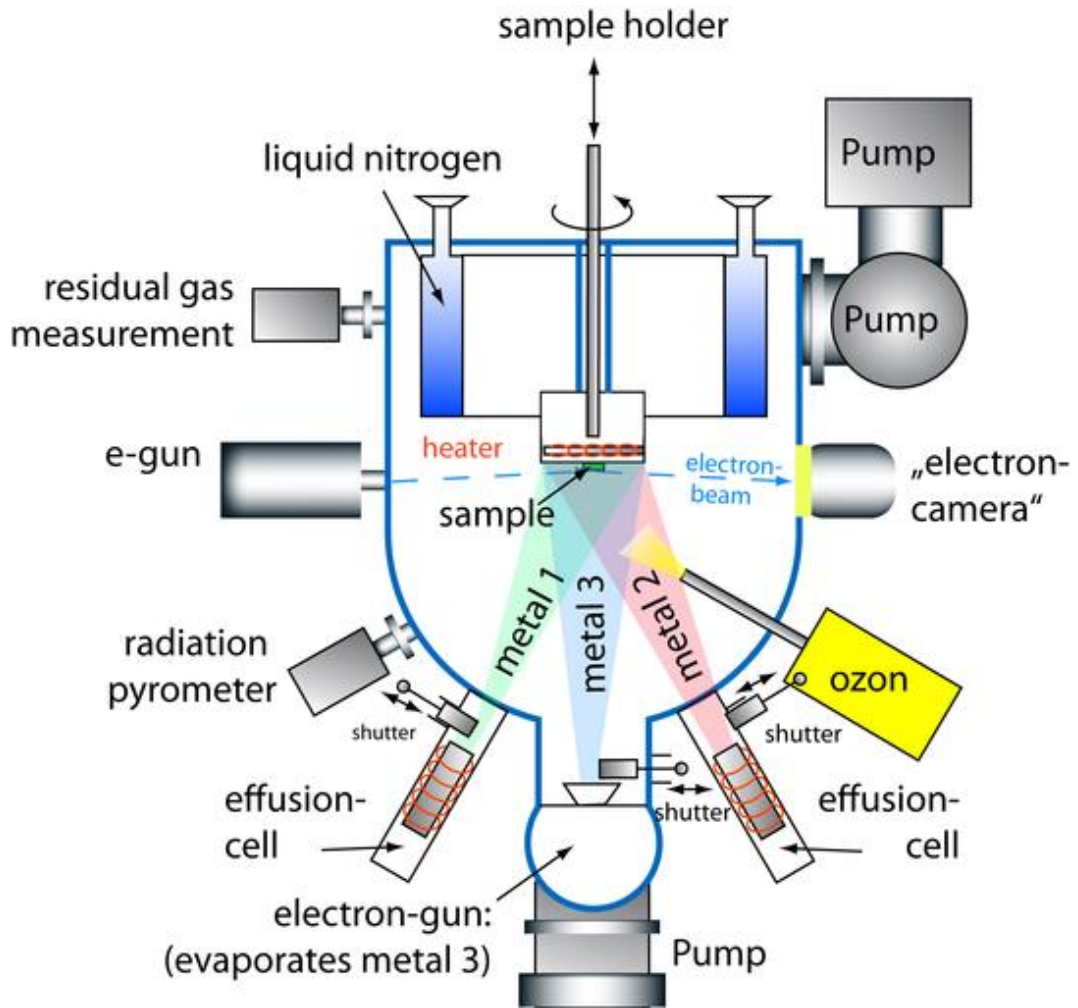


Figure 2.1 Sketch of the MBE growth chamber. Reproduced with permission from Ref. [125].

2.2. Structural and Morphological Characterization

2.2.1. RHEED

Reflection high energy electron diffraction (RHEED) is an important tool to follow the MBE growth process. It is an in-situ monitoring technique which is based on the quasi two-dimensional diffraction of an electron beam from the surface of the growing sample. Thanks to this technique, submonolayer ordering and phase transformations, the transition from 2-D layers to 3-D clusters, details of the shape of small 3-D clusters, and even amorphous-to-crystalline transitions can be investigated quantitatively [81].

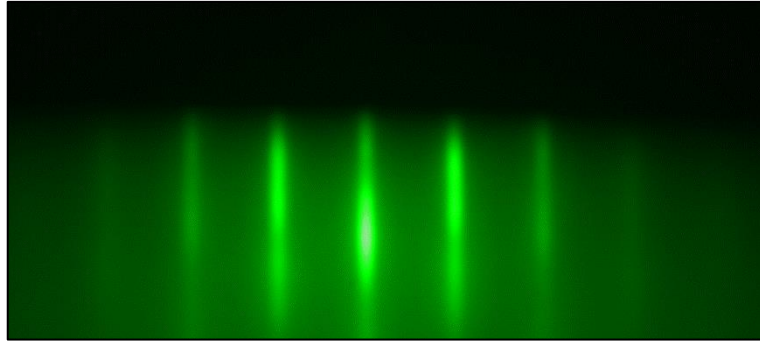


Figure 2.2 RHEED image at the end of the growth of 16x(2//1.5) LNO-LCO superlattice

High electron energies of 10–100 keV are used and the surface sensitivity is achieved by using grazing incident angles (0.1° to 5°).

The formation of the diffraction pattern can be depicted most easily using the Ewald construction. The radius of the Ewald sphere is inversely proportional to the wavelength λ . The intersection of the Ewald sphere and the reciprocal-lattice rods is a graphical solution of the grating equation (Equation 2.1) and therefore yields the diffraction pattern.

$$n\lambda = d(\cos \theta_x - \cos \theta_0) \quad (2.1)$$

As the energy of the incident beam or the angle of incidence is varied, the radius of the Ewald sphere or its orientation relative to the rods changes, consequently also changing the points of intersection with the rods [81].

For a plane wave with a wavelength λ incident at an angle θ_0 (measured from the horizontal plane) on a one-dimensional grating with line spacing d , the diffraction maxima occur at angles θ_x when rays emanating from successive grating lines scatter in phase, i.e., when their path difference is an integral number of wavelengths.

2.2.2. X-Ray diffraction

In this study, X-ray diffraction (XRD) using a XRD diffractometer (Xpert, Philips, 3710 HTK, Cu $K_\alpha=1.54056 \text{ \AA}$) was employed on both powders and sintered pellets (Chapter 3 & 4), in order to check the presence of secondary phases.

For thin film samples (Chapter 4) the arrangement of the atoms can be determined from the measurement of the positions of the Bragg reflections and expressed by Bragg's law:

$$2d \sin \theta = n\lambda \quad (2.2)$$

From the θ angles which give constructive interference, the interatomic distance can be obtained. In order to retrieve a more precise evaluation of the d lattice parameter refinement, the Nelson-Riley function, which takes into account possible sample misalignments, can be used [82]. Here, the lattice parameter is defined by the intercept of the linear fitting obtained by plotting d as a function of the Nelson-Riley function;

$$\left(\frac{\cos \theta^2}{\sin \theta}\right) + \left(\frac{\cos \theta^2}{\theta}\right) \quad (2.3)$$

In the particular case of thin films, together with the stacking of the atomic planes, other types of ordering exist, giving rise to diffraction signals. In particular, additional peaks are present around the main Bragg peaks: they are (i) the Laue fringes, which stem from the overall crystalline ordered volume and whose distance is linked to the sample thickness, and (ii) the superlattice peaks, which reflect periodicity stemming from the presence of an alternation of different phases in the case of periodic multilayers.

These additional peaks can be treated with the following formula

$$\frac{2 \sin \theta}{\lambda} = \frac{1}{d} \pm \frac{n}{\Lambda} \quad (2.4)$$

in which n is an integer that labels the order of the satellite peak around the main Bragg peak and Λ is the modulation length (e.g. the $1m$ thickness or the superlattice unit thickness). In the case of a single phase, in which only the Laue fringes are present, one simply has $\bar{d} = d$.

In the case of superlattices, their fringes are analyzed by taking

$$\bar{d} = \frac{\Lambda}{N_A + N_B} \quad (2.5)$$

Here, N_A and N_B are the number of atomic planes of material A and B in a superlattice unit, respectively. The diffractometer used for the investigations of the samples during this project (model Bruker D8) uses a Bragg-Brentano reaction geometry equipped with a monochromator and a Cu-filament source ($\lambda = 1.54060 \text{ \AA}$). In such a geometry, a typical scan, called $2\theta/\omega$, is performed by changing both the

source and detector positions with respect to the sample: the incident angle ω and the diffracted angle 2θ are coupled in order to ensure the optimal beam collimation thus maximum intensity [78,83].

2.2.3. X-Ray reflectivity

A particular application of x-ray diffraction is x-ray reflectivity (XRR), where one measures the x-ray intensity that is reflected from the surface of the sample at very low angles, starting from 0° . The analysis of X-ray reflectivity (XRR) is a powerful tool in order to get information about thin films morphology. This technique is based on the specular reflection of X-rays at grazing incident angles. In such a configuration, for angles larger than the critical angle, the incident beam is partially reflected and partially refracted by the film surface: the path difference between the reflected and the refracted beam gives rise to interference. As a consequence, one can observe an oscillating intensity behavior of the outgoing beam as a function of the incident angle (the so-called Kiessig fringes), with maxima occurring where the condition for constructive interference is fulfilled. By analyzing the Kiessig fringes, one can easily obtain the film thickness (up to 100 nm) in the case of single phase film using the approximated relation.

$$d \cong \frac{\lambda}{2\Delta\alpha} \quad (2.6)$$

with $\Delta\alpha$ being the distance between two consecutive minima or maxima and λ being the wavelength of the incident beam. Based on a similar approach, one can perform analysis of multilayered structures, given that each constituting phase is characterized by different density thus different refraction index. In this case, the analysis of the reflectivity curve requires the use of simulations, which are typically based on the Parratt equation [84].

By doing this, one can not only get information on the total and the single layer thickness, but also on the surface and the interface roughness, parameters which can be retrieved by analyzing the intensity loss upon beam-sample interaction.

2.2.4. Atomic force microscopy

Atomic force microscopy (AFM) is a technique for the atomic-scale analysis of the surface morphology, which provides useful information on the quality of the samples [85].

AFM can be operated in contact mode, in which repulsive forces generated by the contact between tip and sample are measured, non-contact mode or tapping mode. In the second mode an oscillation of the tip at its resonance frequency is induced: tip-surface interaction tend to disturb such oscillation, and the system adjusts the tip-surface distance in order to maintain a constant frequency. From here, information about the surface morphology is obtained. In the third mode, called tapping mode, the oscillation frequency is increased and an alternated tip sample contact is realized. In this way, more accurate details on the surface morphology are retrieved with respect to the non-contact mode, while a less destructive (for the tip) situation is realized compared to the contact mode

For our measurements, Digital Instruments atomic force microscope with Nanoscope III controller, operated in tapping mode, has been used. Together with surface imaging, also quantitative information about the roughness can be obtained, such as:

Root mean squared roughness, R_{ms}

$$Rms = \sqrt{\frac{1}{L} \int_0^L Z(x)^2 dx} \quad (2.7)$$

Arithmetic average roughness, R_a

$$Ra = \frac{1}{L} \int_0^L Z(x) dx \quad (2.8)$$

Maximum roughness, R_{max}

$$Rmax = \max[Z(x)] \quad (2.9)$$

2.3. Electrical Resistivity and Thermopower Measurements

2.3.1. AC electrochemical impedance spectroscopy

Alternating current (AC) electrochemical impedance spectroscopy (EIS) is a very powerful technique for the characterization of the electrical properties of the materials and of their grain boundaries or interfaces.

EIS consists of the application of an alternating voltage $U(t) = U_0 \cos(\omega t + \theta)$ across the sample and in measuring the current response, $I(t) = I \cos \omega t$, as a function of the angular frequency ω . Here, θ is the phase difference between the voltage and the current: From these, the impedance Z at each frequency can be determined. By taking into account the Euler's formula, the impedance Z^* , can be also written as

$$Z^* = \frac{U(t)}{I(t)} = \frac{U_0}{I_0} \exp(-i\theta) = Z(\cos \theta - j \sin \theta) \quad (2.10)$$

Z^* , can be plotted in the complex plane with the real part $Z' = Z \cos \theta$ on the x axis and the imaginary part $Z'' = Z \sin \theta$ on the y axis (Nyquist plot). In an ideal case, this results in a semicircular arc, which can be modelled using an equivalent circuit containing a resistor R and a capacitor C in parallel, over the whole frequency range [86].

In the Nyquist plot of Z^* the low frequency intercept of the arc with the x axis corresponds to the resistance R , since, when $\omega \rightarrow 0$ the influence of the capacitance vanishes and the DC response is obtained. The inverse of the frequency at the peak gives the relaxation time constant $\tau = \omega^{-1} = RC$.

The semicircles experimentally observed in the EIS spectra are in most of the cases distorted. This non-ideal behavior originates from the effect of the materials inhomogeneity on the distribution of the current density. This makes it difficult to approximate the impedance with an ideal RC circuit and, consequently, the capacitor C is replaced by a constant phase element Q . The capacitance of the contribution is then best calculated from the fitting parameters Q and ϑ according to the following equation

$$C = (R^{1-\vartheta} Q)^{1/\vartheta} \quad (2.11)$$

where ϑ indicates the depression of the semicircle, and it must range between 1 (ideal capacitor) and 0.7 for a sensible fitting.

In this work, impedance spectroscopy measurements were performed using an Alpha-A high resolution dielectric analyzer (Novocontrol) in the frequency range from 2 MHz to 1 Hz and applying a AC voltage of 0.3 V.

The electrical conductivity and the dielectric constant of the bulk were determined from the experimental data, taking into account the geometry of the sample.

$$\sigma_{bulk} = \frac{1}{R_{bulk}} \frac{h}{A} \quad (2.12)$$

$$\varepsilon_{bulk} = \frac{C_{bulk}}{\varepsilon_0} \frac{h}{A} \quad (2.13)$$

h and A being the sample thickness and cross-section, respectively. The calculation of the respective values or the boundaries must take their geometrical parameters into account.

By plotting $\ln Ts$ versus $1/T$ (Arrhenius plot), the slope is proportional to the activation energy E_a can be extracted according to the Eq.(1.58).

In this work, the activation energy of the conductivity was determined from the impedance spectra acquired every 20°C between 350°C and 630°C at the desired partial pressure. The samples were equilibrated at the desired partial pressure for 20 hours before acquiring the final spectrum. The impedance spectra were analyzed with the software Z-View (Scribner Associates).

2.3.2. ZEM 3-M8

The Seebeck coefficient of a material is a measure of the magnitude of an induced thermoelectric voltage in response to a temperature difference across the material.

The essence of a Seebeck measurement is to measure the potential difference $V = \Delta\phi$ across a sample under a fixed temperature gradient (ΔT) at some fixed temperature \bar{T} . The Seebeck coefficient (α) is then taken as $V = \Delta\phi/T$ and $V = \Delta\phi$ is defined at the voltage drop between cold side and hot side of the sample, while ΔT is the corresponding temperature difference $T_h - T_c$. Voltage and temperature are measured at corresponding points on the sample.

A prism or cylindrical sample is set in a vertical position between the upper and lower blocks in the heating furnace (Figure 2.3(b) & (d)). During the measurement, the sample is heated by the heater in the lower block to provide a temperature gradient. The Seebeck coefficient is determined by measuring the upper and lower temperatures T_1 (T_h) and T_2 (T_c) with the thermocouples pressed against the side of the sample, followed by a measurement of the thermal electromotive force (dE) between the same wires on one side of the heating furnace thermocouple (Figure 2.3(b) & (d)). The resistivity can be measured by a two point (only the inner electrodes) or in the four point (outer and inner electrodes) configuration in a sweep mode (ac mode) or a step mode (dc mode). At every set temperature, the voltage gradient and the resistivity are calculated using the average of these three values. Because of the robust construction, it is possible to investigate a wide range of samples. For thin films, substrates with 5 x

5 mm² to 10 x 10 mm² area and bulk samples with a minimum length or diameter of 5 mm can be investigated.

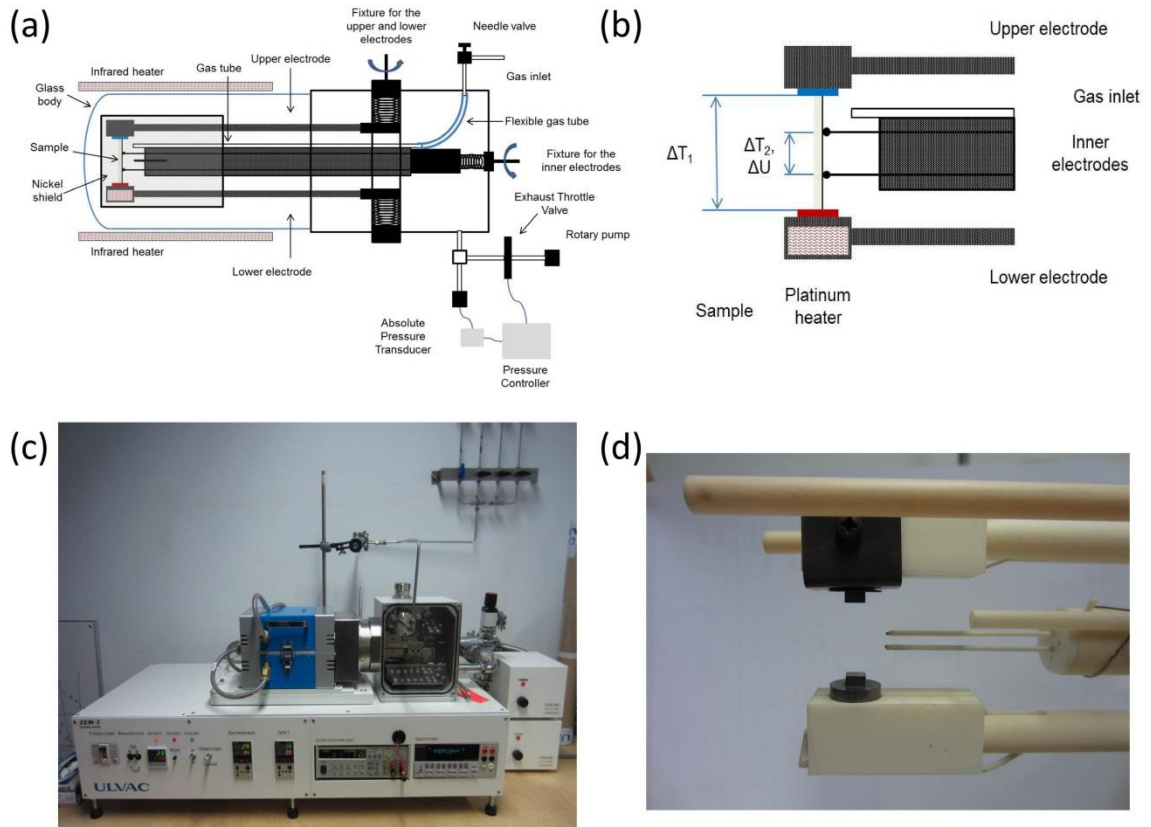


Figure 2.3 (a) Schematic overview of ULVAC ZEM-3 M8 (b) Schematic of the measurement setup (c) The ULVAC ZEM-3 M8 apparatus (d) Sample holder [87]

The measurement of the Seebeck coefficient seems to be a very simple process; however, many specific problems involved make it quite difficult. Uncertainty in the Seebeck and resistivity measurements can arise from a number of sources [88]. According to the round-robin studies for all the ULVAC ZEM 3 results, the scattering data points were about +4% in the entire temperature range. The standard reference materials (Constatan for ULVAC ZEM system) need to be periodically examined after high temperature exposures [89].

Seebeck coefficient measurements of all samples were carried out by using ULVAC ZEM 3 -M8 measurement system which was equipped with Pt clamps for

generation of temperature gradient on the sample at high temperatures (750 °C) under oxidizing condition ($pO_2 = 10^{-4}$ - 1 bar) or reducing condition ($pHe=10^{-4}$ - 1 bar).

The electrical resistance measurements of segregated network composites (Chapter 3) and thin films (Chapter 4) were carried out simultaneously by using the same set up as for the determination of the Seebeck coefficient with the dc four terminal method (Normal mode), in which a constant current (I) was applied to both ends of the sample to measure and determine voltage drop (dV) between the thermo-electromotive force leads.

2.4. Thermal Diffusivity and Specific Heat Measurements

The thermal diffusivity describes how quickly a material reacts to a change of temperature. Different methods can be used to determine the thermal diffusivity and laser flash technique is one of them. In the laser flash thermal diffusivity method, one face of a sample is irradiated by a short (<1 ms) laser pulse. An IR detector monitors the temperature rise of the opposite side of the sample. The thermal diffusivity is calculated from the temperature rise versus time profile [90].

For the bulk sample measurements, a LFA457 MicroFlash (Netzsch, Germany) laser flash system was used (Fig.2.4).

The specific heat is the amount of heat per unit mass required to raise the temperature by one degree Celsius and can be measured by using differential scanning calorimetry (DSC). In differential scanning calorimetry (DSC), the sample material is subjected to a linear temperature program, and the heat flow rate into the sample is continuously measured; this heat flow rate is proportional to the instantaneous specific heat of the sample.

Two sample holders are mounted symmetrically inside an enclosure which is normally held at room temperature. A primary temperature control system controls the average temperature of the two sample holders, using platinum resistance thermometers and heating elements embedded in the sample holders. A secondary temperature control system measures the temperature difference between the two sample holders, and adjusts this difference to zero by controlling a differential component of the total heating power. This differential power is measured and recorded [91].

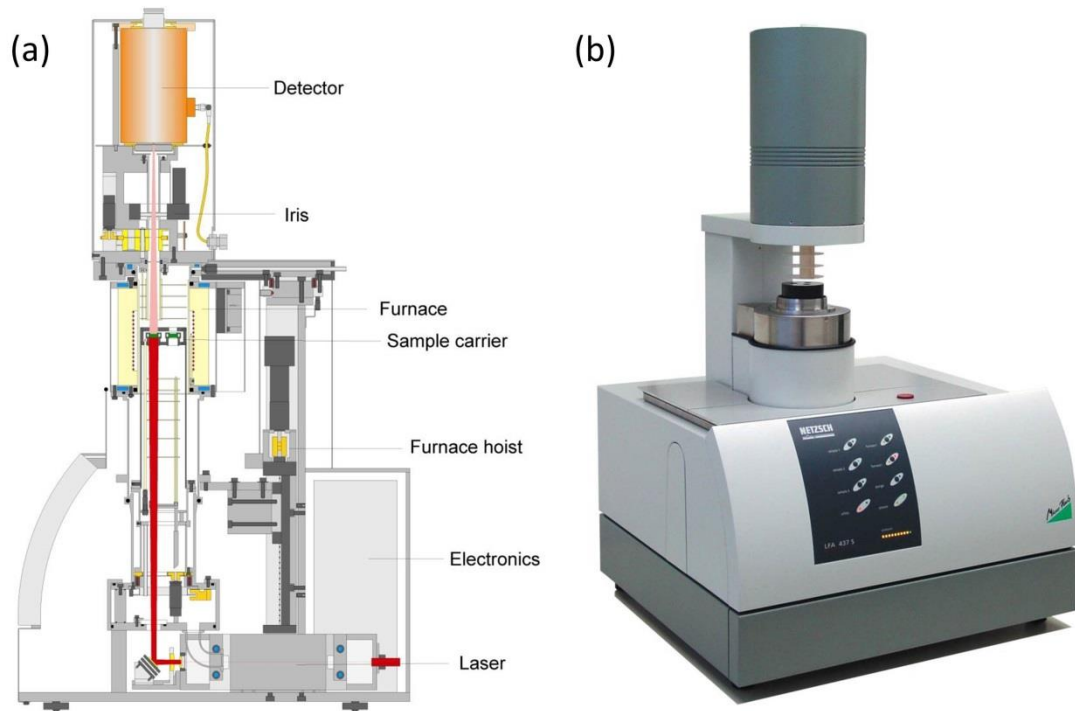


Figure 2.4 (a) Schematic view of LFA-457 MicroFlash (Netzsch, Germany) (b) Image of a device analogous to the one used in this study.

In order to measure the specific heat of a sample, the sample holder temperature is programmed as shown in Figure 2.5. To establish a base line, the program is carried out with no sample present and crucibles are placed in the sample holders. Isothermally, the base line indicates the differential losses of the two sample holders at the initial temperature. This procedure is then repeated, with a weighed sample added to the sample holder. The heat flow rate is obtained according to the formula of equation (2.11). Here H is enthalpy, t is time, m is mass, T is temperature and C_p is specific heat.

$$\frac{dH}{dt} = mC_p \frac{dT}{dt} \quad (2.11)$$

The specific heat measurements for the segregated network composites (Chapter 3) were done by using a DSC NETZSCH STA 449F3 while for the measurements of SrTiO_3 based samples a DSC Perkin Elmer4000 was employed.

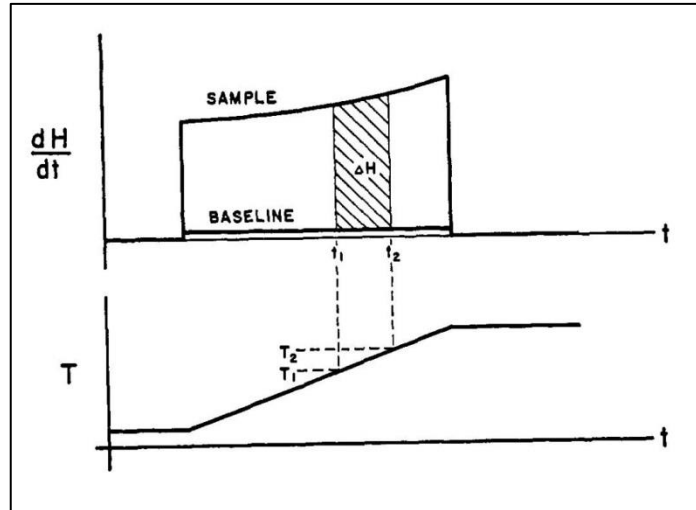


Figure 2.5 *Linear temperature program [91]*

The thermal conductivity was calculated according to the equation (2.10)

$$\kappa = D \cdot C_p \cdot \rho \quad (2.10)$$

where κ is the thermal conductivity; C_p is the specific heat; ρ is the density; D is the thermal diffusivity.

2.5. Microstructural Characterization

Scanning electron microscopy studies were employed for the characterization of the pellets by using Zeiss Merlin field emission scanning electron microscope (FESEM) equipped with back scatter electron detector.

For electron transparent samples, standard sample preparation procedure including mechanical grinding, tripod wedge polishing and argon ion milling with a liquid nitrogen cooled stage was performed. For argon ion thinning, a precision ion polishing system (PIPS II, Model 695) was used at low temperature. For all STEM analyses, a probe-aberration-corrected JEOL JEM-ARM200F STEM equipped with a cold field-emission electron source, a probe C s-corrector (DCOR, CEOS GmbH), a large solid-angle JEOL Centurio SDD-type energy-dispersive X-ray spectroscopy (EDXS) detector, and a Gatan GIF Quantum ERS spectrometer was used. For TEM analyses a image-aberration-corrected JEOL JEM-ARM200F was used.

3. AN ALTERNATIVE COMPOSITE APPROACH TO TAILOR THE THERMOELECTRIC PERFORMANCE

3.1. Introduction & Motivation

Thermoelectric (TE) materials and devices attract increasing attention because of their potential applications in the fields of energy conversion, thermal sensors, and cooling systems for electronic devices [92–94]. The performance of a TE device depends on the figure of merit of the TE materials ($ZT = \alpha^2 \cdot \sigma T / \kappa$). Therefore, in order to have high-performance TE materials, an ideal combination of high power factor ($\alpha^2 \sigma$) and low thermal conductivity (κ) is required. In polycrystalline materials, the situation is more complex due to the presence of grain boundaries in which and in proximity of which the electrical and thermal properties can differ significantly from the bulk. In order to enhance the figure of merit, κ is required to be as small as possible, boundaries can be beneficial as they can selectively scatter phonons and charge carriers [24,31]. As for the electrical conductivity, it is known that the electrical transport along grain boundaries and interfaces can be improved or depressed, even by several orders of magnitudes, as it was shown for example for $\text{LaAlO}_3/\text{SrTiO}_3$ interfaces [95], for nanocrystalline ceria [96] and mesoscopic SrTiO_3 [17]. Therefore, microstructural design particularly of boundaries can be crucial for improving the desired functionality.

The materials used in thermoelectric generators (TEG) should be environmentally friendly, inexpensive, chemically and thermally stable, and scalable for mass production with high mechanical strength [97,98]. Skutterudites, half-Heusler compounds and silicon-based thermoelectric materials are current candidates for medium-high to high temperature applications. In addition, oxide thermoelectric materials seem promising due to their durability at high temperature in air, non-toxicity and low cost [99]. Also, carbides such as SiC are good candidates for high temperature applications, thanks to their thermal, mechanical and chemical stability although their electrical properties cannot compete with skutterudites and half-Heusler compounds [39,100,101]. In this context, it is worth mentioning that SiAlON-based composites are attractive for high-temperature applications for achieving high electrical conductivity without compromising their mechanical properties, as proven by their application in glow plugs and heaters [102,103]. Nonetheless, the thermoelectric properties of SiAlON-based ceramics have not been investigated so far. One of the challenges related to the fabrication of components made of SiALON is due to its relatively poor

densification during sintering. The most common compaction method is gas-pressure-sintering which enables reliable reproducibility and improved properties by only moderate increase of the production costs compared to pressureless sintering [104].

In order to obtain high electrical conductivity in such systems, addition of a highly conductive secondary phase, e.g. Ti(C,N) [46,105,106] or TiB₂ [107] has been extensively studied. Not only a conventional composite approach (i.e. a mechanical mixture of the 2 phases) has been considered in the literature, but also the possibility of achieving a 'segregated network' consisting of a percolating highly conducting second phase (e.g. segregated at grain boundaries of the first phase) for optimizing the thermoelectric properties has been explored as well [108].

Note that according to the models [109–111] for usual multi-component system, the effective figure of merit ($ZT_{\text{effective}}$) and the effective power factor ($PF_{\text{effective}}$) cannot be greater than those of its single constituents, unless interface/boundary effects come into play and become decisive. In a recent example, creation of the metallic 'nanoweb structure' achieved by partially coating grains of the target material with a metallic layer tens of nanometer thick, for example, before consolidation by spark-plasma-sintering delivered a nice example of overcoming the trade off between Seebeck coefficient and electrical conductivity [112].

Starting from these considerations, we investigated here whether obtaining a segregated 3D conductive network surrounding insulating (SiAlON) or semiconducting (SiC) particles may result in higher PF ($\alpha^2\sigma$) than a conventional particle reinforced composite consisting of the very same phases with the same volume fractions (see Fig. 3.1). With this in mind, the goal of this study is to compare the two different composite approaches and study the temperature dependence of the physicochemical quantities relevant for thermoelectricity between 300 and 1000 K of TiCN/SiAlON and TiCN/SiC composites having different microstructure designs.

3.2. Sample Preparation and Characterization

In this section, four different sets of samples were prepared. Firstly, for the particle reinforced composites (PRC), 10 vol.% TiC_{0.7}N_{0.3} (TiCN) with an average particle size <150 nm (Sigma–Aldrich) was mixed to SiAlON powder (MDA Advanced Ceramics Ltd. Eskisehir, Turkey). Secondly, in order to obtain a segregated three-dimensional network, spray-dried SiAlON granules supplied by MDA Advanced Ceramics Ltd. (Eskisehir, Turkey) were coated with TiC_{0.7}N_{0.3} in order to obtain final compositions analogous to the previous ones (SNC) (i.e. 5 and 10 vol.% TiC_{0.7}N_{0.3}).

Note that in this case, the spatial distribution of the second phase is different compared to the first composite. Thirdly, commercially available SiC granules (SIKA Densitac-13, Saint Gobain, Norway) were coated with the same amount of $\text{TiC}_{0.7}\text{N}_{0.3}$. Lastly, The resulting powders were then dry-pressed with a computer controlled automatic uniaxial press (Dorst, Germany) under 200 MPa. Two-stage sintering of the SiAlON-based pellets was carried out in a crucible of hexagonal boron nitride using a gas pressure sintering (GPS) furnace (FCT System GmbH, Germany). The first stage of sintering was achieved at 2213 K for 60 min under a nitrogen gas pressure of 0.2–0.5 MPa. In the second stage, both the peak temperature and gas pressure were raised to 2263 K and 10 MPa respectively, for the same dwell time while the compaction of the SiC-based pellets was carried out in a graphite mold using a spark-plasma-sintering (SPS) furnace (FCT Systems GmbH, Germany) at a maximum temperature of 2323 K (dwell time 10 min) in nitrogen atmosphere. Further details of the preparation route are given elsewhere [47]. The density of the sintered samples was measured by gas pycnometer (AccuPyc 1330). Phase identification was performed by x-ray diffraction (XRD) using a Rigaku Rint (2200-Japan) diffractometer with Ni-filtered $\text{Cu-K}\alpha$ radiation (wavelength = 1.5418 Å).

For SEM investigations, the samples were polished by a conventional polishing method used for ceramic materials. Microstructural characterizations were conducted by using a Zeiss™ Supra 50 VP scanning electron microscope (SEM) attached with an EDX detector (Oxford).

The heat capacities of the samples were measured by DSC (NETZSCH STA 449F3), whereas the thermal diffusivities were determined by laser flash technique (Netzsch-LFA 457) using $10 \times 10 \times 2 \text{ mm}^3$ square samples between 300 K - 1000 K. The thermal conductivity values of these samples were calculated according to the equation 2.10.

The Seebeck coefficients and electrical resistivity of the samples were measured by using an ULVAC ZEM 3-M8 and an Alpha-A high-resolution dielectric analyzer (Novocontrol Technologies GmbH) (ac voltage 0.3 V, frequency range from 2 MHz to 1 Hz, under Ar atmosphere). The analysis of the impedance spectra was performed with the commercial software Z-View 2 by Scribner Associates Inc. The

Seebeck measurements were carried out under He atmosphere without depositing any platinum contacts on the surface of the samples.

The relative uncertainties for the Seebeck coefficient (δ_α), electrical conductivity (δ_σ), and thermal conductivity (δ_κ) were evaluated to be 5%, 10%, and 6%,

respectively. According to uncertainty propagation [88] the uncertainty for the power factor (δ_{PF}) was calculated as $\delta_{PF} = [(2\delta_{\alpha})^2 + \delta_{\sigma}^2]^{1/2} \approx 14\%$, and the relative uncertainty for ZT (δ_{ZT}) was calculated as $\delta_{ZT} = [(2\delta_{\alpha})^2 + \delta_{\sigma}^2 + \delta_{\kappa}^2]^{1/2} \approx 15\%$. The uncertainty bars are not visible for the quantities that drawn in log scale.

3.3. Results and Discussion

3.3.1. Comparison of 2 composite approach in TiCN- SiAlON composites

The temperature dependence of the electrical conductivity (σ), of single phase samples and the composites are shown in Figure 3.2 and the temperature dependence of the electrical conductivity (σ), Seebeck coefficient (α), power factor ($PF = \sigma \cdot \alpha^2$) and the resulting figure of merit ($ZT = PF \cdot T/\kappa$) between 300 and 1000 K for SiAlON-based composites are shown in Figure 3.3.

As shown in Fig. 3.3 (a), SiAlON is a pronounced electrical insulator and below 600 K it was difficult to obtain reliable electrical conductivity data (at this temperature, the total resistance of the sample was 8×10^7 Ohm, corresponding to the upper limit of the impedance spectrometer used here). Above this temperature, the electrical conductivity increases according to a thermally activated transport mechanism with an activation energy of 1.35 eV in reasonable agreement via Ref [35]. On the other hand, TiCN exhibits very high electrical conductivities (on the order of 10^6 Ohm⁻¹m⁻¹). The composites have – as expected - conductivity values lying in-between these two materials.

Nonetheless, a closer look at the electrical conductivity data of the composites reveals substantial differences among the samples. The specimen containing the segregate network (SNC-SiALON-10) has a significantly higher electrical conductivity (by about 5 orders of magnitudes) in a comparison to the particle reinforced composite containing the same amount of second phase (PRC-10). This can be readily explained if one considers the electrical transport properties of TiCN: thanks to the achieved percolating network (see Fig. 3.1 (c-d), its high conductivity dominates also the electrical properties of the segregated composite (SNC- SiALON-10). On the contrary, in the PRC-10 sample, the isolated TiCN particles (10 vol.%) do not allow for a percolating situation to occur.

Comparative XRD patterns of the all composites were shown in Figure 3.2. The main phases in the composites are α -SiAlON, β -SiAlON and TiCN and a little amount SiC.

According to the mixing rule, it is worth noting that for the sample containing 10 vol.% TiCN, the effective electrical conductivity is expected to be about a factor of 10 lower than the conductivity of TiCN. The fact that the electrical conductivity at 623 K is 80 times lower, is indicative of a non-optimal percolating network, which probably suffers also from a certain grain size distribution of the host material.

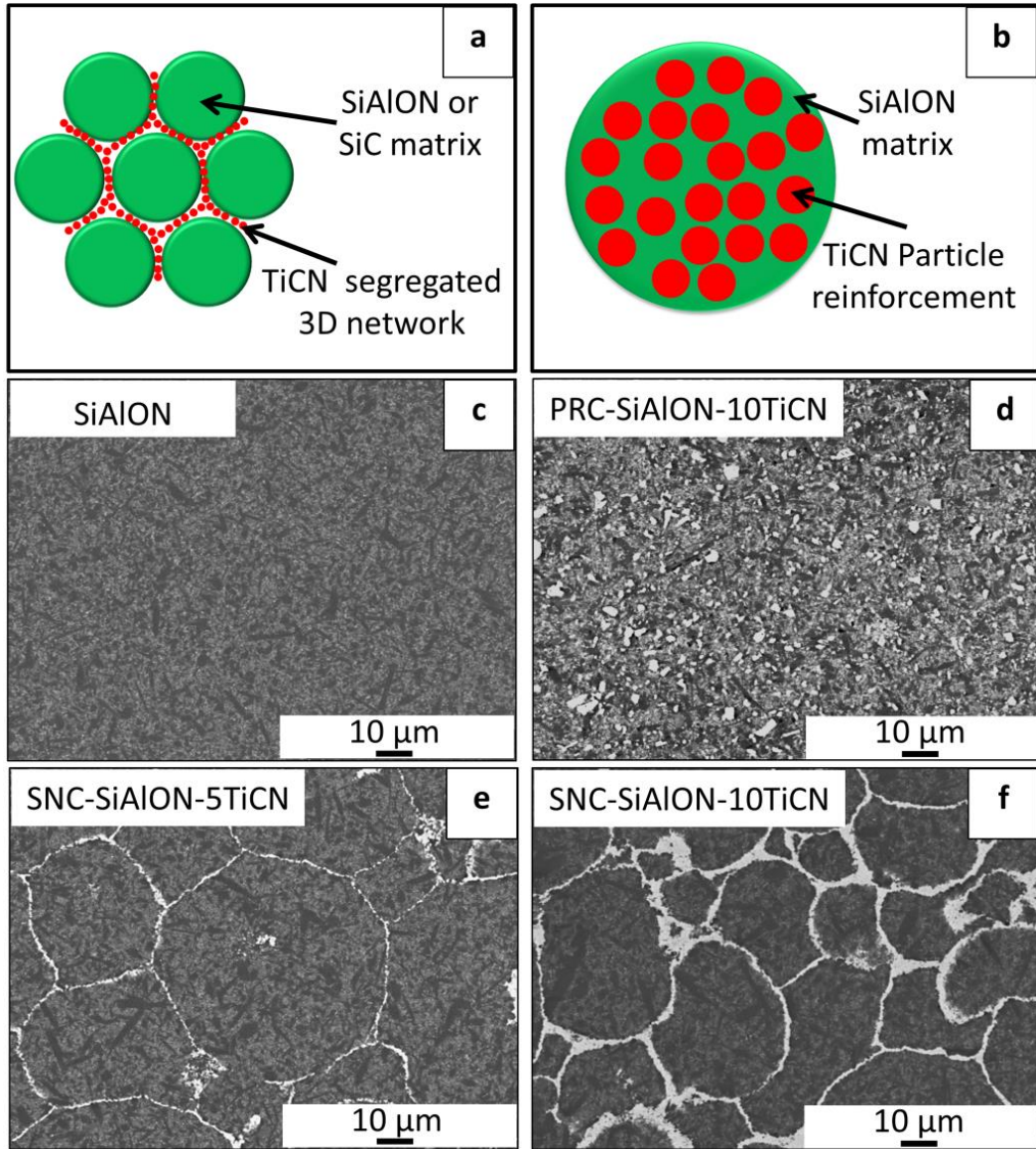


Figure 3.1 (a-b) Schematic microstructural models of the composites investigated in this study. (c-f) SEM-BSE images of polished surface of the composites: (c) SiAlON (d) PRC-SiAlON-10: 10 vol.% TiCN particle reinforced composite (e) SNC-SiAlON-5: 5 vol.% TiCN segregated 3D composite (f) SNC-SiAlON-10: 10 vol.% TiCN segregated 3D network composite.

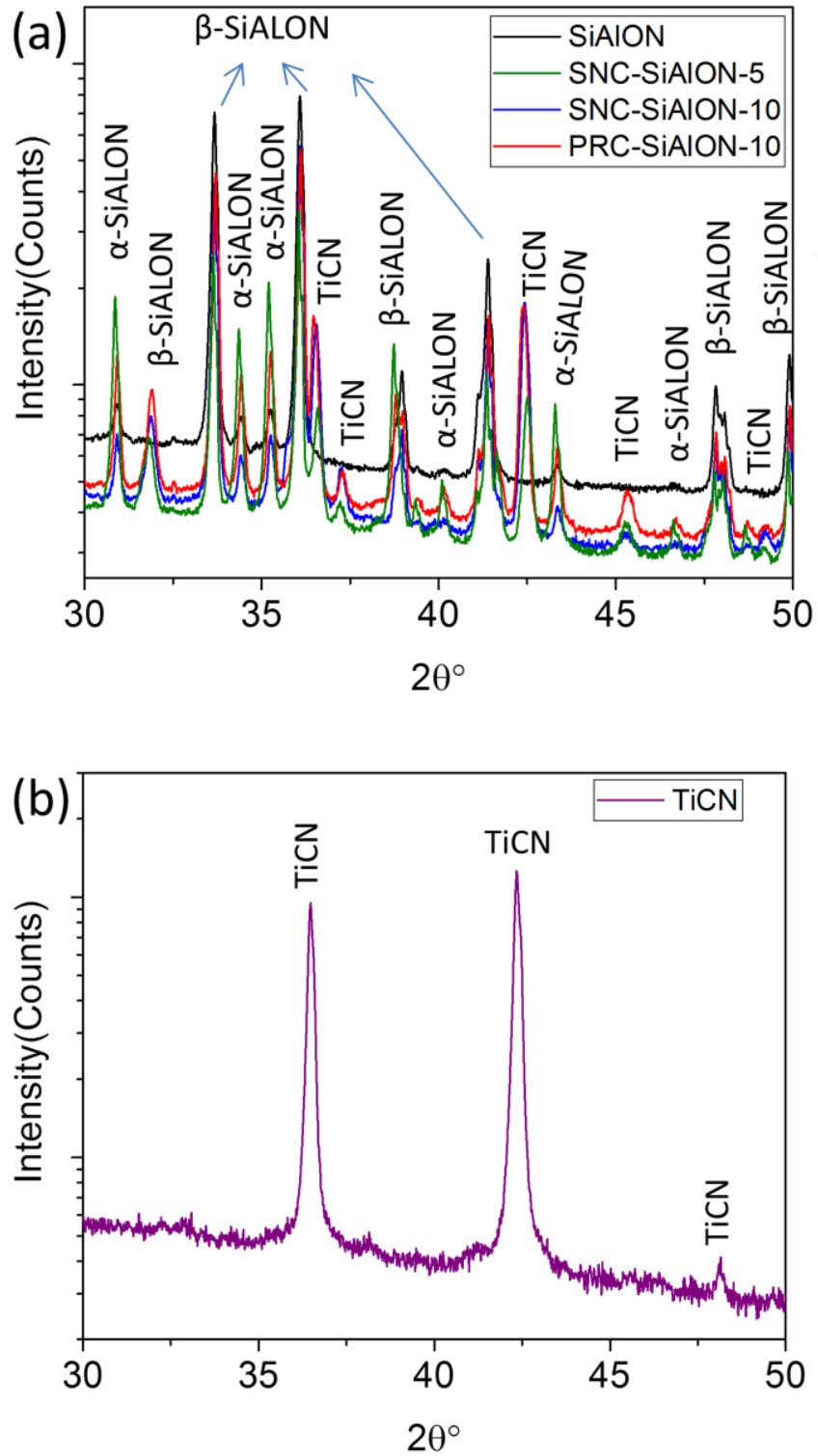


Figure 3.2 XRD pattern of TiCN, SiAlON and SiC based composites. (PRC:particle reinforced composite, SNC:segregated 3D network composite).

Further evidences of effective percolating networks in the SNC samples are provided by the fact that, the measured electrical conductivity is improved by a factor of 2 when the volume fraction of the segregated TiCN phase is doubled (SNC-10 vs. SNC-5). The Seebeck coefficient of sample PRC-10 composite becomes progressively more negative as the temperature increases while it stays almost constant in the SNC-SiALON-5 and SNC-SiALON-10 samples. Interestingly, the larger TiCN volume fraction does not provide any substantial improvement in terms of Seebeck coefficient. All composites considered here exhibit negative Seebeck coefficient values, whose magnitude is however too low to obtain high thermoelectric power in this temperature range (Fig. 3.3 (c)). Due to the highly resistive behavior of the SiALON sample in the low temperature range, it is not possible to acquire reliable Seebeck coefficient data (Fig. 3.3(b)) for $T < 600$ K.

Figure 3.3 (d) shows the temperature dependence of the total thermal conductivity of the samples. The measured thermal conductivity of SNC-SiALON-10 is slightly higher than of PRC-10. This can be rationalized by considering that the more homogeneously dispersed second phase in the PRC sample provides more phonon scattering centers in a comparison to the segregated network of nano TiCN particles. Furthermore, as a side note, the experimental data reveal the thermal conductivity of the TiCN sample alone, to show distinctively different behavior compared to other samples as a function of temperature. As seen in the Fig. 3.5 (d), the reason for this may be the formation of TiO_2 phase during the measurement.

As a consequence of the high electrical conductivity, the power factor (PF) in the SNC- SiALON-10 composite is also higher than in the PRC-10. Moreover, 5 vol.% TiCN additions as in the form of a segregate network (SNC- SiALON-5) is enough to obtain higher PF values than the PRC- SiALON -10 sample. Nonetheless, even if the PF of SNC- SiALON-10 is larger than the PF of PRC-10, it is still low to obtain substantial thermoelectric power generation (Fig. 3.3 (d)).

Likewise, the figure of merit (ZT) for SNC- SiALON-10 is higher than the PRC-10 despite the fact that PRC-10 has much lower thermal conductivity. This is due to the huge increase of the overall electrical conductivity when TiCN is used as a segregated network (Fig 3.3(e)).

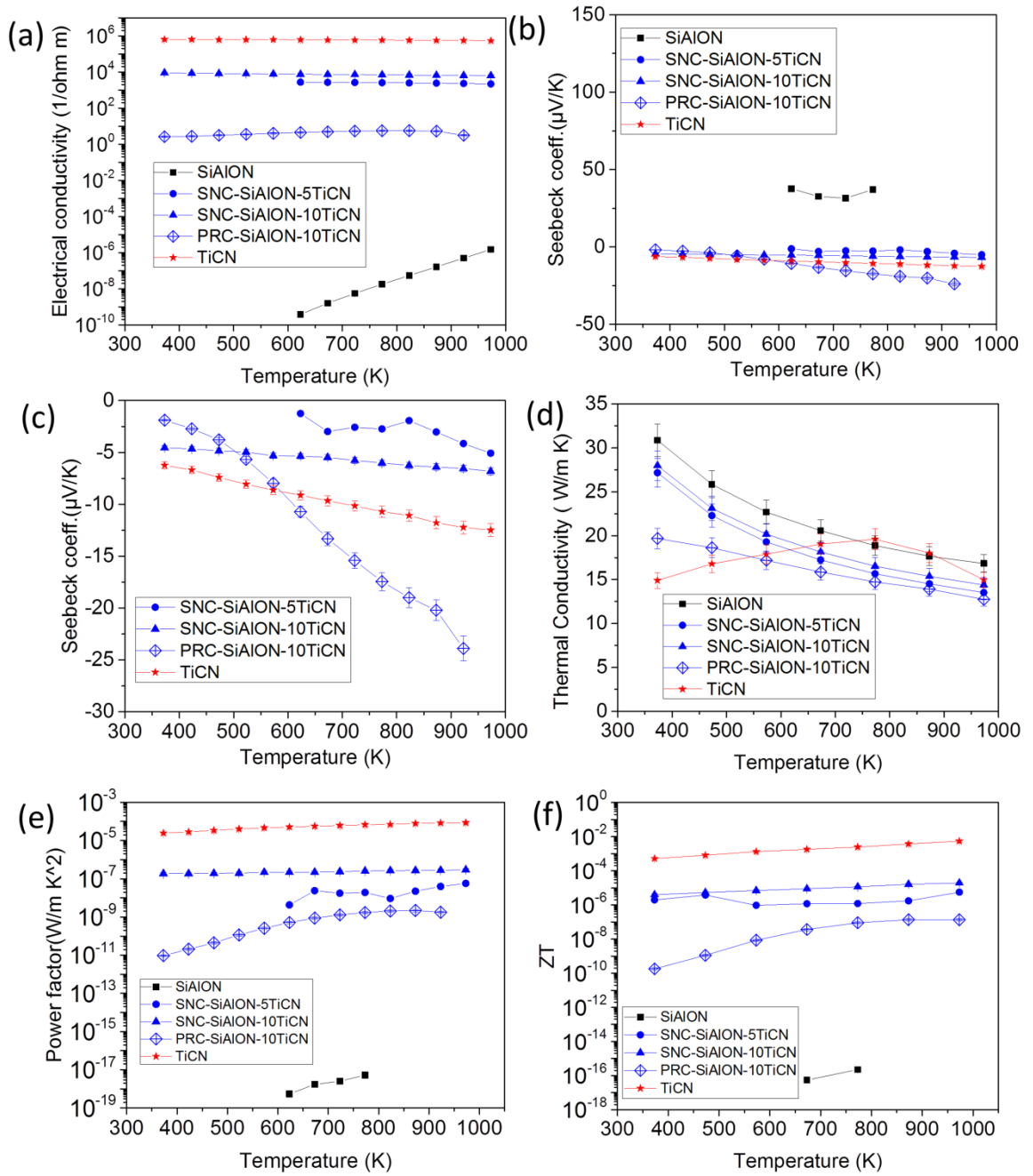


Figure 3.3 (a) Electrical conductivity, σ , (b)&(c) Seebeck coefficient, α , (d) Thermal conductivity, κ , (e) power factor ($\sigma \cdot \alpha^2$) and (f) figure of merit (ZT) measurement of SiAlON based composites as a function of T in He atmosphere. (The uncertainty bars are not visible for the quantities that drawn in log scale)

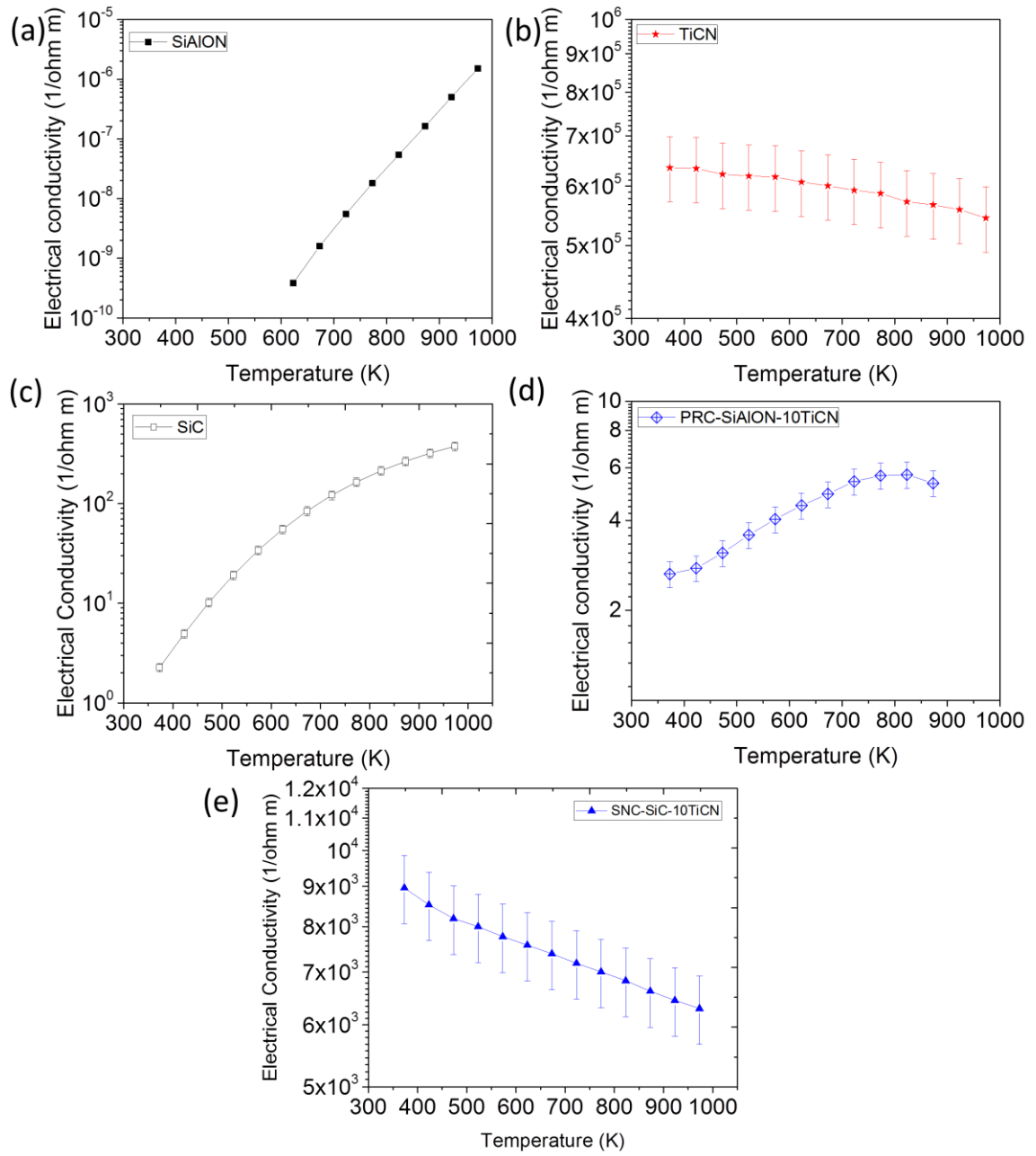


Figure 3.4 Electrical conductivity, σ , of (a) SiAlON (b) TiCN (c) SiC (d) PRC-composite and (e) SNC-composites as a function of T .

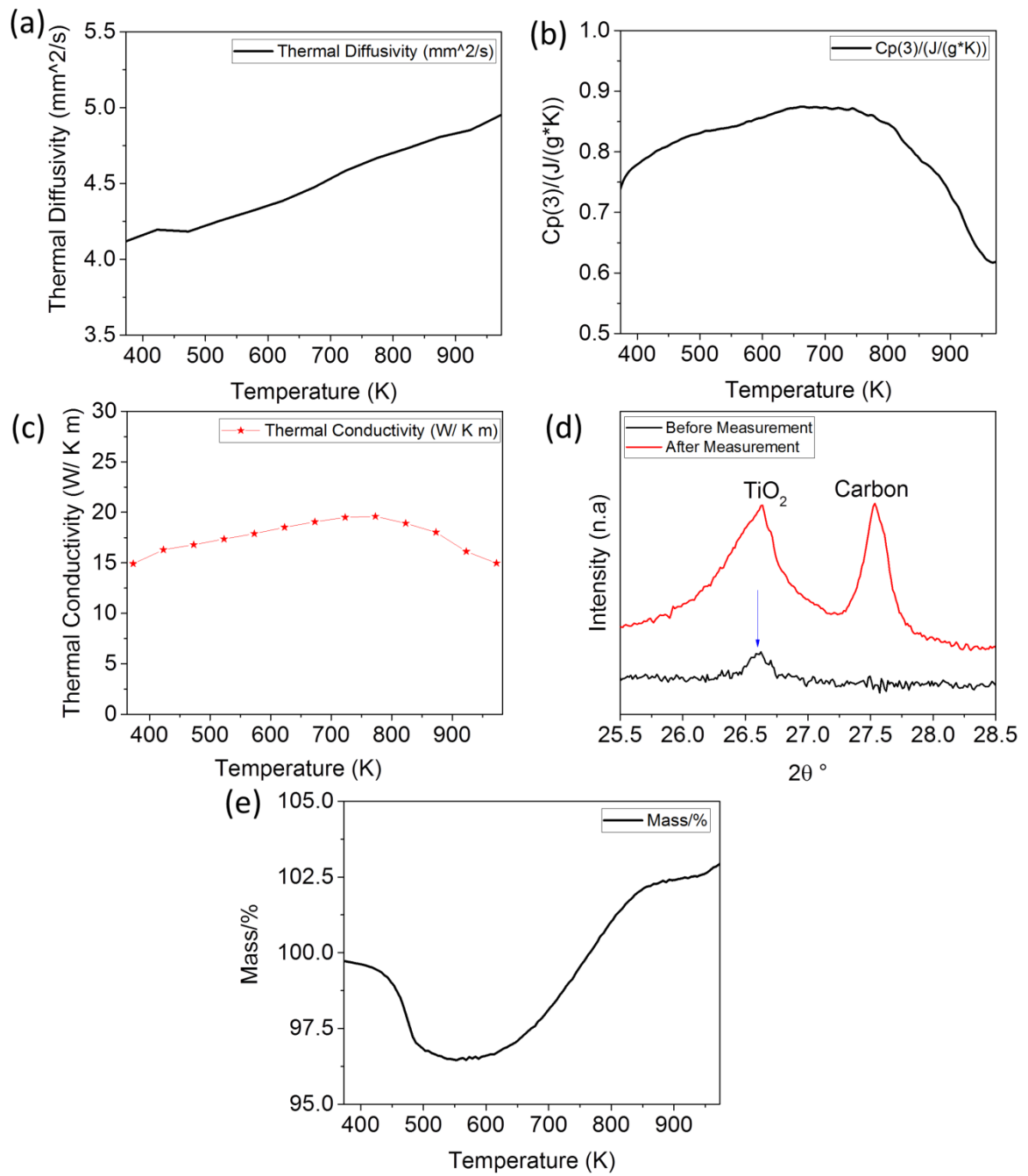


Figure 3.5 (a) Thermal diffusivity, (b) Specific heat, (c) Thermal conductivity, (d) XRD pattern and (e) TG curve taken from TiCN.

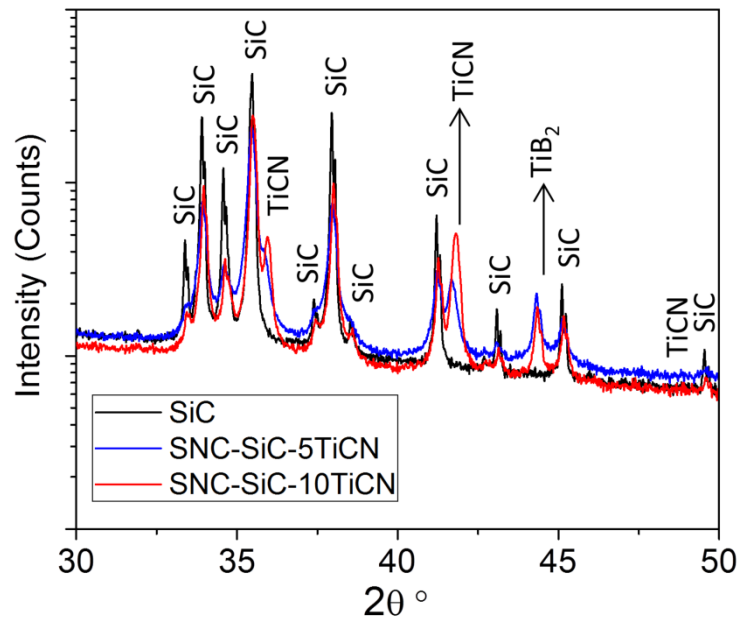


Figure 3.6 XRD patterns of SiC based composites.

3.3.2. Applying SNC method on SiC

Since the segregated network strategy (SNC) yielded better thermoelectric properties than the particle reinforced composite approach, SiC-based composites (having better electric transport properties and yet good stability at high temperatures) were prepared according to the SNC method and their microstructures taken at SEM given in Figure 3.7. In order to compare the results between SiAlON and SiC-based samples, the same amount of TiCN (i.e, 5 and 10 vol.%) was used.

As expected, SiC alone shows intrinsic semiconducting electrical properties characterized by increasing electrical conductivity with increasing temperature; it is 2 ± 0.2 S/m at 373 K while it reaches 380 ± 40 S/m at 973 K (Fig. 3.8(a)).

On the other hand, both SiC composites containing 5 vol.% and 10 vol.% TiCN respectively show extrinsic semiconductor behavior, since below 723-773 K the electrical conductivity decreases with increasing temperature and above this temperature range the electrical conductivity is thermally activated (i.e. it increases with temperature). The electrical conductivity of the composite containing 5 vol.% TiCN (SNC-SiC-5TiCN) slightly decreases from 2×10^3 S/m to 1.5×10^3 S/m, while it decreases from 4×10^3 S/m to 3×10^3 S/m for the samples containing 10 vol.% TiCN (SNC-SiC-10TiCN) (see Fig.3.8(a)). Note that the addition of 10 vol.% TiCN to the SiC matrix as a segregated network ($\sigma = 2\pm 0.2$ S/m at 373 K; $\sigma = 380\pm 40$ S/m at 973 K)

leads to an increase on the electrical conductivity by a factor of about 1900 times at 373 K ($\sigma = 4 \times 10^3 \pm 4 \times 10^2$ S/m) and factor of 12 at 973 K ($\sigma = 4.6 \times 10^3 \pm 4.6 \times 10^2$ S/m).

The pure SiC has a Seebeck coefficient of 670 ± 33 $\mu\text{V/K}$ at 373 K and shows p-type behavior as the Seebeck coefficient is positive which is consistent with the value of additive-free SiC in the literature [113]. As discussed above, TiCN has a negative and low Seebeck coefficient instead. Interestingly, similar to the case of the segregated network in SiAlON, the overall electrical properties of the material are dominated by TiCN which causes the composite to exhibit n-type conductivity and lower Seebeck coefficient. It is worth noting that increasing the amount of TiCN (from 5 to 10 vol.%) does not significantly affect the Seebeck coefficient values. Although the electrical conductivity increases with the addition of TiCN to the system, due to the overall lower Seebeck coefficient values than pure SiC matrix, the PF of the composite is lower than the one of the matrix alone (Figure 3.8(e)). One should note that if the amount of TiCN is below 5 vol.% only a partially connecting network might be obtained instead of a percolating one. The lower amount of TiCN results in higher resistivity and, as the TiCN amount does not have significant effects on the Seebeck coefficient, an improved thermoelectric performance cannot be obtained.

Figure 3.8(d) shows the temperature dependence of the total thermal conductivity of the samples. SiC has a rather high thermal conductivity of 110 ± 6.6 W/m K at 373 K and 58 ± 3.5 W/m K at 973 K. TiCN has low thermal conductivity which is 15 ± 0.9 W/m K at 373 K. Its thermal conductivity increases up to 723 K as the temperature increases, however, a very small decrease is observed above this temperature. The reason for this may be the formation of TiO_2 in TiCN sample at 645 K (see Fig. 3.5). The addition of TiCN provided a 50 % decrease in the thermal conductivity at low temperatures since this second phase dominates the overall thermal and electrical properties of the composites. As the temperature increases, the thermal conductivity decreases as a result of more pronounced umklapp-processes [114]. Due to this effect pure SiC and composites show similar thermal conductivity values at high temperatures.

The matrix material (SiC) exhibits approximately a 120 times higher Seebeck coefficient than the segregated material (TiCN) at 373 K. Although SNC-SiC-10TiCN samples have a higher electrical conductivity by a factor of 1900 when compared to the pure SiC sample, the PF and ZT values of the pure SiC matrix are substantially higher than those of the composite samples.

From the comparison between the SiAlON and SiC-based composites with the equal amount of TiCN, one can readily note that the SiAlON-based composites have factor of 2 higher electrical conductivity values at 373 K (and a factor of 1.4 at 973 K) than SiC based ones. More specifically, SiAlON based composites show metallic behavior while SiC based composites show extrinsic semiconductor behavior (Fig.3.9 (a)). This indicates that TiCN is clearly dominating the system in SiAlON based composites to a larger extent than in the SiC based ones.

As it is expected from the electrical conductivity values, the magnitude of the Seebeck coefficient is lower by factor of 2 at 373 K and of 3 at 973 K than in the SiAlON-based composites. In both systems, increasing the amount of TiCN has a beneficial effect on stabilizing the Seebeck behavior (Fig.3.9 (b)). Figure 3.9(c) shows clearly SiC based composites to have factor of 2.6 at 373 K and 3.6 at 973 K higher thermal conductivities than SiAlON based ones. Changing the amount of TiCN has a visible effect on the thermal conductivity of SiC based composites, whilst this is not the case in SiAlON based composite system.

As a consequence of the high Seebeck coefficient, the SiC based composites have a factor of 2 higher PF at 373 K than the SiAlON based composites and, as the temperature increases, this enhancement reaches almost a factor of 7 (Fig. 3.9(d)). Interestingly, as the thermal conductivity of the SiAlON based samples decreases at low temperatures, SiAlON based composites exhibit higher ZT values despite their low PF in the same temperature range. The ZT parameter of SiAlON based composites is higher by a factor of 2.4 at 373 K and of 3 at 973 K than SiC based ones (Fig. 3.9(e)). Moreover, in contrast to the SiC samples, the SiAlON based composites have higher ZT values than the matrix material as shown in Figure 3.9(f).

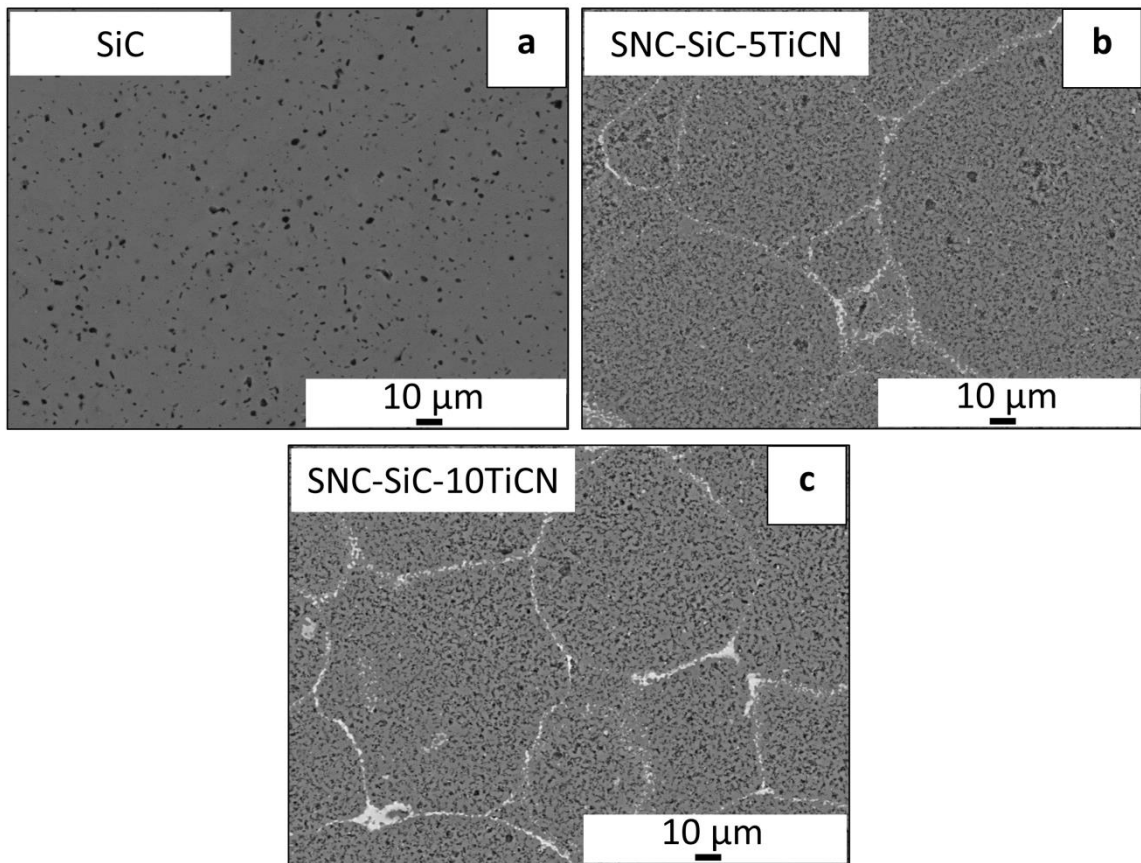


Figure 3.7 SEM-BSE image of polished surface of composites (a) SiC (b) SNC-SiC-5 and (c) SNC-SiC-10.

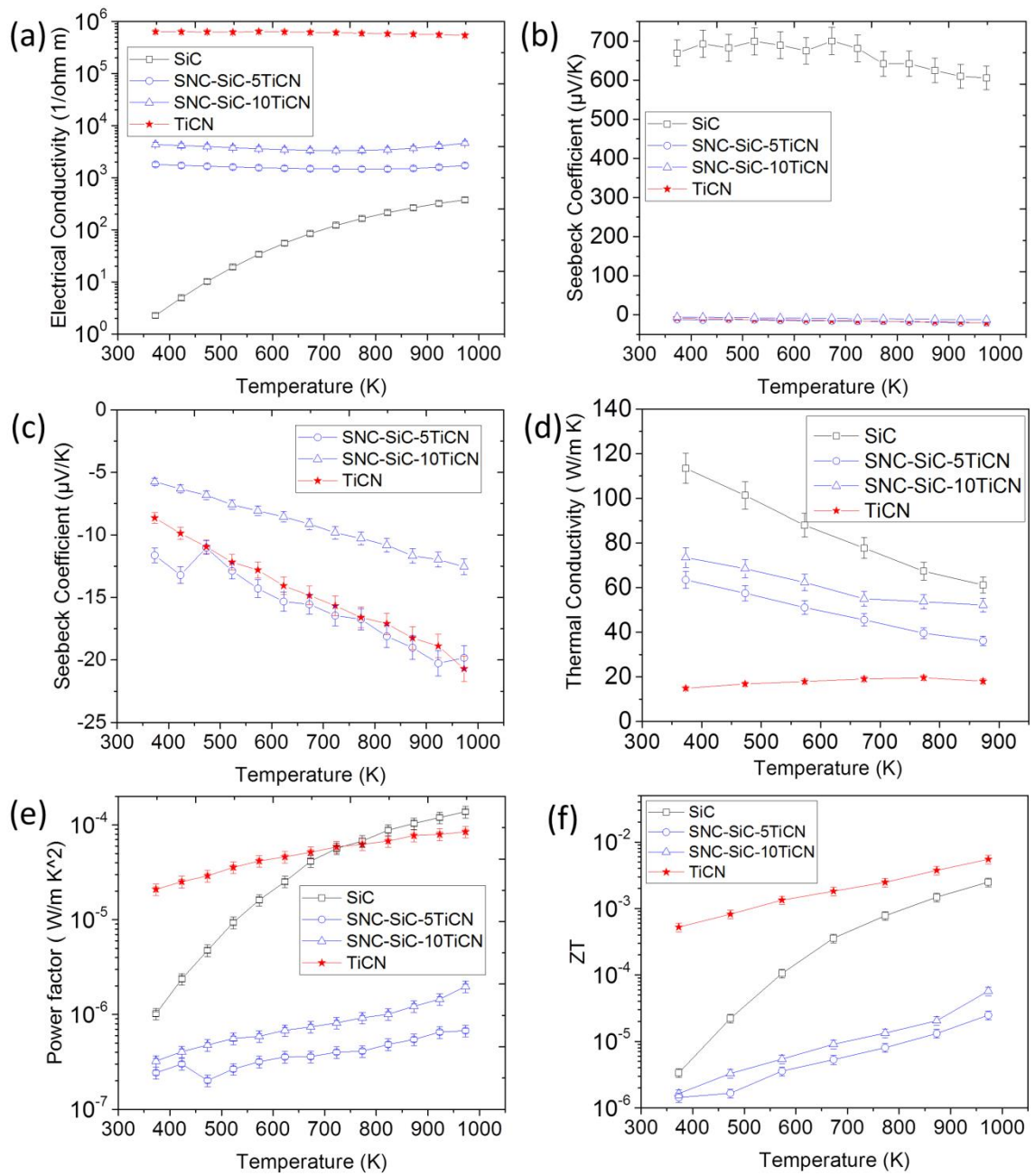


Figure 3.8 a) Electrical conductivity, σ , (b-c) Seebeck coefficient, α , (d) Thermal conductivity, κ , (e) PF ($\sigma \cdot \alpha^2$) (f) ZT measurements of SiC based composites as a function of T . (The uncertainty bars are not visible for the quantities that drawn in log scale)

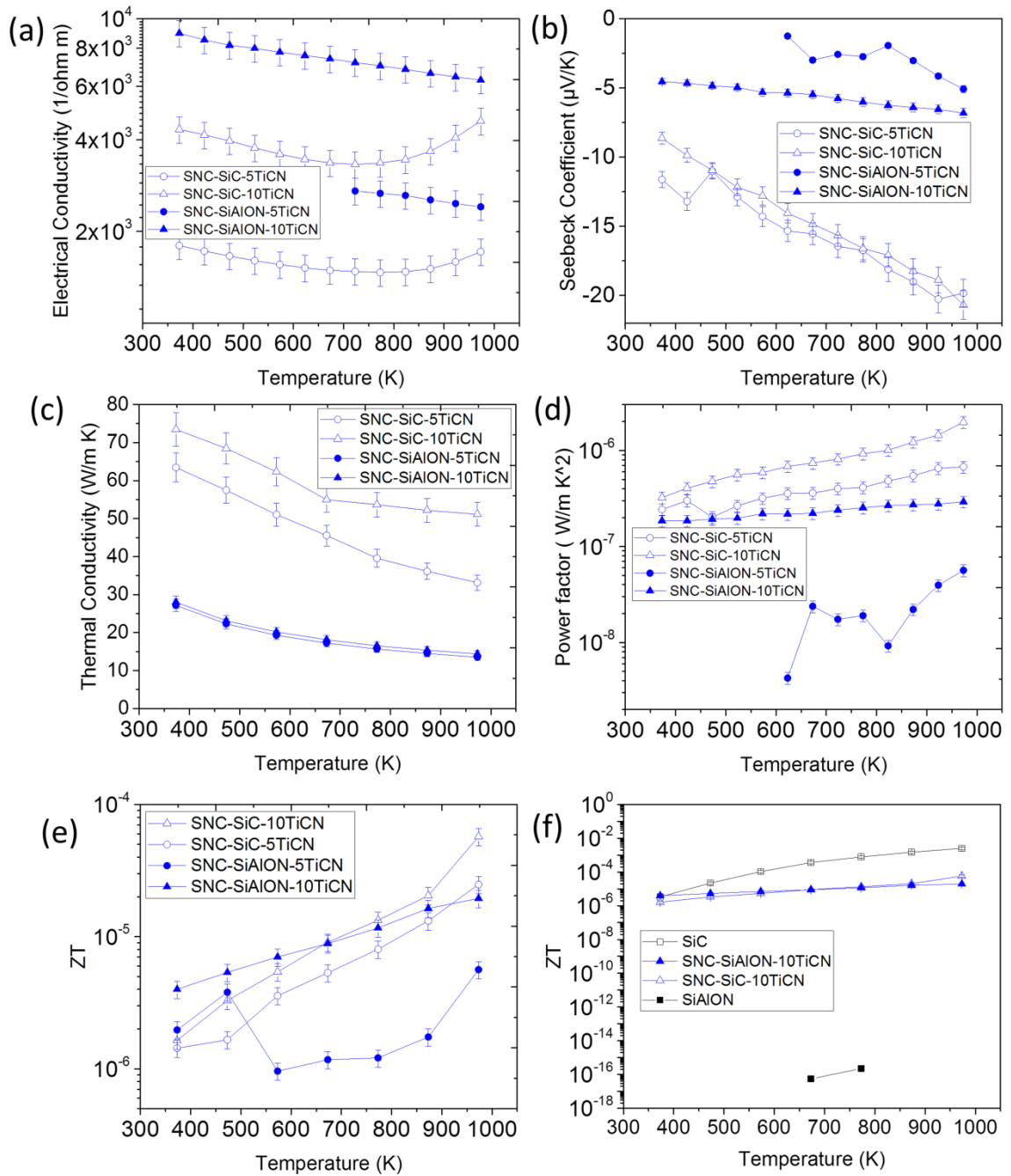


Figure 3.9 Comparison of SiC and SiAlON based composites (a) Electrical conductivity, σ , (b) Seebeck coefficient, α , (c) Thermal conductivity, κ , (d) PF ($\sigma \cdot \alpha^2$) (e-f) ZT measurement as a function of T . (The uncertainty bars are not visible for the quantities that drawn in log scale)

3.3.3. Effect of different coating materials on thermoelectric properties in SiC composites

SiC, B₄C and ZrO₂ were used as a segregated network material for the set of samples that investigated in this section. Detailed information about processing method is given in section 3.1. XRD analyses revealed that no reaction phase occurred after sintering. Back-scattered electron (BSE) images taken from the polished surfaces of the SiC-based composites are displayed in Fig. 3.10. These micrographs, in which the contrast results from the different atomic number (Z) of the constituents, revealed that the preparation of the segregated network by using B₄C and ZrO₂ is partially successful and it is not surprising not to observe the segregated network in BSE image of SNC-10SiC-SiC sample, as the matrix and the segregated network are the same material.

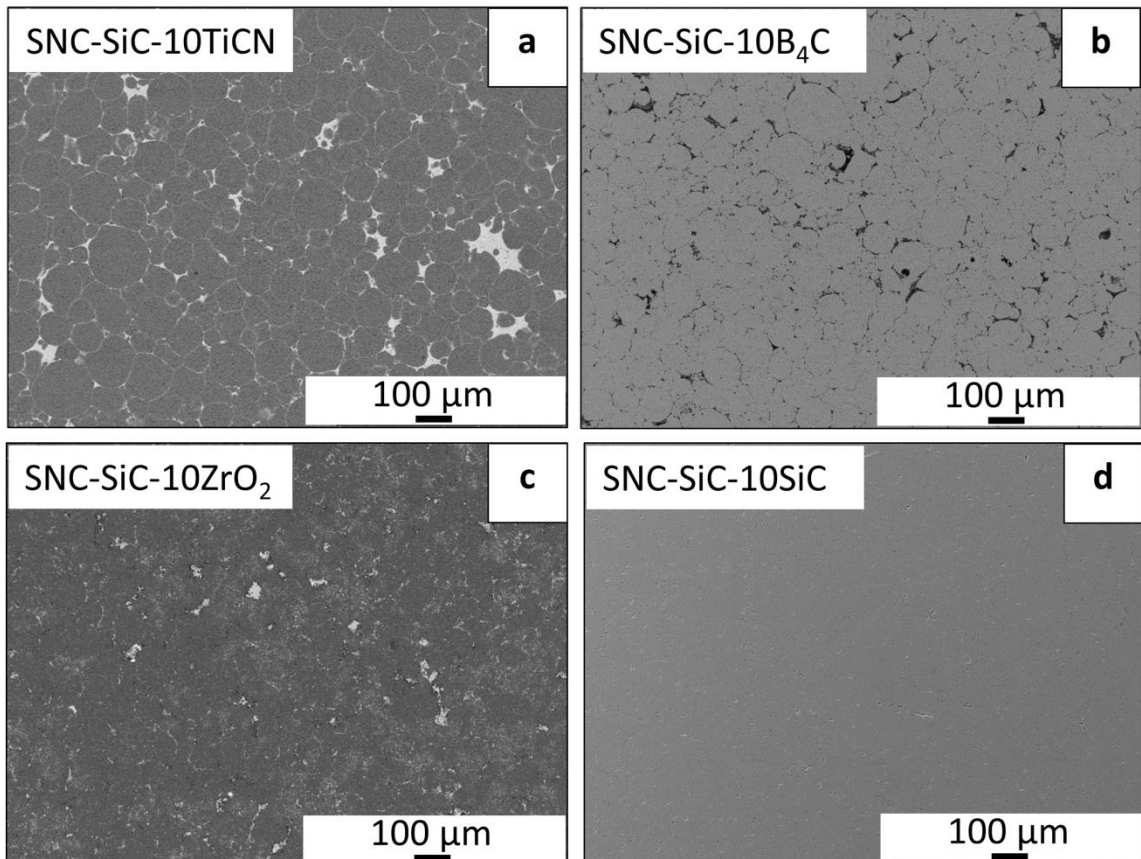


Figure 3.10 SEM-BSE image of polished surface of composites (a) SNC-SiC-10TiCN, (b) PSNC-SiC-10B₄C, (c) PSNC-SiC-10ZrO₂ (d) SiC-10SiC (PSNC: Partially segregated network composite.)

The temperature dependence of the electrical conductivity (σ), Seebeck coefficient (α), power factor ($PF = \sigma \cdot \alpha^2$) and the resulting figure of merit ($ZT = PF \cdot T / \kappa$) between 300 and 1000 K for composites are given in Figure 3.11.

As shown in Fig. 3.11(a), TiCN exhibits the highest electrical conductivity (on the order of $10^6 \text{ Ohm}^{-1} \text{ m}^{-1}$) below 600 K and B_4C exhibits the highest electrical conductivity (on the order of $10^6 \text{ Ohm}^{-1} \text{ m}^{-1}$) over 600 K. The SNC-SiC-TiCN and PSNC-SiC- B_4C composites have, as expected, conductivity values lying in-between these two extremes. SNC-SiC-SiC composite has almost the same electrical conductivity as pure SiC.

A closer look at the electrical conductivity data of the composites reveals that PSNC-SiC-10 B_4C composite has pure semiconductor behavior while PSNC-SiC-10 ZrO_2 composite shows extrinsic semiconductor behavior (Fig. 3.11a). PSNC-SiC-10 B_4C composite exhibits electrical conductivity on the order of $10^3 \text{ Ohm}^{-1} \text{ m}^{-1}$ below 700 K and $10^4 \text{ Ohm}^{-1} \text{ m}^{-1}$ above 700 K. PSNC-SiC-10 ZrO_2 composite exhibits electrical conductivity on the order of $10^4 \text{ Ohm}^{-1} \text{ m}^{-1}$.

The pure B_4C has a Seebeck coefficient of 240 $\mu\text{V}/\text{K}$ at 373 K and shows p-type behavior as the Seebeck coefficient is positive which is consistent with the value of additive-free B_4C in the literature ref [115]. As B_4C has a positive Seebeck coefficient while the other composites not, the overall electrical properties of the materials are dominated by B_4C , and thus the composite exhibits p-type conductivity behavior and similar Seebeck coefficient values (Fig. 3.11(b)). The data of pure ZrO_2 is highly scattered which is not shown here. However PSNC-SiC-10 ZrO_2 composite show n-type behavior according to the Seebeck coefficient values (Fig.3.11(c)).

Although the electrical conductivity increases with the addition of B_4C and ZrO_2 to the system, due to the low Seebeck coefficient values in comparison to pure SiC matrix, the PF of the composite is lower than the one of the matrix alone ((Fig. 3.11(e)). There is no obvious difference between pure SiC and SNC-SiC-10SiC composite system according to all transport property measurement (Fig. 3.11).

Although SNC-SiC-10 B_4C sample has higher PF by a factor of 3.5 than pure SiC sample at 573 K; the ZT values get smaller while the thermal conductivity of the sample gets higher.

As SiC and B_4C are p-type materials, the composites of them shows p-type behavior; similarly, as the TiCN is an n-type material, its composite showed the same type of behavior. As a consequence, by changing the segregated network materials, it is possible to obtain either p or n type behavior. However, it is important in the SNC

method to obtain a 3D network to increase the electrical conductivity, thus optimization of coating parameters for different coating materials should be carried out in the future.

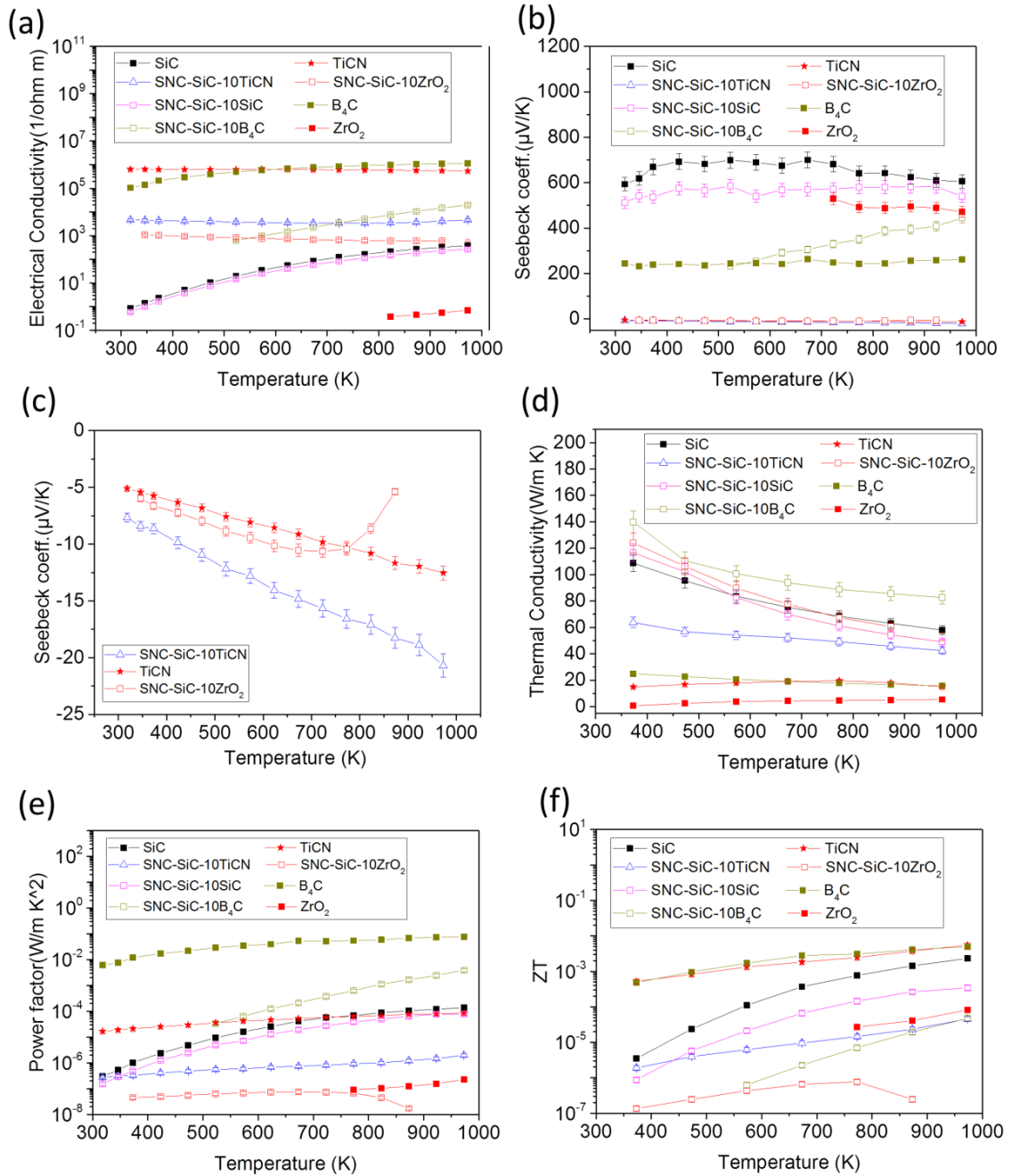


Figure 3.11 (a) Electrical conductivity, σ ; (b-c) Seebeck coefficient, α ; (d) Thermal conductivity, κ ; (e) PF ($\sigma\alpha^2$); (f) ZT measurement of SiC based composites as a function of T

3.3.4. Applying the SNC method to SrTiO₃

As it was mentioned above, oxide thermoelectric materials have recently exhibited promising properties mostly related to their durability at high temperature in air, as well as non-toxicity and low cost [10].

The samples in this section prepared by the segregated network method which was explained in section 3.1. Instead of SiAlON granules, SrTiO₃ granules (supplied by BÜCHI Labortechnik AG, Switzerland) have been chosen as a host material. The aim was to obtain segregated network consist of La_{0.2}Sr_{0.8}TiO₃ (LSTO) around SrTiO₃ granules (Fig.3.12).

La_{0.2}Sr_{0.8}TiO₃ powder was synthesized by solid-state reaction of SrCO₃ (>99%, Sigma Aldrich), La₂O₃ (99%, Sigma Aldrich), and TiO₂ (99.5% Sigma Aldrich). Powders were weighed in the required stoichiometric ratios and mixed by using ball milling in ethanol with ZrO₂ media at 130 rpm for 6 hours. The milled and dried powders were calcined at 1373 K for 1 hour. SrTiO₃ granules supplied by BÜCHI Labortechnik AG, Switzerland were coated with LSTO powder in order to obtain three dimensional network.

In reducing conditions the specimen containing segregated networks (SNC-STO-LSTO) has higher electrical conductivity (by about 5 orders of magnitude at 885 K) in comparison to pure STO. On the other hand in oxidizing conditions the specimen containing LSTO has lower electrical conductivity (by about 3 orders of magnitude at 885 K) in comparison to pure STO (Fig.3.13 (a)).

According to Mott formula¹ carrier concentration is inversely proportional to Seebeck coefficient which results in an inverse proportionality with electrical conductivity. Both SNC-STO-LSTO and pure STO samples under reducing and oxidizing conditions show consistent correlation between Seebeck coefficient and electrical conductivity according to Mott formula. The SNC-STO-LSTO specimen has higher Seebeck coefficient, by a factor of 1.9 as compared to pure STO. Interestingly under oxidized conditions the Seebeck coefficient are roughly the same (Fig.3.13 (b)).

Figure 3.13(c) shows the temperature dependence of the total thermal conductivity of the samples. The measured thermal conductivity of SNC-STO-LSTO is lower than pure STO by a factor of 3.4 and 2.1 under oxidizing and reducing conditions, respectively.

¹ $\alpha = \frac{8\pi^2}{3} \left(\frac{k_B^2 T}{eh^2} \right) m^* \left(\frac{\pi}{3n} \right)^{2/3}$

As a consequence of higher electrical conductivity in the SNC-STO-LSTO composite, the power factor (PF) is also higher (5 orders of magnitude at 885 K) than for pure STO under reducing conditions. However no improvement was obtained under oxidizing conditions although the absolute value of Seebeck coefficient is higher than the reduced samples (Fig.3.13 (d)).

Likewise, the figure of merit (ZT) of SNC-STO-LSTO is higher than pure STO under reducing conditions but lower under oxidizing conditions (Fig.3.13 (e)).

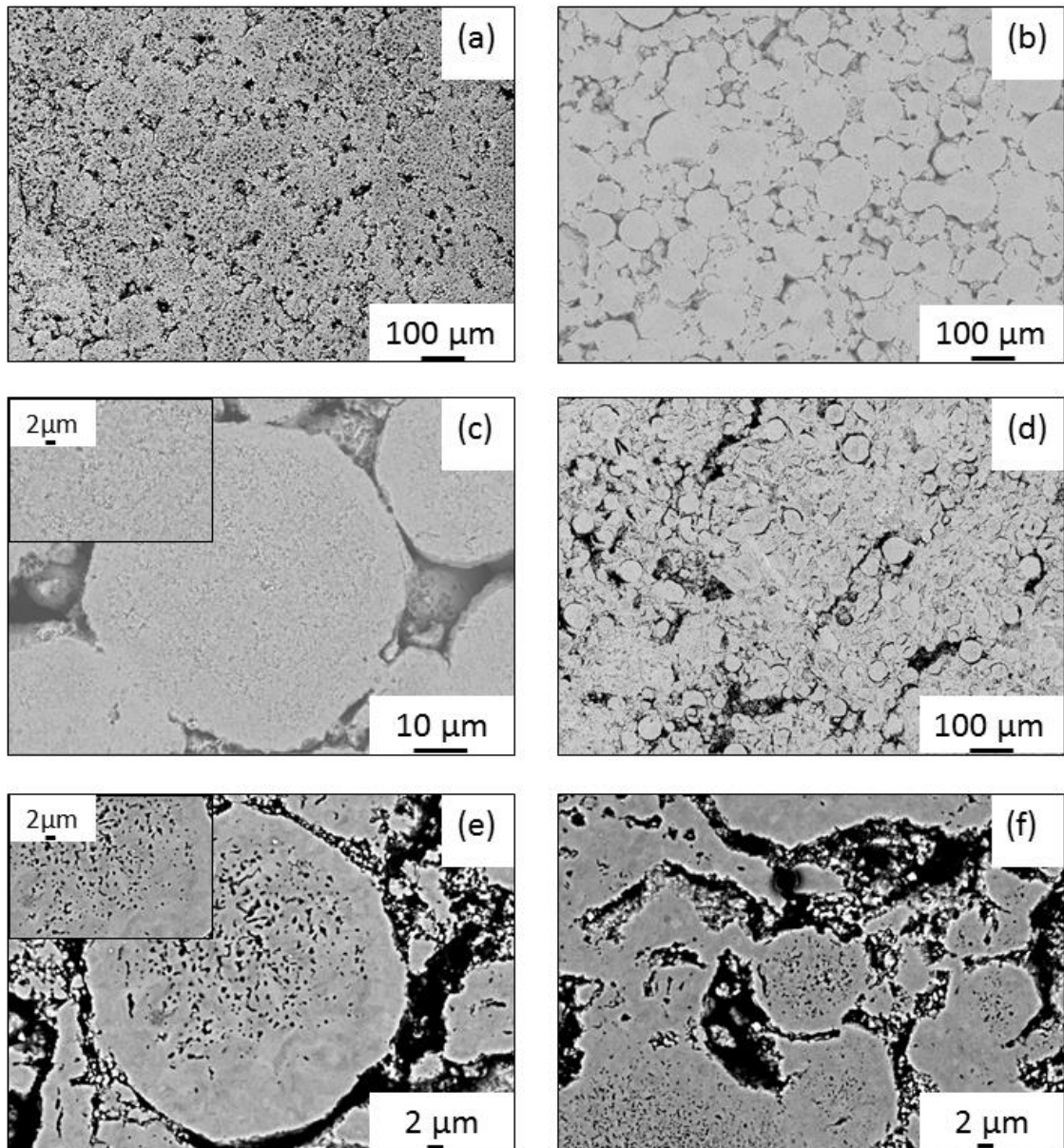


Figure 3.12 SEM-BSE images of polished surface of the composites: (a) SrTiO₃ (b-c) SNC-STO-LSTO_oxidized (d-e-f) SNC-STO-LSTO_reduced composite.

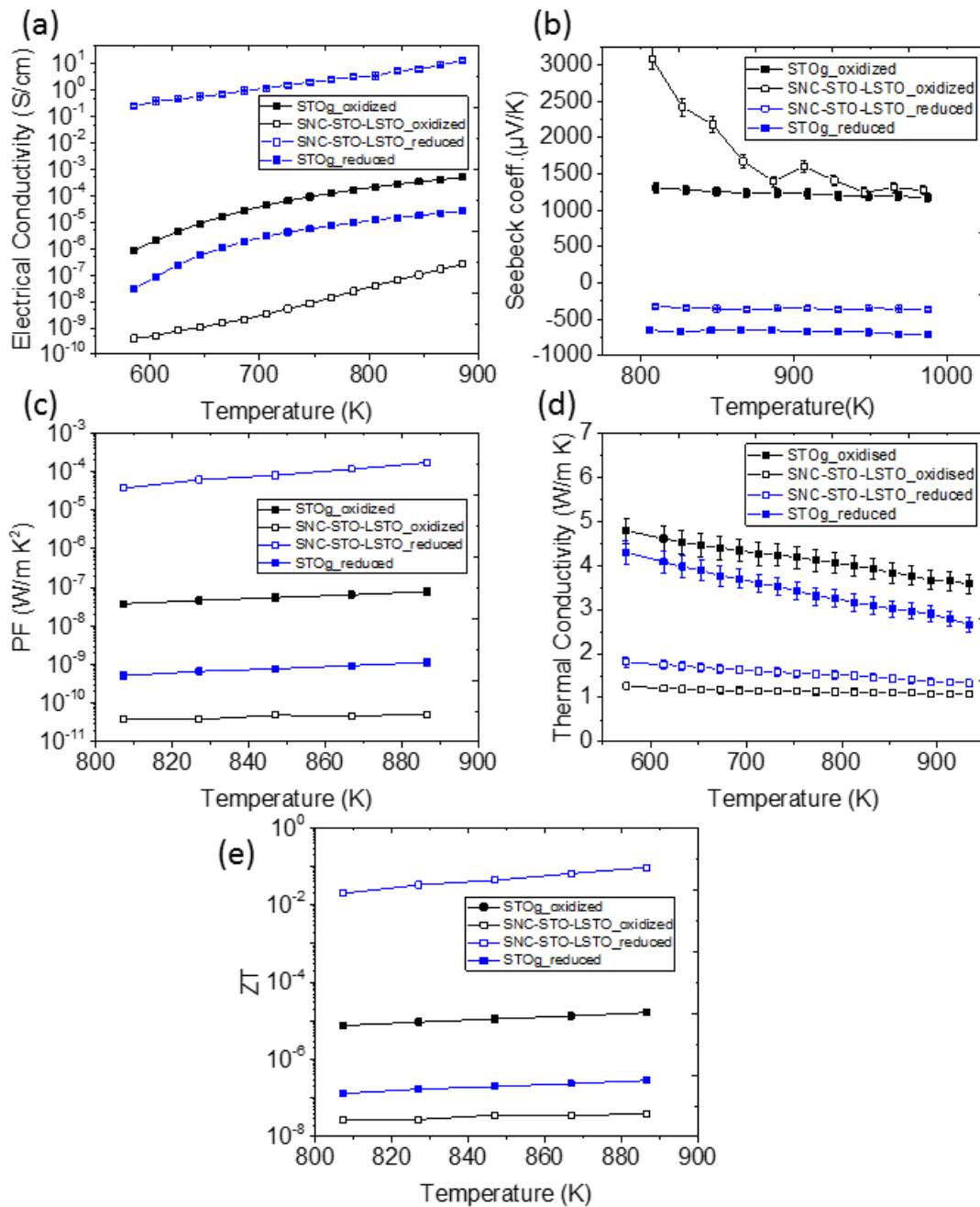


Figure 3.13 a) Electrical conductivity, σ , (b) Seebeck coefficient, α , (c) Thermal conductivity, κ , (d) PF ($\sigma \cdot \alpha^2$) (e) ZT measurement of SrTiO₃ based composites as a function of T. (The uncertainty bars are not visible for the quantities that drawn in log scale)

One should note that porosity as well as morphology of the pores affects the transport properties. La addition prevents densification during sintering in both reducing and oxidizing conditions. Additionally, the pore structure in reduced samples is inhomogeneous unlike the oxidized samples. Large pores were observed around the

granular boundaries and small pores inside the granules under both conditions. There is a sintered core shell exists and the thickness of sintered core is larger in reduced samples (Fig. 3.12 (c-d)). In addition, the reducing conditions hinder the grain growth as well as granular growth which have contribution on increased electrical conductivity.

3.4. Section Conclusion

To sum up, enhanced power factor (PF) and figure of merit (ZT) values have been achieved between 300 and 800 K in SiAlON composites by using TiCN as a segregated three-dimensional network. The results obtained from these composites indicate that the achievement of an 10 vol.% electrically conductive 3D network structure (TiCN) is superimposed to the strongly insulating SiAlON matrix by purposely coating the granules before sintering leads to a significant improvement of the power compared to the matrix phase.

The results obtained from the SiC-based composites reveal that in the case of a more conducting matrix material such as SiC, no enhancement of the power factor compared to the matrix phase is achieved even if TiCN is employed as segregated three-dimensional network. Moreover, although there is no improvement compared to the matrix phase, the power factor of the segregated 10 vol.% TiCN network in SiC is higher than its counterpart having SiAlON as the host material by a factor of 3.3 at 673 K and of 6.8 at 973 K while the ZT is almost the same at 673 K and higher by a factor of 3 at 973 K.

The effect of different coating materials on thermoelectric properties in SiC composites were reported and enhanced PF has been achieved by using B₄C as a segregated three-dimensional network. Although SNC-SiC-10B₄C sample has a higher PF by a factor of 3.5 than pure SiC at 573 K, the ZT values are smaller due to the increased thermal conductivity.

Enhanced PF and ZT have been achieved under reducing conditions by applying the SNC method to SrTiO₃ with La_{0.2}Sr_{0.8}TiO₃ constituting segregated three-dimensional network. Further microstructural analyses such as SEM-EDS are necessary to explain the chemical composition of the core-shell phase.

Preliminary results revealed that SNC method is applicable for various types of ceramic materials.

These findings may be useful for future studies aiming at purposefully designing ceramic microstructures for improving properties of thermoelectric materials.

4. TUNING THE THERMOELECTRIC PROPERTIES BY GRAIN BOUNDARY DECORATION IN SrTiO₃

4.1. Introduction & Motivation

Since high power factor (PF, defined as $\alpha^2\sigma$) was measured in structurally layered materials such as the p-type Na_xCoO_{2.7}, starting a series of investigations on the thermoelectric properties of other oxides [116–119]. CaMnO₃ was one of the first n-type materials investigated among perovskite oxides, but only a few studies have reported ZT values higher than 0.15 [116,120–122]. SrTiO₃ (STO) has now emerged⁸ as a leading high-temperature n-type oxide thermoelectric [123]. Undoped SrTiO₃ has a high Seebeck coefficient $\sim 850 \mu\text{V}/\text{K}$ at 300 K [124]. Lanthanum doping on the A site of SrTiO₃ can show a power factor as high as for Bi₂Te₃ [125,126] and niobium doping on the B site has raised the high-temperature ZT of SrTiO₃ to values around 0.35 [127,128]. A few studies have reported showing an enhanced thermoelectric properties for oxygen-deficient samples [129,130]. *Gregori et al.* [131] investigated the effect of the grain boundaries on both the electrical transport and the thermoelectric properties of SrTiO₃. However, one of the factors limiting the improvement of SrTiO₃-based materials is its high thermal conductivity and its strong temperature dependence [117], frequently limiting ZT to values < 0.2 . Thermal transport in SrTiO₃ is directly correlated with vacancy concentrations and κ can be substantially lowered by cation substitution and disordered site occupancies [132–134]. Neagu and Irvine [135] proposed a mechanism of A-site deficiency to introduce oxygen defects and facilitate further reduction in lattice thermal conductivity (κ_l).

SrTiO₃ is one of the most studied materials in terms of the effects of different additives and processing conditions in thermoelectricity. *Park et al.* [136] achieved ZT values above 0.30 at high temperature for La-doped SrTiO₃ using colloidal synthesis and spark plasma sintering (SPS). *Shakabko et al.* incorporated nitrogen into SrTiO₃ and detected metallic-like electrical conductivity with negative Seebeck coefficients of up to $S = -465 \mu\text{V}/\text{K}$ at room temperature [137]. *Kovalevsky et al.* [138] obtained more modest values with Dy doping. Simultaneous doping by La and Nb and optimizing the reducing atmosphere yielded ZT values ~ 0.2 at moderate temperatures [139,140]. *Dehkordi et al.* [141,142] reported a large improvement of ZT via Pr doping (ZT ~ 0.35). *Kovalevsky et al.* [138,143–145] demonstrated the effect of defect engineering and co-substitutional doping with lanthanide ions (including Dy). The use of highly-reducing sintering conditions generate Ti³⁺, oxygen vacancies,

A-site vacancies and crystallographic shear structures; and enabled increased ZT values up to 0.42 [138,146]. *Backhaus-Ricoult et al.* [146] showed the beneficial effect of inclusions, oxygen vacancies and shear structures of SrTiO₃ matrix on thermal conductivity. *Srivastava et al.* [147] demonstrated the specific contributions from two strategies aiming at enhancing the electron concentration: (i) sintering under reducing conditions (the resulting positively charged oxygen vacancies being electrically compensated by the negatively charged electrons) and (ii) doping the material with donors (La or Nb) which are then compensated by electrons. Besides bulk materials, *Ohta et al.* [124] extrapolated a ZT of 0.24 at 300 K for a superlattice based on SrTiO₃:SrTi_{0.8}Nb_{0.2}O₃. *Abutaha et al.* [148] obtained a very high ZT of 0.46 at 1000 K in superlattice structures of Pr-doped SrTiO_{3-δ} (SPTO) and Nb-doped SrTiO_{3-δ} (STNO) layers. All these studies showed that doping and modifying interfaces play an important role for tailoring the thermoelectric properties. Therefore, microstructural design, particularly of interfaces, can be crucial for improving the desired functionality. In order to increase the ZT parameter, both the electrical conductivity and the thermal conductivity should be adjusted. Grain boundary engineering is one of the well-known approaches that has been used in recent years to adjust (e.g., Σ3 GBs shows the highest conductivity [149] such properties [150]).

The crucial role of boundaries on the overall transport properties especially on electrical conductivity of SrTiO₃ is the main motivation of this study.

In this context, a clear example of the relevance of boundary properties has been provided by *Lupetin et al.*, who investigated the grain size effect on electrical behavior of polycrystalline SrTiO₃ [17]. In particular, it was shown that, by decreasing the grain size, p-type and oxygen vacancy conductivity are depressed whereas n-type conductivity is enhanced by several orders of magnitude in comparison to a microcrystalline sample with the same composition (see Fig. 4.1). Grain boundaries hinder the transport of positively charged mobile carriers (holes and oxygen vacancies) in acceptor-doped SrTiO₃, while they favor instead the transport of excess electrons [151].

The grain boundary properties are significantly different if one considers the situation of donor-doped SrTiO₃ (e.g. with La replacing Sr or Nb replacing Ti). This is because, for such compositions, depending on temperature and oxygen partial pressure, strontium vacancies instead of conduction electrons compensate the positive charge resulting from the donors [152]. The nature of grain boundaries are resistive and to explain this resistive behavior different mechanisms have been proposed such

as trapping of electrons by oxygen diffusion [153], kinetic and space charge effects [154,155] and formation of acceptor defects in the grain boundary core [156]. The studies conducted up to now pointed out how the electrical conductivity might be effectively adjusted by grain boundary engineering. For this reason, in this chapter two strategies for enhancing the electrical conductivity, and therefore ZT, were investigated: (1) reduction of grain size (2) lanthanum decoration under oxidizing and reducing conditions.

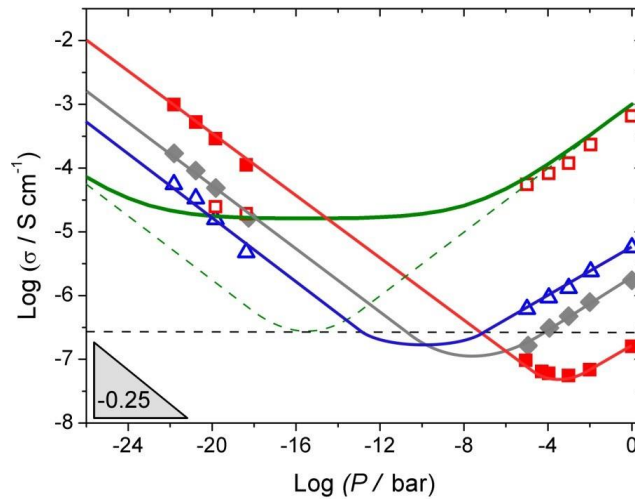


Figure 4.1 Conductivity versus oxygen partial pressure for SrTiO_3 (at $T = 544$ °C). The symbols are assigned as follows: (red open squares) bulk micro-crystalline SrTiO_3 ; (blue open triangles) grain boundaries of the micro-crystalline SrTiO_3 ; (grey diamonds) nano-crystalline SrTiO_3 with the effective grain size of ≈ 30 nm. The continuous green line illustrates the conductivity behavior of the micro-crystalline bulk as expected from the literature [11].

4.2. Sample Preparation and Characterization

Nano-crystalline SrTiO_3 powder (Inframat Advanced Materials (Lot:IAM12308NSTO)) was decorated with 7.2 at% La (which equals roughly a 50% coverage of the SrTiO_3 surface by La ions). The grain boundary decoration was achieved by dissolving the corresponding amount of lanthanum nitrate ($\text{La}(\text{NO}_3)_3 \cdot 6\text{H}_2\text{O}$) (Alfa Aesar, 99.8%, metal basis, Lot:) in bidistilled water and by adding the untreated SrTiO_3 powder to the solution. The mixture was stirred for two hours by a magnetic stirrer. Afterwards, the suspension was dried in a rotary evaporator at 80°C and at 100 mbar and calcined at 550°C for 5 hours under N_2 atmosphere. All nanopowders

(undecorated as well as decorated) were uniaxially pressed at 40 MPa and then sintered in air at 1173 K for 1 hour or 1673 K for 10 hours under air or 2% H_2 -Ar gas mixture. The pellets sintered at 1173 K had a diameter of about 8 mm, a thickness of 2.5 mm and a density of about 45% of the theoretical value whereas the pellets sintered at 1673 K had a diameter of about 6 mm, a thickness of 2.5 mm and a density of about 90% of the theoretical value. The density of ceramics was determined by gas pycnometry (micromeritics AccuPyc 1330) and also by measuring their weight and dimensions. For the samples sintered at 1173 K, due to the high porosity, the geometrical density values turned out to be more reliable than the ones measured by gas pycnometer.

The X-ray diffraction (XRD) (PANalytical, Netherlands) was employed on undecorated, decorated and calcined powders as well as on sintered pellets in order to determine phase purity.

Scanning electron microscopy (SEM) with a field emission gun (Zeiss,Merlin) was used to analyze the microstructure of the sintered pellets.

Inductively coupled plasma-optical emission spectrometry (ICP-OES) (Vista Pro, Varian) analyses were employed to determine the Sr/Ti ratio and the impurity content of the starting powder.

The surface area of the initial SrTiO_3 starting powder was determined by nitrogen adsorption-desorption (quantachrome Autosorb-1 multipoint) in order to determine the required amount of $(\text{La}(\text{NO}_3)_3 \cdot 6\text{H}_2\text{O})$ to cover (decorate) the SrTiO_3 powder.

The heat capacities of the samples were measured by DSC (Perkin Elmer), whereas the thermal diffusivities were determined by laser flash technique (Netzsch-LFA 457) between 300 K - 1000 K. The thermal conductivity values of these samples were calculated according to the equation 2.10

The Seebeck coefficients and electrical resistivity of the samples were measured by using an ULVAC ZEM 3-M8 and the impedance spectrometer Alpha-A high-resolution dielectric analyzer (Novocontrol Technologies GmbH) (ac voltage 0.3 V, frequency range from 2 MHz to 1 Hz, under Ar and O_2 atmosphere). The samples were equilibrated at the desired $p\text{O}_2$ for 20 hours before acquiring the final spectrum. The activation energy of the conductivity was determined from the impedance spectra acquired every 20°C between 400°C and 600°C at $p\text{O}_2 = 1$ bar and at $p\text{O}_2 = 10^{-4}$ bar. The analysis of the impedance spectra was carried out with the commercial software Z-View 2 by Scribner Associates Inc. The Seebeck measurements of the samples

sintered under air were carried out under O₂ atmosphere whereas the samples sintered under 2%H₂-Ar were tested under He atmosphere. For these electrical measurements, platinum electrodes were applied via DC-sputtering on both sides of the samples.

4.3. Results and Discussion

XRD patterns of decorated SrTiO₃ powders before and after calcination are shown in Figure 4.2. They exhibit the characteristic peaks of SrTiO₃. LaNO₃ peaks at lower angles before calcination are visible which disappears after calcination in the decorated sample.

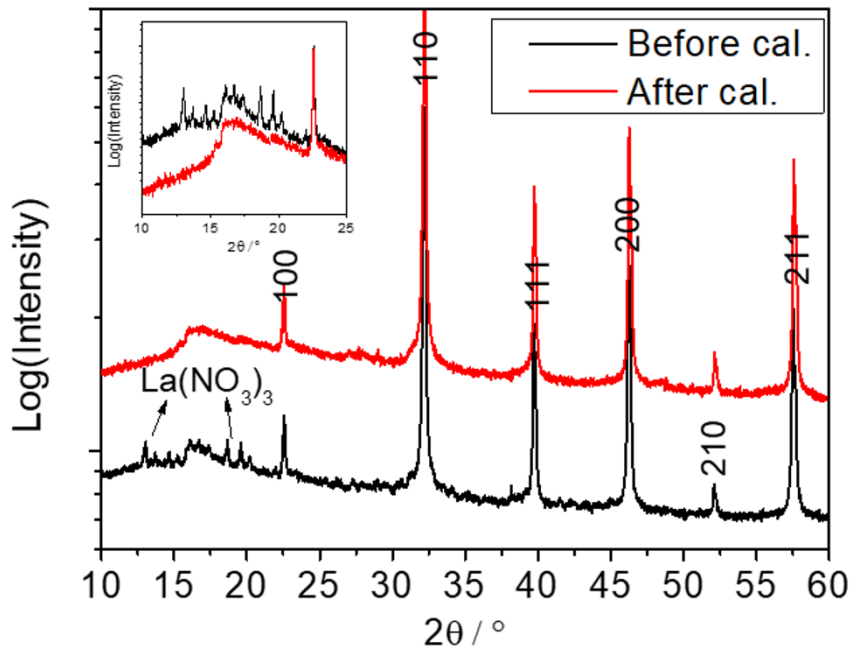


Figure 4.2 XRD patterns of decorated SrTiO₃ powders before and after calcination

Inductively coupled plasma-optical emission spectrometry (ICP-OES) (Vista Pro, Varian) was used to determine the Sr/Ti ratio of the 7.2 at % La decorated powder while the typical impurity content of the commercial nano-crystalline SrTiO₃ powder used in this study can be found somewhere else [157]. The analyses revealed a cation ratio of 49.8 and an amount of La corresponding to 6,9 at%.

As far as porosity is concerned (open or closed), gas pycnometry provides data regarding the closed porosity content and therefore, by comparing the geometrical density with the gas pycnometry results, the open porosity content could be estimated.

Table 4.1 summarizes the geometrical and absolute density data of undecorated and decorated samples sintered under various conditions. Decorated samples have a lower density than the undecorated ones irrespective of the preparation conditions, which indicates that the presence of lanthanum on the surface of the starting SrTiO₃ powder particles has a detrimental effect on densification. With regard to the density data of reduced and oxidized samples, it seems that the sintering atmosphere does not have a distinct effect on the densification process. As for the absolute density values, the experimental data reveal that the percentage of closed porosity is similar among all samples. From the geometrical density values, it can be stated that both decorated and undecorated nano-crystalline SrTiO₃ samples have a similar fraction of open porosity as expected from the lower sintering temperature.

Table 4.1 Geometrical and absolute densities of undecorated and decorated (7.2 at% La) SrTiO₃ samples prepared under different sintering atmospheres.

Samples		Sintering Condition		Geometrical density d_{geo} (%)	Absolute density d_{abs} (%)
		Temperature (K)	Time (h)		
UOM	Undecorated oxidized micro	1673 K - air	10	89.2 ± 3.1	95.2 ± 2.0
DOM	Decorated oxidized micro	1673 K - air	10	81.3 ± 4.0	98.7 ± 3.1
URM	Undecorated reduced micro	1673 K - 2%H ₂ /Ar	10	89.1 ± 3.2	95.6 ± 3.0
DRM	Decorated reduced micro	1673 K - 2%H ₂ /Ar	10	79.8 ± 4.4	97.1 ± 5.1
UON	Undecorated oxidized nano	1173- air	1	46.9 ± 4.7	99.0 ± 8.0
DON	Decorated oxidized nano	1173- air	1	40.0 ± 4.1	96.3 ± 8.4
URN	Undecorated reduced nano	1173- 2%H ₂ /Ar	1	47.8 ± 4.7	94.4 ± 7.9
DRN	Decorated reduced nano	1173- 2%H ₂ /Ar	1	37.8 ± 4.3	96.2 ± 9.5

SEM investigations clearly showed the effect of sintering temperature, atmosphere and La decoration on the final microstructure of the sintered samples. The undecorated reduced micro-crystalline sample has relatively a lower average grain size

than the undecorated oxidized micro-crystalline sample (see Fig. 4.3 (a) and (b)), which indicates that the reducing conditions tend to suppress the grain growth during sintering in the micro-crystalline SrTiO_3 samples.

Decorated micro-crystalline SrTiO_3 samples are characterized by a lower density and the SEM images confirm indeed the presence of a large amount of pores in the microstructure of these samples (see. Fig. 4.3 (c) and (d)).

Moreover, from the electron microscopy analysis it is apparent that the decorated micro-crystalline SrTiO_3 samples have different grain morphology and smaller average grain size when compared to the undecorated micro-crystalline SrTiO_3 samples (Fig. 4.3 (e)-(f) and (g)-(h)). Interestingly, the decorated reduced micro-crystalline SrTiO_3 sample has small pores inside the grains (intragranular porosity) as well as intergranular pores (Fig. 4.4).

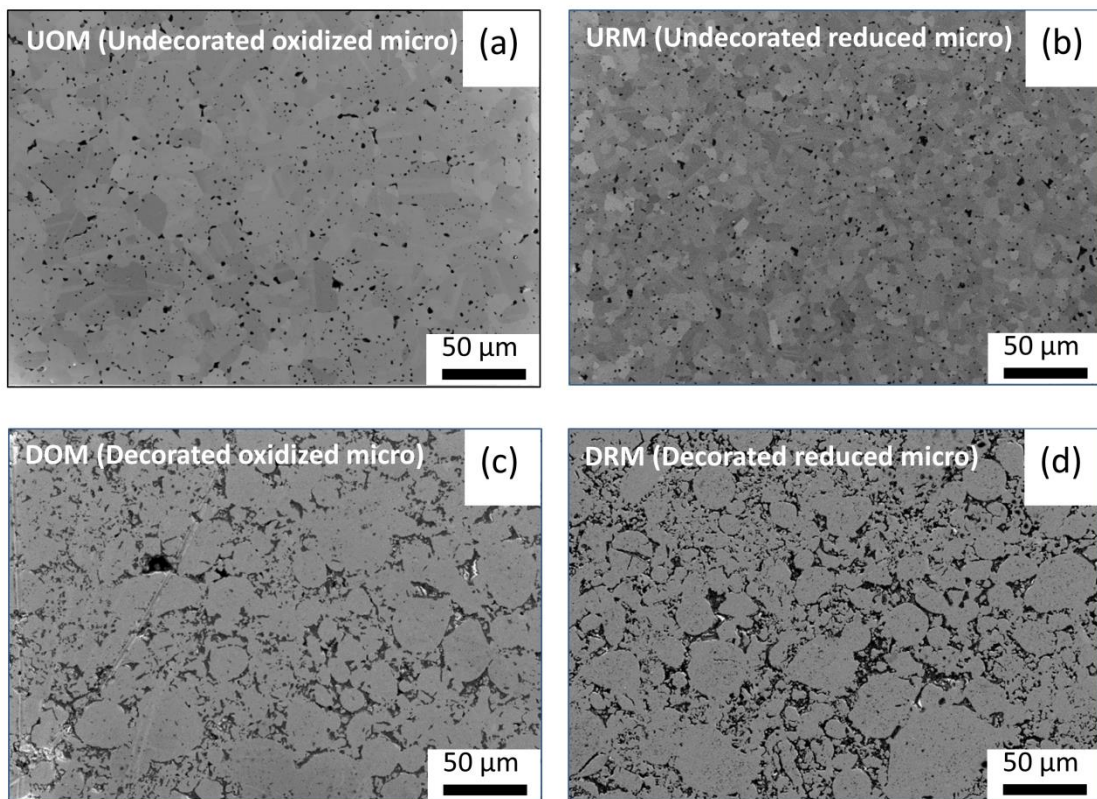


Figure 4.3 SEM-SE image of the SrTiO_3 samples sintered at 1673 K at two different magnifications (a-e) Undecorated oxidized (b-f) Undecorated reduced (c-g) Decorated oxidized (d-h) Decorated reduced (continue).

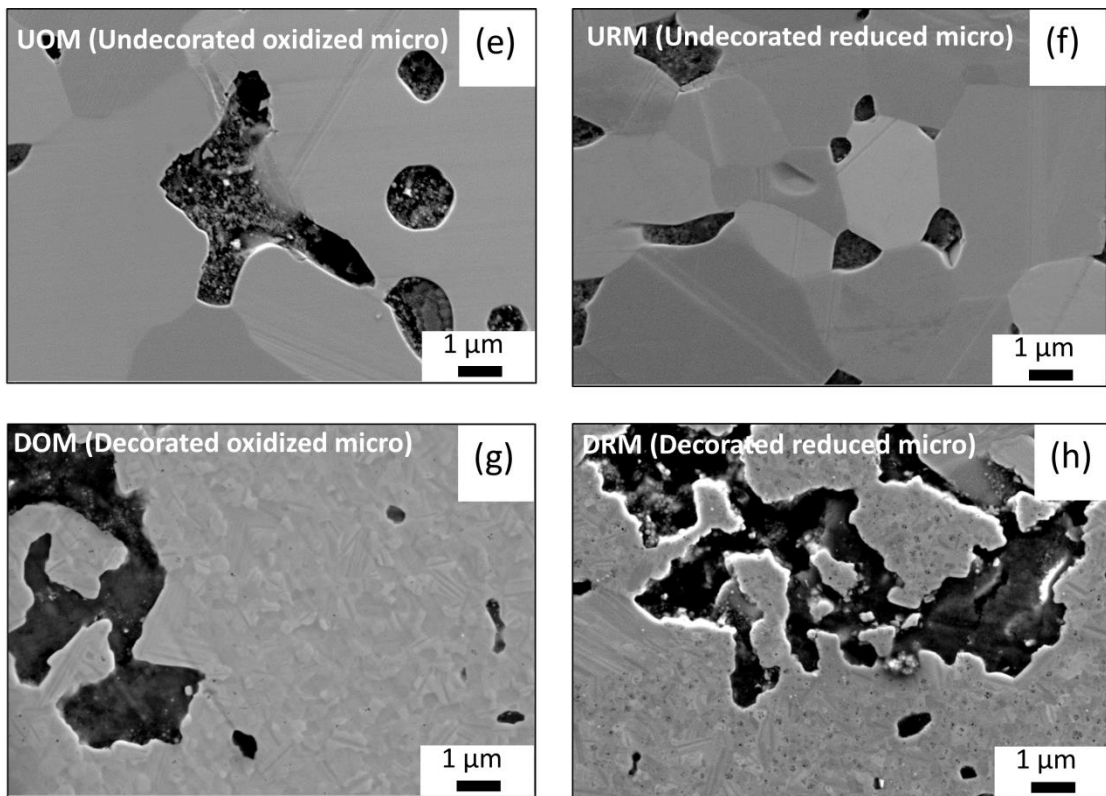


Figure 4.3 SEM-BSE image of the SrTiO_3 samples sintered at 1673 K (a-e) Undecorated oxidized (b-f) Undecorated reduced (c-g) Decorated oxidized (d-h) Decorated reduced.

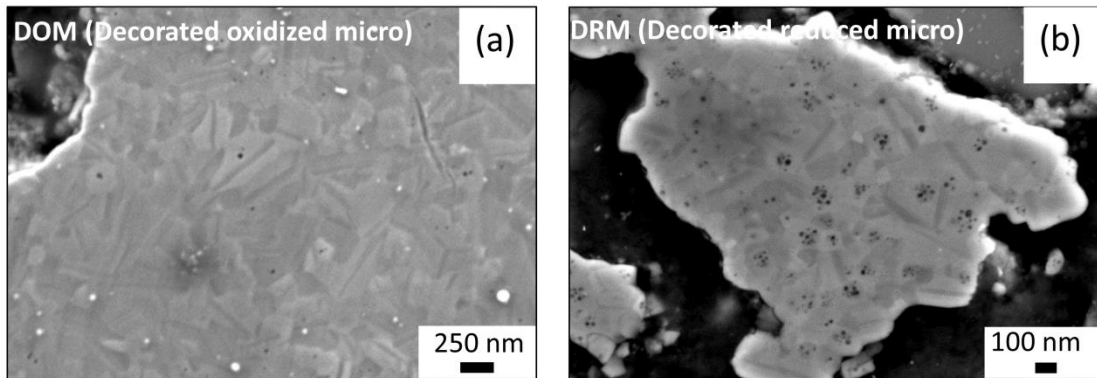


Figure 4.4 SEM-BSE image of the SrTiO_3 samples sintered at 1673 K (a) Decorated oxidized (b) Decorated reduced at higher magnification.

Finally, the SEM results are consistent with the density measurements on undecorated and decorated nano-crystalline SrTiO_3 indicating highly porous microstructures as well as nano sized grains (approximately 60 nm) (Fig. 4.5).

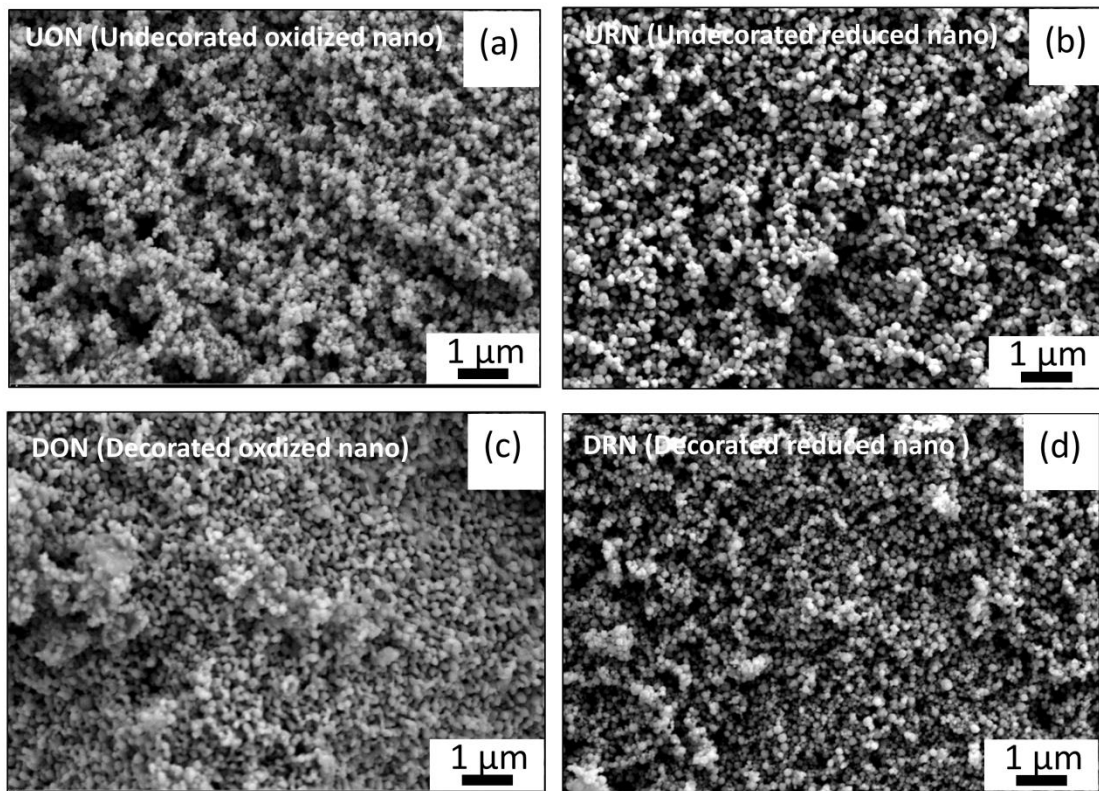


Figure 4.5 SEM-SE image of the SrTiO_3 samples sintered at 1173 K (a-e) Undecorated oxidized (b-f) Undecorated reduced (c-g) Decorated oxidized and (d-h) Decorated reduced.

The microstructure of the samples is of crucial importance for the electrical transport properties because it the concentration of mobile charge carriers at the grain boundary is differs from their concentration by orders of magnitude [13].

Figure 4.6 displays a schema predicting the microstructural model of undecorated and decorated SrTiO_3 samples after sintering as well as the conduction pathways according to the brick layer model which is explained in detail in Chapter 1. In SrTiO_3 with grain boundary cores positively charged, enhanced n-type conductivity is observed along the grain boundaries under reducing conditions, while p-type conductivity as well as oxygen vacancy transport is hindered by the boundaries meaning that the positive charge carriers migrates mostly across grain interior (bulk). If instead the excess charge at the grain boundary cores is negative, enhanced p-type conductivity is expected along the grain boundaries.

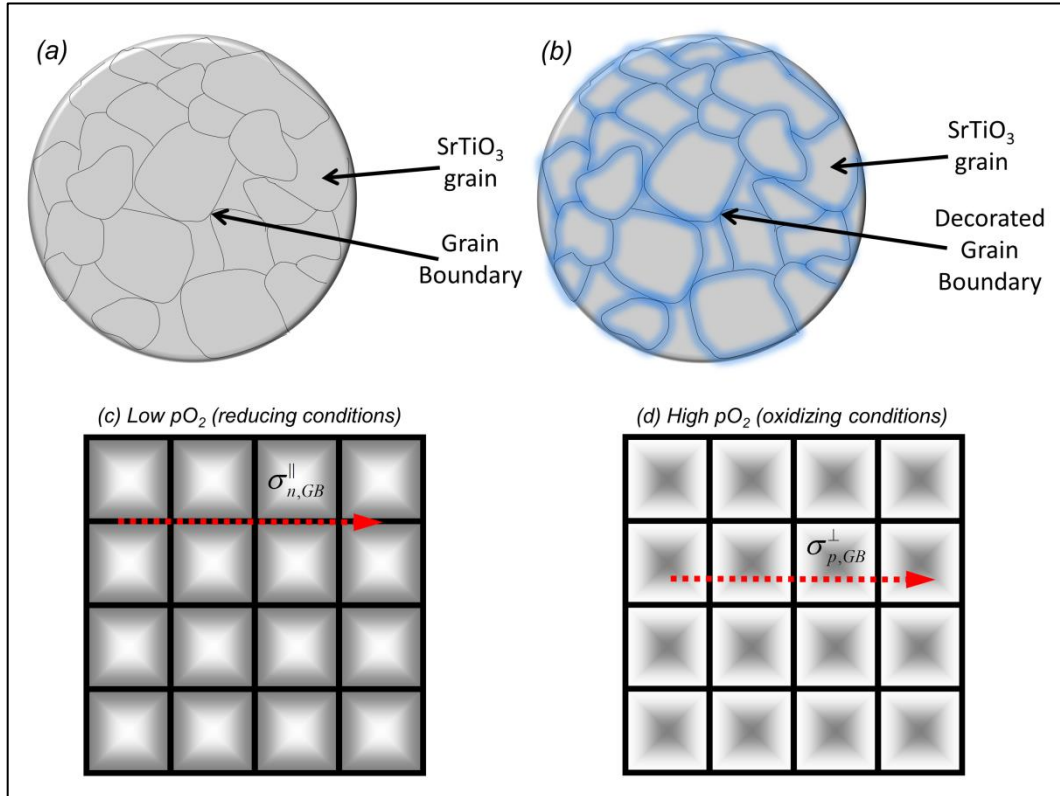


Figure 4.6 Schema of predicted microstructure model (a) undecorated and (b) decorated SrTiO₃ samples after sintering and conduction pathways according to the brick layer model (c) reducing (d) oxidizing conditions.

4.3.1. Effect of La-decoration on the thermoelectric properties of SrTiO₃

The temperature dependence of the electrical conductivity (σ), Seebeck coefficient (α), power factor ($PF = \sigma \cdot \alpha^2$) and the resulting figure of merit ($ZT = PF \cdot T / \kappa$) between 550 and 900 K for undecorated and 7.2 at.% La-decorated SrTiO₃ sintered at 1673 K (Micro) in the air (oxidized) and 2% H₂-Ar mixture (reduced) are summarized in Figure 4.7 (a-e). In the temperature range considered in this work (550-900K) the dominant charge carriers in SrTiO₃ are electrons e^- , holes h^+ and oxygen vacancies $V_o^{\bullet\bullet}$ since the other defects, namely strontium and titanium vacancies can be considered immobile and they do not contribute to the electrical conduction [152,154,158–160].

It is important to note here that the sample prepared under reducing conditions were measured in Ar or He while the specimens sintered in air were measured under nominally pure oxygen. Both undecorated and decorated SrTiO₃ micro-crystalline

samples exhibit higher total electrical conductivities under oxidizing conditions than under reducing conditions. Furthermore, the lanthanum decoration decreases the electrical conductivity irrespective of the atmosphere used during the measurements (Fig. 4.7 (a)).

Figure 4.7 (b) illustrates the temperature dependence of Seebeck coefficient of the same samples. Under both oxidizing and reducing conditions, the lanthanum decoration decreases also the Seebeck coefficient and from its negative values one can conclude that under reducing conditions both undecorated and decorated samples are characterized by a n-type conductivity, as expected from the literature [13].

As a result of higher electrical conductivity and larger Seebeck coefficient in both oxidizing and reducing conditions, the undecorated SrTiO₃ specimen have higher power factor than the lanthanum decorated SrTiO₃ samples (Fig. 4.7 (c)).

Figure 4.7 (d) shows the temperature dependence of the thermal conductivity of the samples. Decorated samples have lower thermal conductivity than undecorated ones. The reason appears to be the poor densification in decorated samples. Lanthanum addition suppresses the densification and hinders sintering to the point that the resulting density is lower than the one of the undecorated specimens. Nonetheless one cannot exclude that a larger thermal scattering at the boundaries due to the presence of an aliovalent cation might contribute to decreasing the overall thermal transport in the decorated SrTiO₃. Finally, we note that the reducing conditions have a detrimental effect on thermal conductivity for both decorated and undecorated samples.

As a consequence, the ZT parameter of the decorated samples is lower than the undecorated ones as shown in Figure 4.7 (e). Therefore, it is evident that oxidizing conditions are more favorable for improving the thermoelectric properties of undecorated micro-crystalline SrTiO₃.

The temperature dependence of the electrical conductivity (σ), Seebeck coefficient (α), power factor ($PF = \sigma \cdot \alpha^2$) and the resulting figure of merit ($ZT = PF \cdot T / \kappa$) between 550 and 900 K for undecorated and 7.2 at.% La-decorated SrTiO₃ sintered at 1173 K (nano-crystalline) in air (oxidized) and 2% H₂-Ar mixture (reduced) are shown in Figure 4.8 (a-e).

Decorated nano-crystalline samples have slightly lower electrical conductivity than undecorated samples and under reducing conditions the electrical conductivity decreases compared to oxidizing conditions (Fig. 4.8 (a)). Figure 4.8 (b) shows the temperature dependence of the Seebeck coefficient of samples. In oxidizing condition decorated samples have slightly higher Seebeck coefficient values.

As a consequence of high electrical conductivity and Seebeck coefficient, the nano-crystalline samples have higher power factor in oxidizing condition rather than reducing conditions.

Figure 4.8 (d) shows the temperature dependence of the thermal conductivity of samples as a function of temperature. Decorated samples have lower thermal conductivity than undecorated ones due to their low density values.

As a result, for the nano-crystalline SrTiO_3 samples, the lanthanum decoration does not provide any improvement of the ZT parameter under oxidizing conditions. However, under reducing conditions owing to the low thermal conductivity caused by the lower density, the decorated nano-crystalline SrTiO_3 samples have slightly higher ZT values than the undecorated nano-crystalline samples below 825 K. Although there is eventually no improvement of the ZT parameter in oxidized nano-crystalline SrTiO_3 samples, slightly higher Seebeck coefficient values were observed in decorated nano-crystalline SrTiO_3 under oxidizing conditions (Fig. 4.8 (e)).

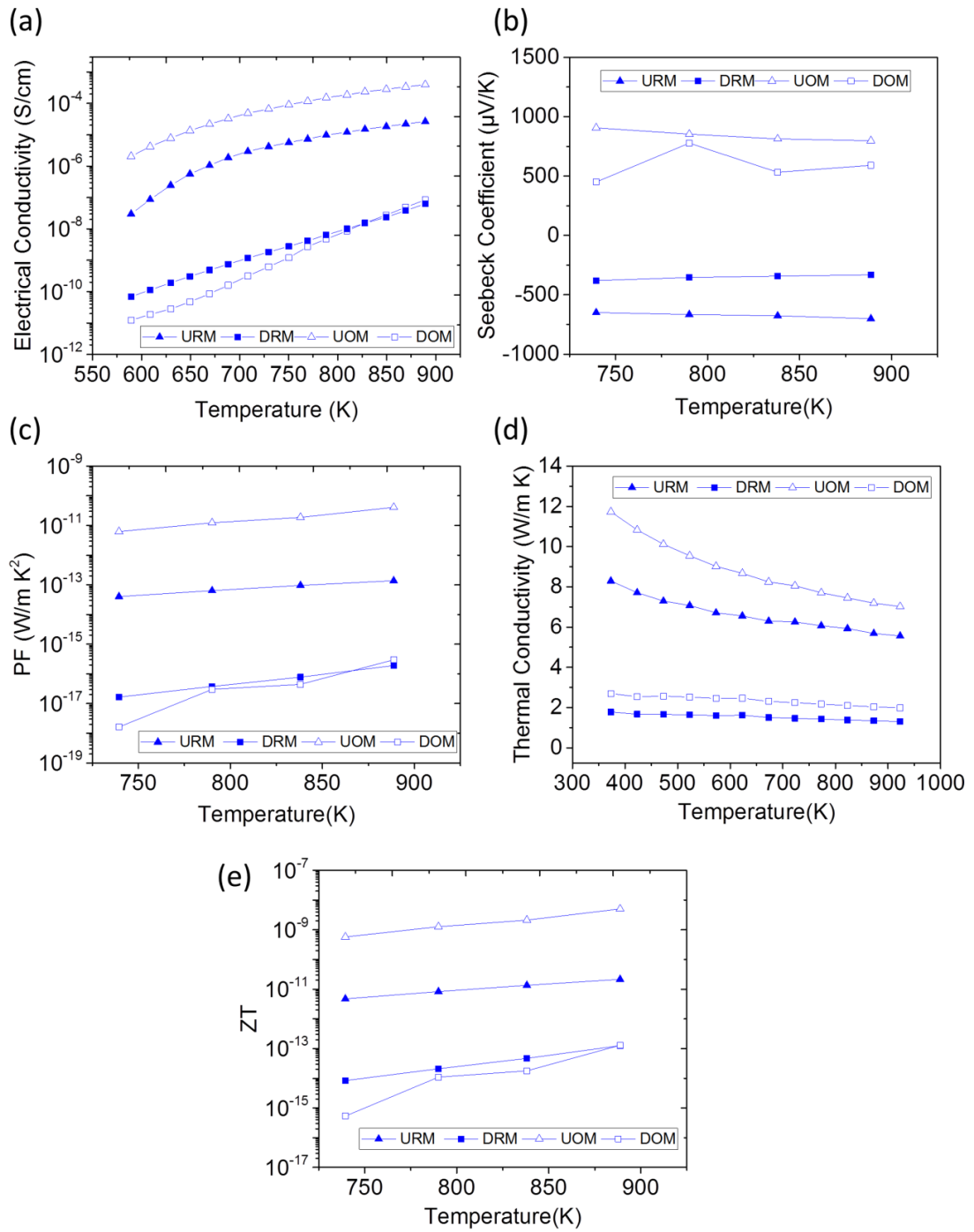


Figure 4.7 a) Electrical conductivity, σ , (b) Seebeck coefficient, α , (c) PF ($\sigma \cdot \alpha^2$), (d) Thermal conductivity, κ , (e) ZT measurement of undecorated (triangles) and 7.2 at.% La-decorated (squares) SrTiO₃ sintered at 1673 K (micro-crystalline) (solid symbols) in air (oxidized) (open symbols) and 2% H₂-Ar mixture (reduced) as a function of T .

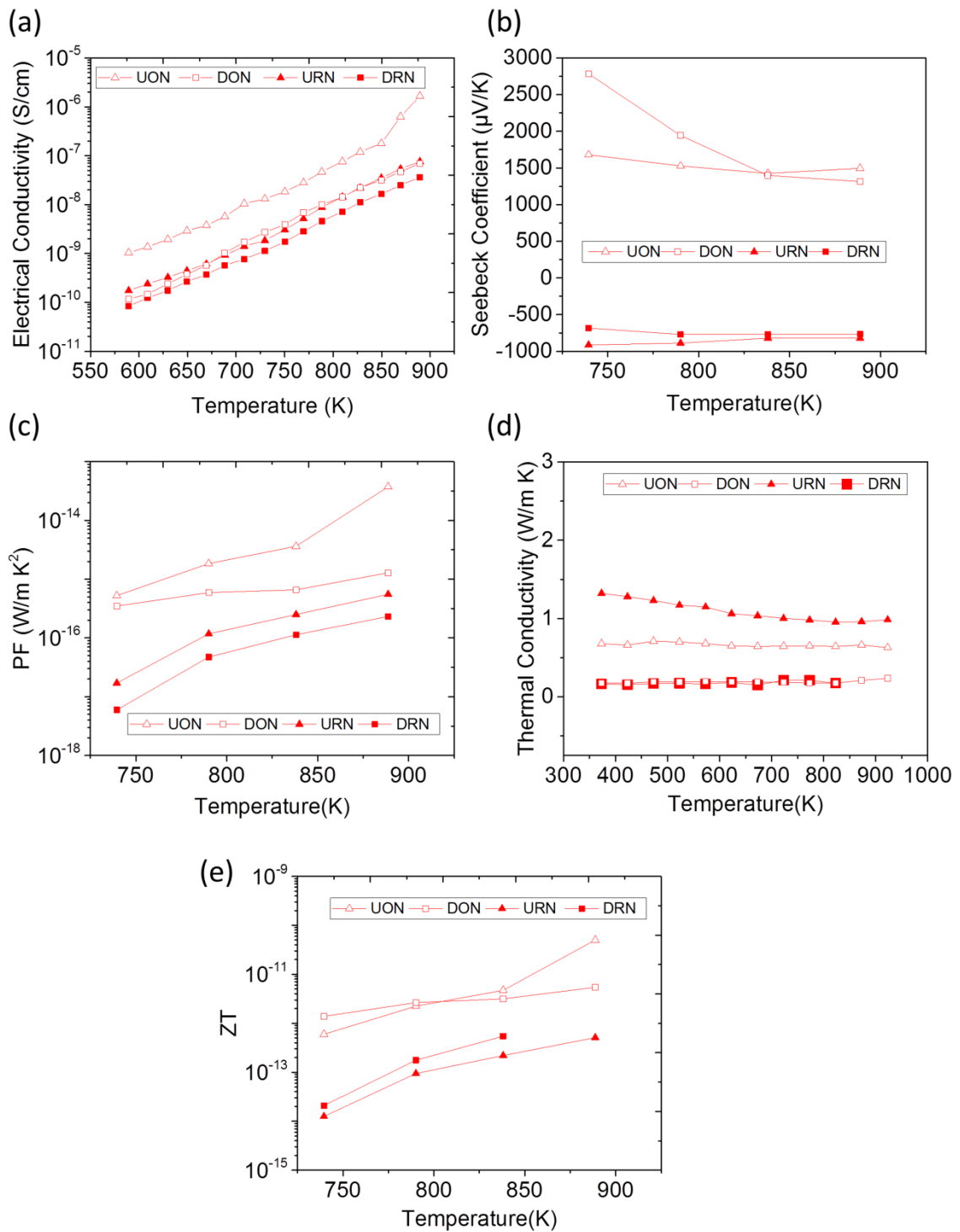


Figure 4.8 (a) Electrical conductivity, σ , (b) Seebeck coefficient, α , (c) PF ($\sigma \cdot \alpha^2$) (d) Thermal conductivity, κ , (e) ZT measurement of undecorated (triangles) and 7.2 at.% La-decorated (squares) SrTiO₃ sintered at 1173 K (nanocrystalline) in air (oxidized) (open symbols) and 2% H₂-Ar mixture (reduced) (solid symbols) as a function of T.

4.3.2. Grain size effect on the thermoelectric properties of decorated SrTiO₃

The temperature dependence of the electrical conductivity (σ), Seebeck coefficient (α), power factor ($PF = \sigma \cdot \alpha^2$) and the resulting figure of merit ($ZT = PF \cdot T / \kappa$) between 550 and 900 K for nano and micro decorated SrTiO₃ samples under oxidized and reduced conditions are displayed in Figure 4.9 (a-e).

The electrical conductivity of nano and micro decorated SrTiO₃ samples are almost similar under both reduced and oxidized conditions (Fig. 4.9 (a)). However, the Seebeck coefficient values of the nano-crystalline decorated SrTiO₃ samples are quite high when compared to their micro-crystalline counterparts (Fig. 4.9 (b)). As a consequence, due to the high absolute Seebeck coefficient values, the highest PF was obtained in the nano decorated SrTiO₃ sample prepared and measured under oxidizing conditions (Fig. 4.9 (c)).

The thermal conductivity of nano-crystalline decorated SrTiO₃ samples is rather low and does not significantly change in the micro-crystalline decorated specimens indicating that, at least for this composition, the microstructure does affect the thermal properties. On the other hand, in the micro-crystalline decorated SrTiO₃ ceramics, under oxidizing conditions a lower thermal conductivity was measured when compared to reducing conditions (Fig. 4.9 (d)). As a result of the lower thermal conductivity and the higher Seebeck coefficient and similar electrical conductivity values, the resulting ZT parameter is higher in nano-crystalline decorated SrTiO₃ samples (Fig. 4.9 (e)).

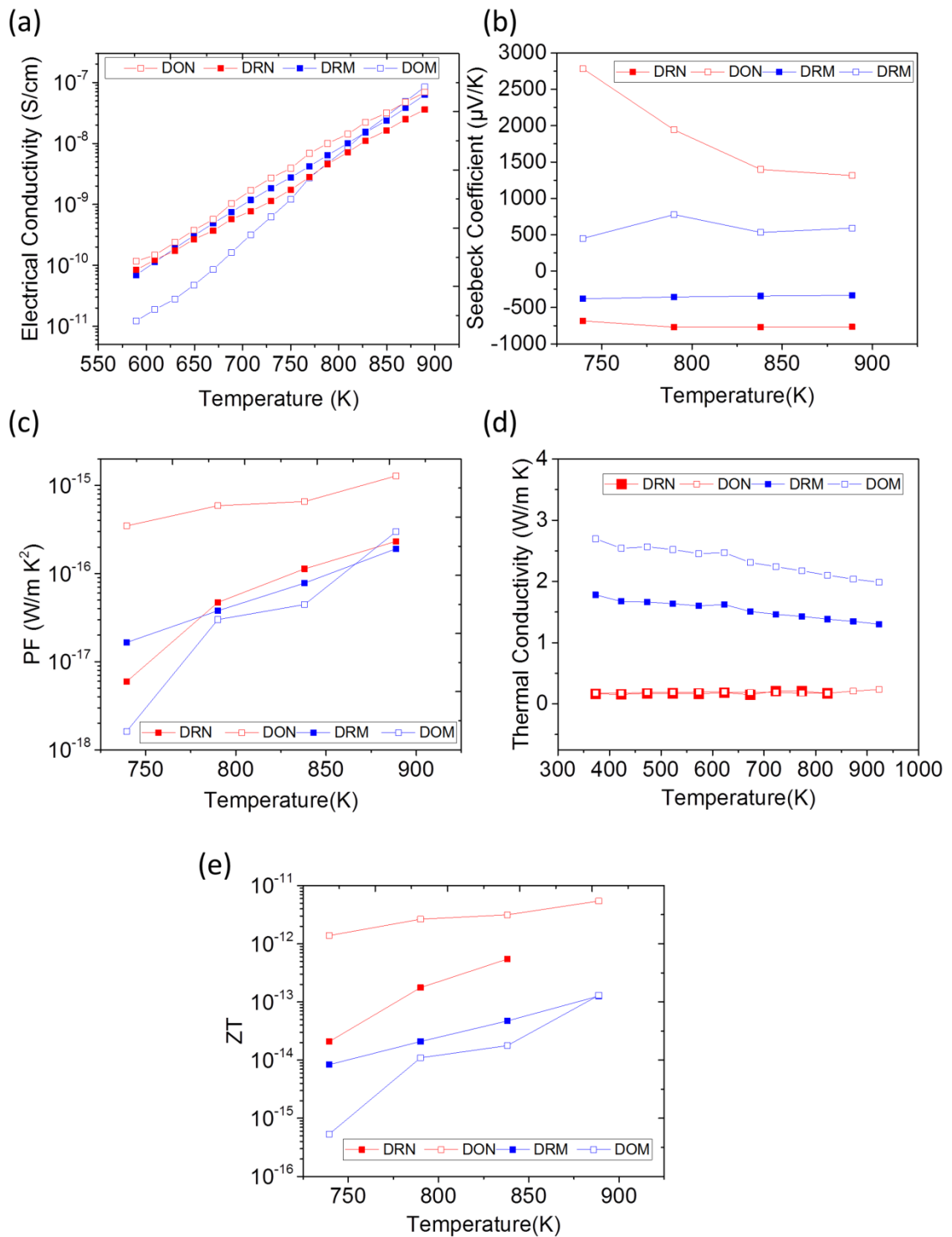


Figure 4.9 (a) Electrical conductivity, σ , (b) Seebeck coefficient, α , (c) PF ($\sigma \cdot \alpha^2$) (d) Thermal conductivity, κ , (e) ZT measurement of nano-crystalline (red) and micro-crystalline (blue) decorated SrTiO_3 sintered under oxidized (open symbols) and reduced (solid symbols) conditions as a function of T .

4.3.3. Impedance spectroscopy analyses

Impedance and modulus spectra acquired from nano-crystalline, decorated and undecorated samples are displayed in Figure 4.10 (oxidized) and Figure 4.11 (reduced). Both impedance and modulus spectra of nano-crystalline samples show one semicircle with a shoulder at low frequencies. Such a shoulder might be due either to electrode effects or to the presence of porosity locally hindering the electric transport (current constriction). It is known that the presence of pores can cause the deviation of current pathways and leads to an additional resistive contribution, which is visible in the impedance spectra [161–163]. In this context, Fleig and Maier described [163] that in poorly sintered ceramics such a resistive behavior results in the appearance of an additional semicircle in the Nyquist plot that depending on its R and C values (adjust time constant) can overlap with either the bulk or the grain boundary contribution. The fit of the impedance spectra was performed by using a single RQ equivalent circuit, in which the resistor R is connected in parallel with a constant phase element and by considering only the first half (in the high-frequency range) of the distorted semicircle. Unexpectedly, such fit yielded values of the dielectric constant (30-35) and electrical capacitance 2-2.5 pF which are not typical for bulk SrTiO₃ (Fig. 4.10 & 4.11).

Impedance and modulus spectra acquired from micro-crystalline, decorated and undecorated samples are displayed in Figure 4.12 (oxidized) and Figure 4.13 (reduced). Contrary to the spectra acquired from nano-crystalline, the low-frequency range of such impedance spectra does not seem to be distorted but it exhibits a well-defined second contribution (Fig. 4.12). Notably, only the impedance spectra acquired from undecorated oxidized micro-crystalline (UOM) samples consist of only a portion of a semicircle (Fig.4.12 (a)). Therefore, for such cases, the fit of the impedance spectra was carried out using an equivalent circuit consisting of a single RQ element. For the remaining specimens, data analyses were performed by using one equivalent circuit consisting of two RQ pairs connected series, R . Such fit yields values of the dielectric constant (90-150) and electrical capacitance 7-15 pF, which were already observed for bulk SrTiO₃ [17,164].

The impedance spectra acquired from undecorated reduced micro-crystalline (URM) sample consists of two semicircles and by fitting with two equivalent circuit dielectric constant was calculated for bulk and grain boundary (Fig. 4.13 (a)). The values are 100-120 F/cm and 1100-2500 F/cm for bulk and the grain boundary, respectively. Contrary to undecorated reduced micro-crystalline sample the impedance

spectra acquired from decorated reduced micro-crystalline (DRM) sample shows one stretched semicircle. However, the modulus plot consists of two semicircles which indicate the presence of two distinct contributions. By fitting with two equivalent circuits dielectric constant was calculated for bulk and grain boundary. The values are 400-500 F/cm and 1350-2500 F/cm for bulk and the grain boundary, respectively. The dielectric constant values of bulk is higher than usual values and it is probably due to current constriction effects resulting from a mixed contribution of bulk and grain boundary [13,164].

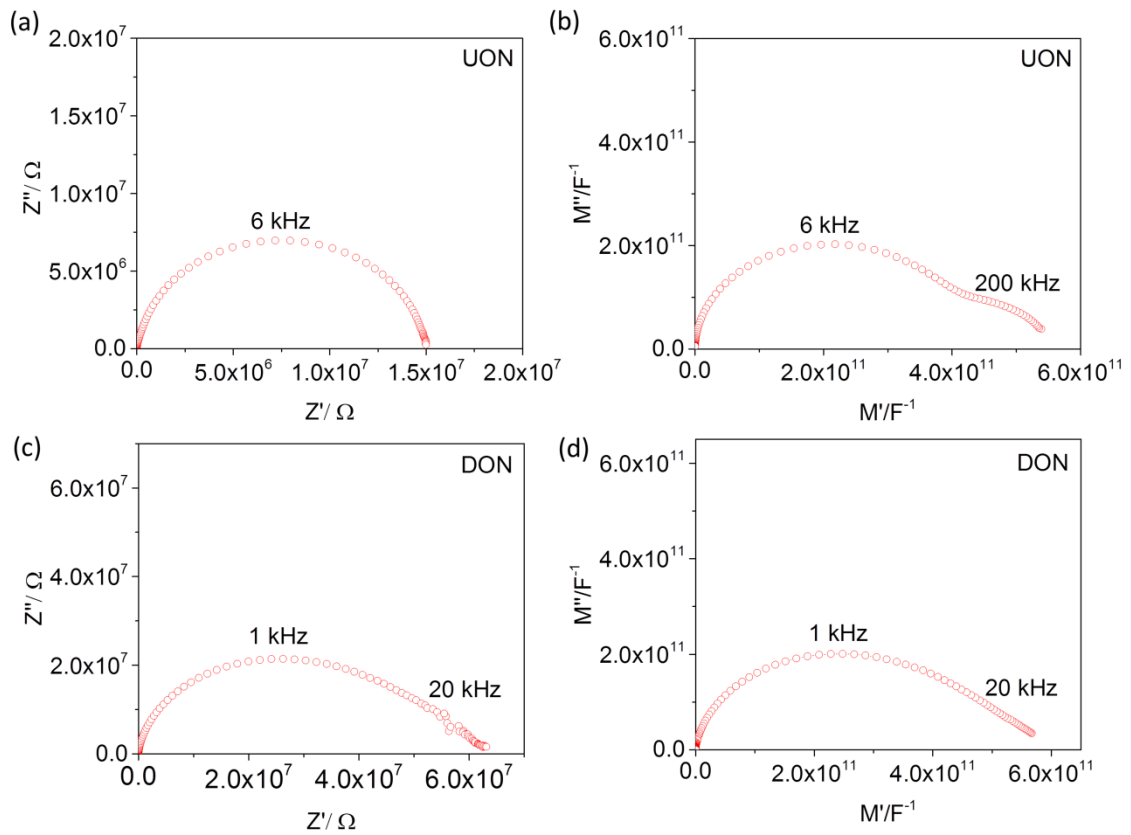


Figure 4.10 Impedance and modulus spectra collected at 827 K in oxygen; (a) and (b) undecorated oxidized nano-crystalline SrTiO₃, (c) and (d) decorated oxidized nano-crystalline SrTiO₃.

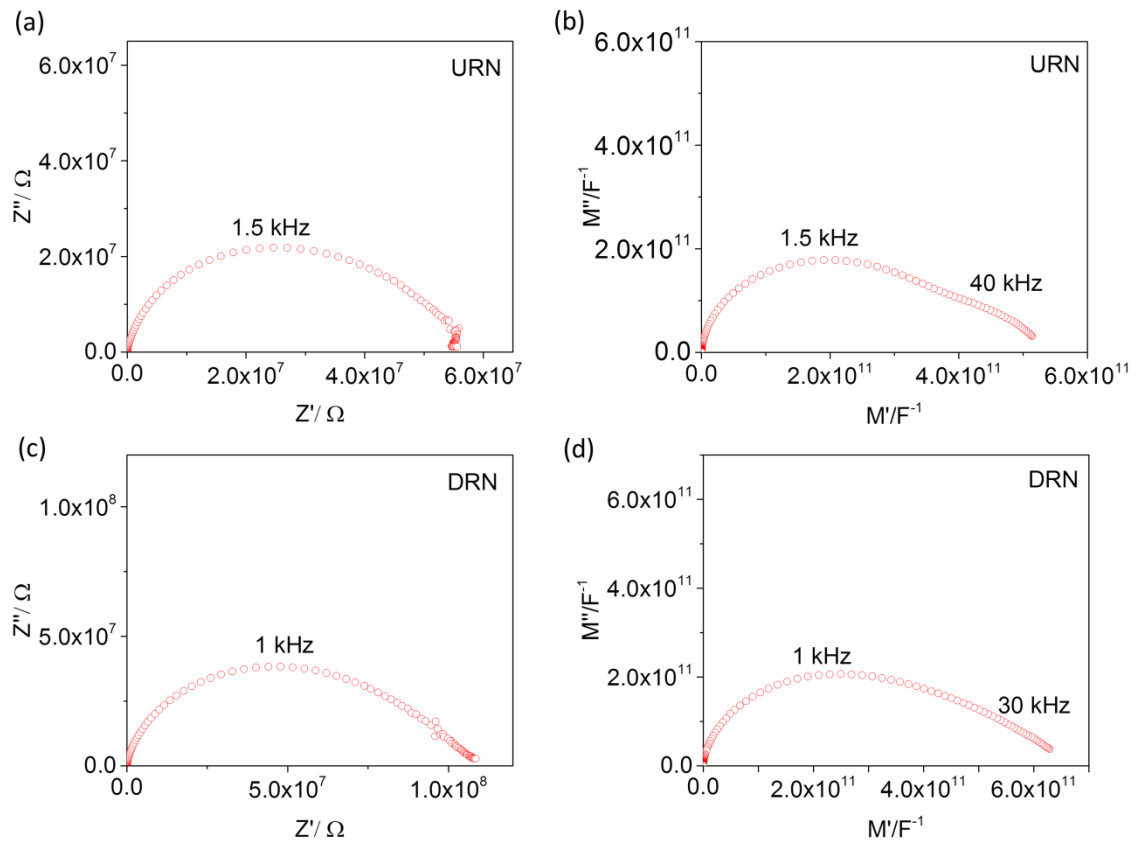


Figure 4.11 Impedance and modulus spectra collected at 827 K in argon; (a) and (b) undecorated reduced nano-crystalline SrTiO_3 , (c) and (d) decorated reduced nano-crystalline SrTiO_3 .

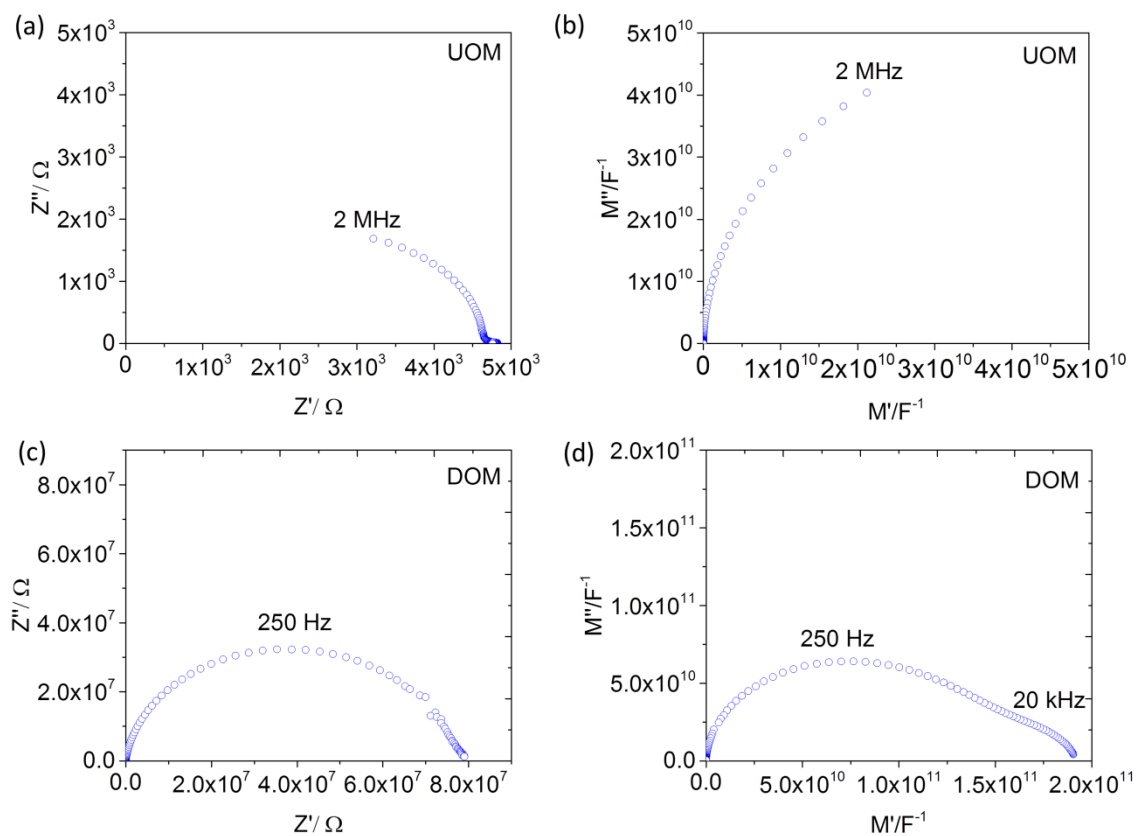


Figure 4.12 Impedance and modulus spectra collected at 827 K in oxygen; (a) and (b) undecorated oxidized micro-crystalline SrTiO_3 , (c) and (d) decorated oxidized micro-crystalline SrTiO_3 .

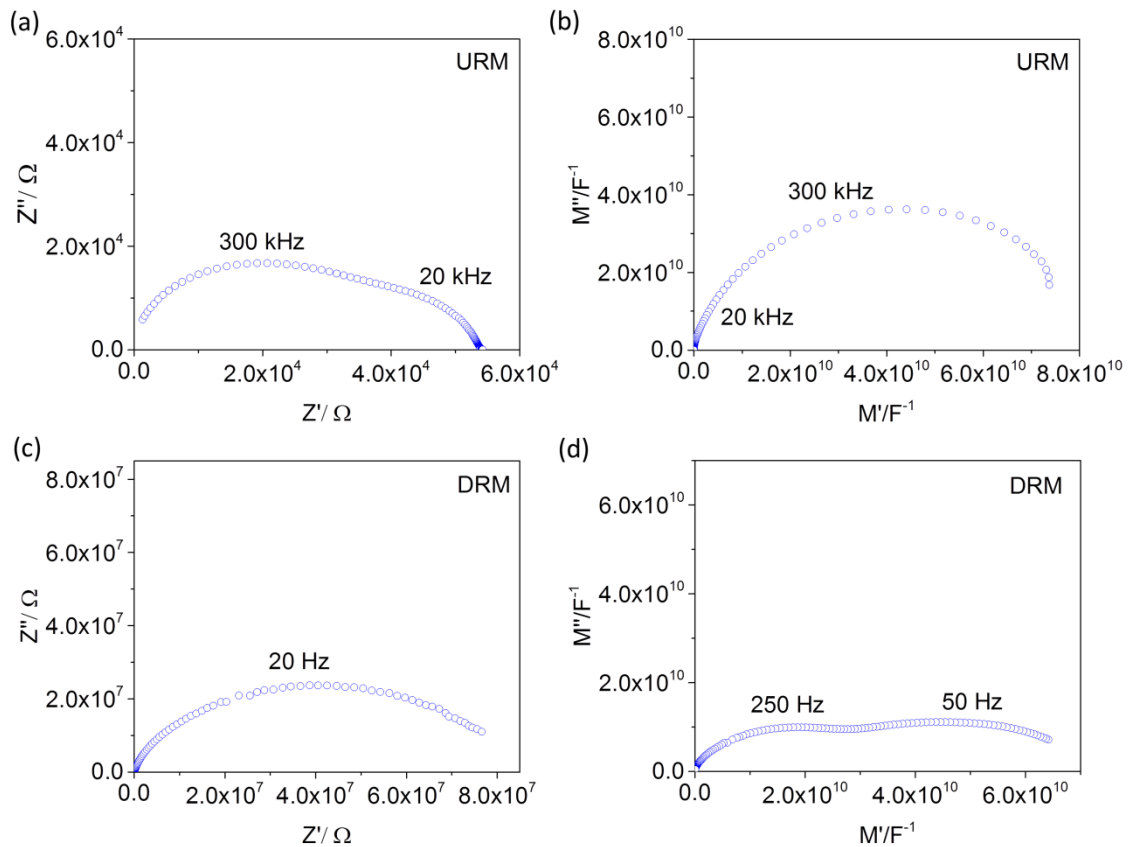


Figure 4.13 Impedance and modulus spectra collected at 827 K in argon (a) and (b) undecorated reduced micro-crystalline SrTiO_3 (c) and (d) decorated reduced micro-crystalline SrTiO_3 .

The Arrhenius plot of bulk conductivities of micro-crystalline samples between 714 K and 833 K is shown in Figure 4.14. The activation energy of the undecorated oxidized micro-crystalline (UOM) SrTiO_3 is 0.75 eV, which agrees very well with the calculated activation energy ($\Delta E = 0.74$ eV) of p-type bulk conductivity of SrTiO_3 [157]. On the other hand, the activation energy of the n-type conductivity obtained from micro-crystalline reduced (URM) SrTiO_3 is 0.78 eV. The decorated oxidized micro-crystalline (DOM) and reduced micro-crystalline (DRM) SrTiO_3 have clearly different activation energies with values of 1.78 and 1.18 eV, respectively (Fig. 4.14).

The Arrhenius plot of total conductivities of nano-crystalline samples between 714 K and 833 K are displayed in Figure 4.15. The activation energy of the undecorated oxidized nano-crystalline (UON) SrTiO_3 is 1.16 eV while the activation energy of nano-crystalline reduced (URN) SrTiO_3 amounts 1.31 eV. The decorated oxidized micro-crystalline (DOM) and the reduced micro-crystalline (DRM) SrTiO_3 exhibit clearly different activation energy values of 1.19 eV and 1.25 eV, respectively

(Fig. 4.15). The reason might be due to the low sintering temperatures employed to minimize the grain growth during sample preparation resulting in the presence of a large fraction of residual porosity, which can increase the experimental uncertainties.

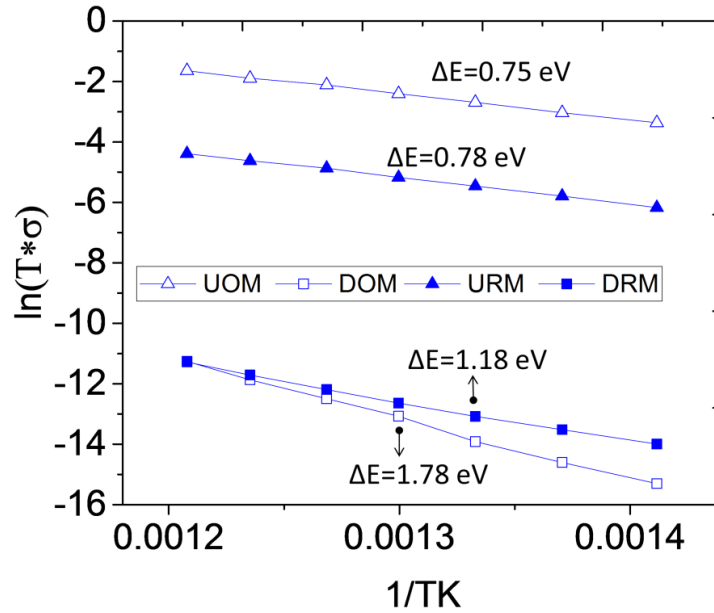


Figure 4.14 Arrhenius plot of conductivities of micro-crystalline samples, undecorated and decorated SrTiO_3 under oxidized and reduced condition.

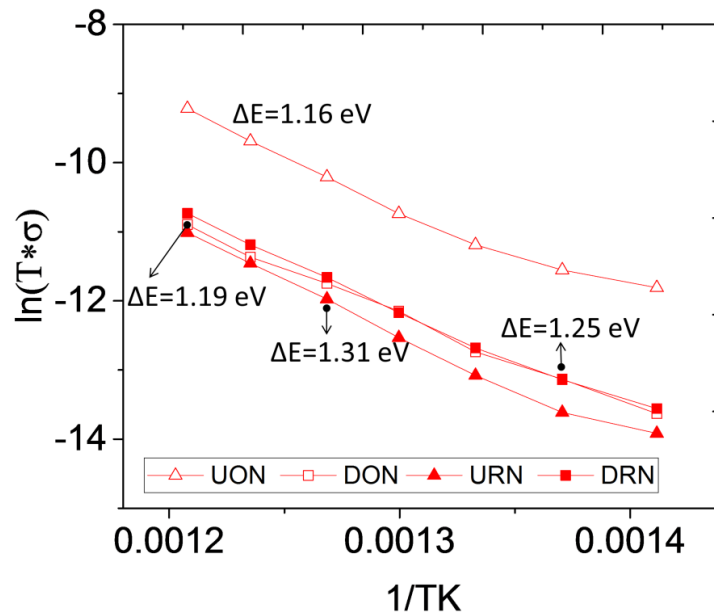


Figure 4.15 Arrhenius plot of conductivities of nano-crystalline samples, undecorated and decorated SrTiO_3 under oxidized and reduced condition.

4.4. Electron Microscopy Studies

For detailed analyses of the transport properties of the La decorated SrTiO₃ samples, it is necessary to determine whether La diffuses into the grain during the sintering process or if it remains at the grain boundary core. For this purpose STEM EELS analyses across the grain boundaries were performed as well as STEM and HRTEM imaging analyses in decorated reduced micro-crystalline (DRM) sample.

Figure 4.16 shows an example of intragranular porosity and stacking faults. Figure 4.17 depicts the HRTEM images and atomically resolved STEM HAADF images showing stacking faults along the [100] zone axis of the decorated reduced micro-crystalline sample. In addition to the stacking faults, the HRTEM image reveals also that there exist square shaped areas which might have different thicknesses or a differently arranged lattice (Fig.4.17 (b)). The atomically resolved STEM HAADF images taken under focus and defocus (39 nm) (Fig. 4.18) from these areas indicated that these areas correspond porous volumes within the grains.

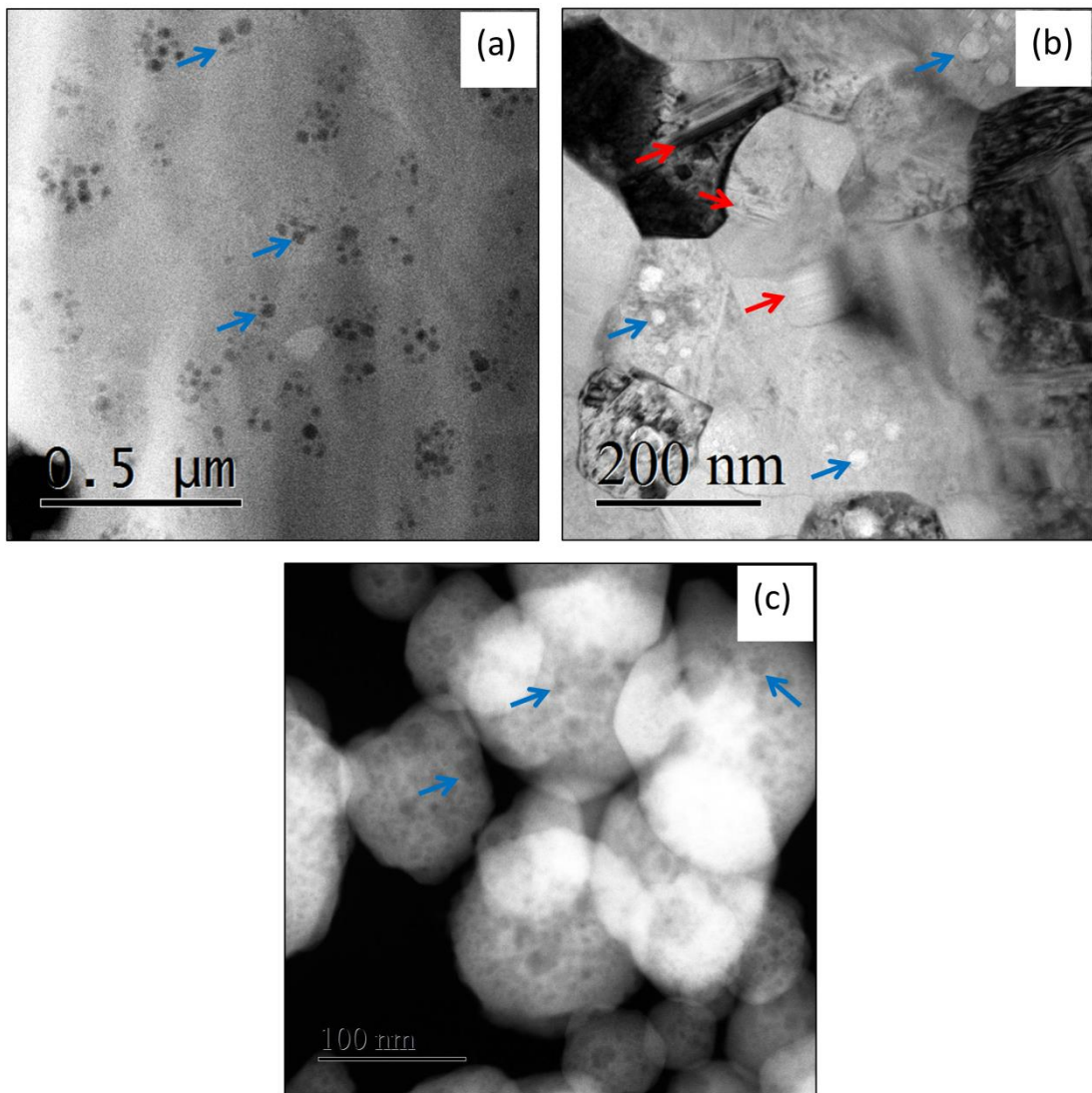


Figure 4.16 (a) STEM HAADF (b) TEM BF images showing the porosity (blue arrows) faults (red arrows) in decorated reduced micro-crystalline sample (c) STEM-HAADF image showing the porosity in of SrTiO₃ powder

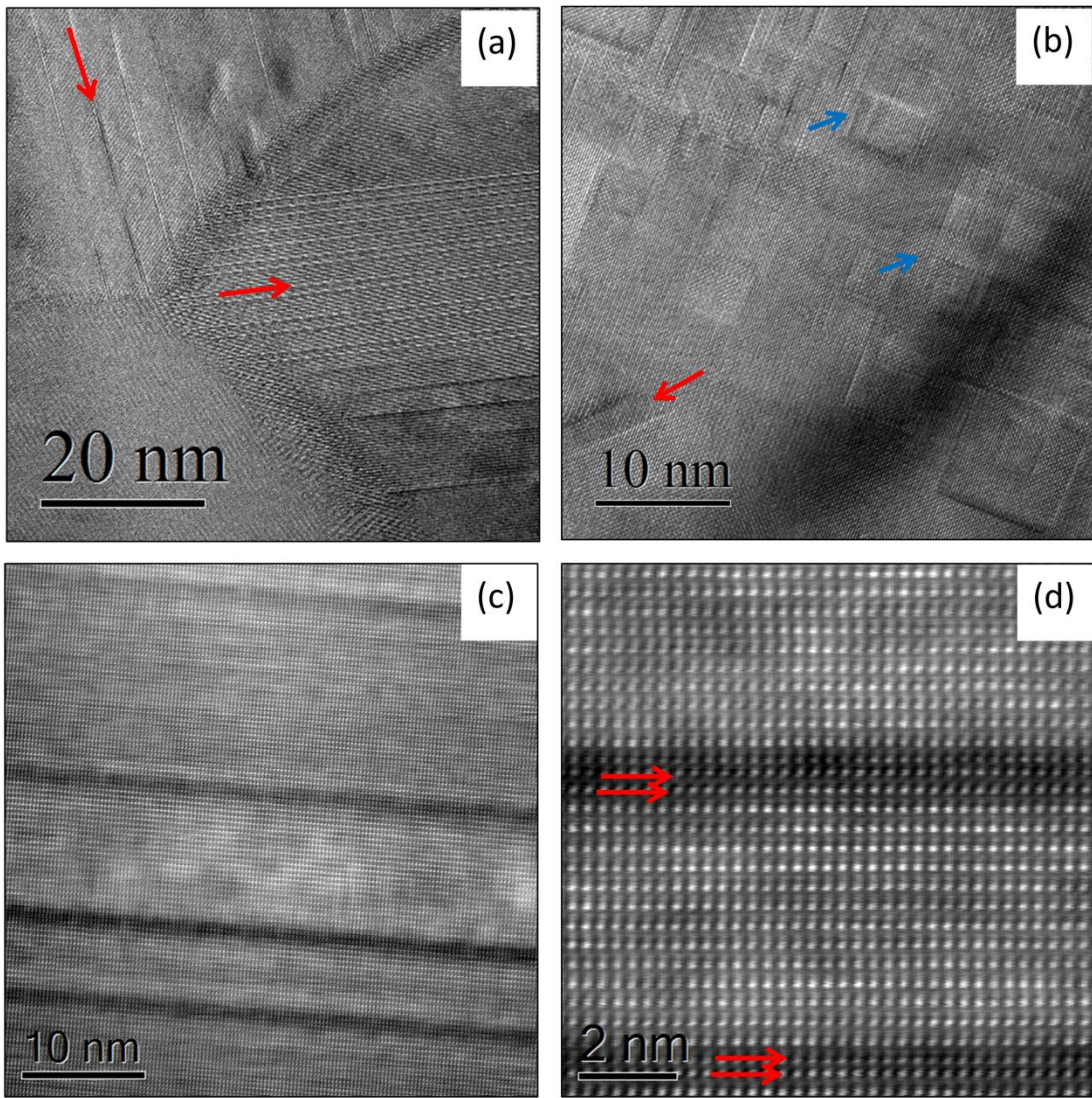


Figure 4.17 (a) & (b) HRTEM images show the porosity (blue arrows) (c) & (d) Atomically resolved STEM HAADF images showing stacking faults (red arrows) in decorated reduced micro-crystalline sample.

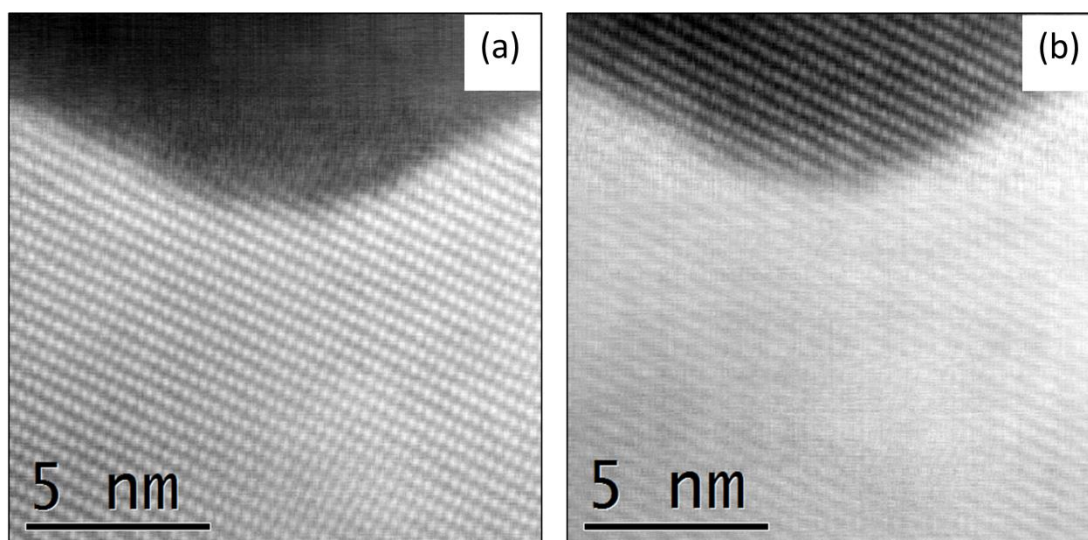


Figure 4.18 *Atomically resolved STEM HAADF images showing the porosity (dark contrasted area) in decorated reduced microcrystalline sample according to (a) focused (b) 39 nm defocused imaging.*

To determine the elemental distribution through a grain boundary STEM HAADF imaging and electron energy-loss spectroscopy (EELS) analyses were performed. Figure 4.19 shows atomically resolved STEM HAADF micrographs taken from the grain boundary region. As STEM HAADF images also provide Z-contrast information (Z being the atomic number), the enhanced brightness suggests La segregation at the boundary. Electron energy-loss spectroscopy (EELS) line-scan analyses confirmed the La segregation as summarized in Fig. 4.20 (c) & (d) while the two-dimensional EELS maps of Fig. 4.21 give a nice spatial rendering of the La segregation at the grain boundaries. Consistently, as a consequence of the Sr substitution by La cations, Sr deficiency was also observed at the boundaries.

It is worth noting that according to the resulting excess of positive charge in the grain boundary core due to La substituting Sr, two distinct charge compensation situations can occur: (1) an increase of the electron concentration in proximity of the boundary resulting in an improvement of the n-type conductivity (which is particularly visible under reducing conditions) or (2) an increase of the negatively charged titanium vacancy. Since in EELS line scan analyses a Ti deficiency together with the Sr deficiency was observed at the grain boundary, meaning that the excess positive

charge due to lanthanum occupying strontium sites is electrically compensated by titanium vacancies (Section 1.4).

However, even in such a situation, one would still expect increased n-type conductivity in decorated reduced microcrystalline sample. As the experimental data do not show an improved n-type transport in the decorated samples, another scenario needs to be taken into account, namely the formation of a very thin insulation layer consisting a Ti deficient phase, which blocks the transport.

If one considers both the defect reactions (Section 1.4) and the phase diagram of $\text{La}_2\text{O}_3\text{-TiO}_2\text{-SrO}$, the formation of such a compound is plausible as shown in the left part of the phase diagram through the red line (Fig. 4.22).

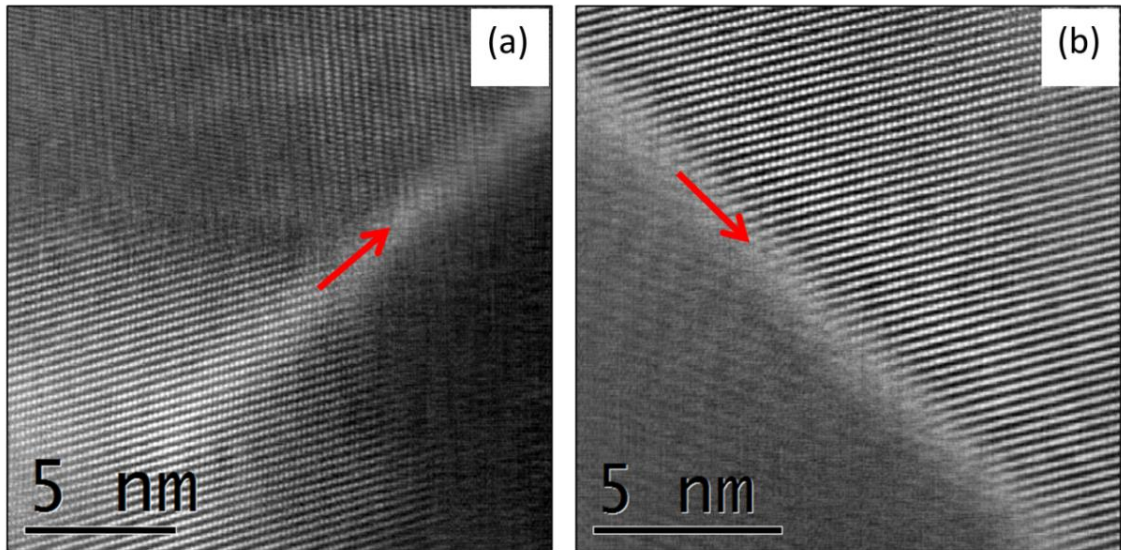


Figure 4.19 *Atomically resolved STEM HAADF images showing the La segregation through the grain boundaries (red arrows) in decorated reduced microcrystalline sample.*

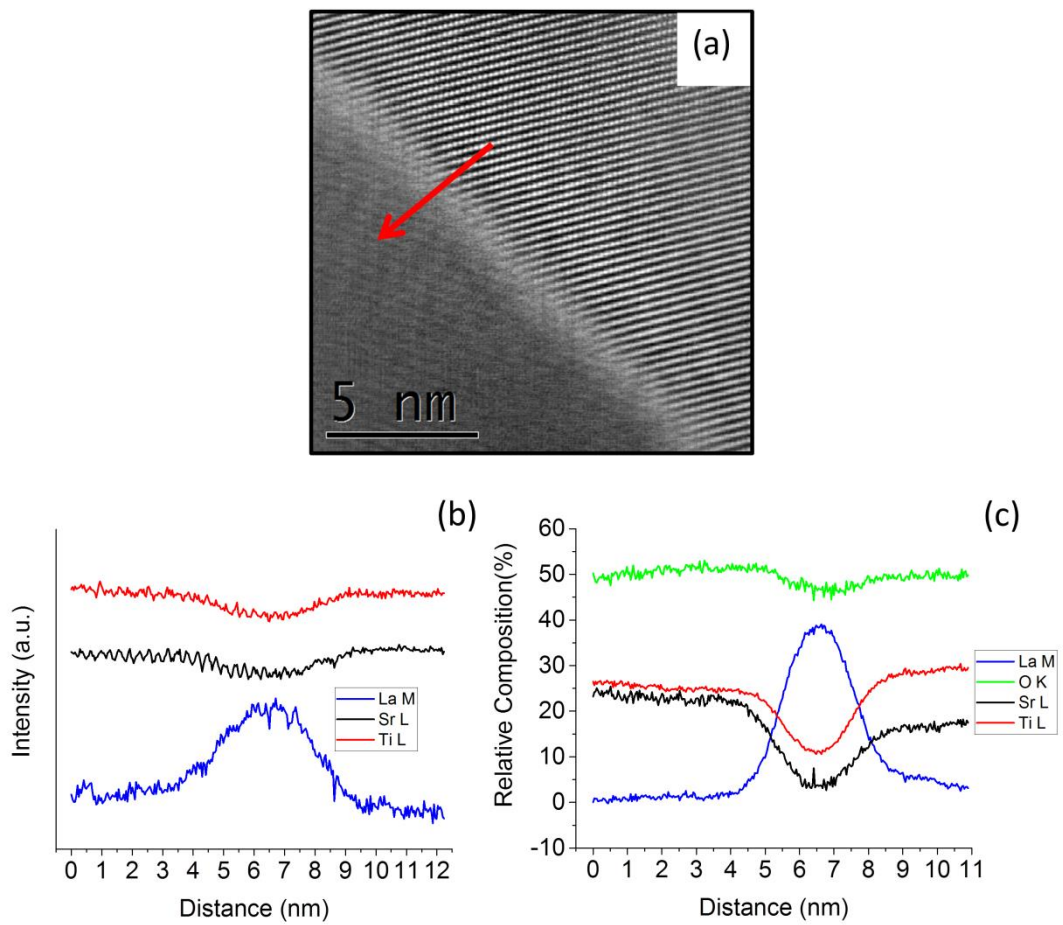


Figure 4.20 (a) STEM HAADF images (b) EELS 1D line scan through a grain boundary (c) Relative composition in decorated reduced micro-crystalline sample.

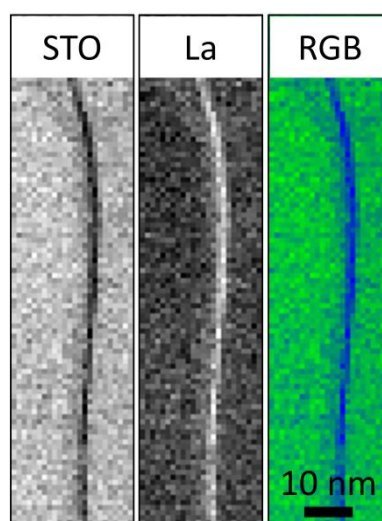


Figure 4.21 EELS 2D maps (La = blue, Sr = green) in decorated reduced micro-crystalline sample.

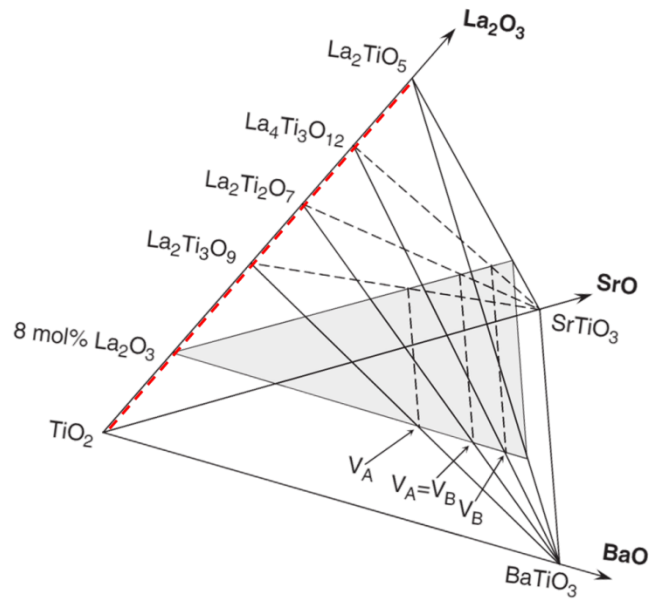


Figure 4.22 Schematic representation of a portion of the $\text{La}_2\text{O}_3\text{-TiO}_2\text{-BaO-SrO}$ quaternary-phase diagram [165].

4.5. Section Conclusions

The influence of lanthanum decoration, size effect as well as sintering atmosphere on the thermoelectric properties of SrTiO_3 has been investigated.

The aim of lanthanum decoration was to improve the ZT parameter by enhancing the thermal scattering at the boundaries and by locally increasing the electrical conductivity. While the presence of lanthanum was indeed beneficial in terms of thermal properties as it reduces the thermal conductivity of all decorated samples, no enhancement of the electrical conductivity was observed. This hinders the possibility of improving the overall ZT parameter of both micro-crystalline and nano-crystalline SrTiO_3 samples under reducing as well as oxidizing conditions. Such a peculiar electrical behavior can be explained in terms of La excess as well as Ti deficiency at the grain boundaries, which were detected during STEM-EELS analyses in decorated reduced micro-crystalline sample. The presence of a secondary phase, whose formation is also supported by STEM data as well as thermodynamic considerations (cf. the phase diagram of $\text{SrO-TiO}_2\text{-La}_2\text{O}_3$) is most likely the reason of the electrical conductivity properties of the decorated samples.

The second purpose of this work was to investigate the role of size effect on the thermoelectric properties.

In this context, undecorated micro-crystalline samples exhibit higher ZT values than the undecorated nano-crystalline samples. Even though nano-crystalline specimens have larger Seebeck coefficient due to their lower electrical conductivity, the ZT parameter could not be improved through the reduction of the grain size. On the other hand, decorated nanocrystalline samples present larger ZT values than their micro-crystalline counterparts, which stem from the higher Seebeck coefficient and the lower thermal conductivity compared to the decorated micro-crystalline samples.

Finally, it is apparent that, at least for SrTiO₃, the electrical conductivity is the dominant property for the determination of the thermoelectric performances. In the specific case of La decorated SrTiO₃ samples, the presence of a secondary phase at the grain boundaries is the main reason of the lack of improvement of the thermoelectric performance.

For a deeper understanding of the electrical transport and of the grain boundary properties, it would be necessary to carry out a more systematic study in terms of La amount to prevent the secondary phase formation.

From a more general perspective instead, it is evident that different solutions need to be considered for simultaneously achieving a decrease of the thermal properties and an enhancement of the electrical transport. Thanks to the high mobility of the electronic charge carriers, it would be desirable to identify a decoration approach able to give rise to a local charge compensation based on an enhancement of the electron concentration rather than via cation vacancies.

5. EFFECT OF INTERFACE MODIFICATION ON THERMOELECTRIC PROPERTIES IN NICKELATE-CUPRATE HYBRID STRUCTURES

5.1. Introduction & Motivation

Most state-of-the-art thermoelectric (TE) materials contain heavy elements such as Bi, Pb, Sb, or Te and exhibit a maximum figure of merit of, $ZT \sim 1-2$. On the other hand, oxides were believed to give rise to a poor TE because of their low carrier mobility and high lattice thermal conductivity [166]. Since the discovery of the well conductive p-type material Na_xCoO_2 in its single crystalline form, oxide materials have been prepared and studied for TE applications [167]. The growth of single crystals is time consuming and expensive, and such limitations lead to the fabrication of high-quality epitaxial films of several oxides such as Na_xCoO_2 , $\text{Ca}_3\text{Co}_4\text{O}_9$ and Nb-SrTiO_3 [168–173]. Thin films of oxides are promising as a thermoelectric material, however, they have not been investigated at the same level of bulk and single crystals [174]. Transition metal oxides (TMOs) are a fascinating class of materials due to their wide range of electronic, chemical and mechanical properties [175]. Cuprates and nickelates are particularly important class of transition metal oxides (TMOs) family because they display a rich spectrum of various competing phases and physical properties [176].

Cu-based compounds, e.g., yttrium barium cuprate $\text{YBa}_2\text{Cu}_3\text{O}_7$ (YBCO) [114] and lanthanum cuprate (La_2CuO_4 , LCO) [177] are among the best known high-temperature superconducting (HTSC) materials of the cuprate family. Thermoelectric properties of Cu-based oxides have also been investigated as well as their superconducting behavior over the last several decades and in several studies large Seebeck coefficients have been reported [178–187]. An additional tuning parameter is seen in the formation of heterostructures and superlattices where interface effect can play a decisive role on determining the given properties. In semiconductor technology, with the formation of $\text{GaAs-Al}_x\text{Ga}_{1-x}\text{As}$ heterostructures and superlattices, a drastic enhancement of charge carrier mobilities have been observed, In the course of improved MBE-based technologies for semiconductor, the word δ -doping was coined i.e. thickness of doping layer between intrinsic semiconductor of thickness of a few unit cell could be proposed.

The development of δ -Sr-doped systems founded initially on semiconductors [188]. *Dingle et al.* observed high electron mobilities at room temperature in $\text{GaAs-Al}_x\text{Ga}_{1-x}\text{As}$ superlattice structures using modulation-doping [189]. The effect of δ -doping with Zn on the superconductivity of $\text{La}_{1.65}\text{Sr}_{0.45}\text{CuO}_4$ - La_2CuO_4 , bilayer films were studied

by Logvenov *et al.* [190]. Baiutti *et al.* demonstrated the significance of unconventional heterogeneous doping based on δ -doping [191] as well as the key role of cationic redistribution in the field of superconductivity for $\text{La}_{2-x}\text{Sr}_x\text{CuO}_{4+\delta}$ compounds [192]. Suyolcu *et al.* investigated the effect of the dopant size on superconductivity in $\text{La}_{1.6}\text{A}_{0.4}\text{CuO}_4\text{-La}_2\text{CuO}_4$ bilayers (with A=Ca, Sr, Ba) [193].

Lanthanum nickelate (LaNiO_3 , LNO) [194] is a well-known conducting perovskite at room temperature. Metal-insulator (MI) transitions, antiferromagnetic ordering and spin glass behavior as well as thermoelectricity have been extensively studied in the past in bulk as well as thin films samples [52,195–199].

The incorporation of functional oxides into real devices requires a full control not only of their bulk properties but also of their interfaces [200]. Oxide interfaces are of interest for their possible superconductive [201,202,75] magnetic [203] and thermoelectric behavior [95,124,204], at their interfaces novel electronic phases can be stabilized that are not available in the parent compounds. For instance, Ohta *et al.* reported large electrical conductivity and thermopower in SrTiO_3 at the interface between TiO_2 and SrTiO_3 in superlattice structures. They suggested that the extraordinary properties were due to the existence of two-dimensional electron (2DEL) gas confined within one unit-cell thick interface [124]. In addition, Ohtomo *et al.* found an unusual, non-bulk-like charge state formed at $\text{LaAlO}_3/\text{SrTiO}_3$ interfaces [95]. Pallecchi *et al.* measured the field-effect transport and thermoelectric properties of the 2DEL at the $\text{LaAlO}_3\text{-SrTiO}_3$ interface in a wide range of gate field values. Their results shows thermopower oscillations [204].

New developments in the scope of understanding the role of surfaces and interfaces opened new possibilities for designing nanoscale materials with enhanced and even novel functionalities [205]. Moreover, as Ravichandrana [206] recently mentioned, the need for fundamental understanding of material properties is as important as the ability to develop a scalable and inexpensive manufacturing process to develop devices and products from these high performance materials [206]. Although there is a variety of deposition techniques available such as atomic layer-by-layer oxide molecular beam epitaxy (ALL-MBE) is one of the most successful methods that made it possible to study the properties of interfaces. In this study, we focused on effect of individual layer thickness and oxygen loss effect on thermoelectric properties of MBE-grown $\text{La}_2\text{CuO}_4/\text{LaNiO}_3$ heterostructures to understand structure property relationship at the atomic level.

5.2. Growth Process & Characterization

Epitaxial superlattices were grown on LaSrAlO_4 (001) substrates (Crystec GmbH), using ozone-assisted MBE [78,80]. One of the difficulties in growing the nickelate-cuprate hybrid structures is that these two materials grow under different deposition conditions.

Both materials grow at low chamber pressure ($\sim 3 \times 10^{-5}$ mbar) but at quite different temperatures. LaNiO_3 (LNO) is deposited at low temperatures ~ 823 °C above which it decomposes into La_2NiO_4 and NiO. La_2CuO_4 (LCO), instead, requires higher temperatures ~ 903 °C [207]. The MBE-grown process requires a very careful control of the ratio between the cations being deposited, which is accomplished by opening and closing of the shutters of effusion cells [78].

For the growth of the samples of the present study, the deposition parameters of previous works were used [37, 39], namely $T \approx 893$ K and pressure $P \approx 2.5 \times 10^{-5}$ Torr (of mixed ozone, molecular and atomic oxygen). After the growth, all samples were cooled under ozone conditions. Only Sr- δ -doped La_2CuO_4 samples were cooled under vacuum starting from a temperature $T \approx 473$ K which ensured no formation of undesired oxygen interstitial defects in the lattice [78].

Electrical conductivity and Seebeck coefficient were measured as a function of temperature between 300 K and 900 K, using a Ulvac ZEM-3 M8. Pt contacts were deposited on the sample by sputtering and resistivity measurements were carried out in normal mode (NM). The detailed information about normal mode (NM) was given in chapter 2.

X-ray diffraction (XRD) and X-ray reflectivity (XRR) analyses were performed both on as grown samples and after the measurement. The detailed information about the techniques was also given in chapter 2.

A digital Instruments atomic force microscope (AFM) with Nanoscope III controller, operated in tapping mode, was used for imaging the surface morphology, which provided useful information about the quality of the samples.

Four different sets of samples were prepared and measured in this study; single phase LNO, single phase LCO; bilayer of LNO/LCO and multilayers. The detailed information about the sample sets are shown in Table 5.1. In this chapter the samples named as “m ($n_1//n_2$)” according to their number of repetition (m) and unit cell (n_1, n_2).

Three steps were performed for the measurements: the first measurement was carried out on an as-grown sample in ZEM-3; the second measurement was performed right after the first measurement cycle, without taking the sample out of the

measurement chamber (before ozone annealing); the third measurement was run after annealing under ozone in MBE chamber to re-establish in the samples the as-grown conditions.

Table 5.1 Information of MBE-grown samples. For the Sr- δ -doped sample, 1 ml Sr indicates the presence of one monolayer of Sr-O atoms (i.e. a Sr-O plane).

	Sample Code	Number of Repetitions (m)	Number of Unit cell (u.c.)	
			LaNiO ₃ (n ₁)	La ₂ CuO ₄ (n ₂)
Single Phase Films	18.5 u.c. LCO		-	18.5
	12 u.c. LCO		-	12
	6 u.c. LCO		-	6
	3 u.c. LCO		-	3
	32 u.c. LNO		32	-
	16 u.c. LNO	-	16	-
	8 u.c. LNO	-	8	-
	4 u.c. LNO	-	4	-
Bilayers	1x(8//6)	-	8	6
	1x(6//8)	-	8	6
Multilayers	4x(8//6)	4x	8	6
	8x(4//3)	8x	4	3
	11x(3//2)	11x	3	2
	16x(2//1.5)	16x	2	1.5
Sr-δ-doped	3x(1mlSr-19mlLCO)	3x	-	9.5

5.3. Results and Discussion

The first step towards the characterization of heterostructures for our study was the measurement of the Seebeck coefficient and electrical conductivity on single phase systems. In the following, the main findings are summarized.

5.3.1. Single phase films

Single phase LNO and LCO films were investigated to analyze the thermoelectric properties of single phase films as a function of temperature and film thickness.

At the end of the growth process we were able to obtain fully epitaxial La_2CuO_4 and LaNiO_3 with various thicknesses (Table 5.1). The corresponding AFM micrographs shown in Figure 5.1 indicate that the LNO single phase film has a smooth surface, whose R_{ms} roughness is comparable with the substrate roughness (~ 0.5 nm). One should mention that as the films get thinner R_{ms} increases as expected.

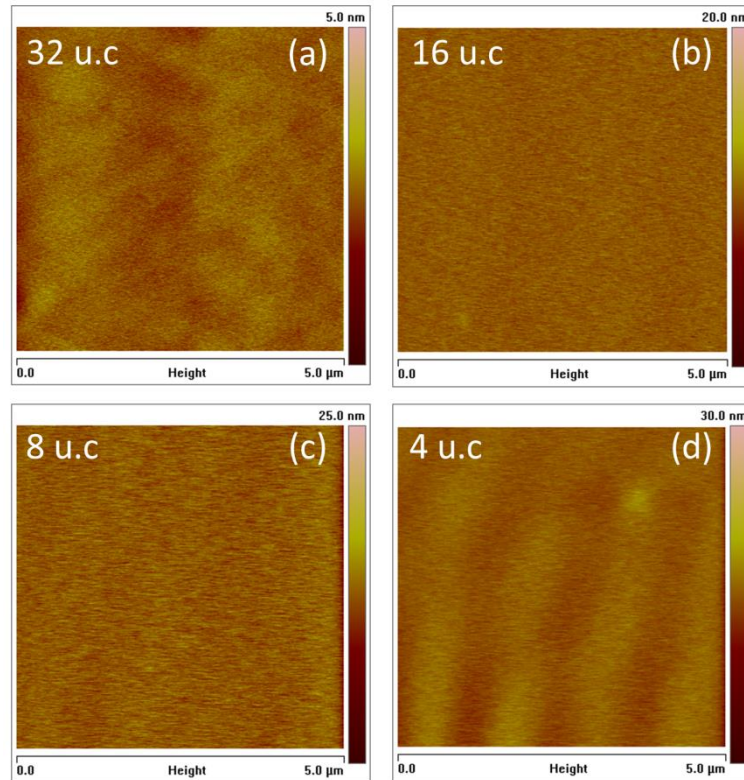


Figure 5.1 The resultant final film surface morphology of LNO single phase films, as measured by AFM in panels (a), (b), (c), (d). R_{ms} roughness values are 0.228 nm, 0.601 nm, 1.12 nm, 1.01 nm, respectively.

In Figure 5.2, $2\theta / \omega$ XRD full scan of LaNiO_3 films with various layer thickness are presented, showing pronounced diffraction of peaks up to (300) index, indicative high crystalline order in the thinner film in comparison to ultrathin films.

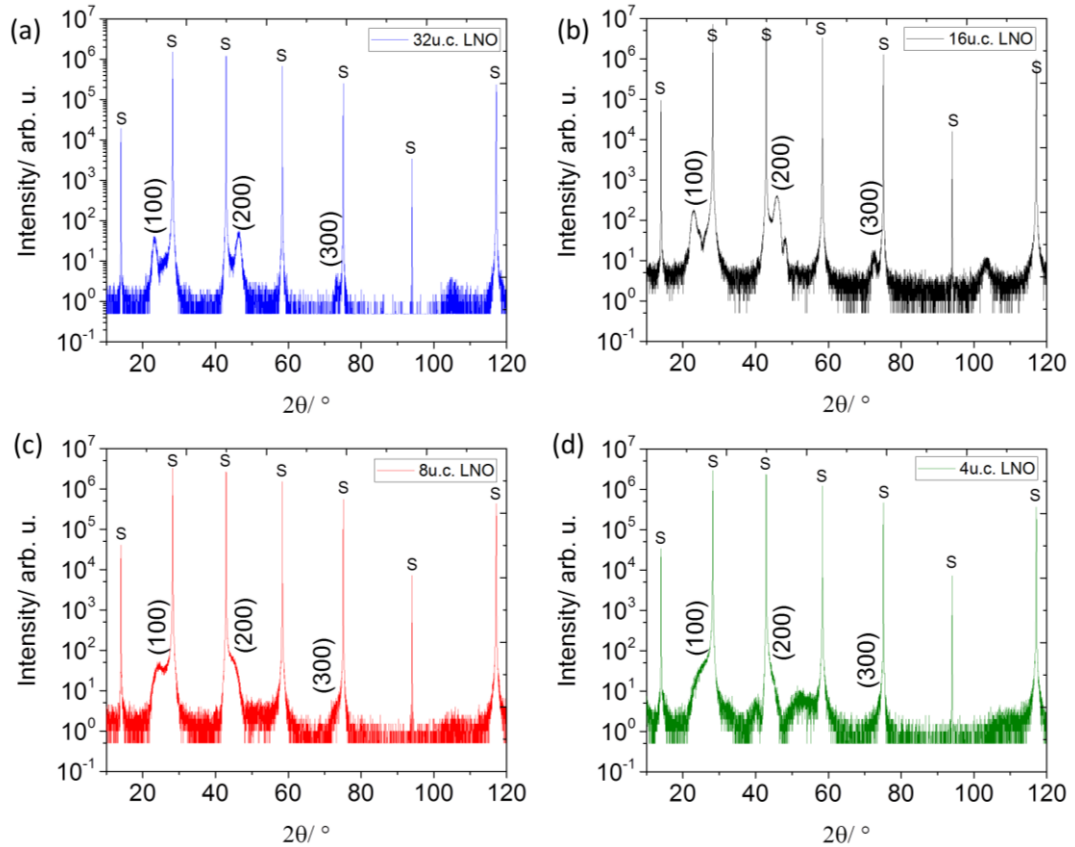


Figure 5.2 XRD fullscan for (a) 32 u.c. (b) 16 u.c. (c) 8 u.c (d) 4 u.c. LaNiO_3 on $\text{LaSrAlO}_4(001)$ (S).

In Figure 5.3 low angle X-ray reflectivity (XRR) analysis of LaNiO_3 films with various layer thicknesses are shown. The data simulation was done by using the Parratt formalism [84] and results in an average period thickness of 66.53 Å and 147.98 Å to be compared with an expected thickness of 62.56 Å and 125.12 Å for 16 u.c. and 32 u.c. LNO, respectively. For ultrathin samples (8 u.c. and 4 u.c.), due to the extremely weak reflecting signal, it was impossible to determine their thickness experimentally.

Any kind of defect, e.g., vacancies, interstitials, grain boundaries and interface roughness, as well as intrinsic effects i.e., reduction of layer thickness and an increase of tensile epitaxial strain leads to a change of the electrical transport properties.

In this chapter we focus on the effect of the reduction of the layer thickness on thermoelectric properties.

Previously, different groups found an increase of resistivity when the LNO layer thickness is decreased [207–212]. However, all of them are based on low temperatures experiments (<300 K), whereas here the temperature range of interest is above 300 K.

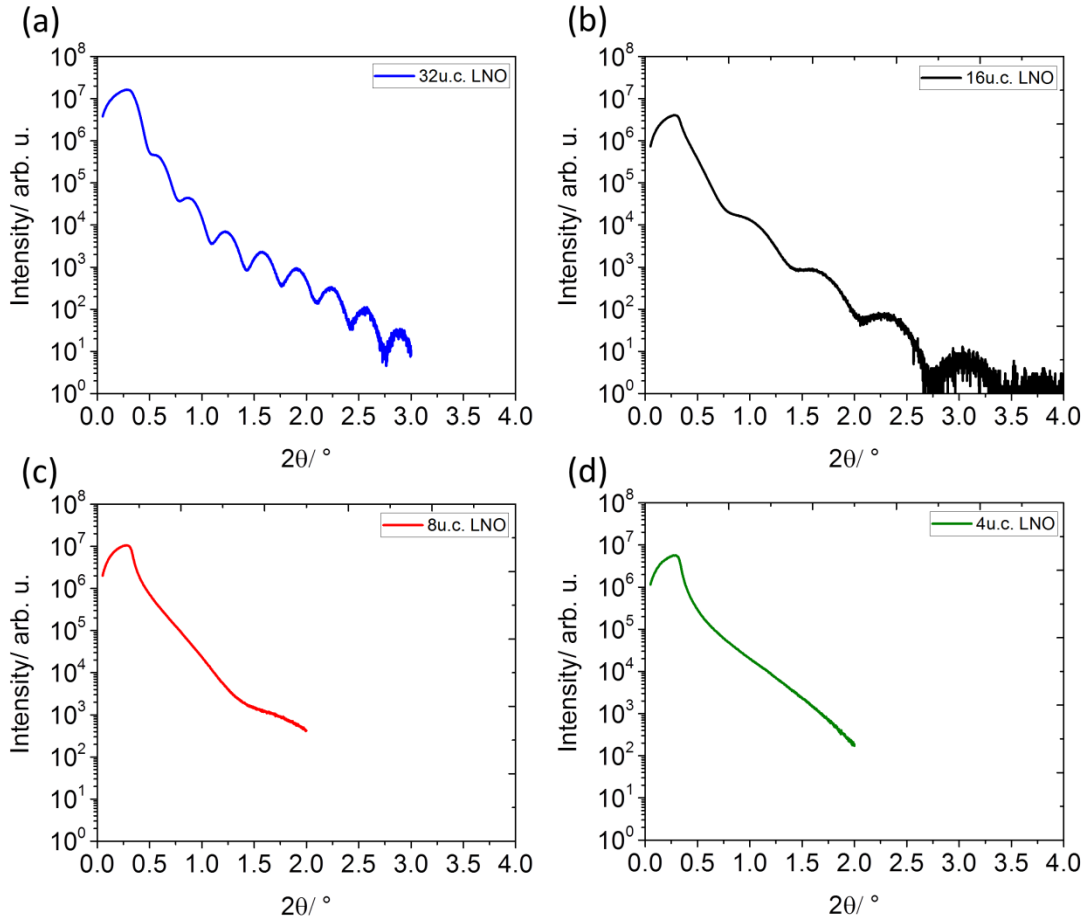


Figure 5.3 Low-angle XRR scan for (a) 32 u.c. (b) 16 u.c. (c) 8 u.c (d) 4 u.c. LaNiO_3 on LaSrAlO_4 (001) (S).

In Figure 5.4., the thermoelectric properties of LaNiO_3 single phase films having various thicknesses are shown. The measurements were carried out only once during heating. The electrical conductivity decreases with decreasing film thickness (Figure 5.4.). The electrical conductivity of structures with different nickelate layer thicknesses is predominantly metallic as shown by the characteristic increase with increasing temperature (Figure 5.4.). The nickelate film with 4 u.c. is semiconducting (Figure 5.4.). A transition from metal to insulator behavior in LNO occurs at nearly 4 u.c for our samples and this is consistent with literature data [210].

All films have negative Seebeck coefficients which indicate n-type behavior. Although there is not a clear trend in the Seebeck coefficient as in the case of the electrical conductivity, it is clear that changing the thickness of LNO layer does not play a significant role for the behavior of the Seebeck coefficient as a function of temperature. Moreover no distinct change was observed in Seebeck coefficient and electrical conductivity when the measurement were carried on 32 u.c. LNO single phase film during the cooling cycle and also after the repetition step (Fig. 5.5).

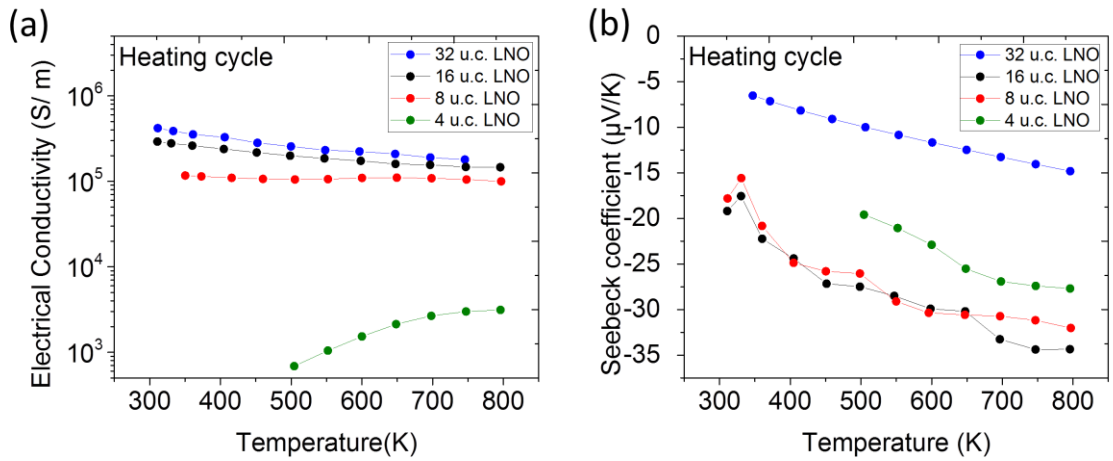


Figure 5.4 (a) Seebeck coefficient (b) Electrical conductivity of LaNiO₃ with different layer thicknesses as a function of temperature.

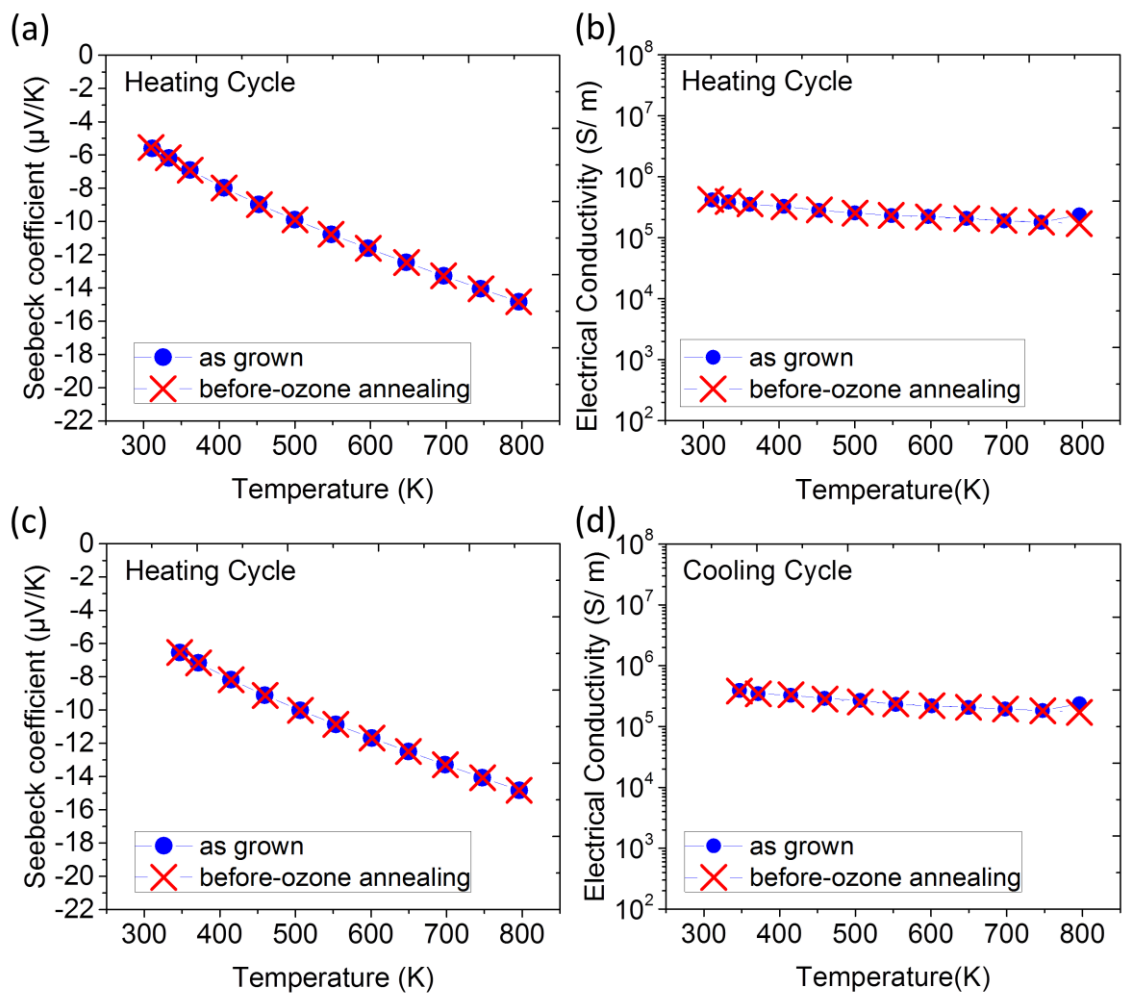


Figure 5.5 (a)-(c) Seebeck Coefficient, (b)-(d) Electrical conductivity of 32 u.c. LaNiO_3 as a function of temperature during heating cooling cycle

The resulting AFM micrograph shown in Figure 5.6 indicates that LCO single phase film has a smooth surface, whose R_{ms} roughness is comparable with the substrate roughness (about 0.5 nm). Unlike LNO single phase film, for the LCO samples, R_{ms} decreases with decreasing film thickness.

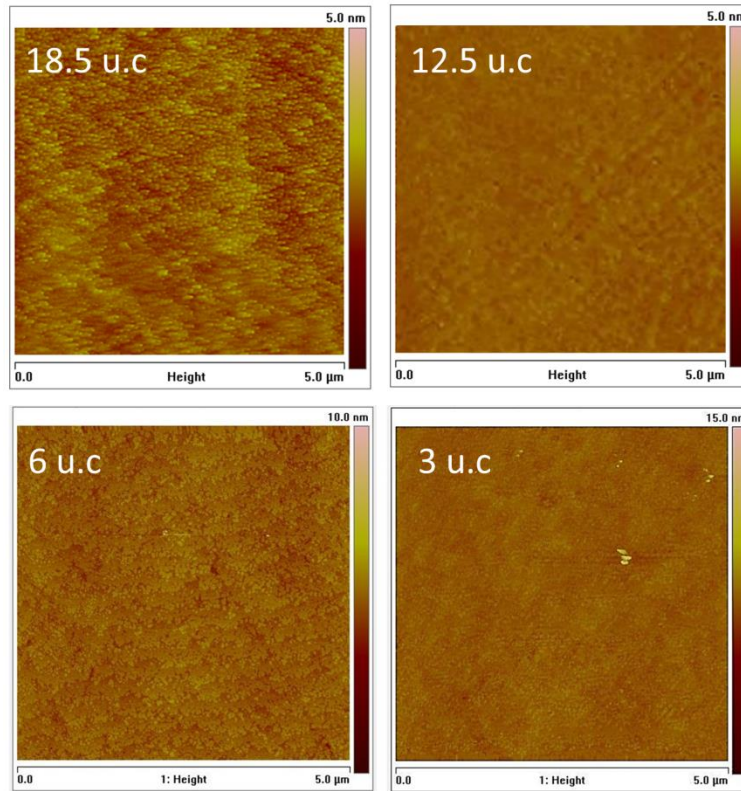


Figure 5.6 The resultant final film topography of LCO single phase films, as measured by AFM in panels (a), (b), (c), (d). Rms roughness values are 0.822, 0.683, 0.420, 0.329 for the micrograph shown in (a), (b), (c) and (d), respectively.

In Figure 5.7, $2\theta / \omega$ XRD full scan of La_2CuO_4 films with various layer thicknesses are reported, showing pronounced diffraction of peaks up to (0014) index, and being indicative of high crystalline order in thinner film in comparison to ultrathin films.

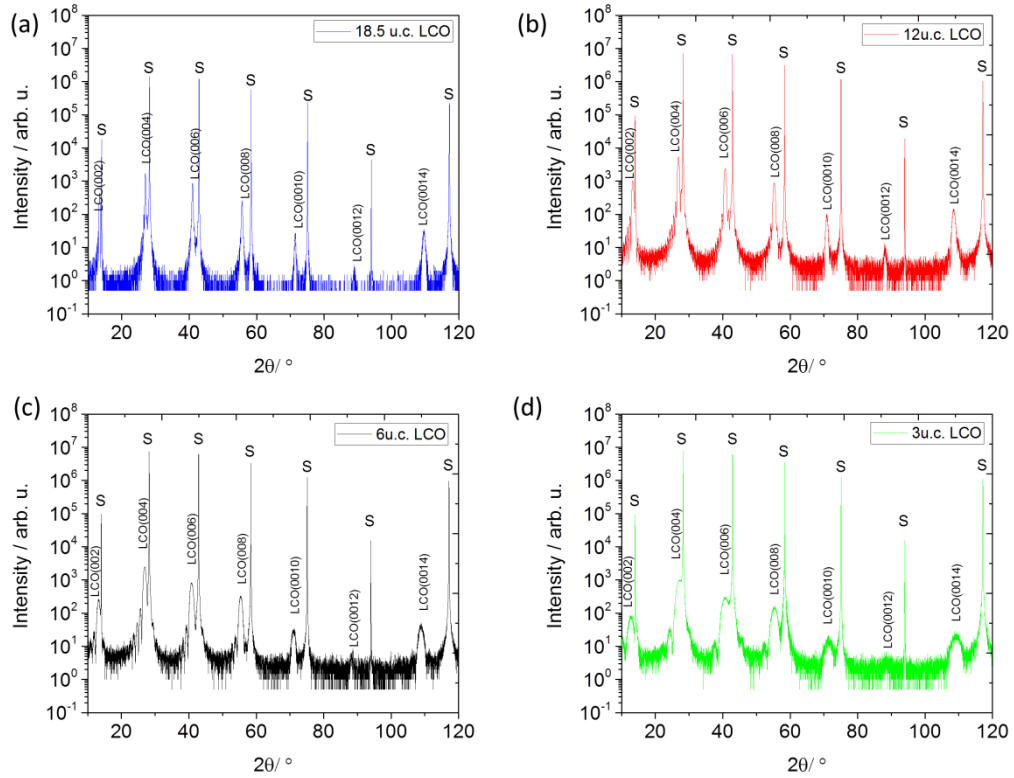


Figure 5.7 XRD patterns of (a) 18.5 u.c. (b) 12 u.c. (c) 6 u.c (d) 3 u.c. La_2CuO_4 on LaSrAlO_4 (001) (S).

In Figure 5.8 a low angle X-ray reflectivity (XRR) analysis of La_2CuO_4 films with various layer thickness is shown. The data simulation was done by using the Parratt formalism measurements in an average period thickness of 187.836 Å and 301.04 Å which is to be compared with the expected thicknesses of 157.92 Å and 243.46 Å for 12 u.c. and 18.5 u.c. LCO, respectively. For ultrathin samples (6 u.c. and 3 u.c.) it was impossible to determine the thickness experimentally.

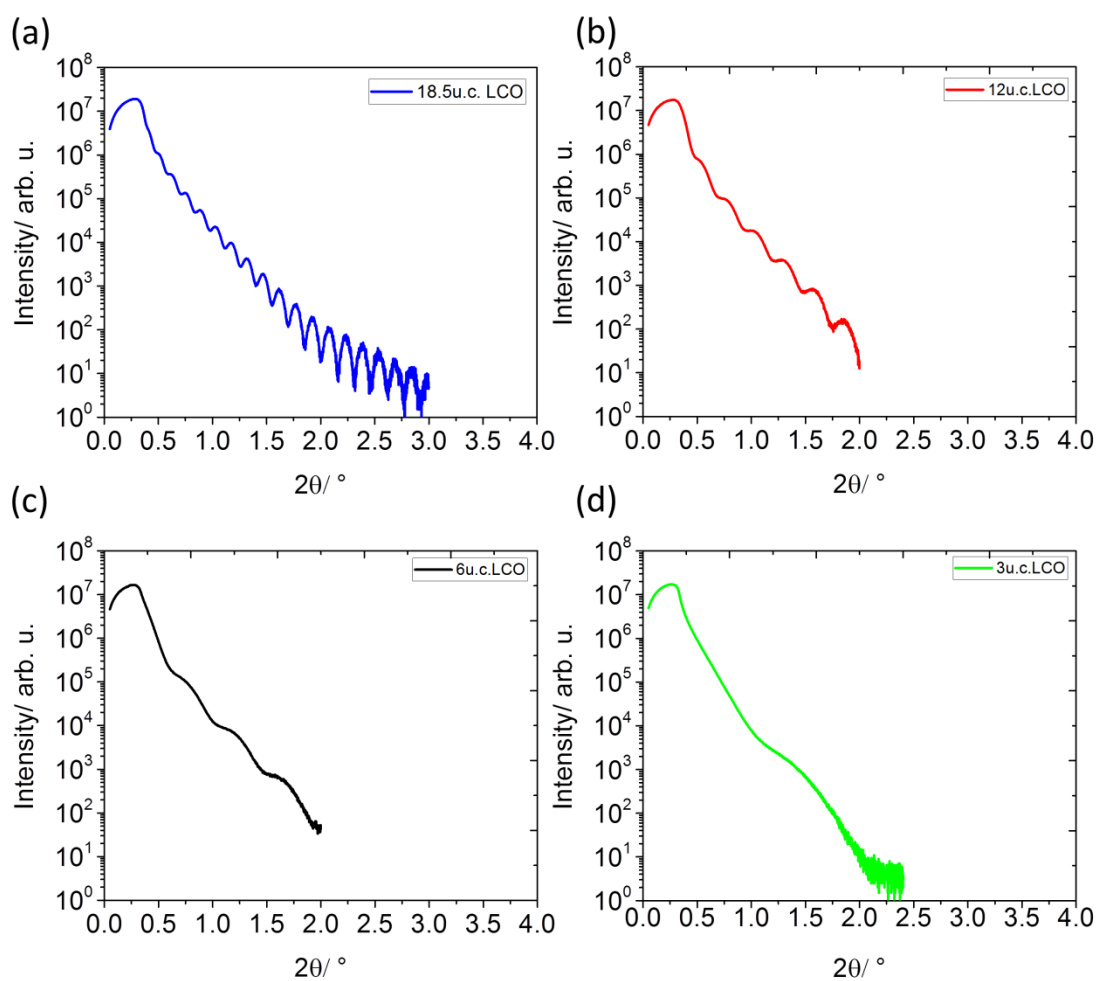


Figure 5.8 Low-angle XRR scan for (a) 18.5 u.c. (b) 12 u.c. (c) 6 u.c (d) 3 u.c. La_2CuO_4 on LaSrAlO_4 (001) (S).

In Figure 5.9, the thermoelectric properties of La_2CuO_4 single phase films grown with various thicknesses and of polycrystalline bulk La_2CuO_4 sample are shown. The measurements were carried out only once during heating. The electrical conductivity slightly decreases and the Seebeck coefficient increases as the film gets thinner. All films exhibit a positive Seebeck coefficient which is an indication of p-type transport.

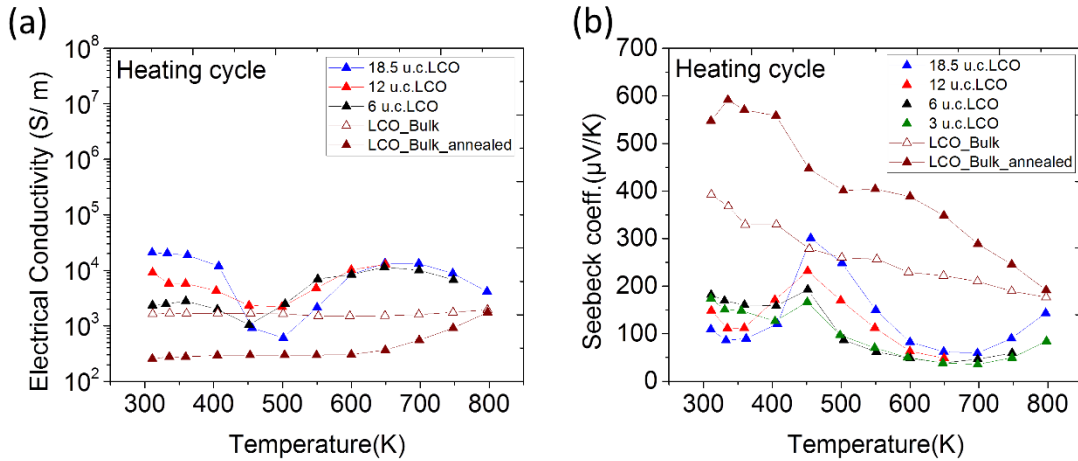


Figure 5.9 (a) *Electrical conductivity and (b) Seebeck coefficient values of La_2CuO_4 with different layer thicknesses as a function of temperature.*

As shown in Figure 5.10, both the as-grown samples (solid blue triangle) and the ozone-annealed (3.3×10^{-5} mbar) samples (crossed blue triangle) exhibit similar electrical behavior within three temperature regions, when the measurement carried out under oxygen atmosphere (950 mbar); however before ozone annealing (unfilled blue triangle) sample shows a different behavior.

When the as grown (solid blue triangle) samples are measured under 950 mbar oxygen (which is less reactive than ozone) the following three regions corresponding to different electrical conductivity properties are observed. In the first region ranging from 300 K up to roughly 450-500 K the electrical conductivity decreases with increasing temperature. This corresponds to the interstitial oxygens are exorporated from the samples with the formation of holes (cf. Equation 1.20) as a consequence of the reduction of oxygen partial pressure compared to the growth condition (ozone atmosphere) to the measurement condition (950 mbar O_2) (Fig. 1.11). In the second region above 550 K, La_2CuO_4 shows a structural phase transition from a low temperature orthorhombic (LTO) (T structure) to a high temperature tetragonal phase (T' structure) The T structure has CuO_6 octahedra and the T' has two dimensional square-planar CuO_4 [213]. which allows the incorporation of oxygen to the lattice. Thus, in the second region ranging between 500 K and 650 K, the incorporation of the oxygen occurs as an effect of the presence of 950 mbar oxygen and the higher temperature. The non-monotonicity is ascribed to kinetics effects, which accelerate at high temperatures. Since a second “desorption temperature point” was reported at 673

K [214,215] the conductivity decreases again above 650 K (third region) due to an excorporation of more stable oxygen species from the lattice.

If the measurements are repeated before ozone annealing (unfilled blue triangle) under oxygen, no abrupt change of both the Seebeck coefficient and electrical conductivity is observed up to at ≈ 550 K most likely because no or less interstitial oxygen is present in the system. Nonetheless, the change of the electrical properties during the 2nd and 3rd temperature range is still observed, since such changes occur due to structural phase transformation. Finally if the sample is annealed under ozone and the measurement is repeated on such an ozone-annealed sample (crossed blue triangle), a recovery of the first behavior is observed.

When the measurements are carried out under He on ozone-annealed samples that already includes interstitial oxygens, an abrupt change of the Seebeck coefficient and electrical conductivity is expected at ≈ 450 K. Unfortunately, such a behavior was not possible to be detected because of a sudden increase of the samples' high-resistive behavior (out of the range of the equipment for the measurement) above 520 K.

The observation of the high-resistive behavior also results from the fact that it is not possible to fill the apical oxygen positions under reducing conditions (950 mbar He atmosphere).

When the measurements are repeated under He, after the 1st measurement the Seebeck coefficient increases to $360 \mu\text{V/K}$ and the electrical conductivity decreases to $9 \times 10^4 \text{ S/m}$ at 300 K. Above 300 K the electrical conductivity stayed almost constant, as the temperature was not high enough (below 650 K) to see the effect of filling the apical oxygen positions. Then at 500 K the measurement was stopped due to the thermal decomposition of the film under reducing conditions (See Fig. 5.11).

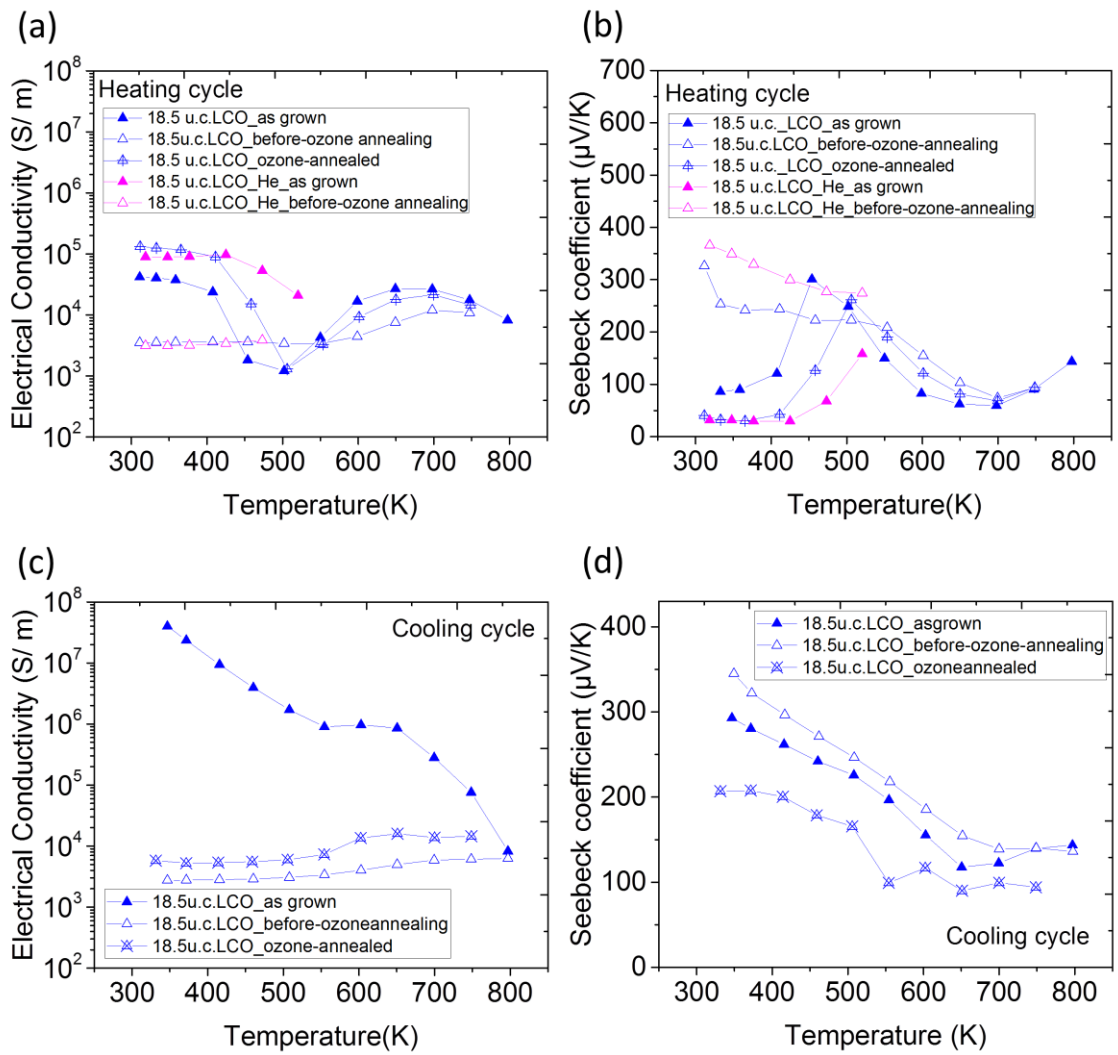


Figure 5.10 (a) and (c) Seebeck coefficient data, (b) and (d) Electrical conductivity data of 18.5 u.c. La_2CuO_4 as a function of temperature during heating and cooling cycle.

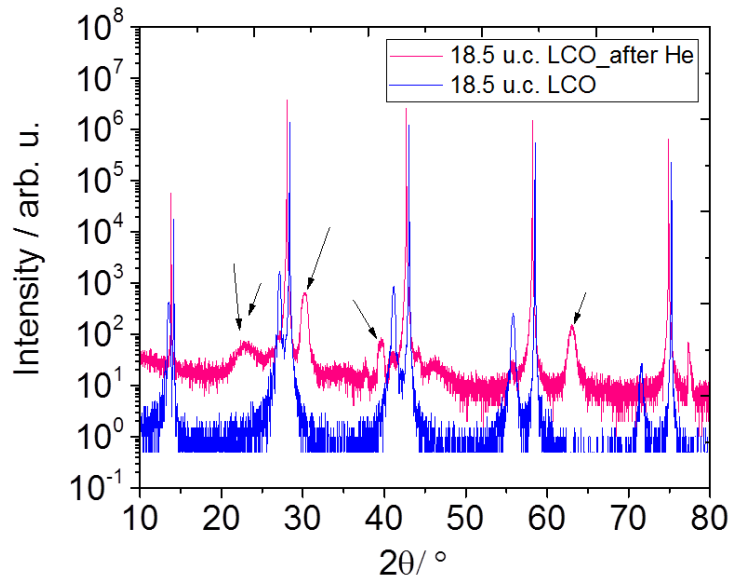


Figure 5.11 XRD patterns after the measurement under He.

5.3.2. Bilayers

LaNiO₃-La₂CuO₄ bilayers were grown and measured to analyze whether the thermoelectric properties change when one combines the very thin layers of two phases. The corresponding AFM micrograph shown in Figure 5.12 indicates that the bilayers (irrespective of the ordering of the two phases) have a smooth surface.

In Figure 5.13, XRD patterns of the bilayers are reported showing pronounced diffraction of peaks for LaNiO₃ up to the (300) plane and La₂CuO₄ up to (0014), indicative for high crystalline order.

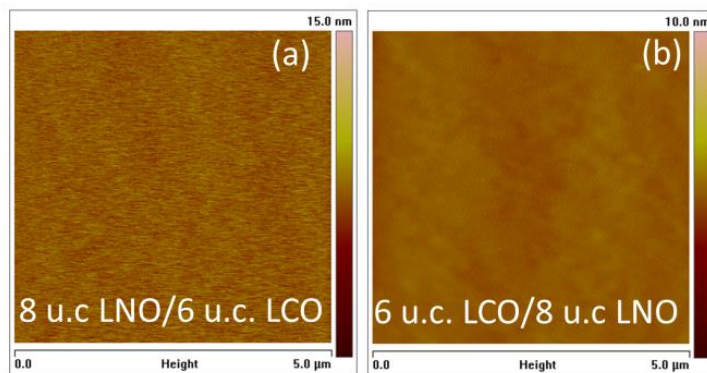


Figure 5.12 AFM micrographs of (a) LNO/LCO and (b) LCO/LNO bilayers. Rms roughness values are 0.572 nm, 0.155 nm, for the micrograph shown in (a) and (b), respectively.

Figure 5.14(a) depicts the results of low angle X-ray reflectivity (XRR) analysis of the LNO/LCO bilayer. The data simulation was performed using the Parratt formalism and results in an average period thickness of 30.2 Å and 89.0 Å, while the expected thickness according to the MBE growth rate was 31.3 Å and 78.6 Å. For the LCO/LNO bilayer, an average period thickness of 85.3 Å and 33.3 Å was obtained from the simulation whilst the expected thickness according to the growing condition was 78.6 Å and 31.3 Å.

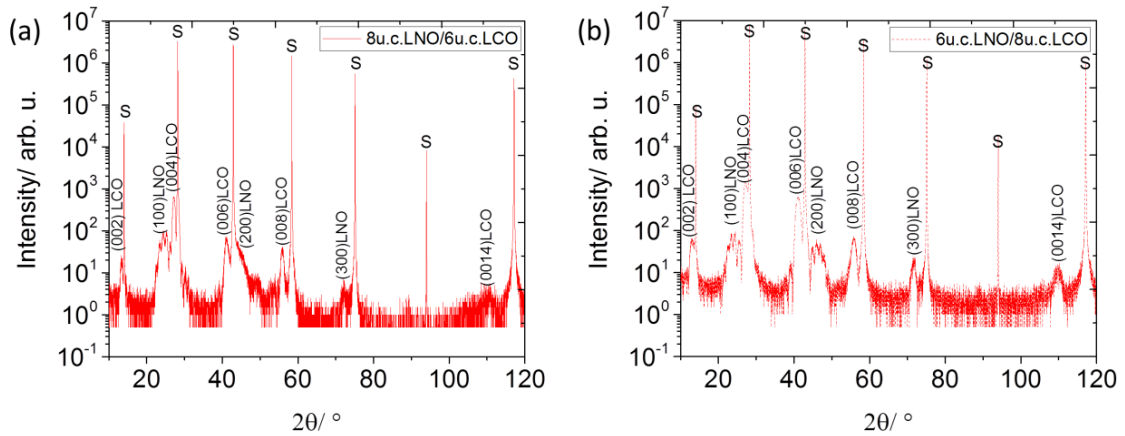


Figure 5.13 XRD patterns for (a) LNO/LCO (b) LCO/LNO bilayers on LaSrAlO₄ (001) (S).

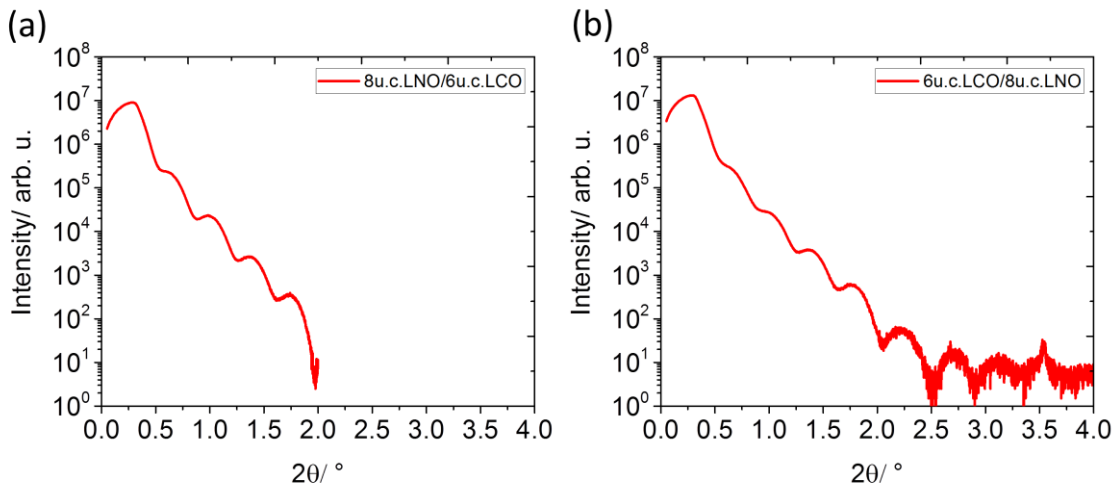


Figure 5.14 Low-angle XRR scan for (a) LNO/LCO (b) LCO/LNO bilayers on LaSrAlO₄ (001) (S).

In Figure 5.15, the thermoelectric properties of bilayers as a function of temperatures are shown during heating and cooling cycle for as grown and annealed

samples. The Seebeck coefficient of both bilayers is negative and its absolute values are similar to the 8 u.c.LNO single phase film (see Fig.5.4.a) The electrical conductivity of both bilayers is in the range of 10^5 S/m which is similar to the 8 u.c.LNO single phase film as well (See Fig.5.4.b).

Such results reveal that the dominant phase is the metallic phase (LaNiO_3) in the bilayer system. The electrical conductivity and the Seebeck coefficient of LNO/LCO bilayer is slightly different than LCO/LNO bilayer which might stem from the different strain relief between the substrate and the first layer.

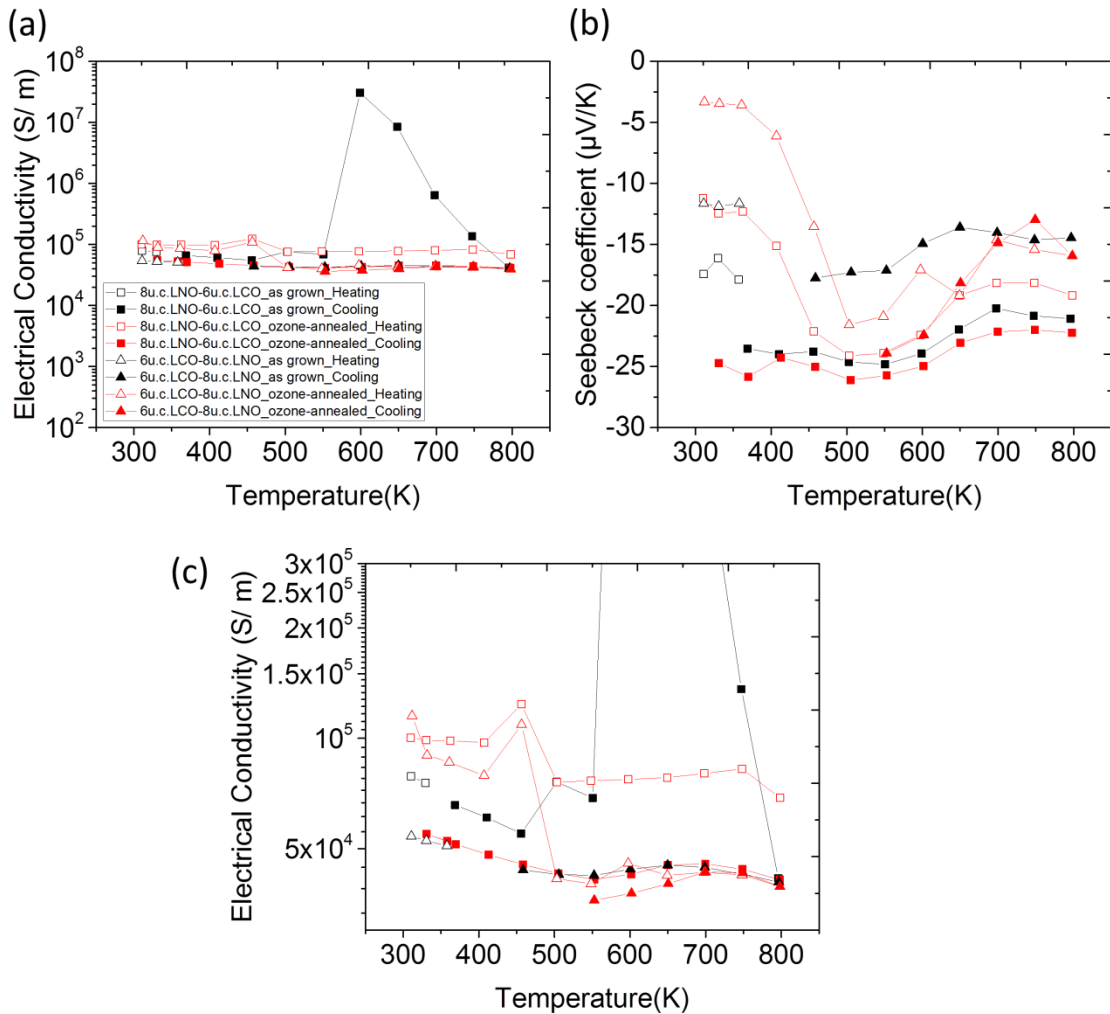


Figure 5.15 (a) Seebeck coefficient (b) & (c) Electrical conductivity of LNO/LCO and LCO/LNO bilayers as a function of temperature.

5.3.3. Multilayers

LaNiO₃-La₂CuO₄ superlattices given in Table 5.1 were grown and measured for two purposes: to analyze the interface effect on the thermoelectric properties as a function of temperature and to identify the most convenient layer thickness of 2 phases in multilayer system. The AFM micrographs shown in Figure 5.16 indicate that multilayers have a smooth surface and as the individual thickness reduces, R_{ms} increases.

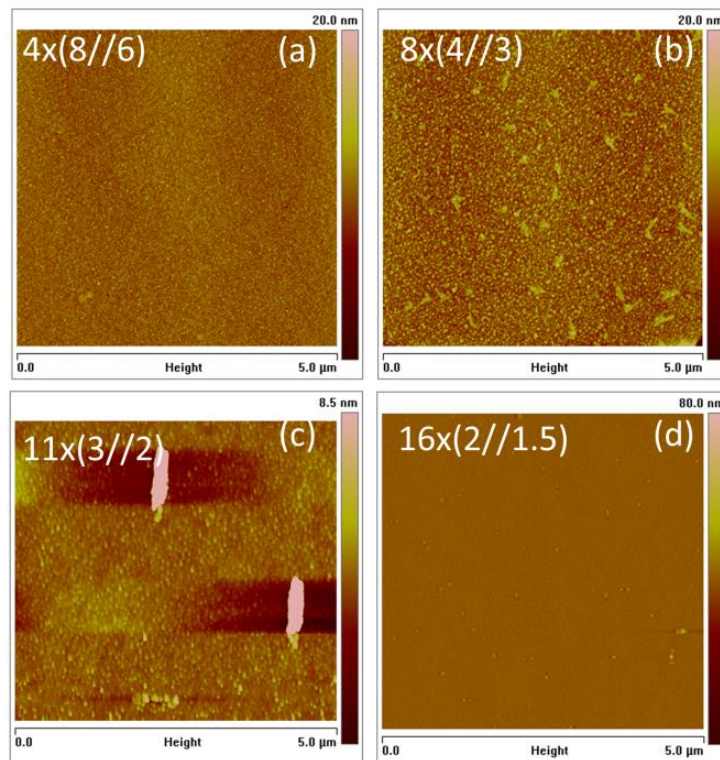


Figure 5.16 AFM micrograph of LNO/LCO multilayers (a) 4x(8//6), (b) 8x(4//3), (c) 11x(3//2), (d) 16x(2//1.5). R_{ms} roughness values are 0.228 nm, 0.601 nm, 1.12 nm, 1.01 nm, respectively.

In Figure 5.17, XRD patterns of multilayers are reported showing pronounced diffraction peaks for LaNiO₃ up to the (300) plane and La₂CuO₄ up to (0014), indicating high crystalline order.

In Figure 5.18, a low angle X-ray reflectivity analysis of multilayers is shown. The data simulation was carried out using the Parratt formalism and result in an average period thickness of 32.1 Å and 84.1 Å while the expected thickness resulting from the MBE growth rate was 31.3Å and 78.1 Å for 4x(8//6). For the 8x(4//3) multilayer average period thickness obtained from the simulation was 12.2 Å and 45.2 Å while the

growing rate indicated 15.6 Å and 39.3 Å, respectively. The third sample (11x(3//2)) has an average period thickness of 12.7 Å and 25.6 Å according to the simulation and an expected thickness of 11.7 Å and 26.2 Å according to the growth rate. Finally the 16x(2//1.5) multilayer has an average period thickness of 9.2 Å and 19.5 Å (simulation) and an expected thickness of 7.8 Å and 19.7 Å in the light of the MBE growth rate.

In Figure 5.19, the Seebeck coefficient of (8//6) bilayer and 4x(8//6) multilayer sample as a function of temperature obtained experimentally as well as calculated from Kirchhoff's law* is shown. The calculated values of the effective Seebeck coefficient (α_e) matched the experimental data rather well, particularly, and unexpectedly, those acquired from the 4x(8//6). The calculation and experimental data showed that LNO phase (conductive phase) dominates the system in terms of Seebeck coefficient and electrical conductivity.

In Figure 5.20, the behavior of the thermoelectric properties of the 4x(8//6) sample as during heating and cooling is shown. It is worth noting that the 4x(8//6) sample is the superlattice which has the thickest individual layers.

First of all, this superlattice exhibits negative Seebeck coefficients, whose values correspond to those of the single phase LNO film. Furthermore, also the electrical conductivity is similar to the conductivity of the single phase LNO film. As it is seen in Fig. 5.20, the first measurement (as grown) and third measurement (after ozone annealing) show the same behavior and there is no sharp change at 450K, which corresponds to the interstitial oxygen loss. In terms of Seebeck coefficient values and metallic behavior in electrical conductivity, it is evident that the LNO phase dominates the electrical properties of the whole superlattice system. Nonetheless, according to the behavior as a function of temperature, an increase of Seebeck coefficient and decrease of electrical conductivity similar to single phase LCO were observed.

$$*\alpha_{||} = \frac{\alpha_A \sigma_A + \frac{d_B}{d_A} \alpha_B \sigma_B}{\alpha_A + \frac{d_B}{d_A} \sigma_A}$$

; α : Seebeck coefficient, σ : Electrical conductivity, d : thickness of the layer (experimental values obtained from XRR). The subscripts A and B refer to different phases A and B.

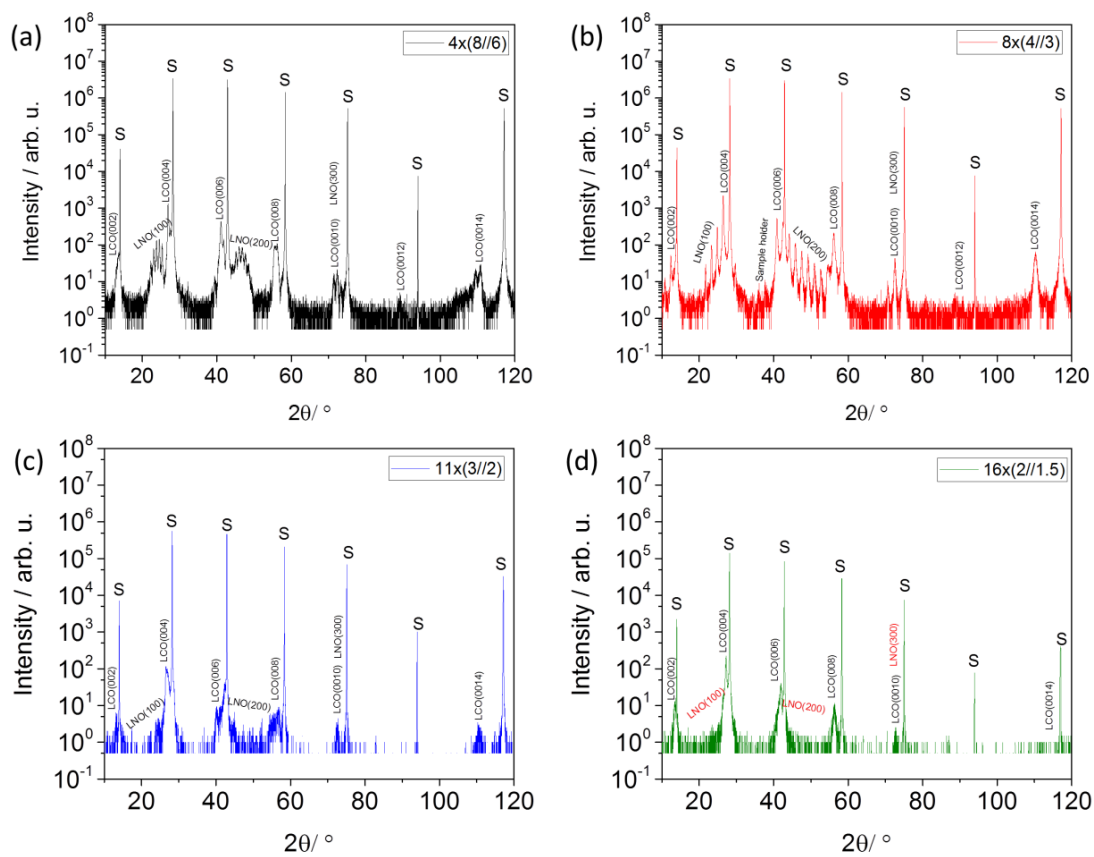


Figure 5.17 XRD patterns acquired from (a) $4x(8//6)$, (b) $8x(4//3)$, (c) $11x(3//2)$, (d) $16x(2//1.5)$, multilayers grown on LaSrAlO_4 (001) (S).

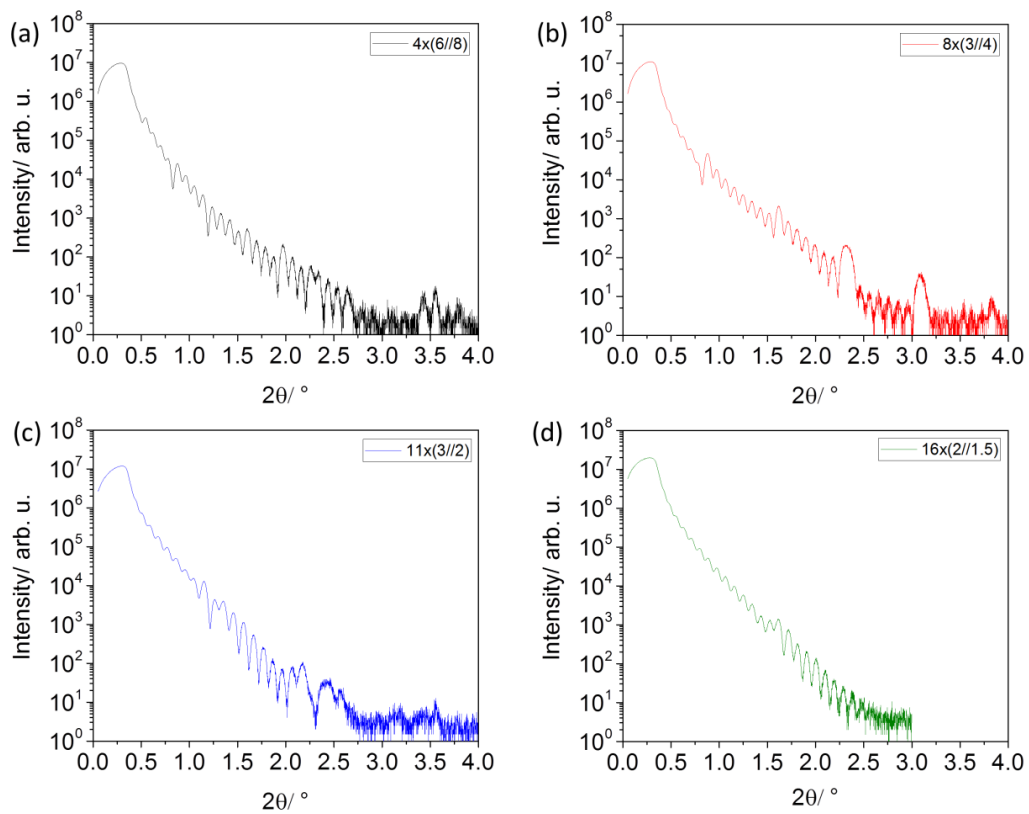


Figure 5.18 Low-angle XRR scan for (a) $4x(8//6)$, (b) $8x(4//3)$, (c) $11x(3//2)$, (d) $16x(2//1.5)$, multilayers on $\text{LaSrAlO}_4(001)$ (S).

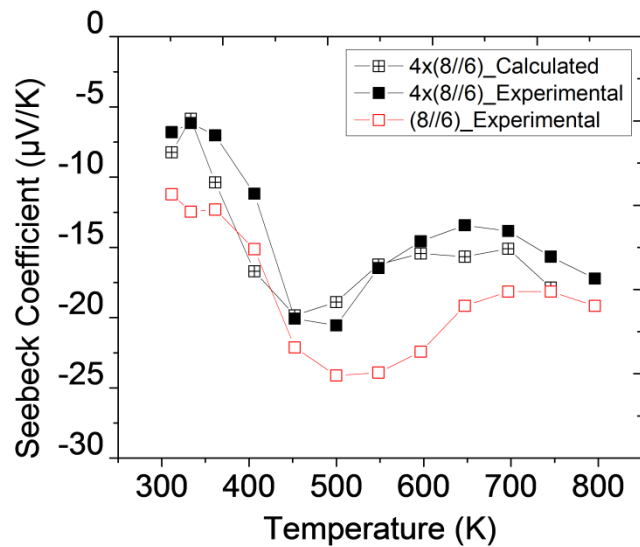


Figure 5.19 Seebeck coefficient of $(8//6)$ bilayer, $4x(8//6)$ multilayer as a function of temperature obtained experimentally and calculated by applying Kirchoff's Law.

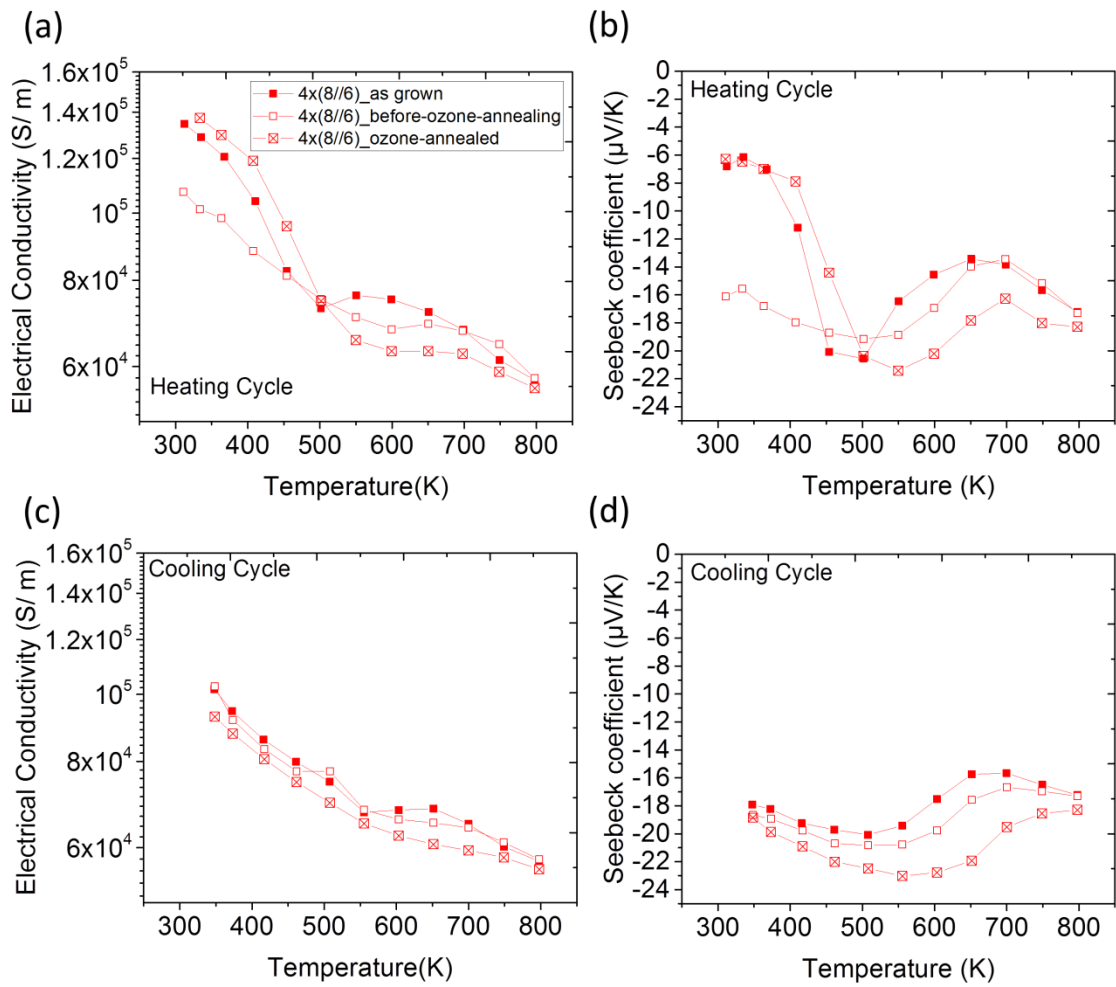


Figure 5.20 (a)-(b) Seebeck coefficient & Electrical conductivity during heating and (c)-(d) Seebeck coefficient & Electrical conductivity during cooling of $4x(8/6)$ multilayer as a function of temperature.

5.3.3.1. Effect of Number of Interfaces

In Figure 5.21, the thermoelectric properties of multilayers as a function of temperatures are shown during heating and cooling cycle. For this set of samples, the number of interfaces has been increased while the total thickness was kept constant. Two significant outcomes can be observed from the transport measurements between 300 K and 800 K.

Firstly, as the constituting layers get thinner, a sign change of the Seebeck coefficient was observed, which might be due to two reasons.

The first explanation refers to a possible cation interdiffusion at the interface. In a previous study, similar hybrid heterostructures grown on LSAT substrates were proven to have chemically incoherent zones at the interface specially when the number of interfaces was high [207]. The authors also observed a shoulder on the high-energy side of the white line of Cu L_3 -peak in XAS spectra which was assigned to holes being present around oxygen atoms resulting from copper substituting nickel. The formation of holes explains in the present study (i) why the abrupt change in Seebeck coefficient and electrical conductivity become more visible at 450 K as the constituting layers get progressively thinner and also (ii) why the thinner the single layers the closer their behavior gets to the one of the single phase LCO film.

The second explanation regards a metal-insulator transition of the LNO phase when the thickness of the film reduces (Fig. 5.4 (b)). As according to the Kirchhoff's law, the dominant phase is the one with the largest electrical conductivity, if the LNO phase becomes insulating, then the LCO phase naturally determined the electrical transport properties of the whole system.

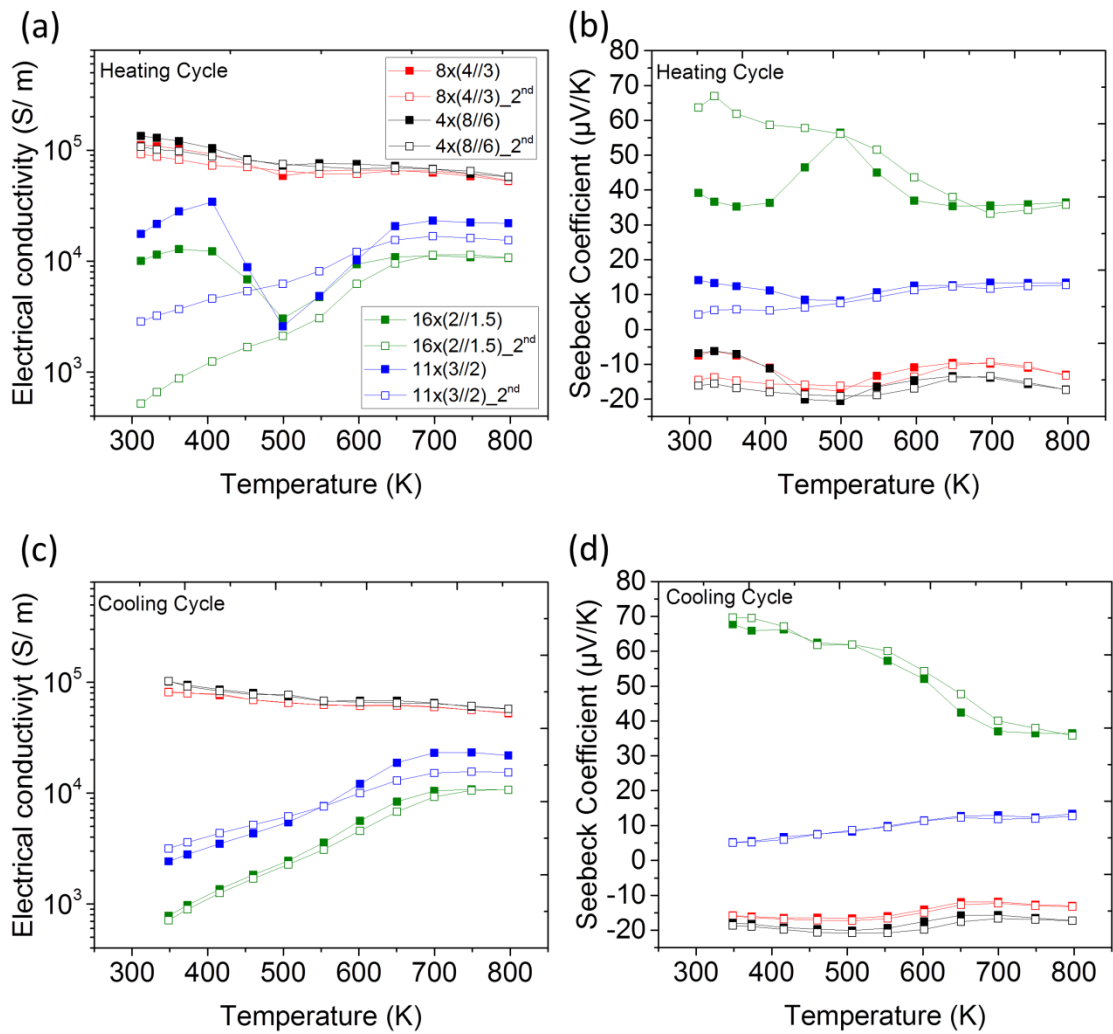


Figure 5.21 (a)-(b) Seebeck coefficient and electrical conductivity measured during heating and (c)-(d) Seebeck coefficient and electrical conductivity measured during cooling.

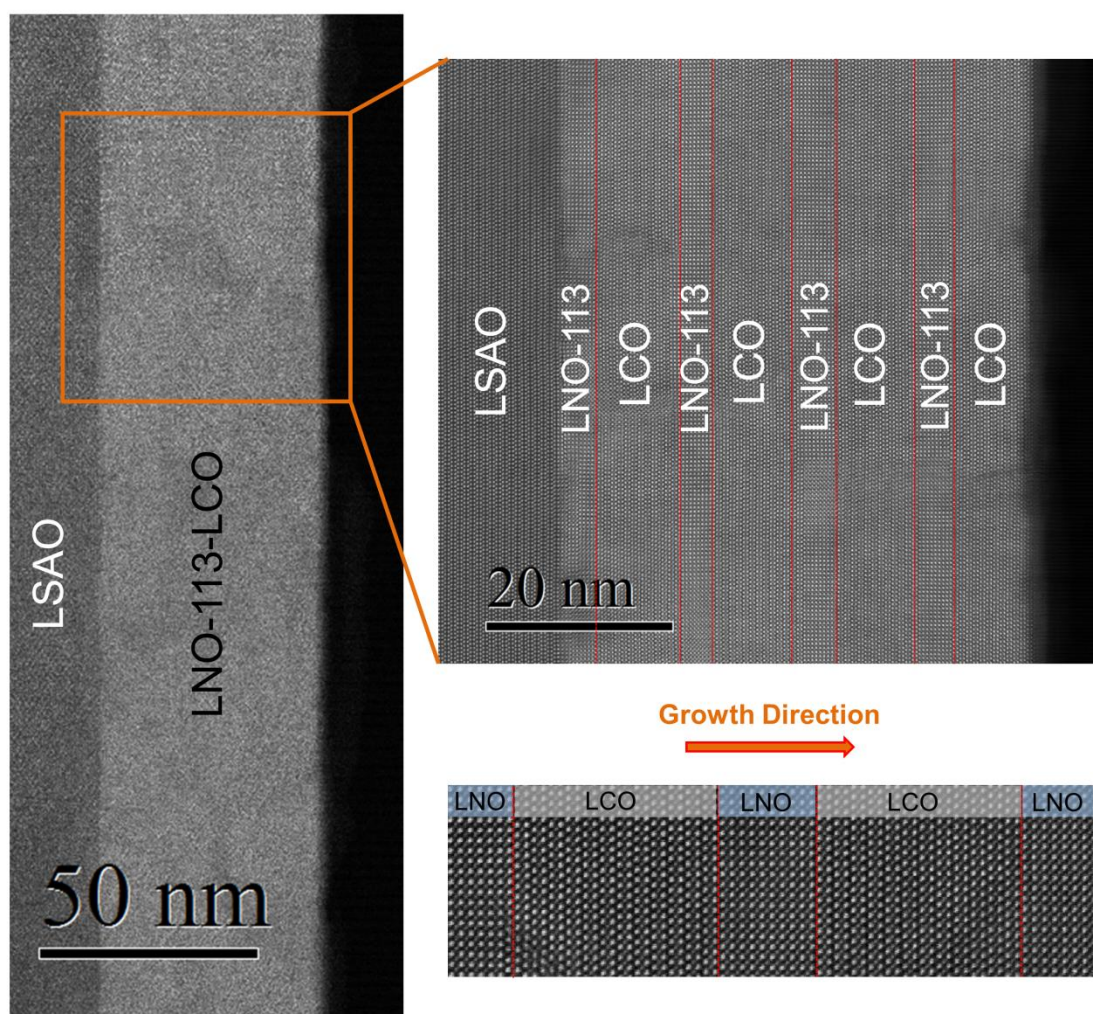


Figure 5.22 STEM images of 4x(8//6)-LCO//LNO sample which were grown on LSAO.

5.3.3.2. Effect of Interstitial Oxygens on δ -Sr-doped La_2CuO_4

In $\text{La}_{2-x}\text{Sr}_x\text{CuO}_{4+\delta}$ compounds, the oxygen content together with the Sr content plays a key role in tuning their electronic structure. The influence of excess oxygen on the thermoelectric properties, which was studied by carrying out annealing processes under different atmosphere in La_2CuO_4 , was discussed in section 5.3.1. As a reminder, in LCO films an abrupt change in Seebeck coefficient and electrical conductivity at ≈ 450 K was observed if the structure contains interstitial oxygen ions.

In vacuum-annealed Sr- δ -doped LCO, which does not have interstitial oxygen ions, no abrupt change was observed at ≈ 450 K which is consistent with the results

obtained from single phase LCO film after the second measurement (Fig. 5.23). There is a slight increase in electrical conductivity and decrease in Seebeck coefficient between 450 K and 650 K was obtained, which can be associated with apical oxygen doping. As it was mentioned in section 5.3.1, such a change might have been seen due to the formation of holes by filling the oxygen vacancies (cf. Equation 1.20) in chapter 1. Since it is possible to have interstitial oxygen ions in the system by ozone annealing, after the first measurement, ozone annealing was carried out on a Sr- δ -doped LCO sample in order to favor the insertion of oxygen into the cuprate lattice. Nevertheless, no abrupt change was observed at ≈ 450 K in this sample either. In addition, the numerical value of Seebeck coefficient and of the electrical conductivity is similar to those of the single phase LCO film after the removal of interstitial oxygens. In LCO, interstitial oxygens diffuse very fast through the a-b plane within the blocks constituted by apical O and La atoms, and promptly fill any vacancies in the apical positions. Instead, the diffusion along the c direction to fill a vacancy in the Cu-O plane requires a much higher activation energy [216,217]. In Sr- δ -doped LCO, in which a Sr-O atomic plane substitutes a La-O atomic plane acts as a negatively charged interface analogously to a charged grain-boundary case in a bicrystal [218], resulting in an enhancement of the positively charged mobile defects (particularly holes) in the adjacent layers [191]. The results indicate that Sr- δ -doping creates a layer blocking the diffusion of interstitial oxygens into the lattice.

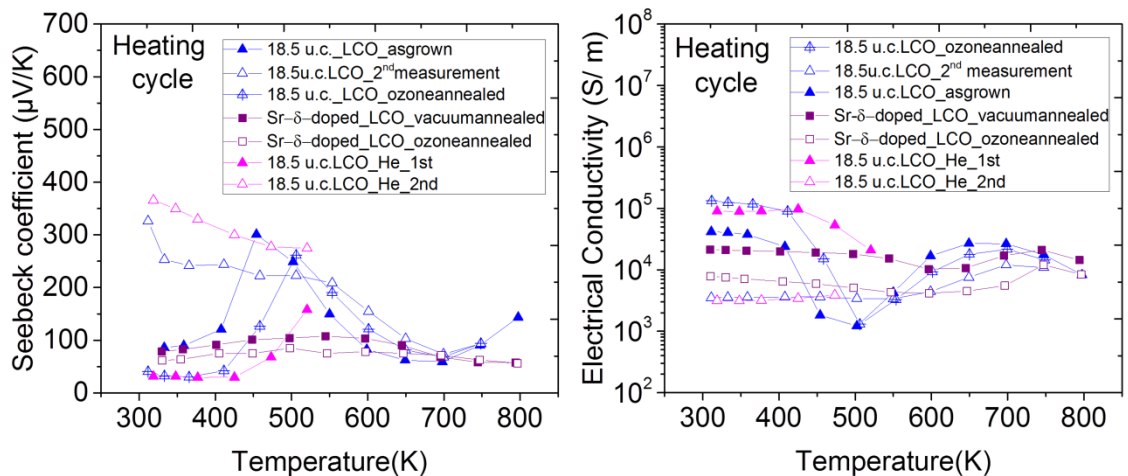


Figure 5.23 (a) Seebeck coefficient (b) Electrical conductivity during heating as a function of temperature.

Moreover, it was found that there is a perceptible intermixing (≈ 50 Å) at the interface which provides different doping levels in Sr- δ -doped LCO [191]. In

comparison to the single phase LCO films, Seebeck coefficient and electrical conductivity values (as well as the temperature dependence of transport properties) show that an overdoped (metallic) region at the interface dominates the system in Sr- δ -doped LCO.

5.4. Summary

In this chapter, the transport properties in La_2CuO_4 and LaNiO_3 single phase films as well as their bilayers and multilayers grown by MBE were investigated. The effect of the thickness of single phase films were studied and, in the LaNiO_3 single phase films, the metal-insulator transition behavior was observed for a film thickness below 2 unit cells. A thickness effect was not present in La_2CuO_4 single phase films. Additionally, the effect of oxygen incorporation and excorporation on the thermoelectric properties was explained in La_2CuO_4 system.

In multilayers, as the constituting layers get thinner, a sign change of the Seebeck coefficient was observed. This result is due to LNO becoming insulating for very small thicknesses while LCO becomes fully dominates the electrical transport properties. Nonetheless, cation intermixing effects at interface might also play a role.

By comparing the thermoelectric properties of the single phase LCO and Sr- δ -doped LCO film, it is concluded that the transport properties of Sr- δ -doped LCO are modified only if a metallic layer in proximity of the δ -doping plane is formed. In LNO-LCO hybrid structures, there is a critical thickness range for the intermixing: when the constituting layers get thinner, we observe an abrupt change in the Seebeck coefficient. In particular, the insulating phase (LCO) becomes more dominant than the metallic phase (LNO) and this which result as a consequence of the wider region of intermixing that behaves like blocking sides, as the constituting layers get thinner. It is expected that intermixing occurs only either as a consequence of layer roughness or due to thermal diffusion (i.e., time-temperature-dependent migration of the dopant into the bulk crystal) [192].

Quantitative AFM analyses indicates an increased layer roughness for thinner films which supports the formation of wider intermixing region as the films get thinner. To strengthen this hypothesis, detailed electron microscopy studies such as STEM, EELS etc. should be performed in the future.

In conclusion, although more detailed experiments (such as synchrotron measurements, soft X-ray analysis, and detailed electron microscopy studies) would be useful for a deeper understanding of the connection between local microstructure and

electrical properties, the present results provide helpful insights on the thermoelectric behavior at the interface of complex oxides.

6. CONCLUSIONS

This dissertation describes the investigation of microstructural design in particular through grain boundaries and interface engineering to tailor the thermoelectric properties of various ceramic materials at intermediate and high temperatures.

An alternative composite approach which is based on a “segregated network concept (SNC)” has been proposed to adjust the transport properties of composite materials. The microstructural design relies on coating microsized insulator granules (e.g. SiALON) with nanosized conductive powders. Scanning electron images proved that a conductive three dimensional network around the insulator granules was successfully obtained. The results of the electrical measurements revealed that in contrast to the conventional “particle reinforced composite” method, 140 times higher ZT parameter was achieved by using said alternative approach for SiALON-based ceramics. In order to establish whether the method is applicable also to other materials, different matrix materials have been employed.

The second part of this study deal with the decoration of the grain boundaries in SrTiO₃ by addition of a lanthanum precursor. The effect of the grain size (microcrystalline/nanocrystalline) as well as the effect of the sintering atmosphere (reducing/oxidizing) was also systematically investigated.

STEM and EELS investigations confirmed the SrTiO₃ grain boundaries to be decorated with lanthanum cations. While the presence of lanthanum was indeed beneficial in terms of thermal properties as it reduced the thermal conductivity of all decorated samples, no enhancement of the electrical conductivity was observed. As the electrical conductivity is the dominant property for improving the thermoelectric performance of a material, such an outcome obviously hindered the possibility of enhancing the overall ZT parameter of both microcrystalline and nanocrystalline SrTiO₃ samples under reducing as well as oxidizing conditions. In the specific case of La decorated SrTiO₃ samples, the reason of such a limited electrical transport was assigned to the presence of titanium depleted secondary phase at the grain boundaries.

Even though the results indicated no improved ZT parameter for these samples, this study showed that the grain boundary decoration is a viable approach for modifying thermal transport properties and Seebeck coefficient of polycrystalline ceramics.

Finally, cuprate-nickelate heterostructures grown by molecular beam epitaxy were studied. The influence of individual layer thicknesses and the effect of oxygen content were discussed in La_2CuO_4 - LaNiO_3 multilayers as well as bilayers and single phase films. The oxygen stoichiometry, which was discussed here in terms of defect chemistry of La_2CuO_4 , appears to play a key role in defining the final properties of the heterostructures. The findings (Fig. 6.1) obtained may be useful for future studies aiming at purposefully designing microstructures for improving and/or understanding the properties of thermoelectric materials.

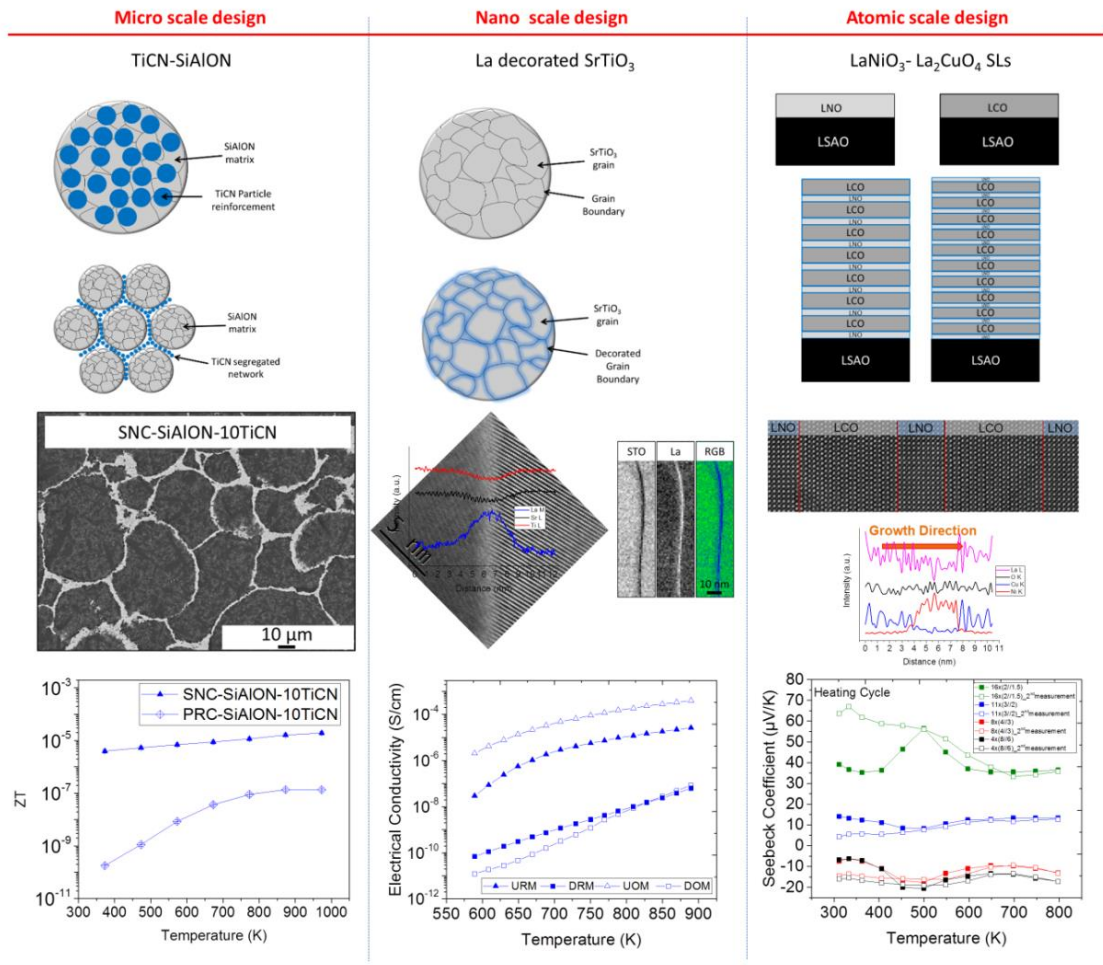


Figure 6.1 Schematic of the summary of the findings in the thesis.

7. REFERENCES

- [1] Turan, Servet, Microstructural Characterization of Silicon Nitride- Silicon Carbide Particulate Composites, University of Cambridge, 1995.
- [2] C. Newey, G. Weaver, eds., Materials Principles and Practice: Electronic Materials Manufacturing with Materials Structural Materials, Butterworth-Heinemann, Milton Keynes, England : London ; Boston, 1986.
- [3] D.A. Porter, K.E. Easterling, Phase Transformations in Metals and Alloys, 2 Sub edition, Chapman & Hall, London, 1992.
- [4] J.M. Howe, Interfaces in Materials: Atomic Structure, Thermodynamics and Kinetics of Solid-Vapor, Solid-Liquid and Solid-Solid Interfaces, 1 edition, Wiley-Interscience, New York, 1997.
- [5] J. Maier, Physical Chemistry of Ionic Materials: Ions and Electrons in Solids, 1 edition, Wiley, Chichester ; Hoboken, NJ, 2004.
- [6] A.P. Sutton, R.W. Balluffi, Interfaces in Crystalline Materials, Oxford University Press, Oxford, New York, 2006.
- [7] D. McLean, Grain boundaries in metals., Clarendon Press, Oxford, 1957. <http://books.google.com/books?id=fkhRAAAAMAAJ>.
- [8] P. Lejček, S. Hofmann, Thermodynamics and structural aspects of grain boundary segregation, Crit. Rev. Solid State Mater. Sci. 20 (1995) 1–85. doi:10.1080/10408439508243544.
- [9] J. Maier, Ionic conduction in space charge regions, Prog. Solid State Chem. 23 (1995) 171–263. doi:10.1016/0079-6786(95)00004-E.
- [10] H.L. Tuller, Ionic conduction in nano-crystalline materials, Solid State Ion. 131 (2000) 143–157. doi:10.1016/S0167-2738(00)00629-9.
- [11] J. Maier, Nanoionics: ion transport and electrochemical storage in confined systems, Nat. Mater. 4 (2005) 805–815. doi:10.1038/nmat1513.
- [12] J. Maier, Nanoionics: ionic charge carriers in small systems, Phys. Chem. Chem. Phys. 11 (2009) 3011–3022. doi:10.1039/B902586N.
- [13] P. Lupetin, Charge carrier defect chemistry of nanoscopic SrTiO₃, Die Ladungsträgerchemie von nanoskopischem SrTiO₃. (2012). doi:<http://dx.doi.org/10.18419/opus-6791>.
- [14] G. Gregori, R. Merkle, J. Maier, Ion conduction and redistribution at grain boundaries in oxide systems, Prog. Mater. Sci. 89 (2017) 252–305. doi:10.1016/j.pmatsci.2017.04.009.

- [15] A. Tschöpe, R. Birringer, Grain Size Dependence of Electrical Conductivity in Polycrystalline Cerium Oxide, *J. Electroceramics*. 7 (2001) 169–177. doi:10.1023/A:1014483028210.
- [16] S. Kim, J. Maier, On the Conductivity Mechanism of Nano-crystalline Ceria, *J. Electrochem. Soc.* 149 (2002) J73–J83. doi:10.1149/1.1507597.
- [17] P. Lupetin, G. Gregori, J. Maier, Mesoscopic Charge Carriers Chemistry in Nano-crystalline SrTiO₃, *Angew. Chem. Int. Ed.* 49 (2010) 10123–10126. doi:10.1002/anie.201003917.
- [18] N. Sata, K. Eberman, K. Eberl, J. Maier, Mesoscopic fast ion conduction in nanometre-scale planar heterostructures, *Nature*. 408 (2000) 946–949. doi:10.1038/35050047.
- [19] E. Gilardi, Interface effects in Y₂Zr₂O₇ thin films, 2016. <http://elib.uni-stuttgart.de/handle/11682/8773> (accessed June 11, 2017).
- [20] Altenkirch, Edmund, *Physikalische Zeitschrift*, (1909) 560–580.
- [21] Altenkirch, Edmund, *Physikalische Zeitschrift*, (1911) 920.
- [22] C. Goupil, *Continuum Theory and Modeling of Thermoelectric Elements*, John Wiley & Sons, 2015.
- [23] D.M. Rowe, *CRC Handbook of Thermoelectrics*, CRC Press, 1995.
- [24] M.S. Dresselhaus, G. Chen, M.Y. Tang, R.G. Yang, H. Lee, D.Z. Wang, Z.F. Ren, J.P. Fleurial, P. Gogna, *New Directions for Nanoscale Thermoelectric Materials Research*, *MRS Online Proc. Libr. Arch.* 886 (2005). doi:10.1557/PROC-0886-F01-01.
- [25] G.J. Snyder, E.S. Toberer, Complex thermoelectric materials, *Nat. Mater.* 7 (2008) 105–114. doi:10.1038/nmat2090.
- [26] M.G. Kanatzidis, Nanostructured Thermoelectrics: The New Paradigm?, *Chem. Mater.* 22 (2010) 648–659. doi:10.1021/cm902195j.
- [27] K.L. Bing, T. Li, H.H. Hng, F. Boey, T. Zhang, S. Li, *Waste Energy Harvesting: Mechanical and Thermal Energies*, Springer Science & Business Media, 2014.
- [28] P.M. Chaikin, G. Beni, Thermopower in the correlated hopping regime, *Phys. Rev. B*. 13 (1976) 647–651. doi:10.1103/PhysRevB.13.647.
- [29] I. Terasaki, High-temperature oxide thermoelectrics, *J. Appl. Phys.* 110 (2011) 053705. doi:10.1063/1.3626459.
- [30] M. Martín-González, O. Caballero-Calero, P. Díaz-Chao, *Nanoengineering thermoelectrics for 21st century: Energy harvesting and other trends in the field*,

Renew. Sustain. Energy Rev. 24 (2013) 288–305.
doi:10.1016/j.rser.2013.03.008.

- [31] T.M. Tritt, B. Zhang, N. Gothard, J. He, X. Ji, D. Thompson, J. Kolis, New Directions in Bulk Thermoelectric Materials Research: Synthesis of Nanoscale Precursors for “Bulk-Composite” Thermoelectric Materials, *MRS Online Proc. Libr. Arch.* 886 (2005). doi:10.1557/PROC-0886-F02-01.
- [32] K. Nielsch, J. Bachmann, J. Kimling, H. Böttner, Thermoelectric Nanostructures: From Physical Model Systems towards Nanograined Composites, *Adv. Energy Mater.* 1 (2011) 713–731. doi:10.1002/aenm.201100207.
- [33] V.A. Izhevskiy, L.A. Genova, J.C. Bressiani, F. Aldinger, Progress in SiAlON ceramics, *J. Eur. Ceram. Soc.* 20 (2000) 2275–2295. doi:10.1016/S0955-2219(00)00039-X.
- [34] S. Somiya, *Advanced Materials '93: Ceramics, Powders, Corrosion and Advanced Processing*, Newnes, 2012.
- [35] M. Mitomo, Y. Uemura, Electrical conductivity of α -sialon ceramics, *J. Mater. Sci.* 16 (1980) 552–554. doi:10.1007/BF00738655.
- [36] Z. Huang, T.-Y. Lü, H.-Q. Wang, J.-C. Zheng, Thermoelectric properties of the 3C, 2H, 4H, and 6H polytypes of the wide-band-gap semiconductors SiC, GaN, and ZnO, *AIP Adv.* 5 (2015) 097204. doi:10.1063/1.4931820.
- [37] F. Bechstedt, P. Käckell, A. Zywietz, K. Karch, B. Adolph, K. Tenelsen, J. Furthmüller, Polytypism and Properties of Silicon Carbide, *Phys. Status Solidi B.* 202 (1997) 35–62. doi:10.1002/1521-3951(199707)202:1<35::AID-PSSB35>3.0.CO;2-8.
- [38] A.R. Powell, L.B. Rowland, SiC materials-progress, status, and potential roadblocks, *Proc. IEEE.* 90 (2002) 942–955.
- [39] C.H. Pai, K. Koumoto, S. Takeda, H. Yanagida, Preparation of SiC hollow particles by gas-phase reaction and thermoelectric properties of sintered bodies, *Solid State Ion.* 32 (1989) 669–677. doi:10.1016/0167-2738(89)90343-3.
- [40] A.A. Adjaottor, E.I. Meletis, S. Logothetidis, I. Alexandrou, S. Kokkou, Effect of substrate bias on sputter-deposited TiCx, TiNy and TiCxNy thin films, *Surf. Coat. Technol.* 76 (1995) 142–148. doi:10.1016/0257-8972(95)02594-4.
- [41] G. Levi, W.D. Kaplan, M. Bamberger, Structure refinement of titanium carbonitride (TiCN), *Mater. Lett.* 35 (1998) 344–350. doi:10.1016/S0167-577X(97)00276-0.

- [42] M. Eizenberg, K. Littau, S. Ghanayem, A. Mak, Y. Maeda, M. Chang, A.K. Sinha, TiCN: A new chemical vapor deposited contact barrier metallization for submicron devices, *Appl. Phys. Lett.* 65 (1994) 2416–2418. doi:10.1063/1.112693.
- [43] T. Polcar, T. Kubart, R. Novák, L. Kopecký, P. Široký, Comparison of tribological behaviour of TiN, TiCN and CrN at elevated temperatures, *Surf. Coat. Technol.* 193 (2005) 192–199. doi:10.1016/j.surfcoat.2004.07.098.
- [44] E. Aslan, N. Camuşcu, B. Birgören, Design optimization of cutting parameters when turning hardened AISI 4140 steel (63 HRC) with Al₂O₃+TiCN mixed ceramic tool, *Mater. Des.* 28 (2007) 1618–1622. doi:10.1016/j.matdes.2006.02.006.
- [45] P.C. Jindal, A.T. Santhanam, U. Schleinkofer, A.F. Shuster, Performance of PVD TiN, TiCN, and TiAlN coated cemented carbide tools in turning, *Int. J. Refract. Met. Hard Mater.* 17 (1999) 163–170. doi:10.1016/S0263-4368(99)00008-6.
- [46] M. Herrmann, B. Balzer, C. Schubert, W. Hermel, Densification, microstructure and properties of Si₃N₄/Ti(C,N) composites, *J. Eur. Ceram. Soc.* 12 (1993) 287–296. doi:10.1016/0955-2219(93)90104-Y.
- [47] E. Ayas, A. Kara, Novel electrically conductive α - β SiAlON/TiCN composites, *J. Eur. Ceram. Soc.* 31 (2011) 903–911. doi:10.1016/j.jeurceramsoc.2010.11.026.
- [48] A. Çelik, E. Ayas, E. Halil, A. Kara, Oxidation behavior of electrically conductive α/β SiAlON composites with segregated network of TiCN, *J. Eur. Ceram. Soc.* 32 (2012) 1395–1403. doi:10.1016/j.jeurceramsoc.2011.03.028.
- [49] P. Kaya, G. Gregori, P. Yordanov, E. Ayas, H.-U. Habermeier, J. Maier, S. Turan, An alternative composite approach to tailor the thermoelectric performance in SiAlON and SiC, *J. Eur. Ceram. Soc.* 37 (2017) 3367–3373. doi:10.1016/j.jeurceramsoc.2017.04.004.
- [50] A.Y. Dobin, K.R. Nikolaev, I.N. Krivorotov, R.M. Wentzcovitch, E.D. Dahlberg, A.M. Goldman, Electronic and crystal structure of fully strained LaNiO_3 films, *Phys. Rev. B.* 68 (2003) 113408. doi:10.1103/PhysRevB.68.113408.
- [51] Š. Masys, V. Jonauskas, Elastic properties of rhombohedral, cubic, and monoclinic phases of LaNiO₃ by first principles calculations, *Comput. Mater. Sci.* 108 (2015) 153–159. doi:10.1016/j.commatsci.2015.06.034.

- [52] R.D. Sánchez, M.T. Causa, A. Caneiro, A. Butera, M. Vallet-Regí, M.J. Sayagués, J. González-Calbet, F. García-Sanz, J. Rivas, Metal-insulator transition in oxygen-deficient LaNiO_{3-x} perovskites, *Phys. Rev. B.* 54 (1996) 16574–16578. doi:10.1103/PhysRevB.54.16574.
- [53] L. Qiao, X. Bi, Direct observation of Ni^{3+} and Ni^{2+} in correlated $\text{LaNiO}_{3-\delta}$ films, *EPL Europhys. Lett.* 93 (2011) 57002. doi:10.1209/0295-5075/93/57002.
- [54] C.-L. Hsiao, W.-C. Chang, X. Qi, Sol–Gel Synthesis and Characterisation of Nanostructured LaNiO_{3-x} for Thermoelectric Applications, *Sci. Adv. Mater.* 6 (2014) 1406–1411. doi:10.1166/sam.2014.1827.
- [55] F.A. Kröger, H.J. Vink, Relations between the Concentrations of Imperfections in Crystalline Solids, *Solid State Phys.* 3 (1956) 307–435. doi:10.1016/S0081-1947(08)60135-6.
- [56] J. Maier, G. Pfundtner, Defect chemistry of the high- T_c superconductors, *Adv. Mater.* 3 (1991) 292–297. doi:10.1002/adma.19910030605.
- [57] E.J. Opila, H.L. Tuller, B.J. Wuensch, J. Maier, Oxygen Tracer Diffusion in $\text{La}_{2-x}\text{Sr}_x\text{CuO}_{4-y}$ Single Crystals, *J. Am. Ceram. Soc.* 76 (1993) 2363–2369. doi:10.1111/j.1151-2916.1993.tb07778.x.
- [58] C. Chaillout, S. Cheong, Z. Fisk, M. Lehmann, M. Marezio, B. Morosin, J. Schirber, THE CRYSTAL-STRUCTURE OF SUPERCONDUCTING LA_2CUO_4 .032 BY NEUTRON-DIFFRACTION, *Phys. C.* 158 (1989). doi:10.1016/0921-4534(89)90315-8.
- [59] D.J.L. Hong, D.M. Smyth, Defect chemistry of undoped La_2CuO_4 , *J. Solid State Chem.* 97 (1992) 427–433. doi:10.1016/0022-4596(92)90052-W.
- [60] V.V. Kharton, A.P. Viskup, A.V. Kovalevsky, E.N. Naumovich, F.M.B. Marques, Ionic transport in oxygen-hyperstoichiometric phases with K_2NiF_4 -type structure, *Solid State Ion.* 143 (2001) 337–353. doi:10.1016/S0167-2738(01)00876-1.
- [61] M.-Y. Su, E.A. Cooper, C.E. Elsbernd, T.O. Mason, High-Temperature Defect Structure of Lanthanum Cuprate, *J. Am. Ceram. Soc.* 73 (1990) 3453–3456. doi:10.1111/j.1151-2916.1990.tb06474.x.
- [62] M.K. Wu, J.R. Ashburn, C.J. Torng, P.H. Hor, R.L. Meng, L. Gao, Z.J. Huang, Y.Q. Wang, C.W. Chu, Superconductivity at 93 K in a new mixed-phase Y-Ba-Cu-O compound system at ambient pressure, *Phys. Rev. Lett.* 58 (1987) 908–910. doi:10.1103/PhysRevLett.58.908.

- [63] J. Maier, On the Conductivity of Polycrystalline Materials, *Berichte Bunsenges. Für Phys. Chem.* 90 (1986) 26–33. doi:10.1002/bbpc.19860900105.
- [64] M.J. Verkerk, B.J. Middelhuis, A.J. Burggraaf, Effect of grain boundaries on the conductivity of high-purity ZrO₂---Y₂O₃ ceramics, *Solid State Ion.* 6 (1982) 159–170.
- [65] T. van Dijk, A.J. Burggraaf, Grain boundary effects on ionic conductivity in ceramic GdxZr1-xO2-(x/2) solid solutions, *Phys. Status Solidi Appl. Res.* 63 (1981) 229–240.
- [66] J. Fleig, J. Maier, The impedance of ceramics with highly resistive grain boundaries: validity and limits of the brick layer model, *J. Eur. Ceram. Soc.* 19 (1999) 693–696. doi:10.1016/S0955-2219(98)00298-2.
- [67] X. Guo, J. Maier, Grain Boundary Blocking Effect in Zirconia: A Schottky Barrier Analysis, *J. Electrochem. Soc.* 148 (2001) E121–E126. doi:10.1149/1.1348267.
- [68] S. Kim, H.J. Avila-Paredes, S. Wang, C.-T. Chen, R.A.D. Souza, M. Martin, Z.A. Munir, On the conduction pathway for protons in nano-crystalline yttria-stabilized zirconia, *Phys. Chem. Chem. Phys.* 11 (2009) 3035–3038. doi:10.1039/B901623F.
- [69] X. Guo, R. Waser, Electrical properties of the grain boundaries of oxygen ion conductors: Acceptor-doped zirconia and ceria, *Prog. Mater. Sci.* 51 (2006) 151–210. doi:10.1016/j.pmatsci.2005.07.001.
- [70] N. Hirosaki, A. Okada, Gas-Pressure Sintering Map for Silicon Nitride-Based Materials, in: M. Koizumi (Ed.), *Hot Isostatic Press. Theory Appl.*, Springer Netherlands, 1992: pp. 143–148. doi:10.1007/978-94-011-2900-8_23.
- [71] R. Oberacker, G. Grathwohl, High Temperature Resistant Silicon-Nitride Ceramics by Optimized Two-Step Gas Pressure Sintering, in: D.M.J. Hoffmann, P.D. h c mult G. Petzow (Eds.), *Tailoring Mech. Prop. Si₃N₄ Ceram.*, Springer Netherlands, 1994: pp. 43–55. doi:10.1007/978-94-011-0992-5_3.
- [72] R. Orrù, R. Licheri, A.M. Locci, A. Cincotti, G. Cao, Consolidation/synthesis of materials by electric current activated/assisted sintering, *Mater. Sci. Eng. R Rep.* 63 (2009) 127–287. doi:10.1016/j.mser.2008.09.003.
- [73] D.V. Quach, J.R. Groza, A. Zavaliangos, U. Anselmi-Tamburini, 10 - Fundamentals and applications of field/current assisted sintering, in: Z.Z. Fang (Ed.), *Sinter. Adv. Mater.*, Woodhead Publishing, 2010: p. 249–275e. doi:10.1533/9781845699949.2.249.

- [74] H.Y. Hwang, Y. Iwasa, M. Kawasaki, B. Keimer, N. Nagaosa, Y. Tokura, Emergent phenomena at oxide interfaces, *Nat. Mater.* 11 (2012) 103–113. doi:10.1038/nmat3223.
- [75] A. Gozar, G. Logvenov, L.F. Kourkoutis, A.T. Bollinger, L.A. Giannuzzi, D.A. Muller, I. Bozovic, High-temperature interface superconductivity between metallic and insulating copper oxides, *Nature.* 455 (2008) 782–785. doi:10.1038/nature07293.
- [76] D.G. Schlom, Molecular Beam Epitaxial Growth of Cuprate Superconductors and Related Phases, PhD Thesis. (1990). <http://adsabs.harvard.edu/abs/1990PhDT.....246S> (accessed May 17, 2017).
- [77] D.G. Schlom, J.N. Eckstein, I. Bozovic, Z. Chen, A.F. Marshall, K.E. von Dessionneck, J. Harris James S., Molecular beam epitaxy: a path to novel high Tc superconductors?, in: 1990: pp. 234–247. doi:10.1117/12.20831.
- [78] F. Baiutti, Heterogeneous doping and superconductivity in La₂CuO₄-based heterostructures, *Heterogene Dotierung und Supraleitfähigkeit in La₂CuO₄-basierten Schichtstrukturen.* (2015). doi:<http://dx.doi.org/10.18419/opus-6884>.
- [79] J N Eckstein, and I. Bozovic, High-Temperature Superconducting Multilayers and Heterostructures Grown by Atomic Layer-By-Layer Molecular Beam Epitaxy, *Annu. Rev. Mater. Sci.* 25 (1995) 679–709. doi:10.1146/annurev.ms.25.080195.003335.
- [80] F. Baiutti, G. Christiani, G. Logvenov, Towards precise defect control in layered oxide structures by using oxide molecular beam epitaxy, *Beilstein J. Nanotechnol.* 5 (2014) 596–602. doi:10.3762/bjnano.5.70.
- [81] M.G. Lagally, D.E. Savage, Quantitative Electron Diffraction from Thin Films, *MRS Bull.* 18 (1993) 24–31. doi:10.1557/S0883769400043414.
- [82] J.B. Nelson, D.P. Riley, An experimental investigation of extrapolation methods in the derivation of accurate unit-cell dimensions of crystals, *Proc. Phys. Soc.* 57 (1945) 160. doi:10.1088/0959-5309/57/3/302.
- [83] E.E. Fullerton, I.K. Schuller, H. Vanderstraeten, Y. Bruynseraede, Structural refinement of superlattices from x-ray diffraction, *Phys. Rev. B.* 45 (1992) 9292–9310. doi:10.1103/PhysRevB.45.9292.
- [84] L.G. Parratt, Surface Studies of Solids by Total Reflection of X-Rays, *Phys. Rev.* 95 (1954) 359–369. doi:10.1103/PhysRev.95.359.
- [85] G. Binnig, C.F. Quate, C. Gerber, Atomic Force Microscope, *Phys. Rev. Lett.* 56 (1986) 930–933. doi:10.1103/PhysRevLett.56.930.

- [86] J.E. Bauerle, Study of solid electrolyte polarization by a complex admittance method, *J. Phys. Chem. Solids*. 30 (1969) 2657–2670. doi:10.1016/0022-3697(69)90039-0.
- [87] S. Heinze, Thermoelectric properties of oxide heterostructures, *Thermoelektrische Eigenschaften von Oxidheterostrukturen*. (2013). doi:http://dx.doi.org/10.18419/opus-6836.
- [88] Mackey, J., Dynys, F., Sehirlioglu, A., Uncertainty analysis for common Seebeck and electrical resistivity measurement systems, *Rev. Sci. Instrum.* 85 (2014) 085119. doi:10.1063/1.4893652.
- [89] H. Wang, S. Bai, L. Chen, A. Cuenat, G. Joshi, H. Kleinke, J. König, H.W. Lee, J. Martin, M.-W. Oh, W.D. Porter, Z. Ren, J. Salvador, J. Sharp, P. Taylor, A.J. Thompson, Y.C. Tseng, International Round-Robin Study of the Thermoelectric Transport Properties of an n-Type Half-Heusler Compound from 300 K to 773 K, *J. Electron. Mater.* 44 (2015) 4482–4491. doi:10.1007/s11664-015-4006-z.
- [90] W.J. Parker, R.J. Jenkins, C.P. Butler, G.L. Abbott, Flash Method of Determining Thermal Diffusivity, Heat Capacity, and Thermal Conductivity, *J. Appl. Phys.* 32 (1961) 1679–1684. doi:10.1063/1.1728417.
- [91] M.J. O'Neill, Measurement of Specific Heat Functions by Differential Scanning Calorimetry., *Anal. Chem.* 38 (1966) 1331–1336. doi:10.1021/ac60242a011.
- [92] L.E. Bell, Cooling, Heating, Generating Power, and Recovering Waste Heat with Thermoelectric Systems, *Science*. 321 (2008) 1457–1461. doi:10.1126/science.1158899.
- [93] G. Chen, M.S. Dresselhaus, G. Dresselhaus, J.-P. Fleurial, T. Caillat, Recent developments in thermoelectric materials, *Int. Mater. Rev.* 48 (2003) 45–66. doi:10.1179/095066003225010182.
- [94] J.-F. Li, S. Tanaka, T. Umeki, S. Sugimoto, M. Esashi, R. Watanabe, Microfabrication of thermoelectric materials by silicon molding process, *Sens. Actuators Phys.* 108 (2003) 97–102. doi:10.1016/S0924-4247(03)00369-8.
- [95] A. Ohtomo, H.Y. Hwang, A high-mobility electron gas at the LaAlO₃/SrTiO₃ heterointerface, *Nature*. 427 (2004) 423–426. doi:10.1038/nature02308.
- [96] E.B. Lavik, I. Kosacki, H.L. Tuller, Y.-M. Chiang, J.Y. Ying, Nonstoichiometry and Electrical Conductivity of Nano-crystalline CeO_{2-x}, *J. Electroceramics*. 1 (2016) 7–14. doi:10.1023/A:1009934829870.
- [97] G. Schierning, R. Chavez, R. Schmechel, B. Balke, G. Rogl, P. Rogl, Concepts for medium-high to high temperature thermoelectric heat-to-electricity

- conversion: a review of selected materials and basic considerations of module design, *Transl. Mater. Res.* 2 (2015) 025001. doi:10.1088/2053-1613/2/2/025001.
- [98] D.K. Aswal, R. Basu, A. Singh, Key issues in development of thermoelectric power generators: High figure-of-merit materials and their highly conducting interfaces with metallic interconnects, *Energy Convers. Manag.* 114 (2016) 50–67. doi:10.1016/j.enconman.2016.01.065.
- [99] Ohtaki, M, Oxide Thermoelectric Materials for Heat-to-Electricity Direct Energy Conversion, Kyushu Univ. Glob. COE Program Nov. Carbon Resour. Sci. Newsl. (2010).
- [100] H. Kitagawa, N. Kado, Y. Noda, Preparation of N-type Silicon Carbide-Based Thermoelectric Materials by Spark Plasma Sintering, *Mater. Trans.* 43 (2002) 3239–3241. doi:10.2320/matertrans.43.3239.
- [101] K. Koumoto, M. Shimohigoshi, S. Takeda, H. Yanagida, Thermoelectric energy conversion by porous SiC ceramics, *J. Mater. Sci. Lett.* 6 (1987) 1453–1455. doi:10.1007/BF01689320.
- [102] V.A. Izhevskiy, L.A. Genova, J.C. Bressiani, F. Aldinger, Progress in SiAlON ceramics, *J. Eur. Ceram. Soc.* 20 (2000) 2275–2295. doi:10.1016/S0955-2219(00)00039-X.
- [103] H. Yurdakul, S. Turan, E. Ayas, O. Tunckan, A. Kara, Analytical transmission electron microscopy observations on the stability of TiCN in electrically conductive α - β SiAlON/TiCN composites, *J. Eur. Ceram. Soc.* 34 (2014) 2905–2911. doi:10.1016/j.jeurceramsoc.2014.03.024.
- [104] G. Petzow, M. Herrmann, Silicon Nitride Ceramics, in: P.D.M. Jansen (Ed.), *High Perform. Non-Oxide Ceram. II*, Springer Berlin Heidelberg, 2002: pp. 47–167. doi:10.1007/3-540-45623-6_2.
- [105] X.N. Gong, J.F. Sun, K. Quan, Y.Q. Meng, Synthesis and Application of Titanium Carbonitride, *Adv. Mater. Res.* 634–638 (2013) 2373–2377. doi:10.4028/www.scientific.net/AMR.634-638.2373.
- [106] D. Jiang, J. Vleugels, O. Van der Biest, W.D. Liu, R. Verheyen, B. Lauwers, Electrically Conductive and Wear Resistant Si₃N₄-Based Composites with TiC_{0.5}N_{0.5} Particles for Electrical Discharge Machining, *Mater. Sci. Forum.* 492–493 (2005) 27–32. doi:10.4028/www.scientific.net/MSF.492-493.27.

- [107] A.H. Jones, C. Trueman, R.S. Dobedoe, J. Huddleston, M.H. Lewis, Production and EDM of Si₃N₄-TiB₂ ceramic composites, *Br. Ceram. Trans.* 100 (2001) 49–54. doi:10.1179/096797801681198.
- [108] J. Bouchet, C. Carrot, J. Guillet, G. Boiteux, G. Seytre, M. Pineri, Conductive composites of UHMWPE and ceramics based on the segregated network concept, *Polym. Eng. Sci.* 40 (2000) 36–45. doi:10.1002/pen.11137.
- [109] D.J. Bergman, O. Levy, Thermoelectric properties of a composite medium, *J. Appl. Phys.* 70 (1991) 6821–6833. doi:10.1063/1.349830.
- [110] D.J. Bergman, L.G. Fel, Enhancement of thermoelectric power factor in composite thermoelectrics, *J. Appl. Phys.* 85 (1999) 8205–8216. doi:10.1063/1.370660.
- [111] J.P. Heremans, C.M. Jaworski, Experimental study of the thermoelectric power factor enhancement in composites, *Appl. Phys. Lett.* 93 (2008) 122107. doi:10.1063/1.2988895.
- [112] T. Mori, T. Hara, Hybrid effect to possibly overcome the trade-off between Seebeck coefficient and electrical conductivity, *Scr. Mater.* 111 (2016) 44–48. doi:10.1016/j.scriptamat.2015.09.010.
- [113] Y. Ohba, T. Shimosaki, H. Era, Thermoelectric Properties of Silicon Carbide Sintered with Addition of Boron Carbide, Carbon, and Alumina, *Mater. Trans.* 49 (2008) 1235–1241. doi:10.2320/matertrans.MRA2007232.
- [114] N.W. Ashcroft, N.D. Mermin, *Solid state physics*, Holt, Rinehart and Winston, New York, 1976.
- [115] M. Bouchacourt, F. Thevenot, The correlation between the thermoelectric properties and stoichiometry in the boron carbide phase B₄C-B_{10.5}C, *J. Mater. Sci.* 20 (n.d.) 1237–1247. doi:10.1007/BF01026319.
- [116] J.W. Fergus, Oxide materials for high temperature thermoelectric energy conversion, *J. Eur. Ceram. Soc.* 32 (2012) 525–540. doi:10.1016/j.jeurceramsoc.2011.10.007.
- [117] K. Koumoto, Y. Wang, R. Zhang, A. Kosuga, R. Funahashi, *Oxide Thermoelectric Materials: A Nanostructuring Approach*, (2010).
- [118] G. Ren, J. Lan, C. Zeng, Y. Liu, B. Zhan, S. Butt, Y.-H. Lin, C.-W. Nan, High Performance Oxides-Based Thermoelectric Materials, *JOM.* 67 (2015) 211–221. doi:10.1007/s11837-014-1218-2.

- [119] W. Liu, Q. Jie, H.S. Kim, Z. Ren, Current progress and future challenges in thermoelectric power generation: From materials to devices, *Acta Mater.* 87 (2015) 357–376. doi:10.1016/j.actamat.2014.12.042.
- [120] L. Bocher, M.H. Aguirre, D. Logvinovich, A. Shkabko, R. Robert, M. Trottmann, A. Weidenkaff, $\text{CaMn}_{1-x}\text{Nb}_x\text{O}_3$ ($x \leq 0.08$) Perovskite-Type Phases As Promising New High-Temperature n-Type Thermoelectric Materials, *Inorg. Chem.* 47 (2008) 8077–8085. doi:10.1021/ic800463s.
- [121] M. Molinari, D. A. Tompsett, S. C. Parker, F. Azough, R. Freer, Structural, electronic and thermoelectric behaviour of CaMnO_3 and $\text{CaMnO}_{3-\delta}$, *J. Mater. Chem. A.* 2 (2014) 14109–14117. doi:10.1039/C4TA01514B.
- [122] D. Srivastava, F. Azough, R. Freer, E. Combe, R. Funahashi, D.M. Kepaptsoglou, Q.M. Ramasse, M. Molinari, S.R. Yeandel, J.D. Baran, S.C. Parker, Crystal structure and thermoelectric properties of Sr–Mo substituted CaMnO_3 : a combined experimental and computational study, *J. Mater. Chem. C.* 3 (2015) 12245–12259. doi:10.1039/C5TC02318A.
- [123] H. Ohta, K. Sugiura, K. Koumoto, Recent Progress in Oxide Thermoelectric Materials: p-Type $\text{Ca}_3\text{Co}_4\text{O}_9$ and n-Type SrTiO_3 –, *Inorg. Chem.* 47 (2008) 8429–8436. doi:10.1021/ic800644x.
- [124] H. Ohta, S. Kim, Y. Mune, T. Mizoguchi, K. Nomura, S. Ohta, T. Nomura, Y. Nakanishi, Y. Ikuhara, M. Hirano, H. Hosono, K. Koumoto, Giant thermoelectric Seebeck coefficient of a two-dimensional electron gas in SrTiO_3 , *Nat. Mater.* 6 (2007) 129–134. doi:10.1038/nmat1821.
- [125] T. Okuda, K. Nakanishi, S. Miyasaka, Y. Tokura, Large thermoelectric response of metallic perovskites: $\text{Sr}_{1-x}\text{La}_x\text{TiO}_3$ for $0 < x < 0.1$, *Phys. Rev. B.* 63 (2001) 113104. doi:10.1103/PhysRevB.63.113104.
- [126] H. Muta, K. Kurosaki, S. Yamanaka, Thermoelectric properties of reduced and La-doped single-crystalline SrTiO_3 , *J. Alloys Compd.* 392 (2005) 306–309. doi:10.1016/j.jallcom.2004.09.005.
- [127] S. Ohta, H. Ohta, K. Koumoto, Grain Size Dependence of Thermoelectric Performance of Nb-Doped SrTiO_3 Polycrystals, *J. Ceram. Soc. Jpn.* 114 (2006) 102–105. doi:10.2109/jcersj.114.102.
- [128] K. Kato, M. Yamamoto, S. Ohta, H. Muta, K. Kurosaki, S. Yamanaka, H. Iwasaki, H. Ohta, K. Koumoto, The effect of Eu substitution on thermoelectric properties of $\text{SrTi}_{0.8}\text{Nb}_{0.2}\text{O}_3$, *J. Appl. Phys.* 102 (2007) 116107. doi:10.1063/1.2822142.

- [129] J. Liu, C.L. Wang, W.B. Su, H.C. Wang, P. Zheng, J.C. Li, J.L. Zhang, L.M. Mei, Enhancement of thermoelectric efficiency in oxygen-deficient $\text{Sr}_{1-x}\text{La}_x\text{TiO}_{3-\delta}$ ceramics, *Appl. Phys. Lett.* 95 (2009) 162110. doi:10.1063/1.3254219.
- [130] W. Gong, H. Yun, Y.B. Ning, J.E. Greedan, W.R. Datars, C.V. Stager, Oxygen-deficient SrTiO_{3-x} , $x = 0.28, 0.17,$ and 0.08 . Crystal growth, crystal structure, magnetic, and transport properties, *J. Solid State Chem.* 90 (1991) 320–330. doi:10.1016/0022-4596(91)90149-C.
- [131] G. Gregori, S. Heinze, P. Lupetin, H.-U. Habermeier, J. Maier, Seebeck coefficient and electrical conductivity of mesoscopic nano-crystalline SrTiO_3 , *J. Mater. Sci.* 48 (2012) 2790–2796. doi:10.1007/s10853-012-6894-0.
- [132] W.S. Choi, H.K. Yoo, H. Ohta, Polaron Transport and Thermoelectric Behavior in La-Doped SrTiO_3 Thin Films with Elemental Vacancies, *Adv. Funct. Mater.* 25 (2015) 799–804. doi:10.1002/adfm.201403023.
- [133] S.R. Popuri, A.J.M. Scott, R.A. Downie, M.A. Hall, E. Suard, R. Decourt, M. Pollet, J.-W.G. Bos, Glass-like thermal conductivity in SrTiO_3 thermoelectrics induced by A-site vacancies, *RSC Adv.* 4 (2014) 33720–33723. doi:10.1039/C4RA06871H.
- [134] Z. Lu, H. Zhang, W. Lei, D.C. Sinclair, I.M. Reaney, High-Figure-of-Merit Thermoelectric La-Doped A-Site-Deficient SrTiO_3 Ceramics, *Chem. Mater.* 28 (2016) 925–935. doi:10.1021/acs.chemmater.5b04616.
- [135] D. Neagu, J.T.S. Irvine, Enhancing Electronic Conductivity in Strontium Titanates through Correlated A and B-Site Doping, *Chem. Mater.* 23 (2011) 1607–1617. doi:10.1021/cm103489r.
- [136] K. Park, J. Sung Son, S. Ill Woo, K. Shin, M.-W. Oh, S.-D. Park, T. Hyeon, Colloidal synthesis and thermoelectric properties of La-doped SrTiO_3 nanoparticles, *J. Mater. Chem. A.* 2 (2014) 4217–4224. doi:10.1039/C3TA14699E.
- [137] A. Shkabko, M.H. Aguirre, I. Marozau, M. Doebeli, M. Mallepell, T. Lippert, A. Weidenkaff, Characterization and properties of microwave plasma-treated SrTiO_3 , *Mater. Chem. Phys.* 115 (2009) 86–92. doi:10.1016/j.matchemphys.2008.11.024.
- [138] A.V. Kovalevsky, A.A. Yaremchenko, S. Populoh, P. Thiel, D.P. Fagg, A. Weidenkaff, J.R. Frade, Towards a high thermoelectric performance in rare-earth substituted SrTiO_3 : effects provided by strongly-reducing sintering

- conditions, *Phys. Chem. Chem. Phys.* 16 (2014) 26946–26954. doi:10.1039/C4CP04127E.
- [139] T. Teranishi, Y. Ishikawa, H. Hayashi, A. Kishimoto, M. Katayama, Y. Inada, Thermoelectric Efficiency of Reduced SrTiO₃ Ceramics Modified with La and Nb, *J. Am. Ceram. Soc.* 96 (2013) 2852–2856. doi:10.1111/jace.12379.
- [140] H.C. Wang, C.L. Wang, W.B. Su, J. Liu, H. Peng, J.L. Zhang, M.L. Zhao, J.C. Li, N. Yin, L.M. Mei, Substitution effect on the thermoelectric properties of reduced Nb-doped Sr_{0.95}La_{0.05}TiO₃ ceramics, *J. Alloys Compd.* 486 (2009) 693–696. doi:10.1016/j.jallcom.2009.07.041.
- [141] A.M. Dehkordi, S. Bhattacharya, J. He, H.N. Alshareef, T.M. Tritt, Significant enhancement in thermoelectric properties of polycrystalline Pr-doped SrTiO_{3-δ} ceramics originating from nonuniform distribution of Pr dopants, *Appl. Phys. Lett.* 104 (2014) 193902. doi:10.1063/1.4875925.
- [142] C. Chen, T. Zhang, R. Donelson, T.T. Tan, S. Li, Effects of yttrium substitution and oxygen deficiency on the crystal phase, microstructure, and thermoelectric properties of Sr_{1-1.5x}Y_xTiO_{3-δ} (0 ≤ x ≤ 0.15), *J. Alloys Compd.* 629 (2015) 49–54. doi:10.1016/j.jallcom.2014.12.125.
- [143] A.V. Kovalevsky, S. Populoh, S.G. Patrício, P. Thiel, M.C. Ferro, D.P. Fagg, J.R. Frade, A. Weidenkaff, Design of SrTiO₃-Based Thermoelectrics by Tungsten Substitution, *J. Phys. Chem. C.* 119 (2015) 4466–4478. doi:10.1021/jp510743h.
- [144] A.V. Kovalevsky, A.A. Yaremchenko, S. Populoh, A. Weidenkaff, J.R. Frade, Effect of A-Site Cation Deficiency on the Thermoelectric Performance of Donor-Substituted Strontium Titanate, *J. Phys. Chem. C.* 118 (2014) 4596–4606. doi:10.1021/jp409872e.
- [145] A.A. Yaremchenko, S. Populoh, S.G. Patrício, J. Macías, P. Thiel, D.P. Fagg, A. Weidenkaff, J.R. Frade, A.V. Kovalevsky, Boosting Thermoelectric Performance by Controlled Defect Chemistry Engineering in Ta-Substituted Strontium Titanate, *Chem. Mater.* 27 (2015) 4995–5006. doi:10.1021/acs.chemmater.5b01389.
- [146] M. Backhaus-Ricoult, J.R. Rustad, D. Vargheese, I. Dutta, K. Work, Levers for Thermoelectric Properties in Titania-Based Ceramics, *J. Electron. Mater.* 41 (2012) 1636–1647. doi:10.1007/s11664-012-2019-4.
- [147] D. Srivastava, C. Norman, F. Azough, M.C. Schäfer, E. Guilmeau, D. Kepaptsoglou, Q.M. Ramasse, G. Nicotra, R. Freer, Tuning the thermoelectric

- properties of A-site deficient SrTiO₃ ceramics by vacancies and carrier concentration, *Phys. Chem. Chem. Phys.* 18 (2016) 26475–26486. doi:10.1039/C6CP05523K.
- [148] A.I. Abutaha, S.R.S. Kumar, K. Li, A.M. Dehkordi, T.M. Tritt, H.N. Alshareef, Enhanced Thermoelectric Figure-of-Merit in Thermally Robust, Nanostructured Superlattices Based on SrTiO₃, *Chem. Mater.* 27 (2015) 2165–2171. doi:10.1021/acs.chemmater.5b00144.
- [149] M. Leonhardt, J. Jamnik, J. Maier, In Situ Monitoring and Quantitative Analysis of Oxygen Diffusion Through Schottky-Barriers in SrTiO₃ Bicrystals, *Electrochem. Solid-State Lett.* 2 (1999) 333–335. doi:10.1149/1.1390827.
- [150] T. Watanabe, S. Tsunekawa, X. Zhao, L. Zuo, The Coming of Grain Boundary Engineering in the 21st Century, in: *Microstruct. Texture Steels*, Springer, London, 2009: pp. 43–82. doi:10.1007/978-1-84882-454-6_4.
- [151] X. Guo, J. Fleig, J. Maier, Separation of Electronic and Ionic Contributions to the Grain Boundary Conductivity in Acceptor-Doped SrTiO₃, *J. Electrochem. Soc.* 148 (2001) J50–J53. doi:10.1149/1.1389344.
- [152] R. Moos, K.H. Hardtl, Defect Chemistry of Donor-Doped and Undoped Strontium Titanate Ceramics between 1000° and 1400°C, *J. Am. Ceram. Soc.* 80 (1997) 2549–2562. doi:10.1111/j.1151-2916.1997.tb03157.x.
- [153] G.H. Jonker, Some aspects of semiconducting barium titanate, *Solid-State Electron.* 7 (1964) 895–903. doi:10.1016/0038-1101(64)90068-1.
- [154] R. Meyer, R. Waser, Resistive donor-doped SrTiO₃ sensors: I, basic model for a fast sensor response, *Sens. Actuators B Chem.* 101 (2004) 335–345. doi:10.1016/j.snb.2004.04.004.
- [155] R. Meyer, R. Waser, J. Helmbold, G. Borchardt, Observation of Vacancy Defect Migration in the Cation Sublattice of Complex Oxides by ^{18}O Tracer Experiments, *Phys. Rev. Lett.* 90 (2003) 105901. doi:10.1103/PhysRevLett.90.105901.
- [156] Y.-M. Chiang, T. Takagi, Grain-Boundary Chemistry of Barium Titanate and Strontium Titanate: I, High-Temperature Equilibrium Space Charge, *J. Am. Ceram. Soc.* 73 (1990) 3278–3285. doi:10.1111/j.1151-2916.1990.tb06450.x.
- [157] Weissmayer, Michael, *Influencing the Ionic Space Charge Potential in Grain Boundaries of Oxide Ceramics*, University of Stuttgart, 2017.

- [158] I. Denk, J. Claus, J. Maier, Electrochemical Investigations of SrTiO₃ Boundaries, *J. Electrochem. Soc.* 144 (1997) 3526–3536. doi:10.1149/1.1838044.
- [159] I. Denk, W. Münch, J. Maier, Partial Conductivities in SrTiO₃: Bulk Polarization Experiments, Oxygen Concentration Cell Measurements, and Defect-Chemical Modeling, *J. Am. Ceram. Soc.* 78 (1995) 3265–3272. doi:10.1111/j.1151-2916.1995.tb07963.x.
- [160] R. Waser, Electronic properties of grain boundaries in SrTiO₃ and BaTiO₃ ceramics, *Solid State Ion.* 75 (1995) 89–99. doi:10.1016/0167-2738(94)00152-1.
- [161] J. Fleig, J. Maier, Finite element calculations of impedance effects at point contacts, *Electrochimica Acta.* 41 (1996) 1003–1009. doi:10.1016/0013-4686(95)00431-9.
- [162] J. Fleig, P. Pham, P. Sztulzaft, J. Maier, Inhomogeneous current distributions at grain boundaries and electrodes and their impact on the impedance, *Solid State Ion.* 113 (1998) 739–747. doi:10.1016/S0167-2738(98)00400-7.
- [163] J. Fleig, J. Maier, Finite-Element Calculations on the Impedance of Electroceramics with Highly Resistive Grain Boundaries: I, Laterally Inhomogeneous Grain Boundaries, *J. Am. Ceram. Soc.* 82 (1999) 3485–3493. doi:10.1111/j.1151-2916.1999.tb02270.x.
- [164] P. Balaya, J. Jamnik, J. Fleig, J. Maier, Mesoscopic electrical conduction in nano-crystalline SrTiO₃, *Appl. Phys. Lett.* 88 (2006) 062109. doi:10.1063/1.2171798.
- [165] L. Wang, Y. Sakka, Y. Shao, G.A. Botton, T. Kolodiaznyi, Coexistence of A- and B-Site Vacancy Compensation in La-Doped Sr_{1-x}BaxTiO₃, *J. Am. Ceram. Soc.* 93 (2010) 2903–2908. doi:10.1111/j.1551-2916.2010.03810.x.
- [166] J. He, Y. Liu, R. Funahashi, Oxide thermoelectrics: The challenges, progress, and outlook, *J. Mater. Res.* 26 (2011) 1762–1772. doi:10.1557/jmr.2011.108.
- [167] I. Terasaki, Y. Sasago, K. Uchinokura, Large thermoelectric power in NaCo₂O₄ single crystals, *Phys. Rev. B.* 56 (1997) R12685–R12687. doi:10.1103/PhysRevB.56.R12685.
- [168] H. Ohta, A. Mizutani, K. Sugiura, M. Hirano, H. Hosono, K. Koumoto, Surface Modification of Glass Substrates for Oxide Heteroepitaxy: Pasteable Three-Dimensionally Oriented Layered Oxide Thin Films, *Adv. Mater.* 18 (2006) 1649–1652. doi:10.1002/adma.200502606.

- [169] K. Sugiura, H. Ohta, K. Nomura, M. Hirano, H. Hosono, K. Koumoto, High electrical conductivity of layered cobalt oxide $\text{Ca}_3\text{Co}_4\text{O}_9$ epitaxial films grown by topotactic ion-exchange method, *Appl. Phys. Lett.* 89 (2006) 032111. doi:10.1063/1.2234277.
- [170] K. Sugiura, H. Ohta, K. Koumoto, Thermoelectric Performance of Epitaxial Thin Films of Layered Cobalt Oxides Grown by Reactive Solid-Phase Epitaxy with Topotactic Ion-Exchange Methods, *Int. J. Appl. Ceram. Technol.* 4 (2007) 308–317. doi:10.1111/j.1744-7402.2007.02145.x.
- [171] S. Ohta, T. Nomura, H. Ohta, M. Hirano, H. Hosono, K. Koumoto, Large thermoelectric performance of heavily Nb-doped SrTiO_3 epitaxial film at high temperature, *Appl. Phys. Lett.* 87 (2005) 092108. doi:10.1063/1.2035889.
- [172] D. Kurita, S. Ohta, K. Sugiura, H. Ohta, K. Koumoto, Carrier generation and transport properties of heavily Nb-doped anatase TiO_2 epitaxial films at high temperatures, *J. Appl. Phys.* 100 (2006) 096105. doi:10.1063/1.2362990.
- [173] K.H. Lee, A. Ishizaki, S.W. Kim, H. Ohta, K. Koumoto, Preparation and thermoelectric properties of heavily Nb-doped $\text{SrO}(\text{SrTiO}_3)_1$ epitaxial films, *J. Appl. Phys.* 102 (2007) 033702. doi:10.1063/1.2764221.
- [174] P. Mele, Nanostructured Thin Films of Thermoelectric Oxides, in: P. Mele, T. Endo, S. Arisawa, C. Li, T. Tsuchiya (Eds.), *Oxide Thin Films Multilayers Nanocomposites*, Springer International Publishing, 2015: pp. 123–155. doi:10.1007/978-3-319-14478-8_8.
- [175] Y. Tokura, N. Nagaosa, Orbital Physics in Transition-Metal Oxides, *Science*. 288 (2000) 462–468. doi:10.1126/science.288.5465.462.
- [176] A. Biswas, K.-S. Kim, Y.H. Jeong, Metal-Insulator Transitions and non-Fermi Liquid Behaviors in 5d Perovskite Iridates, *ArXiv150804929 Cond-Mat.* (2016). doi:10.5772/61285.
- [177] J.G. Bednorz, K.A. Müller, Possible High T_c Superconductivity in the Ba — La — Cu — O System, in: H.R. Ott (Ed.), *Ten Years Supercond. 1980–1990*, Springer Netherlands, 1986: pp. 267–271. doi:10.1007/978-94-011-1622-0_32.
- [178] W.J. Macklin, P.T. Moseley, On the use of oxides for thermoelectric refrigeration, *Mater. Sci. Eng. B.* 7 (1990) 111–117. doi:10.1016/0921-5107(90)90015-4.
- [179] N. Nguyen, F. Studer, B. Raveau, Oxydes ternaires de cuivre a valence mixte de type K_2NiF_4 deficitaires en oxygene: Evolution progressive d'un etat semi-

- conducteur vers un état semi-métallique des oxydes $\text{La}_{2-x}\text{Sr}_x\text{CuO}_{4-x+2\delta}$, *J. Phys. Chem. Solids.* 44 (1983) 389–400. doi:10.1016/0022-3697(83)90066-5.
- [180] A.P. Gonçalves, I.C. Santos, E.B. Lopes, R.T. Henriques, M. Almeida, M.O. Figueiredo, Transport properties of the oxides $\text{Y}_{1-x}\text{Pr}_x\text{Ba}_2\text{Cu}_3\text{O}_{7-\delta}$ ($0 \leq x \leq 1$): Effects of band filling and lattice distortion on superconductivity, *Phys. Rev. B.* 37 (1988) 7476–7481. doi:10.1103/PhysRevB.37.7476.
- [181] A.P.G. Kutty, S.N. Vaidya, Effect of pressure on the thermoelectric power and resistivity of some high- T_c oxides, *High Temp. High Press.* 20 (1988) 475–478.
- [182] S.I. Seok, D.S. Park, S.J. Park, The effect of Cu-sites doping on electrical properties of La_2CuO_4 as thermoelectric material, *J. Mater. Sci. Mater. Electron.* 6 (1995) 140–143. doi:10.1007/BF00190544.
- [183] A.A. Sattar, K.M. El-Shokrofy, A.M. Samy, I. Kashif, A.A. Ghani, High-temperature anomalies of the electrical resistivity and thermoelectric power in $\text{La}_{(2-x)}\text{R}_x\text{CuO}_4$ ($\text{R} = \text{Y}$ and Fe ; $x = 0.0$ and 0.05), *J. Phys. Appl. Phys.* 30 (1997) 266. doi:10.1088/0022-3727/30/2/013.
- [184] Y. Liu, Y.-H. Lin, B.-P. Zhang, H.-M. Zhu, C.-W. Nan, J. Lan, J.-F. Li, High-Temperature Thermoelectric Properties in the $\text{La}_{2-x}\text{R}_x\text{CuO}_4$ ($\text{R}: \text{Pr}, \text{Y}, \text{Nb}$) Ceramics, *J. Am. Ceram. Soc.* 92 (2009) 934–937. doi:10.1111/j.1551-2916.2009.02952.x.
- [185] J.E. Rodriguez, YBCO samples as a possible thermoelectric material, in: 2005: pp. 3605–3608. doi:10.1002/pssc.200461769.
- [186] Y. Horiuchi, W. Tamura, T. Fujii, I. Terasaki, In-plane thermoelectric properties of heavily underdoped high-temperature superconductor $\text{Bi}_2\text{Sr}_2\text{CaCu}_2\text{O}_{8+\delta}$, *Supercond. Sci. Technol.* 23 (2010) 065018. doi:10.1088/0953-2048/23/6/065018.
- [187] S. Heinze, H.-U. Habermeier, G. Cristiani, S.B. Canosa, M.L. Tacon, B. Keimer, Thermoelectric properties of $\text{YBa}_2\text{Cu}_3\text{O}_{7-\delta}$ - $\text{La}_{2/3}\text{Ca}_{1/3}\text{MnO}_3$ superlattices, *Appl. Phys. Lett.* 101 (2012) 131603. doi:10.1063/1.4754707.
- [188] E.F. Schubert, Delta doping of III-V compound semiconductors: Fundamentals and device applications, *J. Vac. Sci. Technol.* 8 (1990) 2980–2996.
- [189] R. Dingle, H.L. Störmer, A.C. Gossard, W. Wiegmann, Electron mobilities in modulation-doped semiconductor heterojunction superlattices, *Appl. Phys. Lett.* 33 (1978) 665. doi:10.1063/1.90457.

- [190] G. Logvenov, A. Gozar, I. Bozovic, High-Temperature Superconductivity in a Single Copper-Oxygen Plane, *Science*. 326 (2009) 699–702. doi:10.1126/science.1178863.
- [191] F. Baiutti, G. Logvenov, G. Gregori, G. Cristiani, Y. Wang, W. Sigle, P.A. van Aken, J. Maier, High-temperature superconductivity in space-charge regions of lanthanum cuprate induced by two-dimensional doping, *Nat. Commun.* 6 (2015) 8586. doi:10.1038/ncomms9586.
- [192] F. Baiutti, G. Gregori, Y. Wang, Y.E. Suyolcu, G. Cristiani, P.A. van Aken, J. Maier, G. Logvenov, Cationic Redistribution at Epitaxial Interfaces in Superconducting Two-Dimensionally Doped Lanthanum Cuprate Films, *ACS Appl. Mater. Interfaces*. 8 (2016) 27368–27375. doi:10.1021/acsami.6b09739.
- [193] Y.E. Suyolcu, Y. Wang, F. Baiutti, A. Al-Temimy, G. Gregori, G. Cristiani, W. Sigle, J. Maier, P.A. van Aken, G. Logvenov, Dopant size effects on novel functionalities: High-temperature interfacial superconductivity, *Sci. Rep.* 7 (2017) 453. doi:10.1038/s41598-017-00539-4.
- [194] A. Wold, B. Post, E. Banks, Rare Earth Nickel Oxides, *J. Am. Chem. Soc.* 79 (1957) 4911–4913. doi:10.1021/ja01575a022.
- [195] N. Gayathri, A.K. Raychaudhuri, X.Q. Xu, J.L. Peng, R.L. Greene, Electronic conduction in LaNiO_{3-x} : the dependence on the oxygen stoichiometry x , *J. Phys. Condens. Matter*. 10 (1998) 1323. doi:10.1088/0953-8984/10/6/015.
- [196] G. Herranz, F. Sánchez, J. Fontcuberta, V. Laukhin, J. Galibert, M.V. García-Cuenca, C. Ferrater, M. Varela, Magnetic field effect on quantum corrections to the low-temperature conductivity in metallic perovskite oxides, *Phys. Rev. B*. 72 (2005) 014457. doi:10.1103/PhysRevB.72.014457.
- [197] A. Tiwari, K.P. Rajeev, Electrical transport in $\text{LaNiO}_{(3-x)}$, *J. Phys. Condens. Matter*. 11 (1999) 3291. doi:10.1088/0953-8984/11/16/010.
- [198] E.J. Moon, J.M. Rondinelli, N. Prasai, B.A. Gray, M. Kareev, J. Chakhalian, J.L. Cohn, Strain-controlled band engineering and self-doping in ultrathin LaNiO_3 films, *Phys. Rev. B*. 85 (2012) 121106. doi:10.1103/PhysRevB.85.121106.
- [199] X. Ding, Q.M. Chen, J. Ma, M. Theingi, Y.J. Li, H. Zhang, Laser Induced Thermoelectric Voltage Effect of $\text{LaNiO}_3/\text{LaAlO}_3$ Multilayer, *Key Eng. Mater.* 519 (2012) 184–187. doi:10.4028/www.scientific.net/KEM.519.184.
- [200] J. Mannhart, D.G. Schlom, Oxide Interfaces—An Opportunity for Electronics, *Science*. 327 (2010) 1607–1611. doi:10.1126/science.1181862.

- [201] A. Tsukazaki, A. Ohtomo, T. Kita, Y. Ohno, H. Ohno, M. Kawasaki, Quantum Hall Effect in Polar Oxide Heterostructures, *Science*. 315 (2007) 1388–1391. doi:10.1126/science.1137430.
- [202] N. Reyren, S. Thiel, A.D. Caviglia, L.F. Kourkoutis, G. Hammer, C. Richter, C.W. Schneider, T. Kopp, A.-S. Ruetschi, D. Jaccard, M. Gabay, D.A. Muller, J.-M. Triscone, J. Mannhart, Superconducting Interfaces Between Insulating Oxides, *Science*. (2007). doi:10.1126/science.1146006.
- [203] J. Chakhalian, J.W. Freeland, G. Srajer, J. Stremper, G. Khaliullin, J.C. Cezar, T. Charlton, R. Dalgliesh, C. Bernhard, G. Cristiani, H.-U. Habermeier, B. Keimer, Magnetism at the interface between ferromagnetic and superconducting oxides, *Nat. Phys.* 2 (2006) 244–248. doi:10.1038/nphys272.
- [204] I. Pallecchi, F. Telesio, D. Li, A. Fête, S. Gariglio, J.-M. Triscone, A. Filippetti, P. Delugas, V. Fiorentini, D. Marré, Giant oscillating thermopower at oxide interfaces, *Nat. Commun.* 6 (2015) 6678. doi:10.1038/ncomms7678.
- [205] M. Lorenz, M.S.R. Rao, T. Venkatesan, E. Fortunato, P. Barquinha, R. Branquinho, D. Salgueiro, R. Martins, E. Carlos, A. Liu, F.K. Shan, M. Grundmann, H. Boschker, J. Mukherjee, M. Priyadarshini, N. DasGupta, D.J. Rogers, F.H. Teherani, E.V. Sandana, P. Bove, K. Rietwyk, A. Zaban, A. Veziridis, A. Weidenkaff, M. Muralidhar, M. Murakami, S. Abel, J. Fompeyrine, J. Zuniga-Perez, R. Ramesh, N.A. Spaldin, S. Ostanin, V. Borisov, I. Mertig, V. Lazenka, G. Srinivasan, W. Prellier, M. Uchida, M. Kawasaki, R. Pentcheva, P. Gegenwart, F.M. Granozio, J. Fontcuberta, N. Pryds, The 2016 oxide electronic materials and oxide interfaces roadmap, *J. Phys. Appl. Phys.* 49 (2016) 433001. doi:10.1088/0022-3727/49/43/433001.
- [206] J. Ravichandran, Thermoelectric and thermal transport properties of complex oxide thin films, heterostructures and superlattices, *J. Mater. Res.* (2016) 1–21. doi:10.1557/jmr.2016.419.
- [207] F. Wrobel, Structural and electronic properties of nickelate heterostructures, (2016). doi:http://dx.doi.org/10.18419/opus-8924.
- [208] J. Son, P. Moetakef, J.M. LeBeau, D. Ouellette, L. Balents, S.J. Allen, S. Stemmer, Low-dimensional Mott material: Transport in ultrathin epitaxial LaNiO₃ films, *Appl. Phys. Lett.* 96 (2010) 062114. doi:10.1063/1.3309713.
- [209] R. Scherwitzl, S. Gariglio, M. Gabay, P. Zubko, M. Gibert, J.-M. Triscone, Metal-Insulator Transition in Ultrathin LaNiO₃ Films, *Phys. Rev. Lett.* 106 (2011) 246403. doi:10.1103/PhysRevLett.106.246403.

- [210] P.D.C. King, H.I. Wei, Y.F. Nie, M. Uchida, C. Adamo, S. Zhu, X. He, I. Božović, D.G. Schlom, K.M. Shen, Atomic-scale control of competing electronic phases in ultrathin LaNiO_3 , *Nat. Nanotechnol.* 9 (2014) 443–447. doi:10.1038/nnano.2014.59.
- [211] A.X. Gray, A. Janotti, J. Son, J.M. LeBeau, S. Ueda, Y. Yamashita, K. Kobayashi, A.M. Kaiser, R. Sutarto, H. Wadati, G.A. Sawatzky, C.G. Van de Walle, S. Stemmer, C.S. Fadley, Insulating state of ultrathin epitaxial LaNiO_3 thin films detected by hard x-ray photoemission, *Phys. Rev. B.* 84 (2011) 075104. doi:10.1103/PhysRevB.84.075104.
- [212] R. Scherwitzl, S. Gariglio, M. Gabay, P. Zubko, M. Gibert, J.-M. Triscone, Metal-Insulator Transition in Ultrathin LaNiO_3 Films, *Phys. Rev. Lett.* 106 (2011) 246403. doi:10.1103/PhysRevLett.106.246403.
- [213] M. Naito, A. Tsukada, T. Greibe, H. Sato, Phase control in $\text{La}_{2-2x}\text{CuO}_{4+\delta}$ epitaxial thin films, *ArXivcond-Mat0209277*. (2002) 140. doi:10.1117/12.455498.
- [214] F. Cordero, R. Cantelli, Interstitial O and O vacancies in $\text{La}_2\text{CuO}_{4+\delta}$ during high-temperature treatments, *Phys. C Supercond.* 312 (1999) 213–224. doi:10.1016/S0921-4534(98)00712-6.
- [215] Z.G. Li, A. hamed, W.J. Zhu, P.H. Hor, Gas effusion studies of oxygen-doped cuprates, *Phys. C Supercond.* 341 (2000) 567–568. doi:10.1016/S0921-4534(00)00595-5.
- [216] F. Cordero, C.R. Grandini, R. Cantelli, Structure, mobility and clustering of interstitial O in $\text{La}_2\text{CuO}_{4+\delta}$ in the limit of small δ , *Phys. C Supercond.* 305 (1998) 251–261. doi:10.1016/S0921-4534(98)00301-3.
- [217] F. Cordero, R. Cantelli, Interstitial O and O vacancies in $\text{La}_2\text{CuO}_{4+\delta}$ during high-temperature treatments, *Phys. C Supercond.* 312 (1999) 213–224.
- [218] J. Maier, Ionic conduction in space charge regions, *Prog. Solid State Chem.* 23 (1995) 171–263. doi:10.1016/0079-6786(95)00004-E.

CURRICULUM VITAE

Name- Surname : Pinar KAYA
Foreign Language : English (Advanced), German (A2)
Place of Birth and Date : Ankara/ 1984
E-mail : P.Kaya@fkf.mpg.de

Education & Experience

- 2014 – 2017 Max-Planck Institute for Solid State Research, Physical Chemistry of Solids, Stuttgart, GERMANY/ PhD Degree (Experimental part)
- 2011 – 2014 Anadolu University, Eskişehir, TURKEY, Department of Materials Science & Engineering/ PhD Degree (Lecture part & Qualifying exam) (3.76/ 4)
- 2011 – 2017 Anadolu University, Eskişehir, TURKEY, Department of Materials Science & Engineering/ Research & Teaching Assistant
- 2007 – 2010 Anadolu University, Eskişehir, TURKEY, Graduate School of Natural Science, Nanotechnology/ M.Sc. Degree (3.58/ 4)
- 2010 April University of Leeds, Leeds Electron Microscopy and Spectroscopy Centre (LEMAS), Leeds, UK/ Researcher & Trainee
- 2002 – 2007 Anadolu University, Eskişehir, TURKEY, Material Science and Engineering/ Undergraduate Degree (3.01/ 4) (3rd place)
- 2006 Spring Technische Universität Hamburg Harburg, GERMANY, Department of Materials Science and Engineering/ Erasmus Student

Conferences and Congresses

- **Kaya, P.**, Gregori G., Baiutti, F., Yordanov, P., Suyolcu Y. E., van Aken, P. A., Cristiani, G., Habermeier, H.-U., Logvenov, G., Maier, J. Influence of interstitial oxygen on thermoelectric properties in $\text{La}_{2-x}\text{Sr}_x\text{CuO}_{4+\delta}$, 3rd Functional Oxide Thin Films for Advanced Energy and Information Technology Conference, Rome, Italy, 5-8 July 2017 (**Poster presentation**)
- **Kaya, P.**, Gregori, G., Yordanov, P., Ayas, E., Habermeier, H. U., Maier, J., & Turan, S. (2017). An alternative composite approach to tailor the thermoelectric

performance in SiAlON, E-MRS Spring Meeting, Strasbourg, France, 22 - 26 May 2017 **(Oral presentation)**

- 5th School Materials for Energy and Sustainability-” and 3rd “EPS-SIF International School on Energy” joined School, Erice, Italy, 13-19 July 2016 **(Participant)**
- IMPRS - Electrochemical Energy Conversion and Storage School, 24-26 October 2016, Max-Planck Institute, Stuttgart, GERMANY **(Participant)**
- **Kaya, P.**, & Turan, S. (2016). Electron Microscopy Study on Hydrothermally Synthesized $(\text{SnO}_2)_x(\text{ZnO})_{1-x}$ Powders., Microscopy and Microanalysis (M&M 2016), Columbus, Ohio, USA, July 24-28 **(Poster presentation)**
- **Kaya, P.**, Kalemantas, A., Arslan, G., Kara, F., & Turan, S., Electron Microscopy Study on the Effect of Si_3N_4 addition to $\text{B}_4\text{C-SiC-Al}$ Composites. Microscopy and Microanalysis (M&M 2016), Columbus, Ohio, USA, July 24-28 **(Poster presentation)**
- **Kaya, P.**, Cinar, A. and Turan, S., "Microstructure and Transport Properties of Pressureless Sintered AlN Ceramics", 22nd National Electron Microscopy Conference, Istanbul, Turkey, September 2015 **(Oral presentation)**
- **Kaya, P.**, Demirel, D. and Turan. S., "Synthesis and Microstructural Characterization of Co-Based Oxide Particles For Thermoelectric Applications" 34th Annual International Conference on Thermoelectrics, 13th European Conference on Thermoelectrics, Dresden, GERMANY, July 2015 **(Poster presentation)**

Articles Published

- **Kaya, P.**, Gregori, G., Yordanov, P., Ayas, E., Habermeier, H. U., Maier, J., & Turan, S. (2017). *An alternative composite approach to tailor the thermoelectric performance in SiAlON and SiC*. Journal of the European Ceramic Society, 37(10), 3367-3373.
- **Kaya, P.**, & Turan, S. (2016). Electron Microscopy Study on Hydrothermally Synthesized $(\text{SnO}_2)_x(\text{ZnO})_{1-x}$ Powders. Microscopy and Microanalysis, 22, 3.
- **Kaya, P.**, Kalemantas, A., Arslan, G., Kara, F., & Turan, S. (2016). Electron Microscopy Study on the Effect of Si_3N_4 addition to $\text{B}_4\text{C-SiC-Al}$ Composites. Microscopy and Microanalysis, 22, 1886-1887.
- Aciksari, C., Tunçolu, İ.G., Suvacı, E., Özel, E., **Kaya, P.**, Rembeza, S., Rembeza, E., Plotnikova, E. and Kosheleva, N. (2016). *The Role of Cation Concentration on*

- Particle Formation Mechanism during Hydrothermal Synthesis of Nanosized Tin Oxide (SnO₂).*" Journal of the Australian Ceramic Society Volume 52, no. 1: 60-71.
- Demirel, S., Oz, E., Altin, E., Altin, S., Bayri, A., **Kaya, P.**, Turan, S. and Avci, S. (2015). "*Growth mechanism and magnetic and electrochemical properties of Na_{0.44} MnO₂ nanorods as cathode material for Na-ion batteries.*" Materials Characterization 105: 104-112.
 - Genç, A., **Kaya, P.**, Ayas, E., Öveçoğlu, M.L. and Turan, S. (2013). "*Microstructural evolution of mechanically alloyed and spark plasma sintered Ni–W alloy matrix composites.*" Journal of Alloys and Compounds 571: 159-167.
 - Kalemtaş, A., Topates, G., Bahadır, O., **Kaya, P.**, Mandal, H. (2013). "*Thermal properties of pressureless melt infiltrated AlN–Si–Al composites.*" Transactions of Nonferrous Metals Society of China 23, no. 5: 1304-1313.

Scientific Memberships

- 2004, Turkish Ceramic Society
- 2004, European Ceramic Society
- 2007, Turkish Electron Microscopy Society
- 2007, European Microscopy Society
- 2013, International Thermoelectric Society